MICROCOPY RESOLUTION TEST CHART
NATIONAL BUREAU OF STANDARDS-1963-A

RADC-TR-82-151
Final Technical Report
December 1982

DIGITAL COMMUNICATIONS IN SPATIALLY DISTRIBUTED INTERFERENCE CHANNELS

Rensselaer Polytechnic Institute

J.W. Modestino, D.G. Daut, V.M. Eyuboglu, K.Y. Jung, K.R. Matis and A.Y. Ningo

APPROVED FOR PUBLIC RELEASE; DISTRIBUTION UNLIMITED

DTIC
ELECTF
MAY 6 1983

A

ROME AIR DEVELOPMENT CENTER
Air Force Systems Command
Griffiss Air Force Base, NY 13441

83 05 06 108

This report has been reviewed by the RADC Public Affairs Office (PA) and is releasable to the National Technical Information Service (NTIS). At NTIS it will be releasable to the general public, including foreign nations.

RADC-TR-82-151 has been reviewed and is approved for publication.

APPROVED: *John O'Graniero*

JOHN A. GRANIERO
Project Engineer

APPROVED: *Bruno Beek*

BRUNO BEEK
Technical Director
Communications Division

FOR THE COMMANDER: *John P. Huss*

JOHN P. HUSS
Acting Chief, Plans Office

REPORT DOCUMENTATION PAGE		READ INSTRUCTIONS BEFORE COMPLETING FORM
1. REPORT NUMBER RADC-TR-82-151	2. GOVT ACCESSION NO. AD-A127741	3. RECIPIENT'S CATALOG NUMBER
4. TITLE (and Subtitle) DIGITAL COMMUNICATIONS IN SPATIALLY DISTRIBUTED INTERFERENCE CHANNELS		5. TYPE OF REPORT & PERIOD COVERED Final Technical Report July 80 - March 81
		6. PERFORMING ORG. REPORT NUMBER N/A
7. AUTHOR(s) J.W. Modestino K.Y. Jung D.C. Daut K.R. Mathis V.M. Eyuboglu A.Y. Ningo		8. CONTRACT OR GRANT NUMBER(s) F30602-78-C-0083
9. PERFORMING ORGANIZATION NAME AND ADDRESS Rensselaer Polytechnic Institute Electrical, Computer & Systems Engineering Troy NY 12181		10. PROGRAM ELEMENT, PROJECT, TASK AREA & WORK UNIT NUMBERS 61102F 2305J8P6
11. CONTROLLING OFFICE NAME AND ADDRESS Rome Air Development Center (DCCR) Griffiss AFB NY 13441		12. REPORT DATE December 1982
		13. NUMBER OF PAGES 218
14. MONITORING AGENCY NAME & ADDRESS(If different from Controlling Office) Same		15. SECURITY CLASS. (of this report) UNCLASSIFIED
		15a. DECLASSIFICATION/DOWNGRADING SCHEDULE N/A

16. DISTRIBUTION STATEMENT (of this Report)

Approved for public release; distribution unlimited

17. DISTRIBUTION STATEMENT (of the abstract entered in Block 20, if different from Report)

Same

18. SUPPLEMENTARY NOTES

RADC Project Engineer: John A. Graniero (DCCR)

19. KEY WORDS (Continue on reverse side if necessary and identify by block number)
Digital Communications
Encoding/Decoding
Error Correction Codes
Adaptive Arrays

20. ABSTRACT (Continue on reverse side if necessary and identify by block number)
This report is concerned with the characteristics of the structure and performance of digital communication systems operating in spatially distributed interference channels when a multi-element array processing capability is available. It represents one phase of a continuing investigation and covers the period 1 July 1980 through 31 March 1981.

This report is organized into five parts. Part I describes an optimum receiver structure for digital communication in spatially distributed (over)

DD FORM 1473   EDITION OF 1 NOV 65 IS OBSOLETE
1 JAN 73

interference when a multi-element array capability is available and under specific and somewhat simplified modeling assumptions. The results are useful in demonstrating the subtle interactions between spatial and temporal processing characteristics of an optimum receiver, particularly the modulation/coding tradeoffs. Part II discusses some new reduced complexity soft-decision decoding algorithms for linear block codes while Part III describes some new rational-rate convolutional code constructions. Both of these should be useful in impulsive or burst interference environments. In Part V we describe some results on the modeling and analysis of selected linear and nonlinear receiver structures in impulsive or burst noise channels. Finally, an outline of how multi-element adaptive array processing structures are to be incorporated into the RPI developed Interactive Communications Simulator (ICS) is provided in Part V. It should be noted that these four parts have been written as logically distinct entities and as a result there is some repetition of basic material.

Abstract

This report is concerned with the characterization of the structure
and performance of digital communication systems operating in spatially
distributed interference channels when a multi-element array processing
capability is available. It represents one phase of a continuing investi-
gation and covers the period 1 July, 1980 through 31 March, 1981.

This report is organized into five parts. Part I describes an optimum
receiver structure for digital communication in spatially distributed inter-
ference when a multi-element array capability is available and under spec-
ific and somewhat simplified modeling assumptions. The results are useful
in demonstrating the subtle interactions between spatial and temporal pro-
cessing characteristic of an optimum receiver, particularly the modulation/
coding tradeoffs. Part II discusses some new reduced compexity soft-
decision decoding algorithms for linear block codes while Part III describes
some new rational-rate convolutional code constructions. Both of these
should be useful in impulsive or burst interference environments. In Part
IV we describe some results on the modeling and analysis of selected linear
and nonlinear receiver structures in impulsive or burst noise channels.
Finally, an outline of how multi-element adaptive array processing struct-
ures are to be incorporated into the RPI developed Interactive Communica-
tions Simulator (ICS) is provided in Part V. It should be noted that these
four parts have been written as logically distinct entities and as a result
there is some repetition of basic material.

Accession For

NTIS GRA&I	☑
DTIC TAB	☐
Unannounced	☐
Justification	

By

Distribution/

Availability Codes

Dist	Avail and/or Special

i

TABLE OF CONTENTS   PAGE

Glossary of Frequently Used Terminology

ALCR – Average Level-Crossing Rate

APD – Amplitude Probability Distribution

BFSK – Binary Frequency-Shift Keyed

BPSK – Binary Phase-Shift Keyed

CCV – Code Connection Vector

Ch.f. – Characteristic Function

DPSK – Differential Phase-Shift Keyed

E_b/N_0 – Bit Energy to Noise Spectral Density

E_s/N_0 – Symbol Energy to Noise Spectral Density

GSNR – Generalized Signal-to-Noise Ratio

ICS – Interactive Communications Simulator

ISI – Intersymbol Interference

LMS – Least Mean-Square

ML – Maximum Likelihood

MSK – Minimum Shift Keyed

p.d.f. – Probability Density Function

P_b – Bit Error Probability

P_e – Symbol Error Probability

QPSK – Quadrature Phase-Shift Keyed

VA – Viterbi Algorithm

ZMNL – Zero-Memory Nonlinearity

PART I

ADAPTIVE MULTI-ELEMENT RECEIVER STRUCTURE FOR MAXIMUM-LIKELIHOOD

SEQUENCE ESTIMATION IN A SPATIALLY DISTRIBUTED INTERFERENCE CHANNEL

I. Introduction:

In synchronous carrier-modulated digital communication systems the main impediments to reliable transmission are intersymbol interference (ISI), additive channel noise, and errors associated with the ancillary functions of phase tracking and symbol synchronization. For single-element systems, receiver structures have been devised [1]-[3] which deal with these issues in an optimum manner. Specifically, under appropriate modeling assumptions, the reception problem is posed as one of maximum-likelihood (ML) sequence estimation. This assures that the receiver is optimum in the sense of minimizing the sequence-error probability, provided, of course, that all sequences are equally likely. By now these single-element receiver structures have been thoroughly researched and are quite well understood.

In an increasing number of important applications, however, one of the major impediments to reliable communications is the effect of spatially distributed interference. This may be due to hostile electronic countermeasures (ECM) or jamming, or unintentional radio-frequency interference (RFI). With the addition of a multi-element array capability it is possible to provide spatial filtering in an effort to combat this interference by exploiting its spatially distributed nature. It is of some interest then to explore the structure and properties of ML sequence estimating receivers under the assumption of spatially distributed interference and the availability of an adaptive multi-element array capability.

The present report describes some preliminary work directed toward the development of optimum adaptive multi-element receiver structures for digital communications in the presence of spatially distributed interference.

Specifically, we describe an optimum receiver structure under specific modeling assumptions for ML estimation of a linear carrier-modulated binary data sequence. This optimum structure consists of an interference suppression spatial filter followed by a matched filter sampled at the baud rate, and a recursive nonlinear processor employing the Viterbi algorithm (VA) to perform ML sequence estimation. The result is a practically implementable optimum spatial/temporal processor which provides a significant multi-element extension of previous single-element receiver structures described in [2],[3].

Some preliminary modeling assumptions are provided in Section II. This is followed by the development of the optimum ML receiver structure in Section III. The VA sequence estimator is described in Section IV. An adaptive implementation of the ML receiver structure is described in Section V. Finally, a summary and conclusions can be found in Section VI.

II. Preliminaries:

In what follows we will make exclusive use of complex signal and noise representations. Specifically, the received signal at the output of the i'th array element is assumed of the form

$$r_i(t) = \sqrt{2} \; \text{Re}\{\tilde{r}_i(t)e^{j2\pi f_c t}\} \quad ; \quad i=1,2,\ldots,N, \tag{1}$$

where f_c is an assumed known carrier frequency in Hz and $\tilde{r}_i(t) = r_{ci}(t) - jr_{si}(t)$ is the corresponding complex envelope. The quantities $r_{ci}(t)$ and $r_{si}(t)$ are lowpass waveforms representing the inphase and quadrature (I/Q) components, respectively. We assume that $\tilde{r}_i(t)$ can be expressed in the form

$$\tilde{r}_i(t) = \tilde{s}_{i0}(t;\underline{\tilde{c}},\tau,\phi) + \tilde{n}_i(t) \quad ; \quad i=1,2,\ldots,N, \tag{2}$$

where $\tilde{n}_i(t)$ is the total additive noise, consisting of both spatially distributed interference and thermal element noise, at the output of the i'th element

and $\tilde{s}_{i0}(t;\underline{\tilde{c}},\tau,\phi)$ is the corresponding signal component. The quantity[†] $\underline{\tilde{c}}$ is a complex vector of dimension 2M+1 representing the binary data sequence to be transmitted in a manner specific to the modulation strategy in use while τ and ϕ represent unknown timing delay and phase offset, respectively. We suppose that the complex envelope of the signal component can in turn be expressed as

$$\tilde{s}_{i0}(t;\underline{\tilde{c}},\tau,\phi) = \int_{-\infty}^{\infty} \tilde{h}_{i0}(t-\sigma)\tilde{s}(\sigma;\underline{\tilde{c}},\tau,\phi)d\sigma \; ; \quad i=1,2,\ldots,N. \tag{3}$$

Here $\tilde{s}(t;\underline{\tilde{c}},\tau,\phi)$ is the transmitted signal component as it would appear at the output of an ideal isotropic sensor. The quantity $\tilde{h}_{i0}(t)$ in (3) represents the complex impulse response of the signal path, including channel filtering effects and propagation across the array aperture. For example, if no channel filtering effects are present $\tilde{h}_{i0}(t)=\delta(t-\tau_{i0})e^{j2\pi f_c \tau_{i0}}$ where τ_{i0} is the relative delay in receiving the signal component at the i'th sensor measured with respect to some fixed phase center or origin of spatial coordinates. The impulsive component accounts for the group delay of the complex envelope, while the complex expoential accounts for the relative phase shift of the carrier. The quantities τ_{i0}, i=1,2,...,N can generally be calculated from knowledge of the signal direction and the assumed array geometry. For example, consider the linear array illustrated in Fig. 1 with signal direction indicated by the angle θ_s measured with respect to boresight. If the distance in wavelengths of the i'th element from the origin is d_i' then $\tau_{i0}=\pm d_i'\sin\theta_s$, i=1,2,...,N with the algebraic sign depending upon which side of the phase center the element lies. In what follows, we assume that the signal direction,

---

[†] In what follows all vectors are to be considered column vectors so that $\underline{\tilde{c}}^T=(\tilde{c}_{-M},\tilde{c}_{-M+1},\ldots,\tilde{c}_0,\ldots,\tilde{c}_{M-1},\tilde{c}_M)$.

θ_s in Fig. 1, is known a priori although this could be included in addition to τ and ϕ as a parameter to be estimated.

In general, some channel filtering is present so that the signal path impulse response function can be represented as $\tilde{h}_{i0}(t)=\tilde{h}_c(t-\tau_{i0})e^{j2\pi f_c\tau_{i0}}$, where $\tilde{h}_c(t)$ is the channel impulse response common to all elements. For the channels of interest, the bandwidth B_c will always be such that $B_c\tau_{i0}<<1$ and hence $\tilde{h}_c(t-\tau_{i0})\approx\tilde{h}_c(t)$, $i=1,2,\ldots,N$. Under this assumption $\tilde{h}_{i0}(t)=\tilde{h}_c(t)e^{j2\pi f_c\tau_{i0}}$, $i=1,2,\ldots,N$, which will be the form used in what follows.

The transmitted signals of interest will be assumed of the form[†]

$$\tilde{s}(t;\underline{\tilde{c}},\tau,\phi)=\sum_{m=-M}^{M}\tilde{c}_m\tilde{g}(t-mT_s-\tau)e^{j\phi}; \quad -(M+1/2)T_s\leq t\leq(M+1/2)T_s , \qquad (4)$$

where T_s is the channel signaling element or baud interval and $\tilde{g}(t)$ is a complex lowpass pulse-like waveform vanishing outside the interval $-T_s/2\leq t\leq T_s/2$. It follows, according to preceding comments, that

$$\tilde{s}_{i0}(t;\underline{\tilde{c}},\tau,\phi)=\sum_{m=-M}^{M}\tilde{c}_m\tilde{h}(t-mT_s-\tau)e^{j(\phi+\phi_{i0})}; \quad i=1,2,\ldots,N , \qquad (5)$$

where $\phi_{i0}\overset{\Delta}{=}2\pi f_c\tau_{i0}$ and $\tilde{h}(t)=\tilde{g}(t)\otimes\tilde{b}_c(t)$ represents the convolution of the baseband pulse waveform and the channel impulse response.

Consider now the additive noise term $\tilde{n}_i(t)$ in (2). We assume this can be written in the form

$$\tilde{n}_i(t)=\tilde{y}_{i0}(t)+\tilde{w}_i(t); \quad i=1,2,\ldots,N , \qquad (6)$$

where $\tilde{y}_{i0}(t)$ represents spatially distributed interference at the output of the i'th element and $\tilde{w}_i(t)$ is a complex zero-mean white Gaussian noise (WGN) process assumed independent from element-to-element. Specifically,

---

[†] Note that we are restricting attention to linear carrier modulation formats. Certain offset quadrature modulation schemes such as MSK do not fit into this formulation.

$\tilde{w}_i(t) = w_{ci}(t) - jw_{si}(t)$, with the I/Q components $w_{ci}(t)$ and $w_{si}(t)$ mutually independent WGN processes with double-sided noise spectral density $N_0/2$ watts/Hz. We assume that $\tilde{y}_i(t)$ can be represented in the form

$$\tilde{y}_{i0}(t) = \sum_{j=1}^{J} \tilde{y}_j(t-\tau_{ij})e^{j\phi_{ij}} \; ; \quad i=1,2,\ldots,N \; . \qquad (7)$$

Here $\tilde{y}_j(t)$ represents the j'th interference component originating from some unknown direction. For example, in the case of a linear array, the direction of the j'th interferer is indicated by the off-boresight angle θ_j as illustrated in Fig. 1. The quantity τ_{ij} represents the relative delay experienced by the j'th interfering signal as intercepted at the i'th element, $i=1,2,\ldots,N$, $j=1,2,\ldots,J$. Again, in the case of a linear array we have $\tau_{ij}=\pm d_i'\sin\theta_j$. Similarly, the phase factors ϕ_{ij} in (7) are given by $\phi_{ij}=2\pi f_c \tau_{ij}$.

The individual interfering signals $\tilde{y}_j(t)$, $j=1,2,\ldots,J$ are generally complex broadband processes. We will make the simplifying assumption in what follows that these quantities are all complex mutually uncorrelated zero-mean Gaussian processes with covariance functions[†]

$$K'_{\tilde{y}_j \tilde{y}_j}(t,s) = E\{\tilde{y}_j(t)\tilde{y}_j^*(s)\} \; ; \quad j=1,2,\ldots,J \; . \qquad (8)$$

It follows that the total noise power $\tilde{n}_i(t)$ at the output of the i'th sensor is Gaussian with cross-covariance function

$$K_{\tilde{n}_i \tilde{n}_j}(t,s) = K_{\tilde{y}_i \tilde{y}_j}(t,s) + N_0\delta(t-s) \; ; \quad i=j$$
$$= K_{\tilde{y}_i \tilde{y}_j}(t,s) \qquad\qquad ; \quad i\neq j \qquad (9)$$

where

$$K_{\tilde{y}_i \tilde{y}_j}(t,s) = E\{\tilde{y}_{i0}(t)\tilde{y}_{j0}^*(s)\} = \sum_{k=1}^{J} K'_{\tilde{y}_k \tilde{y}_k}(t-\tau_{ik}, s-\tau_{jk})e^{j(\phi_{ik}-\phi_{jk})}. \qquad (10)$$

This information will be made use of in what follows.

---

† We have tried to indicate complex scalar quantities with a tilde "~". Covariance functions, system transfer functions and all matrix quantities will be implicitly assumed complex so that the tilde will be eliminated.

III. Maximum-Likelihood Receiver Structure:

The element output signal can be expressed in vector form as

$$\tilde{\underline{r}}(t) = \tilde{\underline{s}}_0(t;\tilde{\underline{c}},\tau,\phi)+\tilde{\underline{n}}(t) \tag{11}$$

where $\tilde{\underline{r}}^T(t)=(\tilde{r}_1(t),\tilde{r}_2(t),\ldots,\tilde{r}_N(t))$ with $\tilde{\underline{s}}_0(t;\tilde{\underline{c}},\tau,\phi)$ and $\tilde{\underline{n}}(t)$ obtained similarly from the corresponding elements of $\tilde{\underline{r}}(t)$. Given the quantities $\tilde{\underline{c}},\tau,\phi$, and, of course, the signal phase factor $\underline{\phi}_0^T=(\phi_{10},\phi_{20},\ldots,\phi_{NQ})$, the signal vector $\tilde{\underline{s}}_0(t;\tilde{\underline{c}},\tau,\phi)$ is completely known[†]. The quantity $\tilde{\underline{r}}(t)$ is then a complex Gaussian process with mean-value function $\tilde{\underline{s}}_0(t;\tilde{\underline{c}},\tau,\phi)$ and covariance matrix $\underline{\underline{K}}_{\tilde{r}\tilde{r}}(t,s)=\underline{\underline{K}}_{\tilde{n}\tilde{n}}(t,s)$ where[††]

$$\underline{\underline{K}}_{\tilde{n}\tilde{n}}(t,s)=E\{\tilde{\underline{n}}(t)\tilde{\underline{n}}^\dagger(s)\}=\underline{\underline{K}}_{\tilde{y}\tilde{y}}(t,s)+N_0\,\underline{\underline{I}}\,\delta(t-s)\ . \tag{12}$$

Here $\underline{\underline{I}}$ is the NxN identity matrix and $\underline{\underline{K}}_{\tilde{y}\tilde{y}}(t,s)\overset{\Delta}{=}E\{\tilde{\underline{y}}_0(t)\tilde{\underline{y}}_0^\dagger(s)\}$ is the covariance matrix associated with the vector interference process $\tilde{\underline{y}}_0^T(t)=(\tilde{y}_{10}(t),\tilde{y}_{20}(t),\ldots,\tilde{y}_{N0}(t))$. From previous comments

$$\underline{\underline{K}}_{\tilde{y}\tilde{y}}(t,s)=\begin{bmatrix} K_{\tilde{y}_1\tilde{y}_1}(t,s) & K_{\tilde{y}_1\tilde{y}_2}(t,s) & \cdots\cdots\cdots & K_{\tilde{y}_1\tilde{y}_N}(t,s) \\ K_{\tilde{y}_2\tilde{y}_1}(t,s) & K_{\tilde{y}_2\tilde{y}_2}(t,s) & \cdots\cdots\cdots & K_{\tilde{y}_2\tilde{y}_N}(t,s) \\ \vdots & \vdots & & \vdots \\ K_{\tilde{y}_N\tilde{y}_1}(t,s) & K_{\tilde{y}_N\tilde{y}_2}(t,s) & \cdots\cdots\cdots & K_{\tilde{y}_N\tilde{y}_N}(t,s) \end{bmatrix}, \tag{13}$$

with the cross-covariance terms $K_{\tilde{y}_i\tilde{y}_J}(t,s)$ given by (10).

As a relatively straightforward application of known results (cf. [4], [5]), it can be shown that the log-likelihood functional for observing $\tilde{\underline{r}}(t)$ given fixed values of the parameters $\tilde{\underline{c}}$, τ, and ϕ is given by

---

[†] The signal path overall impulse response function $\tilde{h}(t)$ is also assumed known.

[††] Here, and in what follows, the symbol "$\dagger$" will represent complex conjugate transpose.

$$\ell\{\tilde{\underline{r}}(t);\tilde{\underline{c}},\tau,\phi\}= \text{Re}\left\{ \int_{-\infty}^{\infty}\int_{-\infty}^{\infty} \tilde{\underline{r}}^{\dagger}(t)\underline{\underline{Q}}_{\tilde{n}\tilde{n}}(t,u)\tilde{\underline{s}}_0(u;\tilde{\underline{c}},\tau,\phi)dtdu\right\}$$

$$-\frac{1}{2}\int_{-\infty}^{\infty}\int_{-\infty}^{\infty} \tilde{\underline{s}}_0^{\dagger}(t;\tilde{\underline{c}},\tau,\phi)\underline{\underline{Q}}_{\tilde{n}\tilde{n}}(t,u)\tilde{\underline{s}}_0(u;\tilde{\underline{c}},\tau,\phi)dtdu \quad , \qquad (14)$$

where $\underline{\underline{Q}}_{\tilde{n}\tilde{n}}(t,u)$ is an NxN Hermitian matrix, called the inverse covariance matrix, satisfying

$$\int_{-\infty}^{\infty} \underline{\underline{K}}_{\tilde{n}\tilde{n}}(t,u)\underline{\underline{Q}}_{\tilde{n}\tilde{n}}(u,s)du = \underline{\underline{I}}\ \delta(t-s) \quad . \qquad (15)$$

Substitution of (5) into the argument of the first term on the right-hand side of (14) yields

$$\int_{-\infty}^{\infty}\int_{-\infty}^{\infty} \tilde{\underline{r}}^{\dagger}(t)\underline{\underline{Q}}_{\tilde{n}\tilde{n}}(t,u)\tilde{\underline{s}}_0(u;\tilde{\underline{c}},\tau,\phi)dtdu$$

$$= \tilde{\underline{r}}^{\dagger}\tilde{\underline{c}} \quad , \qquad (16)$$

where $\tilde{\underline{r}}$ is now a vector of length 2M+1, with components defined according to

$$\tilde{r}_m = \int_{-\infty}^{\infty}\int_{-\infty}^{\infty} \tilde{\underline{r}}^{T}(t)\underline{\underline{Q}}_{\tilde{n}\tilde{n}}^{*}(t,u)\tilde{h}^{*}(u-mT_s-\tau)e^{-j\phi}\tilde{\underline{\xi}}_0 dtdu \quad ; \ m=0,\pm1,\ldots,\pm M. \quad (17)$$

Here[†] $\tilde{\underline{\xi}}_0$ is a complex N-vector defined according to $\tilde{\underline{\xi}}_0^{T}=(e^{-j\phi_{10}},e^{-j\phi_{20}},\ldots,e^{-j\phi_{N0}})$. After some simple algebra it can be shown that $\tilde{r}_m$ can be expressed in the form

$$\tilde{r}_m = \int_{-\infty}^{\infty} \tilde{\underline{r}}^{T}(t)e^{-j\phi}\underline{\underline{G}}^{*}(t-(mT_s+\tau))\tilde{\underline{\xi}}_0 dt$$

$$=\tilde{\underline{\xi}}_0^{T}\tilde{\underline{x}}_m \qquad ; \ m=0,\pm1,\pm2,\ldots,\pm M \quad , \qquad (18)$$

where

$$\tilde{\underline{x}}_m = \left[\underline{\underline{G}}^{\dagger}(-t) \otimes \{\tilde{\underline{r}}(t)e^{-j\phi}\}\right]\Big|_{t=mT_s+\tau} \quad ;m=0,\pm1,\pm2,\ldots,\pm M \quad , \qquad (19)$$

---

† As we will see $\tilde{\underline{\xi}}_0$ is merely a beam-steering vector which allows pointing
a beam in the known signal direction.

with

$$\underline{\underline{G}}(t) \triangleq \int_{-\infty}^{\infty} \underline{\underline{Q}}_{\widetilde{nn}}(t-u)\widetilde{h}(u)du \ ; \quad -\infty < t < \infty,\tag{20}$$

and we have implicitly assumed here, and in what follows, that the interference process $\underline{\widetilde{y}}_0(t)$ is wide-sense stationary (w.s.s.) so that $\underline{\underline{K}}_{\widetilde{nn}}(t,u)=\underline{\underline{K}}_{\widetilde{nn}}(t-u)$ and similarly, at least for long observation intervals, that $\underline{\underline{Q}}_{\widetilde{nn}}(t,u)=\underline{\underline{Q}}_{\widetilde{nn}}(t-u)$. Equivalently, it can be shown that $\underline{\underline{G}}(t)$ satisfies the matrix integral equation

$$\int_{-\infty}^{\infty} \underline{\underline{K}}_{\widetilde{nn}}(t,s)\underline{\underline{G}}(s)ds=\underline{\underline{I}}\ \widetilde{h}(t) \ ; \quad -\infty < t < \infty.\tag{21}$$

The quantity $\underline{\widetilde{x}}_m$, m=0, 1, 2,..., M in (19) has an interpretation as the sampled output of a multi-channel filter with impulse response matrix $\underline{\underline{G}}^{\dagger}(-t)$ and input $\underline{\widetilde{r}}(t)e^{-j\phi}$. Sampling is assumed to take place at the times $t=mT_s+\tau$, m=0,±1,±2,...,±M. The vector $\underline{\widetilde{x}}_m$ is then weighted by the beam-steering vector $\underline{\widetilde{\xi}}_0$ to form $\widetilde{r}_m$ according to (18). This weighting effectively orients the array of elements to point in the known signal direction. A block diagram of a scheme for generating the sequence $\{\widetilde{r}_m\}$ is then as illustrated in Fig. 2. Note that the beam steering is accomplished at the output of the multi-channel filter and not the input as in most conventional adaptive array systems. It should also be noted that in the absence of spatially distributed interference, or indeed merely the absence of correlation across the array elements, (21) is trivially solved with $\underline{\underline{G}}(t)$ proportional to a diagonal matrix with $\widetilde{h}(t)$ along the main diagonal.

In a similar manner, it can be shown that the integral appearing in the second term in (14) can be expressed as

$$\int_{-\infty}^{\infty}\int_{-\infty}^{\infty} \underline{\underline{s}}_0^{\dagger}(t;\underline{c},\tau,\phi)\underline{\underline{Q}}_{\widetilde{nn}}(t,u)\underline{\underline{s}}_0(u;\underline{c},\tau,\phi)dtdu=\underline{c}^{\dagger}\underline{\underline{H}}\ \underline{c} \ ,\tag{22}$$

where $\underline{\underline{H}}$ is an Hermitian matrix of size (2M+1)x(2M+1) independent of the

observations with (m,n) element h_{m-n} given by

$$\tilde{h}_{m-n} = \underline{\xi}_0^\dagger \left\{ \int_{-\infty}^\infty \int_{-\infty}^\infty \tilde{h}^*(t-mT_s-\tau) \underline{\underline{Q}}_{\tilde{n}\tilde{n}}(t-u) \tilde{h}(u-nT_s-\tau) \, dt \, du \right\} \underline{\xi}_0; \quad m,n=0,\pm 1,$$
$$\ldots, \pm M. \quad (23)$$

Again we assume that all quantities in (23) are known so that $\underline{\underline{H}}$ in (22) is readily evaluated.

It follows from the preceding that the log-likelihood functional in (14) can then be expressed in the form

$$\ell\{\underline{\tilde{r}}(t); \underline{\tilde{c}}, \tau, \phi\} = \text{Re}\{\underline{\tilde{r}}^\dagger \underline{\tilde{c}}\} - (1/2)\underline{\tilde{c}}^\dagger \underline{\underline{H}} \, \underline{\tilde{c}}$$
$$= (1/2)\{\underline{\tilde{r}}^\dagger \underline{\tilde{c}} + \underline{\tilde{c}}^\dagger \underline{\tilde{r}} - \underline{\tilde{c}}^\dagger \underline{\underline{H}} \, \underline{\tilde{c}}\} \quad (24)$$
$$= (1/2)\{\underline{\tilde{r}}^\dagger \underline{\underline{H}}^{-1}\underline{\tilde{r}} - (\underline{\tilde{c}} - \underline{\underline{H}}^{-1}\underline{\tilde{r}})^\dagger \underline{\underline{H}}(\underline{\tilde{c}} - \underline{\underline{H}}^{-1}\underline{\tilde{r}})\}$$

where the last equality is easily verified through simple vector-matrix algebra. The objective then is to choose estimates $\hat{\underline{\tilde{c}}}, \hat{\tau}$ and $\hat{\phi}$ to maximize this quantity. It should be clear from (24) that the vector $\underline{\tilde{r}}$, representing the sequence of outputs from the processor illustrated in Fig. 2, provides a sufficient statistic for extracting all the parameters.

The system illustrated in Fig. 2 for generating the sequence of observables $\{\tilde{r}_m\}$ provides combined spatial/temporal processing in the single multi-channel filter with impulse response matrix $\underline{\underline{G}}^\dagger(-t)$. It may be desirable in some cases to separate the spatial and temporal processing to the extent possible. Indeed, this is generally the case in conventional array processing systems. This can be accomplished by observing that $\tilde{r}_m$ in (17) can alternately be expressed in the form

$$\tilde{r}_m = \left[\tilde{h}^*(-t) \otimes \{\tilde{x}'(t)e^{-j\phi}\} \right]\Big|_{t=mT_s+\tau} \quad ; m=0,\pm 1,\ldots,\pm M, \quad (25)$$

where now

$$\tilde{x}'(t) = \underline{\xi}_0^T [\underline{\underline{Q}}_{\tilde{n}\tilde{n}}(t) \otimes \underline{\tilde{r}}(t)] \quad ; \quad -\infty < t < \infty. \quad (26)$$

The term within brackets in (26) represents again a combined spatial/temporal multi-channel filtering operation although the common "matched filtering" operation, represented by the convolution with $h^*(-t)$, is now performed separately at the array output. This is illustrated in block diagram form in Fig. 3 where the spatial/temporal processor in the array forming network now has impulse response matrix $\underset{\approx}{Q}_{nn}(t)$.

In either case, the multi-element ML processor then chooses the estimated sequence $\hat{\underline{c}}$ to maximize the log-likelihood functional in (24) while the timing and phase estimates, $\hat{\tau}$ and $\hat{\theta}$ respectively, solve the coupled equations

$$\frac{\partial \ell\{\tilde{r}(t);\hat{\underline{c}},\hat{\tau},\hat{\phi}\}}{\partial \hat{\tau}} = 0 \qquad (27a)$$

and

$$\frac{\partial \ell\{\tilde{r}(t);\hat{\underline{c}},\hat{\tau},\hat{\phi}\}}{\partial \hat{\theta}} = 0 \quad . \qquad (27b)$$

Clearly then $\hat{\underline{c}}$ is chosen as the "legitimate" sequence minimizing the performance measure

$$J(\tilde{\underline{c}}) = (\tilde{\underline{c}} - \underset{\approx}{H}^{-1}\tilde{\underline{r}})^{\dagger} \underset{\approx}{H} (\tilde{\underline{c}} - \underset{\approx}{H}^{-1}\tilde{\underline{r}}). \qquad (28)$$

Note that the solution is not merely $\hat{\underline{c}} = \underset{\approx}{H}^{-1}\tilde{\underline{r}}$ since this is in general analog-valued and need not be a legitimate data sequence. As shown in [2], the operation $\underset{\approx}{H}^{-1}$ represents an equalizer, in this case attempting both to equalize the effects of ISI and spatially distributed interference. The conventional approach to obtaining $\hat{\underline{c}}$ is to pass the observation sequence, represented in this case by $\tilde{\underline{r}}$, through an equalizer and then quantize the output on a symbol-by-symbol basis to the closest valid data symbol value. In the next section we describe how the VA can be used to choose the ML estimate $\hat{\underline{c}}$. First we show how the estimates $\hat{\tau}$ and $\hat{\phi}$ can be chosen in a decision-directed manner to satisfy the ML equation (27).

Suppose that a sequence of observations each of total length $(2M+1)T_s$ are made by sliding the observation window by K baud at each iteration. Let $\tilde{r}_i(t)$ represent the N-vector of observations obtained at the i'th iteration, i.e., for t in the range $(iK-M-1/2)T_s \leq t \leq (iK+M+1/2)T_s$. Note that if $K=2M+1$ there will be no overlap in the observation windows while if $K=1$ the window is merely slid by one baud each iteration. At any rate, according to (24) the log-likelihood functional is given by

$$\ell\{\tilde{r}_i(t);\underline{\tilde{c}}_i,\tau,\phi\} = \text{Re}\{\underline{\tilde{c}}_i^\dagger \underline{\tilde{r}}_i\} - (1/2)\underline{\tilde{c}}_i^\dagger \underline{\underline{H}} \, \underline{\tilde{c}}_i \quad , \tag{29}$$

where now $\underline{\tilde{r}}_i^T = (\tilde{r}_{iK-M}, \tilde{r}_{iK-M+1}, \ldots, \tilde{r}_{iK}, \ldots, \tilde{r}_{iK+M})$, and similarly, $\underline{\tilde{c}}_i^T = (\tilde{c}_{iK-M}, \tilde{c}_{iK-M+1}, \ldots, \tilde{c}_{iK}, \ldots, \tilde{c}_{iK+M})$. It follows that

$$\frac{\partial\ell\{\underline{\tilde{r}}_i(t);\underline{\tilde{c}}_i,\tau,\phi\}}{\partial\tau} = \text{Re}\{\underline{\tilde{c}}_i^\dagger \underline{\overset{*}{r}}_i\} \quad , \tag{30a}$$

and

$$\frac{\partial\ell\{\underline{\tilde{r}}_i(t);\underline{\tilde{c}}_i,\tau,\phi\}}{\partial\phi} = \text{Im}\{\underline{\tilde{c}}_i^\dagger \underline{\tilde{r}}_i\} \quad , \tag{30b}$$

where according to either (18) or (25) we have the m'th element of $\underline{\overset{*}{r}}_i$ given by

$$\overset{*}{r}_{i,m} = \frac{d}{dt}\{\underline{\xi}_0^T[\underline{g}^\dagger(-t) \otimes \{\underline{\tilde{r}}_i(t)e^{-j\phi}\}]\}\Big|_{t=(iK+m)T_s+\tau} \quad ; m=0,\pm1,\ldots,\pm M \tag{31a}$$

or †

$$\overset{*}{r}_{i,m} = \frac{d}{dt}[\tilde{h}*(-t) \otimes \{\tilde{x}_i'(t)e^{-j\phi}\}]\Big|_{t=(iK+m)T_s+\tau} \quad ; m=0,\pm1,\ldots,\pm M \quad , \tag{31b}$$

respectively. In either case, the estimates can be generated recursively according to the stochastic gradient schemes

$$\hat{\phi}_{i+1} = \hat{\phi}_i + \alpha_i \text{Im}\{\underline{\hat{\tilde{c}}}_i^\dagger \underline{\tilde{r}}_i\} \quad ; \quad i=0,1,\ldots \tag{32a}$$

and

$$\hat{\tau}_{i+1} = \hat{\tau}_i + \beta_i \text{Re}\{\underline{\hat{\tilde{c}}}_i^\dagger \underline{\overset{*}{r}}_i\}; \quad i=0,1,\ldots \quad , \tag{32b}$$

$\dagger$ Again $\tilde{x}_i'(t)$ represents observations on $\tilde{x}'(t)$ over the window $(iK-M-1/2)T_s \leq t \leq (iK+M+1/2)T_s$.

Here $\hat{\theta}_0$, $\hat{\tau}_0$ are arbitrary and the positive real step sizes $\{\alpha_i\}$ and $\{\beta_i\}$ must be specified. Note that the recursive estimators described by (32) are decision-directed in the sense that estimated sequences $\{\hat{\tilde{c}}_i\}$ are actually used in place of the actual but unknown sequences $\{\tilde{c}_i\}$. The resulting decision-directed structure is illustrated in Fig. 4.

As a special case, suppose we use non-overlapping blocks (i.e., K=2M+1) of matched filter outputs with

$$\sum_{i=0}^{\infty} \alpha_i = \infty \quad ; \quad \sum_{i=0}^{\infty} \alpha_i^2 < \infty \qquad (33)$$

and similarly for $\{\beta_i\}$. This is the so-called Robbins-Monro⁺ stochastic approximation algorithm. Here it can be shown that convergence to the true ML estimates is obtained both in mean-square and with probability one. In practice it may be desirable to update the timing and phase errors more frequently, say at the baud rate by taking K=1. Convergence is not assured in this case.

IV. Viterbi Algorithm Sequence Estimator:

We describe now how the VA is to be used to obtain the ML estimate $\hat{\tilde{c}}$ of a transmitted data sequence $\tilde{c}$. For the moment assume that the m'th sequence⁺ $\tilde{c}_m$ of length 2M+1 is transmitted. According to (24) the log-likelihood functional can be written as

$$\ell\{\tilde{r}(t); \tilde{c}_m\} = \text{Re}\{\tilde{c}_m^{\dagger} \tilde{r}\} - (1/2)\tilde{c}_m^{\dagger} \underline{H} \, \tilde{c}_m$$
$$= \sum_{i=-M}^{M} \text{Re}\{\tilde{c}_{mi}^* \tilde{r}_i\} - \frac{1}{2} \sum_{i=-M}^{M} \sum_{j=-M}^{M} \tilde{c}_{mi}^* \tilde{h}_{i-j} \tilde{c}_{mj} \, , \qquad (34)$$

where for simplicity we have neglected the symbol timing and phase tracking errors τ and ϕ, respectively. The quadratic term can then be written as

---

⁺ This notation differs somewhat from that used in association with (29) and the sequel. Hopefully the meaning in either case is clear from the context.

1-13

$$\sum_{i=-M}^{M} \sum_{j=-M}^{M} \tilde{c}_{mi}^* \tilde{h}_{i-j} \tilde{c}_{mj} = \sum_{i=-M}^{M} |\tilde{c}_{mi}|^2 \tilde{h}_0 + 2\text{Re} \left\{ \sum_{i=-M}^{M} \sum_{j=-M}^{i-1} \tilde{c}_{mi}^* \tilde{h}_{i-j} \tilde{c}_{mj} \right\}$$

$$= \sum_{i=-M}^{M} |\tilde{c}_{mi}|^2 \tilde{h}_0 + 2\text{Re} \left\{ \sum_{i=-M}^{M} \tilde{c}_{mi}^* \sum_{k=1}^{M+i} \tilde{h}_k \tilde{c}_{m,i-k} \right\} . \quad (35)$$

We assume that the filter memory is such that $h_k \approx 0$ for $k \geq K$, where $K \ll M$. It follows that

$$\ell\{\tilde{\underline{r}}(t); \tilde{\underline{c}}_m\} = \sum_{i=-M}^{M} \left[\text{Re}\{\tilde{c}_{mi}^* \tilde{r}_i\} - (1/2)|\tilde{c}_{mi}|^2 \tilde{h}_0 - \text{Re}\left\{ \tilde{c}_{mi}^* \sum_{k=1}^{\min(K-1,M+i)} \tilde{h}_k \tilde{c}_{m,i-k} \right\} \right] , \quad (36)$$

or equivelently,

$$\ell\{\tilde{\underline{r}}(t); \tilde{\underline{c}}_m\} = \sum_{\ell=-M}^{M} \lambda_\ell^{(m)} \quad (37)$$

where $\lambda_\ell^{(m)}$ is the "branch metric" associated with the ℓ'th branch along the m'th path given by

$$\lambda_\ell^{(m)} \triangleq \text{Re}\{\tilde{c}_{m\ell}^* \tilde{r}_\ell\} - (1/2)|\tilde{c}_{m\ell}|^2 \tilde{h}_0 - \text{Re}\left\{ \tilde{c}_{m\ell}^* \sum_{k=1}^{\min(K-1,M+\ell)} \tilde{h}_k \tilde{c}_{m,\ell-k} \right\} . \quad (38)$$

Note that evaluation of the branch metric $\lambda_\ell^{(m)}$ requires knowledge of at most $K-1$ past data symbols, i.e., $\tilde{c}_{m,\ell-k}, k=0,1,\ldots,\min(K-1,M+\ell)$. Indeed, the summation in the last term of (38) represents a finite-impulse response (FIR) filtering operation which can be implemented as a transversal filter. A scheme for evaluating this branch metric is illustrated in Fig. 5.

The totality of possible paths or data sequences can then be described in terms of a trellis structure defined in terms of the $K-1$ most recent symbols. Define the cumulative path metric up to level k in the trellis according to

$$d_k(\tilde{\underline{r}}, \tilde{\underline{c}}_m) = \sum_{\ell=-M}^{k} \lambda_\ell^{(m)} , \quad (39)$$

with $d_{-M-1}(\tilde{\underline{r}}, \tilde{\underline{c}}_m) = 0$ for all m. The VA then searches the trellis attempting to find that path which maximizes the cumulative path metric through level M

1-14

of the trellis. A block diagram illustrating the operation of the ML

sequence estimator employing the VA is then illustrated in Fig. 6. Act-

ually, there is no need to impose a block structure on the VA sequence

estimator. Specifically, the scheme can be made synchronous with the baud

rate by outputing a delayed symbol estimate $\tilde{c}_{i-D}$ during the i'th baud

interval with D>>K an appropriate delay. The estimate $\tilde{c}_{i-D}$ is selected as

the symbol in the corresponding position along the surviving path with the

largest cumulative path metric at level i. This is a relatively straight-

forward application of the VA as used in practice.

V. Adaptive Implementation:

In the preceding we have assumed explicit knowledge of the complex

channel response $\tilde{h}_c(t)$, or equivalently $\tilde{h}(t)$, as well as the covariance

matrix $\underline{K}_{\tilde{y}\tilde{y}}(t,s)$ of the interference component as described by (13). In

particular, this allowed evaluation of the spatial/temporal matched filters

in either Fig. 2 or Fig. 3, as well as the sampled channel correlation matrix

$\underline{H}$ defined through (23). Recall that this latter quantity was required for

calculation of the branch metrics in the VA as illustrated in Fig. 5. Un-

fortunately, information on $\tilde{h}(t)$ and $\underline{K}_{\tilde{y}\tilde{y}}(t,s)$ is not generally available and

one must then seek an adaptive implementation of the ML receiver structure.

One adaptive implementation, suggested by the approach in [3], is to

approximate the unknown spatial/temporal filtering operations by a class of

finite-parameter filters whose parameter values can be adaptively adjusted

to approximate the desired response. There are two different approaches here

depending upon whether the implementation in Fig. 2 or that in Fig. 3 is

employed. In the latter there must be two adaptive loops; one to adjust

elements of the temporal matched filter $h^*(-t)$, and a second to adjust

elements of the multi-channel spatial/temporal filter represented by $\underline{\underline{Q}}_{\tilde{n}\tilde{n}}(t)$.
The first, strictly temporal loop, can be implemented exactly as in [3],
while the second spatial/temporal processor can be implemented using con-
ventional adaptive array techniques [6], [7]. Specifically, the matrix filter
$\underline{\underline{Q}}_{\tilde{n}\tilde{n}}(t)$ in Fig. 3 is replaced by a bank of transversal filters with tap spacing
T no more than $1/2B_0$ where B_0 is the signal bandwidth. The array output
signal $\tilde{x}'(t)$ is filtered in a post-array lowpass filter and presented as
input to an adaptive algorithm, such as the least mean-square (LMS) algorithm.
A reference input $\hat{d}(t)$ can be obtained in a decision-directed fashion as the
quantity[†]

$$\hat{\tilde{s}}(t;\hat{\underline{\tilde{c}}},\hat{\tau},\hat{\phi}) = \sum_{m=-M}^{M} \hat{\tilde{c}}_m \hat{\tilde{h}}(t-mT_s-\hat{\tau})e^{j\hat{\phi}} \; ; \; -(M+1/2)T_s \leq t \leq (M+1/2)T_s \; , \tag{40}$$

where $\{\hat{\tilde{c}}_m\}$ represents ML estimates from the output of the VA and $\hat{\tau},\hat{\phi}$ are
corresponding timing and phase estimates. The quantity $\hat{\tilde{h}}(t)$ represents an
estimate of the modulator/channel impulse response $\tilde{h}(t)$ as obtained in the
first adaptive loop. Note that the VA must make use of the esti-
mated response $\underline{\underline{Q}}_{\tilde{n}\tilde{n}}(t)$ in computing the quantity $\tilde{h}_\ell$ according to (23) which
is required in branch metric computations. Existing adaptive array schemes
generally assume that $\underline{\underline{Q}}_{\tilde{n}\tilde{n}}(t)$ can be approximated by a parallel bank of trans-
versal filters without any interacting terms. This is equivalent to assuming
that $\underline{\underline{Q}}_{\tilde{n}\tilde{n}}(t)$ is diagonal[††]. It is not clear how this assumption degrades poten-
tial performance although it is a reasonable assumption for wideband inter-
ference. We will not discuss this approach further since it is a relatively
straightforward application of existing techniques.

[†] This assumes that appropriate delays in the VA sequence estimator are
accounted for.
[††] Note that in this case the beam steering network in Fig. 3 can be inter-
changed with the spatial/temporal filter, as is the case in most existing
adaptive array systems.

The adaptive implementation of the scheme in Fig. 2 is somewhat more interesting and apparently has not been described previously. Here we assume that the filtering operation represented by $\underline{\underline{G}}^{\tilde{T}}(-t)$ can be approximated by a network of transversal filters, each of length L with tap spacing T no more than $1/2B_0$ seconds. Specifically, the system transfer matrix of this approximating network is diagonal of the form[†]

$$\underline{\underline{H}}(j\omega) = \begin{bmatrix} H(j\omega;\underline{\tilde{g}}_1) & & & & 0 \\ & H(j\omega;\underline{\tilde{g}}_2) & & & \\ & & \ddots & & \\ & & & \ddots & \\ 0 & & & & H(j\omega;\underline{\tilde{g}}_N) \end{bmatrix} \tag{41}$$

where $\underline{\tilde{g}}_i$, i=1,2,...,N is an L-vector representing the weights of the corresponding transversal filter such that

$$H(j\omega;\underline{\tilde{g}}_i) = \tilde{g}_{i,1} + \tilde{g}_{i,2}e^{-j\omega T} + \cdots \tilde{g}_{i,L}e^{-j(L-1)\omega T}$$

$$= \sum_{\ell=1}^{L} \tilde{g}_{i,\ell}e^{-j(\ell-1)\omega T} \quad . \tag{42}$$

As noted previously, the beam steering network in Fig. 2 can then precede the spatial/temporal processor. Let $\tilde{r}'_i(t)$, i=1,2....,N represent the corresponding input to this processor and define the L-vectors

$$\underline{\tilde{r}}'_i(t) = \begin{bmatrix} \tilde{r}'_i(t) \\ \tilde{r}'_i(t-T) \\ \vdots \\ \tilde{r}'_i(t-(L-1)T) \end{bmatrix} \quad ; \quad i=1,2,...,N \quad . \tag{43}$$

Finally, define the vector $\underline{\tilde{r}}'(t)$ of dimension NL as

---

[†] It can be shown that no loss of generality results from the assumption of diagonal form.

$$\tilde{\underline{r}}'(t) = \begin{bmatrix} \tilde{\underline{r}}_1'(t) \\ \hline \tilde{\underline{r}}_2'(t) \\ \hline \vdots \\ \hline \tilde{\underline{r}}_N'(t) \end{bmatrix} \quad , \tag{44}$$

Then the output signal $\tilde{r}(t)$ in Fig. 2 is given by

$$\tilde{r}(t) = \tilde{\underline{g}}^T \tilde{\underline{r}}'(t) \tag{45}$$

where

$$\tilde{\underline{g}} = \begin{bmatrix} \tilde{\underline{g}}_1 \\ \hline \tilde{\underline{g}}_2 \\ \hline \vdots \\ \hline \tilde{\underline{g}}_N \end{bmatrix} \quad . \tag{46}$$

Similarly, the temporal filter $\hat{h}(t)$ is approximated by a transversal filter of length $2L'+1$ with corresponding tap vector $\tilde{\underline{q}}^T = (\tilde{q}_{-L'}, \tilde{q}_{-L'+1}, \cdots, \tilde{q}_0, \cdots, \tilde{q}_{L'-1}, \tilde{q}_{L'})$. The received signal estimate, corresponding to (40), is then

$$\hat{\tilde{s}}(t; \hat{\underline{c}}, \hat{\tau}, \hat{\phi}) = \sum_{\ell=-L'}^{L'} \hat{\tilde{c}}_{m-\ell} \tilde{q}_\ell \quad , \quad t = mT_s + \hat{\tau} \quad . \tag{47}$$

The error signal $\tilde{e}(t) \triangleq \tilde{r}(t) - \tilde{d}(t)$ is then formed with $\tilde{d}(t)$ set equal to the decision-directed signal estimate of (47). At the sampling instants then we have

$$\tilde{e}_m = \tilde{e}(mT + \tau)$$
$$= \tilde{\underline{g}}^T \tilde{\underline{r}}' - \tilde{\underline{q}}^T \hat{\underline{c}} \tag{48}$$

and it is possible to choose both $\tilde{\underline{g}}$ and $\tilde{\underline{q}}$ to minimize the quadratic performance criterion

$$J(\tilde{\underline{g}}, \tilde{\underline{q}}) = E\{|\tilde{e}_m|^2\} \quad . \tag{49}$$

1-18

At this point standard stochastic gradient procedures, such as the LMS algorithm, can be applied to minimize (49) with respect to both $\tilde{g}$ and $\tilde{q}$. The details remain to be worked out.

VI. Summary and Conclusions:

We have described a novel adaptive multi-element receiver structure for ML sequence estimation in a spatially distributed interference channel. This structure provides adaptive element weighting and simultaneous data demodulation, phase tracking and bit synchronization. The structure differs from the conventional approach where these functions are all performed separately and independently. A present weakness of the result is the assumption of Gaussian interference. Hopefully this can be removed in future work. Nevertheless, the present structure is interesting for the light it sheds on how an optimum processor is implemented. In particular, the adaptive array weighting should be combined with the modulation and/or coding into an integrated spatial/temporal processor.

References

1. G. D. Forney, "Maximum-Likelihood Sequence Estimation of Digital Sequences in the Presence of Intersymbol Interference", IEEE Trans. Inform. Theory, Vol. IT-18, pp. 363-378, May 1972.

2. H. Kobayashi, "Simultaneous Adaptive Estimation and Decision Algorithm for Carrier Modulated Data Transmission Systems", IEEE Trans. Commun. Technol., Vol. COM-19, pp. 268-280, June 1971.

3. G. Ungerboeck, "Adaptive Maximum-Likelihood Receiver for Carrier-Modulated Data-Transmission Systems", IEEE Trans. on Commun., Vol. COM-22, pp. 624-636, May 1974.

4. H. L. Van Trees, _Detection, Estimation and Modulation Theory; Part I-Detection, Estimation, and Linear Modulation Theory_, John Wiley & Sons, Inc., New York, 1968.

5. C. W. Helstrom, _Statistical Theory of Signal Detection_, Pergamon Press, Inc., New York, 1968.

6. W. F. Gabriel, "Adaptive Arrays - An Introduction", IEEE Proc., Vol. 64, pp.239-272, Feb. 1976.

7. R. A. Monzingo and T. W. Miller, _Introduction to Adaptive Arrays_, John Wiley & Sons, Inc., New York, 1980.
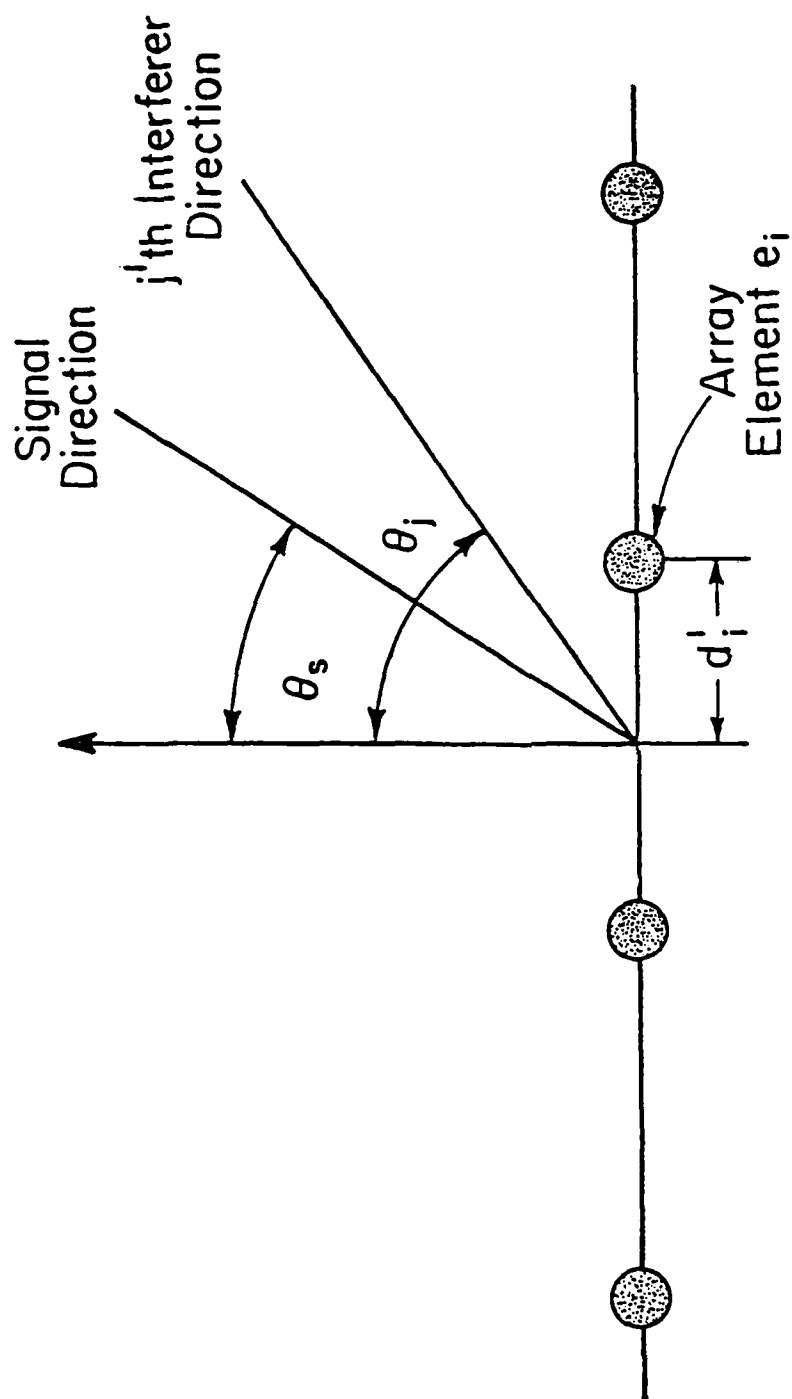
Figure 1

Illustration of Signal and Interferer

Direction for a Linear Array.
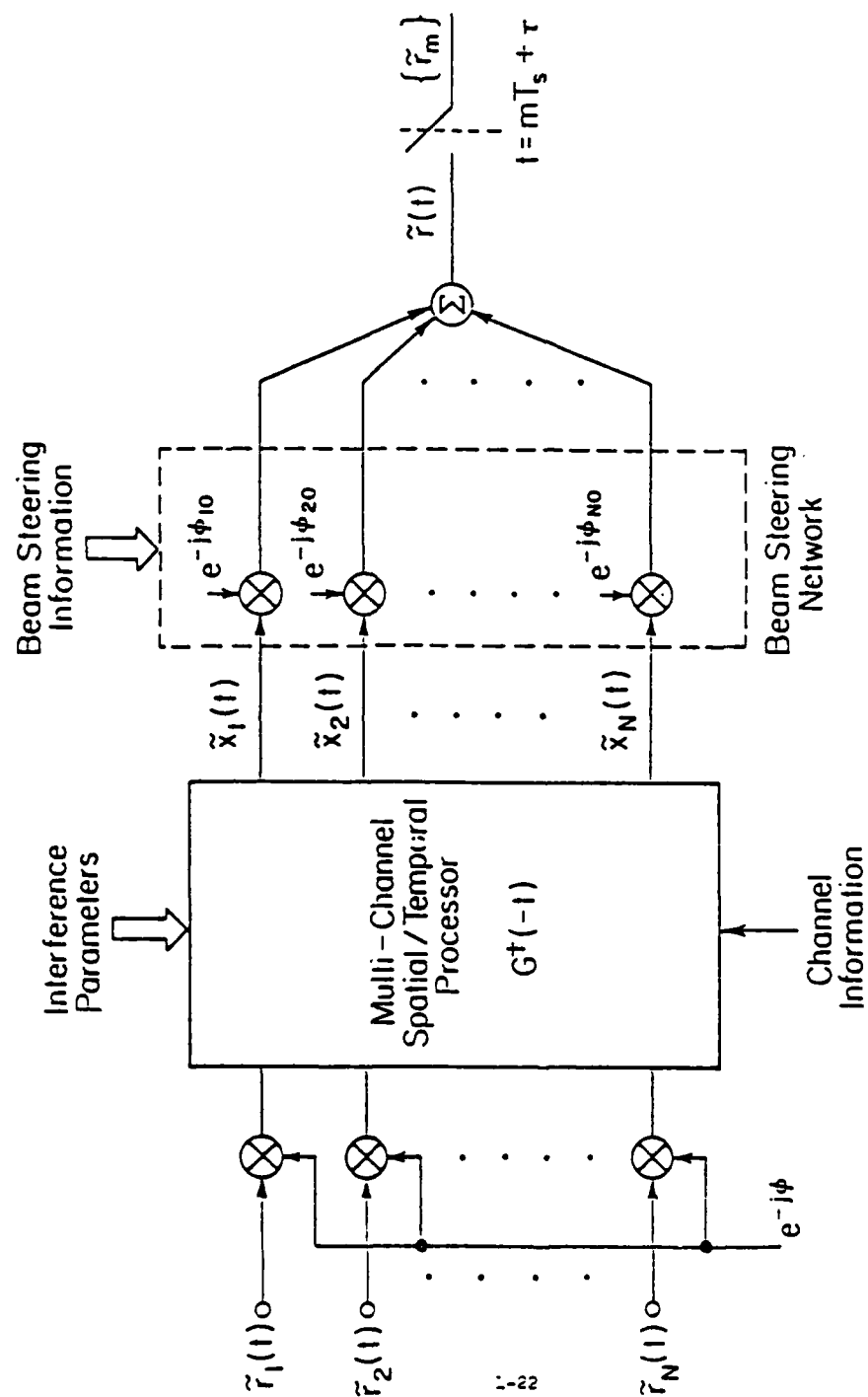
Figure 2

Spatial/Temporal Processor for Generating Observation
Sequence in Maximum-Likelihood Receiver.
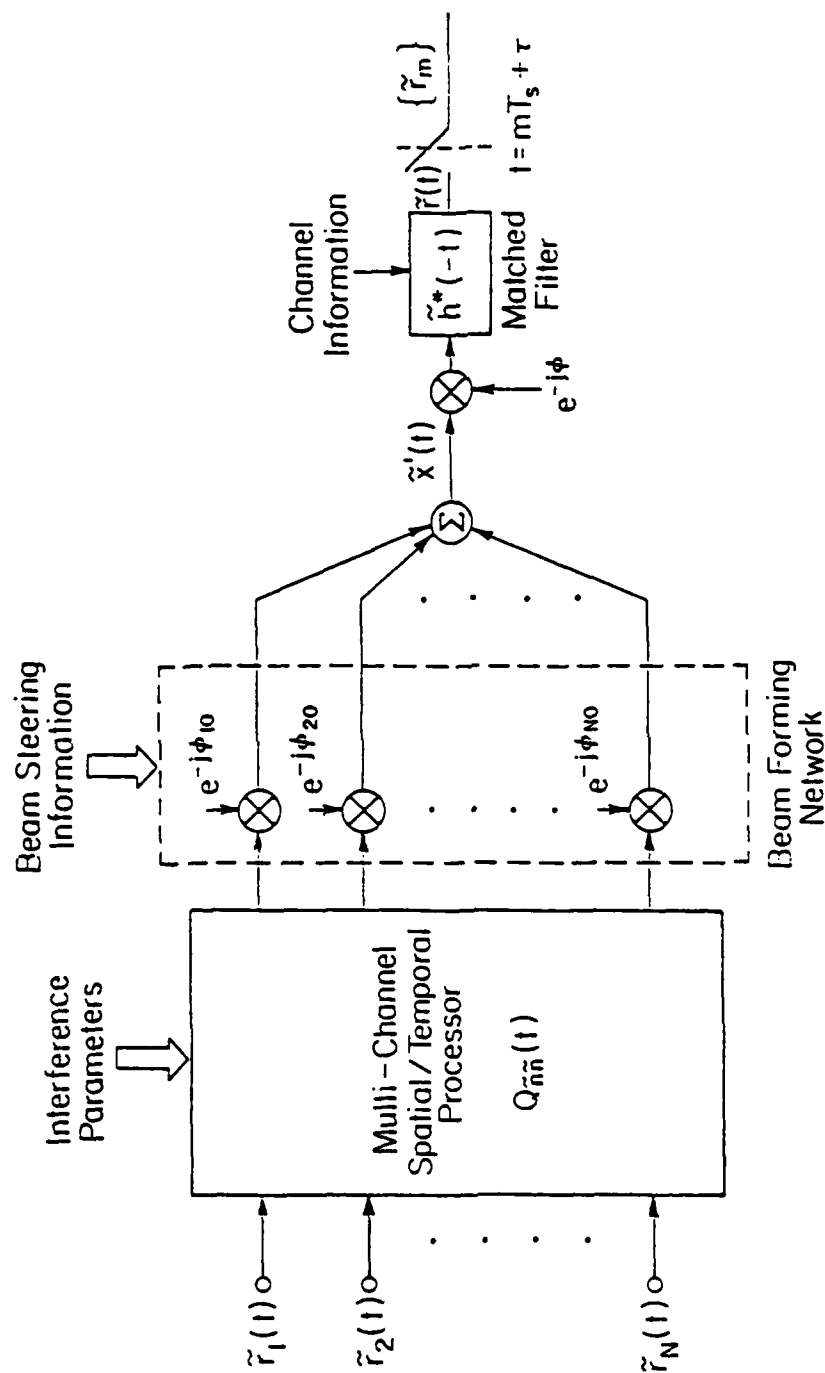
Figure 3

Alternative Multi-Channel Processor for Generating Observation
Sequence in Maximum-Likelihood Receiver.

Correlator I : Re $\{\tilde{c}_i^\dagger \tilde{r}_i\}$
Correlator II : Im $\{\tilde{c}_i^\dagger \tilde{r}_i\}$
Updates Every K Baud
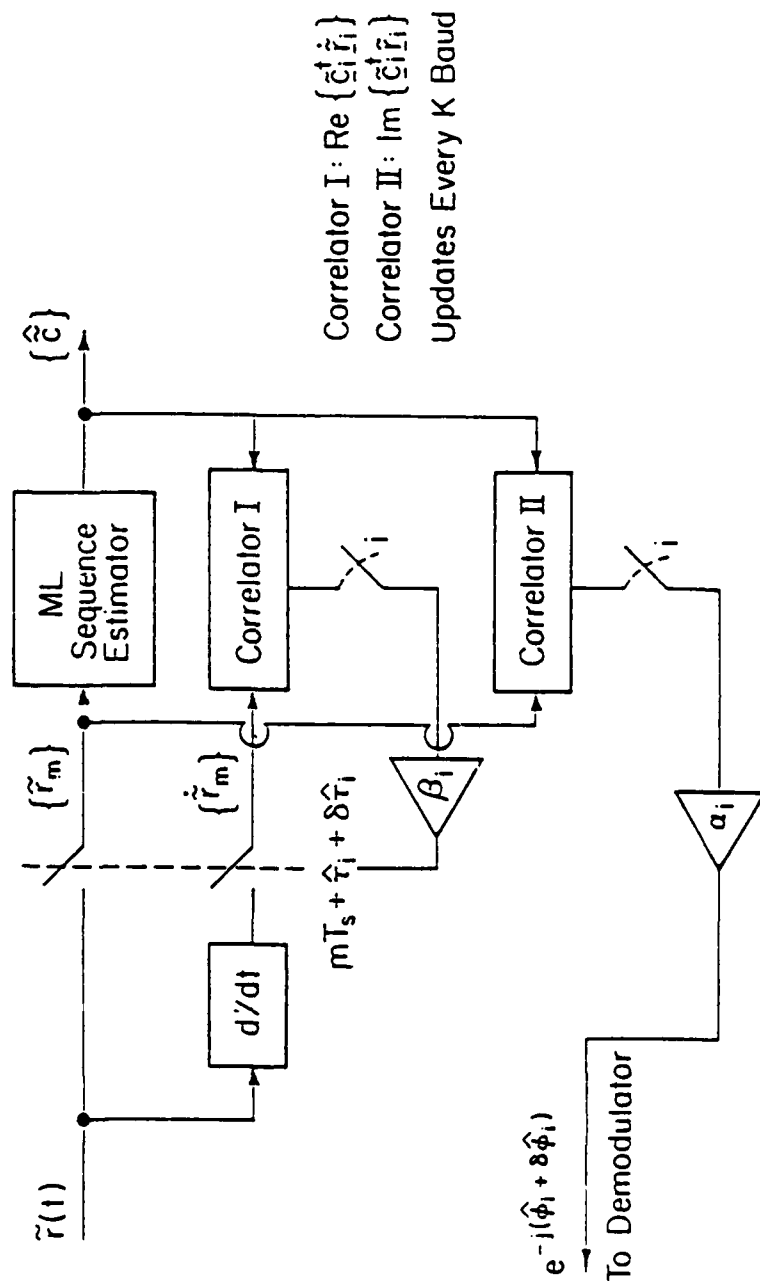
Figure 4

Block Diagram of Decision-Directed Receiver.

1-24
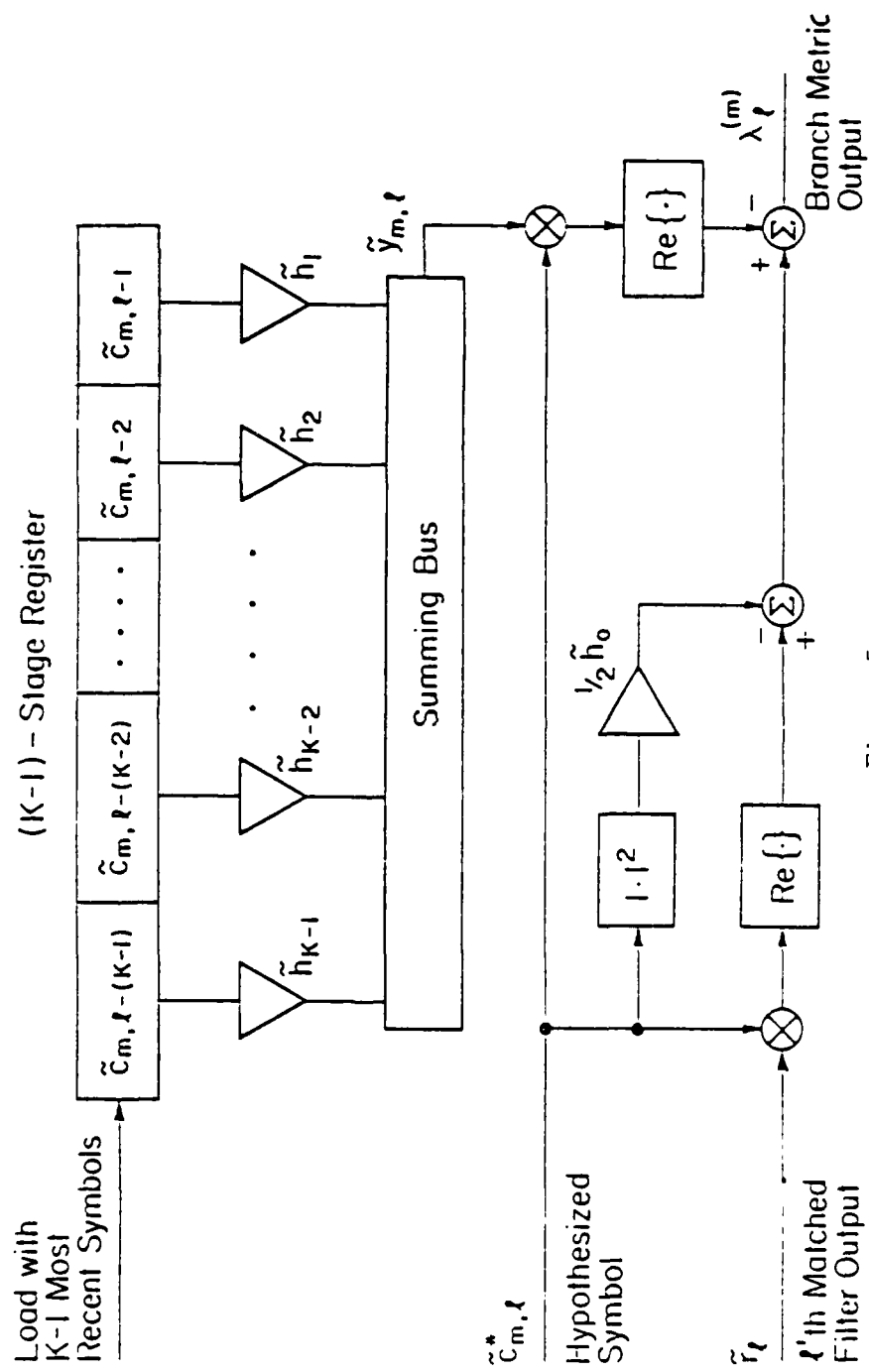
Figure 5

Scheme for Evaluating Branch Metric.

1-25
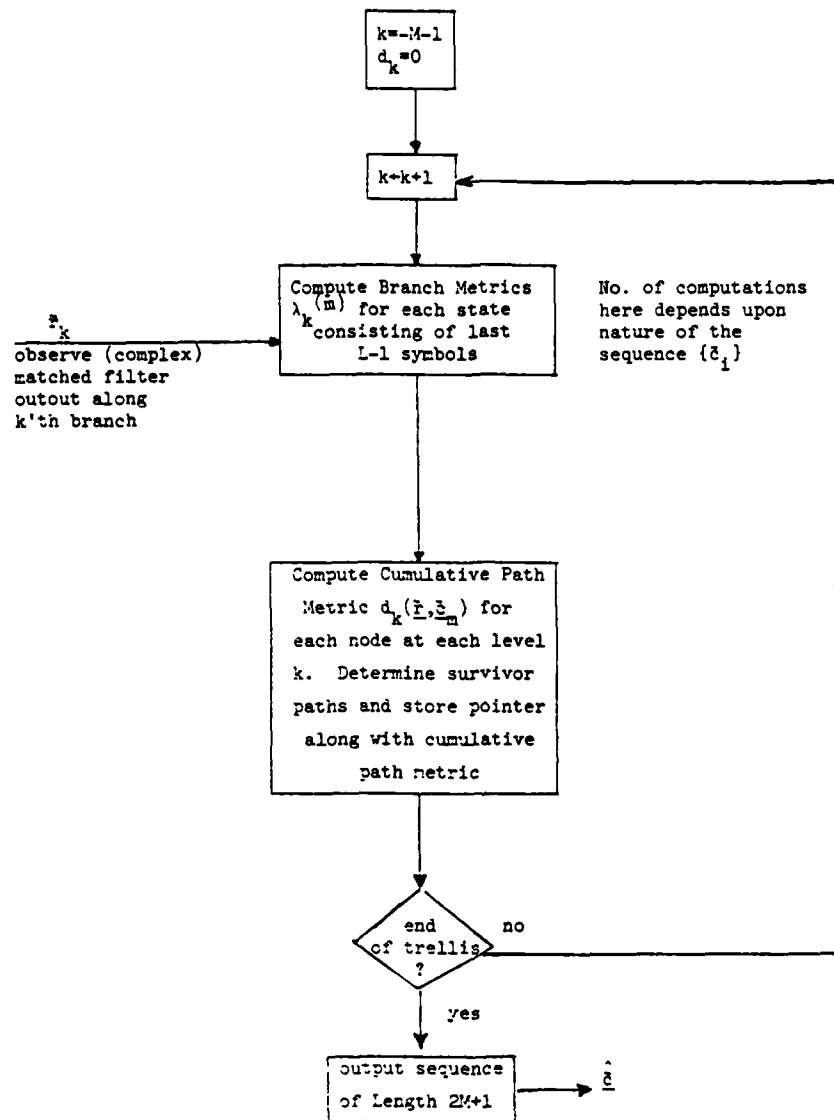
Figure 6

Operation of the ML Sequence Estimator Employing the VA.

PART II

REDUCED-SEARCH SOFT-DECISION TRELLIS

DECODING OF LINEAR BLOCK CODES

I. Introduction:

Several authors have devised decoding schemes for linear block codes which utilize the channel measurement information contained in a real-valued decision statistic available at the output of a receiver [1]-[6]. However, most of these algorithms are either unreasonably complex or are applicable only to restricted classes of codes.

Wolf [6] has proposed an algorithm which has an interesting representation as a search for the maximum likelihood path through a trellis which can be defined for a block code. This scheme applies the Viterbi algorithm (VA) to perform the search and has been shown to perform maximum-likelihood decoding. Unfortunately, the computational complexity of the VA increases with the width of the trellis to be searched. In its application to the decoding of convolutional codes, the VA becomes computationally unfeasable for codes of constraint length greater than 10 or 12. There is a similar limitation when the VA is used for maximum likelihood decoding of linear (n,k) block codes over $GF(q)$. The width of the trellis in this case can be as high as $q^{(n-k)}$ and the VA is too complex for many codes of even moderate length.

This paper is concerned with the development of a reduced-search algorithm which is, in a sense, a generalization of the VA. The complexity of this algorithm is a function of several parameters and we demonstrate that the algorithm gives performance close to the VA when applied to the block code trellis defined by Wolf at the same time the complexity is significantly reduced. Related algorithms have been applied in maximum-likelihood sequence estimation on intersymbol interference (ISI) channels [10], [11].

II. Trellis Decoding of Linear Block Codes:

When applied to the maximum-likelihood decoding of an (n,k) linear block code, the VA is used to search a trellis which is defined in terms of the

parity check equations satisfied by the 2^k code words of the code. The decoder attempts to track the "state" of the partial parity check sum:

$$\underline{S}(k) = \sum_{i=1}^{k} z_i \, \underline{h}_i, \quad k=0,1,\ldots,n \quad .$$

Here, h_i represents the i'th column of the $(n-k) \times n$ parity check matrix $\underline{H}$ and z_i is the i'th entry in a binary row vector $\underline{z}$. To each sequence z_i, $i=1,2,\ldots,n$ there corresponds a sequence of parity check sums $\underline{S}(k)$, $k=1,2,\ldots,n$.

We can use a trellis diagram to represent the evolution in time of this sequence of parity check sums. The partial parity check sum can be considered a state so that the trellis diagrams the transitions between these states from one node level to the next.

A trellis for a $(5,3)$ code with parity check matrix

$$\underline{H} = \begin{bmatrix} 1 & 1 & 0 & 1 & 0 \\ 1 & 0 & 1 & 0 & 1 \end{bmatrix} \, ,$$

is shown in Fig. 1. Each binary n-tuple traces a distinct path through the trellis corresponding to a sequence of transitions of the parity check states.

We know that for each of the 2^k binary sequences of length n which are in the code the corresponding sequence of parity check states must end with the all zeros state, i.e., $\underline{S}(n) = \underline{0}$ since

$$\underline{x} \, \underline{H}^T = \sum_{i=1}^{n} x_i \, \underline{h}_i = \underline{0} \, ,$$

if $\underline{x}$ is a codeword.

Clearly, then, a path through the trellis corresponding to a codeword must terminate at the all zero node at the final level.

The VA operates by finding the path through the code trellis, corresponding to a codeword, which maximizes the log-likelihood functional

$$L_m\{\underline{r}\} = \log f_{\underline{r}|\underline{x}_m}(\underline{r}|\underline{x}_m) \, ,$$

where $\underline{r}$ represents the real-valued receiver output sequence and $f_{\underline{r}|\underline{x}_m}(\cdot|\underline{x}_m)$ describes the channel transition probability mechanism. If we assume that the channel affects each transmitted symbol independently, the log-likelihood functional becomes

$$L_m\{\underline{r}\} = \sum_{i=1}^{n} \log f(r_i|x_{mi}) \, .$$

In the particular case of matched filter reception of binary antipodal signals transmitted over an additive white Gaussian noise (AWGN) channel, the receiver output sequence is of the form:

$$r_i = \begin{cases} \sqrt{2E_s/N_0} + n_i & ; \quad x_i = 0 \\ -\sqrt{2E_s/N_0} + n_i & ; \quad x_i = 1 \, . \end{cases}$$

where E_s is the signal energy, $N_0/2$ is the double-sided noise spectral density in watts/Hz, and n_i is a zero-mean Gaussian variate possessing unit variance.

III. A Trellis Searching Algorithm :

We consider a section of a directed trellis of the general form of Fig. 2. The full trellis may be very wide. In general, however, we will consider searching a selected sub-trellis of the full trellis which has a much smaller width.

We associate a distinct state $S_i(k)$ with each node at any given node level k. Nodes at a certain node level are connected to nodes at the next level by directed lines called branches. We denote the set of branches emanating from a particular node $S_i(k)$ by $\Gamma_i(k)$ and the size of this set by $L_i(k)$. We sometimes wich to consider a distinguished subset of $\Gamma_i(k)$. A subset of $\Gamma_i(k)$ will be denoted as $\Gamma_i'(k)$ and the size will be denoted by $L_i'(k)$. Finally, each branch in the trellis has associated with it a branch symbol $x_{i,j}(k)$ and a branch metric $d_{i,j}(k)$. The quantities x,d and S are illustrated in Fig. 2.

For each node at any given node level k it is possible to describe a path incident upon the node by a sequence of branch symbols

$$\underline{x} = (x_0, x_1, \ldots, x_{k-1}) ,$$

where x_j corresponds to the branch travelled from a node at the j'th node level to its successor at the (j+1)'st level. We also associate with this path a cumulative path metric value d which is the sum of the branch metric values for the branches in the incident path.

At a given node level k, we assume that we have stored a list of nodes. The list also contains a branch sequence and cumulative path metric corresponding to a selected incident path for each of the nodes on the list. This list for a given node level k is shown at the left at the bottom of Fig. 2.

We now describe a procedure for stepping through the trellis to the next node level, thereby extending the paths and creating a new list at level k+1. We do this by attempting to extend each of the paths on the back list (labeled B in Fig. 2) to a new node which will then be placed on a forward list (labeled F in the figure).

2-5

For each of the nodes on the back list at level k, the following steps are performed:

1. Choose a subset $\Gamma_i'(k)$ of the set $\Gamma_i(k)$ cf branches emanating from the node to be extended to nodes at the next node level. This subset contains $L_i'(k)$ branches.

2. Extend the path by traveling along one of the $L_i'(k)$ branches in the subset $\Gamma_i'(k)$ emanating from this node to a new node at level k+1. Update the cumulative path metric by including the contribution from the branch metric associated with the branch just extended.

3. Search the forward list F to determine if the new node is already present. If the node is not present, go directly to setp 5. If the node is present continue to step 4.

4. Compare the cumulative path metric just calculated with the corresponding metric already on the forward list. If the new metric is larger, go to step 5. If not, go to step 6.

5. Extend the path sequence from the present node by adding the branch symbol associated with the current branch to the path sequence associated with the node under consideration. Replace the cumulative path metric and path symbol from the node on the forward list with those just produced from the transition from the node on the back list. This effectively connects the node on the forward list to the node under consideration on the backward list.

6. If all the $L_i'(k)$ branches emanating from the node on the back list have not been exhausted, go to step 2.

The forward list will be complete after we have performed the extension procedure for each of the nodes on the back list. At this time we purge all but the M nodes with the highest path value. We can also reorder the list any way we desire (e.g., in order of decreasing metric value).

Once the above steps have been performed at any given node level the algorithm is complete and we have proceeded one level further in the trellis. The forward list becomes the back list and the process is repeated until we have come to the end of the trellis.

This algorithm has some similarity to the (M,L) algorithm described by Anderson and Mohan [7]. It is one of a class of tree searching schemes called breadth first algorithms. If $M = q^{n-k}$ (we do not purge any nodes at any node level) and we extend each of the branches emanating from the nodes, this algorithm is equivalent to the Viterbi algorithm and will perform true maximum-likelihood decoding. We now demonstrate the application of the algorithm to soft-decision decoding of linear block codes and show how the channel reliability information can be used to determine an appropriate subset of the branches to be extended from each node.

IV. Application to Soft-Decision Decoding of Binary Block Codes:

The algorithm described above can be used to search the parity check trellis defined previously. In this case the branch symbols are simply the transmitted symbols with $x_{i,j}(k)=0,1$. The branch metrics for binary antipodal signaling in AWGN then become

$$d_{i,j}(k) = r_k(-1)^{x_{i,j}(k)},$$

with r_k representing the k'th component in the received real-valued n-vector $\underline{r}=(r_1,r_2,\ldots,r_n)$. We also associate a real-valued vector $\underline{\alpha}=(\alpha_1,\alpha_2,\ldots,\alpha_n)$ called the reliability vector. These positive numbers give a measure of the

reliability of the received symbols if the receiver were forced to make a hard decision. Thus of α_i is large, it is more probable that a decision made by the receiver upon the transmitted symbol is correct. For Gaussian channels, the magnitude of the real-valued matched filter output provides an effective measure of the reliability of the corresponding hard decision estimate. We can use this channel reliability information to aid in selecting a subset of the parity check trellis to be searched. At the first k node levels for an (n,k) linear code each node on the trellis will have 2 branches emanating from it. The width of the trellis is bounded by $\min\{2^{n-k},2^k\}$.

As an example, the trellis for the Golay (24,12) code contains $2^{12}=4096$ nodes or states at its widest point. There is no advantage in using the VA for this code since word correlation decoding gives the same performance with about the same complexity.

If we receive a certain n-tuple r and several of the reliability numbers are large, we may accept the corresponding hard-decision outputs as correct. In terms of the trellis this means that at certain node levels we extend the trellis along only the branch corresponding to the hard-decision receiver output. At certain reliable node levels, then, the trellis does not grow in width, since there will be only one branch emanating from each node. The VA applied to a sub-trellis generated in this way is equivalent to correlating the received vector r against a subset of the codewords. This set is generated by accepting the receiver hard-decision outputs for the symbols in the k-p most likely information positions and allowing all possible combinations in the remaining symbol positions. In this way, the decoder correlates against a set of code words which all agree with the hard-decision estimate in the most likely k-p information symbols but otherwise exhaust all other combinations of digits in the remaining positions. The size of the subset of code words, and hence the complexity of the corresponding subtrellis,

2-8

will be a function of the number of unconstrained information symbol positions p. The choice p=k corresponds to true maximum-likelihood (ML) decoding provided $M=2^{n-k}$, while the opposite extreme p=0 corresponds to simply accepting the receiver hard decision outputs in the k information positions.

The full algorithm proceeds by first generating a subtrellis by fixing k-p of the most reliable information symbols. This subtrellis is then searched up to the k'th node level, extending the M most likely paths at each node level. Finally, after the k'th node level, the VA is applied to extend the surviving paths to the final all zeros node and select a codeword.

The parity check trellis for the Hamming (7,4) code is shown in Fig. 3. An example of a subtrellis generated for this code is shown in Fig. 4. In this case we have taken p=2. The real received vector $\underline{r}$ is shown along with the reliability vector $\underline{\alpha}$ and the corresponding receiver hard decision estimate.

V. Computational Complexity:

Massey [8] has defined 3 quantities which are useful in the determination of a trellis decoder complexity. The number of digit metrics, N_m, to be evaluated in order to compute path metrics is equal to the total number of digits on all branches of the trellis. The number of metric comparisons, N_c, is just the number of nodes in the trellis which have two entering branches. Finally, the number of accumulators, N_a, is equal to the maximum number of nodes or states which must be stored at any given node level as the decoder progresses through the trellis. For standard maximum likelihood deocding of a given (n,k) lineat block code, Massey has developed the following bounds on these computational parameters:

$$N_m \leq 2^{n-k+1} [2k-n+2]-4 \quad , \tag{1a}$$

$$N_c \leq 2^{n-k} [2k-n+1]-1 \quad , \tag{1b}$$

and

$$N_a \leq 2^{n-k} \quad , \tag{1c}$$

valid[†] for k≥n-k, or equivalently R=k/n≥1/2.

It has been demonstrated in [8] that the trellis can be simplified in certain special cases and the computational quantities N_m, N_c, N_a correspondingly reduced. One method of simplification involves rearranging the columns of the parity check matrix resulting in a nonsystematic code. It is not clear, however, that this procedure would offer significant simplification in the case of the longer, more practical codes. The conclusions then is that computational complexity is essentially exponential in n-k.

We now examine how the computational quantities are affected by the trellis searching algorithm presented here. Consider the parameter N_a. When the complexity is constrained by M, it is clear that the number of states can never exceed 2^M, since only M nodes are extended forward at each node level. When the complexity is constrained by p, the trellis can double in width at most p times. Therefore, the number of states can grow to a maximum of 2^p. Taking into account the original maximum likelihood bound, and again assuming k≥n-k, we have the result:

$$N_a \leq 2 \quad , \tag{2}$$

with $\gamma \overset{\Delta}{=} \min(n-k,\ p,\ \log_2 M)$.

Next, consider the quantity N_c for the case k_n-k. At node levels k, k+1,..., n exactly one branch emerges from each node. Since all paths from the nodes retained at level k must remerge to join at the final node, the number of metric comparisons in this portion of the trellis will be equal to one less than the number of states present at node level k. Since we have constrained the maximum number of states

_____

† Similar but less useful bounds are available for R<1/2.

to be less than 2^γ , the number of metric comparisons in the
tail of the trellis can be no greater than $2^\gamma-1$. Paths in the full trellis may
also remerge at levels n-k+1,...,k. If we retain only 2^γ states at any level,
it is clear that we can have at most $2^{\gamma-1}$ remergences at the next node level,
necessitating 1 metric comparison for each. At these node levels then, the
number of metric comparisons does not exceed $(2k-n)2^{\gamma-1}$. The number of metric
comparisons within the entire trellis therefore satisfies:

$$N_c \leq (2^\gamma-1)+(2k-n)^{\gamma-1} \quad ,$$

or the weaker bound

$$N_c \leq 2^\gamma[2k-n+1]-1 \quad . \tag{3}$$

Finally, we consider the quantity N_m, the number of metric digit calcula-
tions. This is simply the total number of branches in the reduced state trell-
is. Since N_a is the maximum number of accumulators, the worst case occurs
when the trellis expands to its full width at the earliest node levels and
remains at this width until it is forced to close in the tail section. Under
these conditions, if 2^γ is the maximum number of accumulators or nodes, the
trellis will have 2^{i+1} branches traveling forward from nodes at level i up
to node level . At levels γ, $\gamma+1$,...,$n-\gamma-1$ there will be at most $2 \cdot 2^\gamma$
branches traveling forward to the next node level. Finally, in the tail at
levels $n-\gamma$, $n-\gamma+1$,...,$n-1$ there will be 2^{n-i} branches traveling forward from
node level i for $i=n-\gamma,n-\gamma+1,\ldots,n-1$. This gives a total of

$$\sum_{i=0}^{\gamma-1} 2^{i+1} + \sum_{i=1}^{n-2\gamma} 2^{\gamma+1} + \sum_{i=n-\gamma}^{n-1} 2^{n-i} = \sum_{i=1}^{\gamma} 2^{i+1} + \sum_{i=1}^{n-2\gamma} 2^{\gamma+1}$$

$$= 2^{\gamma+2}-4 + \sum_{i=1}^{n-2\gamma} 2^{\gamma+1}$$

metric computations under worst case conditions. Assuming $2\gamma < n$ then we have the bound

$$N_m \leq 2^{\gamma+1}[2k-n+2]-4 \quad . \tag{4}$$

Comparing the bounds in (2)-(4) with the corresponding results in (1) it is clear that the decoding complexity can be controlled through choice of M and p to aboid the exponential dependence upon (n-k) associated with the full trellis search. As an example of the use of these bounds consider the situation illustrated previously in Fig. 4 for the Hamming (7,4) code. A comparison between the actual computational complexity of the reduced-search algorithm[†] and the preceding bounds is provided in Table 1. Also included is a comparison between the actual values for the best nonsystematic implementation of this code using a full trellis search (ML decoding) and the corresponding bounds predicted from (1). We feel that these bounds do provide a reasonable indication of actual computational effort and indicate the potential computational advantages of the reduced-search trellis decoding algorithm when applied to larger more powerful codes.

VI. Simulation Results:

We have performed extensive simulations of the reduced-search trellis algorithm on the R.P.I. Interactive Communication Simulator (ICS)[9]. This is an extensive hardware-software system for interactive simulation of a variety of point-to-point communication systems. In addition to the decoder, the other components of the system model included a binary equiprobable source, a block

---

† It should be noted that although there are 22 branches in the trellis of Fig. 4, only 16 branch metrics need be computed since the branch metric in the fixed positions are common to all paths and thus need not be computed.

encoder, a BPSK modulator and demodulator and an AWGN channel. To insure
statistical accuracy over the range of signal to noise ratios which were
simulated, 10^7 symbols were processed by the system for each test case.

The codes we chose for the simulations were the Hamming $(7,4)$ and Golay
$(23,12)$ perfect codes along with their extended versions, the Hamming $(8,4)$
and Golay $(24,12)$. We discuss only the results for the extended codes. Re-
sults for the perfect codes are similar.

In the first set of simulations illustrated in Fig.'s 5 and 6, M was set
equal to the maximum width of the trellis. In this case, no nodes are purged
from the list at any node level. At the same time, p (the number of uncon-
strained information positions) was varied and a simulation was performed for
each choice of this parameter. For the Hamming code, we have chosen p=0,1,2,
3,4. As indicated previously, the case p=0 corresponds to simply accepting
the receiver hard decision outputs and thus the upper curve in the figure
represents uncoded performance. For purposes of comparison we have also dis-
played the performance of a conventional hard-decision algebraic decoder.
This is a decoder whose estimate of the transmitted codeword is the code-
word at the minimum Hamming distance from the receiver hard decision vector z.
Note that for p=2 the performance of the trellis decoder is about .5dB better
than that of the conventional algebraic decoder, whereas p=3 gives perform-
ance nearly eaual to maximum-likelihood.

For the Golay code, we have chosen p=0,3,5,7. The full trellis for the
Golay code as too complex to search within a reasonable time and therefore
the maximum-likelihood performance p=12 is not shown. We have included a lower

bound on correlation decoding (cf. [1]) for purposes of comparison. Note that for the Golay code, the choice of p=3 gives performance nearly equal to the conventional decoder.

In the second set of simulations (Fig.'s 7,8) we have set p to its maximum value and have purged all but M nodes at each node level. For the Hamming code, we have chosen M=1,2,4,8,16. For M=4 the trellis decoder performs about .8dB better than the conventional decoder and M=8 gives essentially maximum-likelihood performance. For the Golay code, we have chosen M=1,4,16,64,128. In this case, M=16 gives performance comparable to the conventional decoder.

In the third and final set of simulations (Fig.'s 9,10) we have set the value of M to a fixed intermediate value and varied p. A simulation was again performed for each choice of p. For the Hamming code, we chose M=4 and p=1,2,3. For the case p=3, the performance is essentially the same as in Fig. 8 for M=4. For the Golay code, we chose M=64 and p=3,5,7,9. For p=7 the performance is about the same as in Fig. 8 for M=64.

VII. Summary and Conclusions:

We have described a general algorithm which performs a reduced complexity search of an appropriately defined trellis. This algorithm can be applied to the decoding of linear block codes. Through computer simulation we have demonstrated the tradeoff between computational complexity and bit error performance for two such codes. Interesting research directions would be to develop explicit performance bounds as a function of M and p and to apply the algorithm in the decoding of convolutional codes.

References

1. D. Chase, "A Class of Algorithms for Decoding Block Codes with Channel Measurement Information", IEEE Trans. Inform. Theory, Vol. IT-18, pp. 170-181, Jan. 1972.

2. L. D. Baumert and R. K. McElice, "Soft Decision Decoding of Block Codes", The Deep Space Progress Report 42-47, Jet Propulsion Lab. Pasadena, CA., pp. 60-64, August 1978.

3. L. R. Bahl, J. Cooke, F. Jelinek, and J. Raviv, "Optimal Decoding of Linear Codes for Minimizing Symbol Error Rate", IEEE Trans. Inform. Theory, Vol. IT-20, pp. 284-287, March 1974.

4. C. Hartman and L. Rudolph, "An Optimum Symbol By Symbol Decoding Rule for Linear Codes", IEEE Trans. Inform. Theory, Vol. IT-22, pp. 514-517, September 1976.

5. H. J. Greenberger, "Approximate Maximum Likelihood Decoding of Block Codes", JPL Publication 78-107, Jet Propulsion Lab., Pasadena, CA., February 1978.

6. J. K. Wolf, "Efficient Maximum Likelihood Decoding of Linear Block Codes Using a Trellis", IEEE Trans. Inform. Theory, Vol. IT-24, pp. 76-80, January 1978.

7. J. B. Anderson and S. Mohan, "A Systematic Analysis of Cost For Sequential Coding Algorithms", CRL Internal Report Series No. CRL-56, Communications Research Laboratory, McMaster University, Hamilton, Ontario, Canada.

8. J. L. Massey, "Foundations and Methods of Channel Coding", Proc. of the International Conf. on Inform. Theory and Systems, NTC-FACHBENCHTE, Vol. 65, Berlin, Sept. 18-20, 1978.

9. J. W. Modestino, G. R. Redinbo, K. R. Matis, and K. Y. Jung, "Digital Simulation of Communication Systems", Proc. of National Telecommunications Conf., Washington, D.C., Dec. 1979.

10. G. J. Foschini, "A Reduced-State Variant of Maximum-Likelihood Sequence Detection Attaining Optimum Performance for High Signal-to-Noise Performance", IEEE Trans. Inform. Theory, Vol. IT-24, pp. 605-609, Sept. 1977.

11. F. L. Vermuellen and M. E. Hellman, "Reduced-State Viterbi Decoding for Channels with Intersymbol Interference", Proc. of International Conference on Communications, Minneapolis, MN., June 1974.

Quantity	Reduced Search Algorithm M=4, p=2		Full Search Algorithm M=8, p=4	
	Actual Values	Bounds	Actual Values[†]	Bounds
N_m	16	20	34	44
N_c	3	7	11	15
N_a	4	4	6	8

† Actual Values for best
    nonsystematic implementation.

Table 1

Computational Requirements for Soft-Decision

Trellis Decoding of Hamming (7,4) Code.
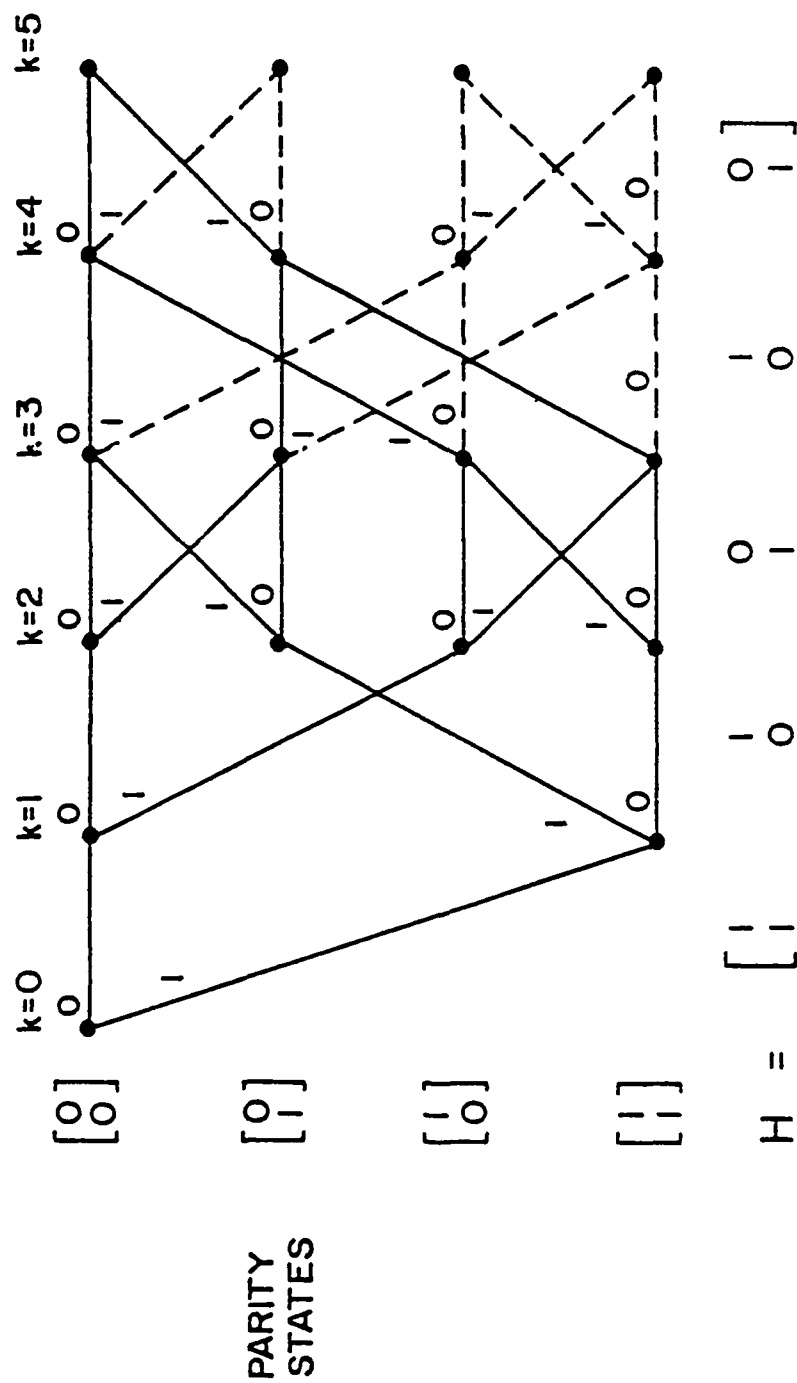
Figure 1

Trellis for Binary (5,3) Code
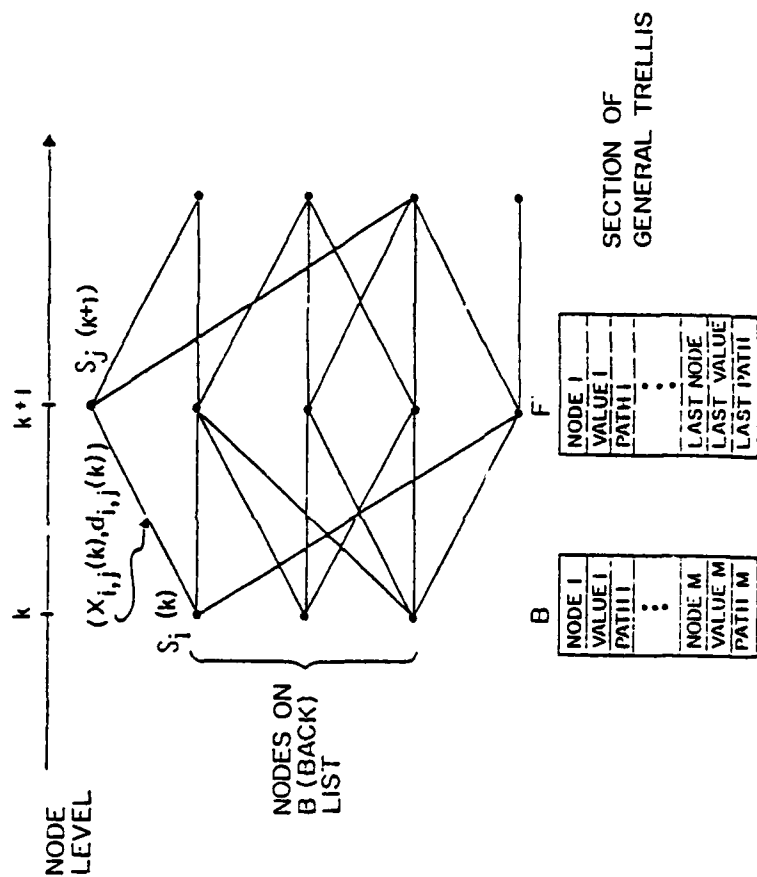
Figure 2

Section of General Trellis
Illustrating Pertinent Quantities
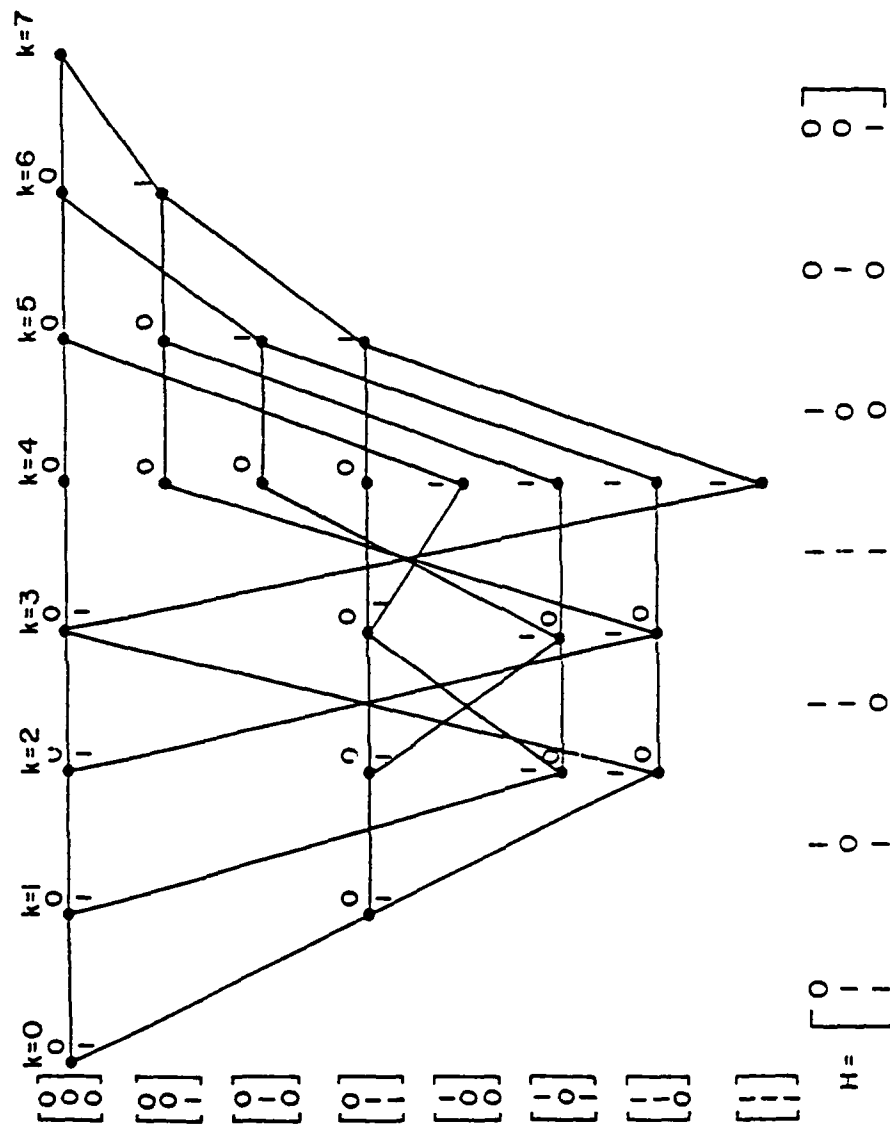
Figure 3

Terminated Trellis for Hamming (7,4) Code
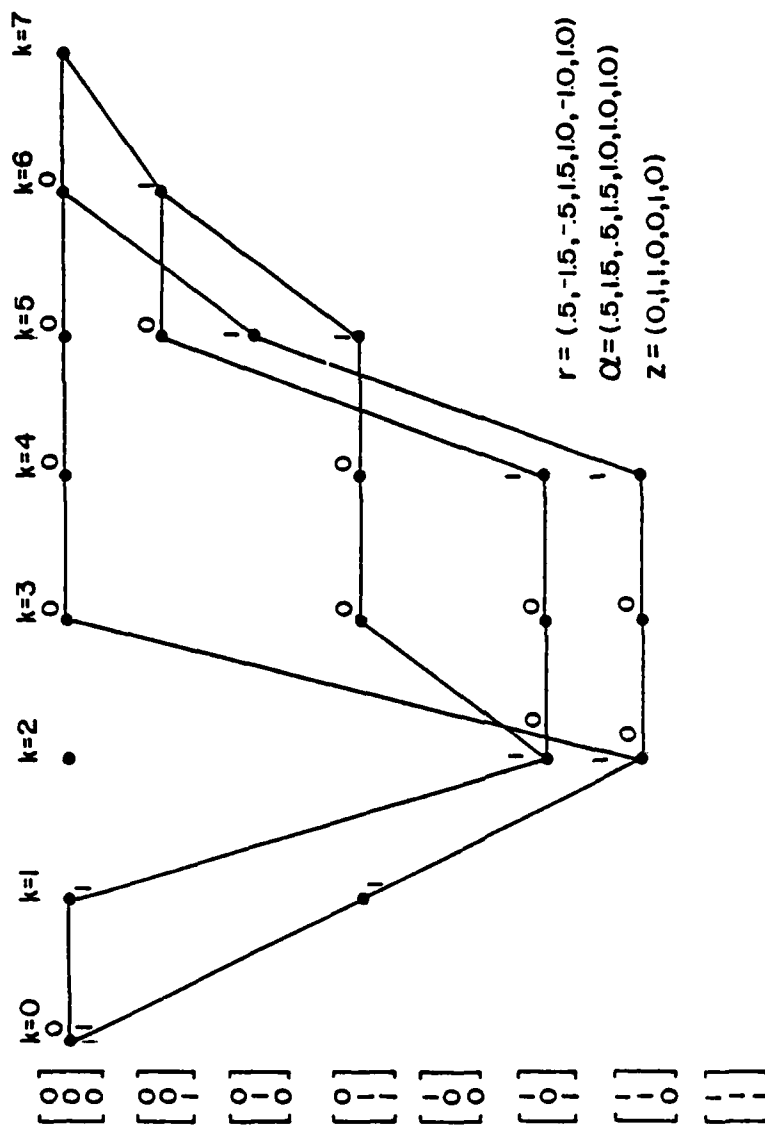
Figure 4

Subtrellis for Manning (7,4) Code
Generated by Use of Reliability Information

$r = (.5, -.15, -.5, .15, 1.0, -1.0, 1.0)$
$\alpha = (.5, .15, .5, .15, 1.0, 1.0, 1.0)$
$z = (0, 1, 1, 0, 0, 1, 0)$
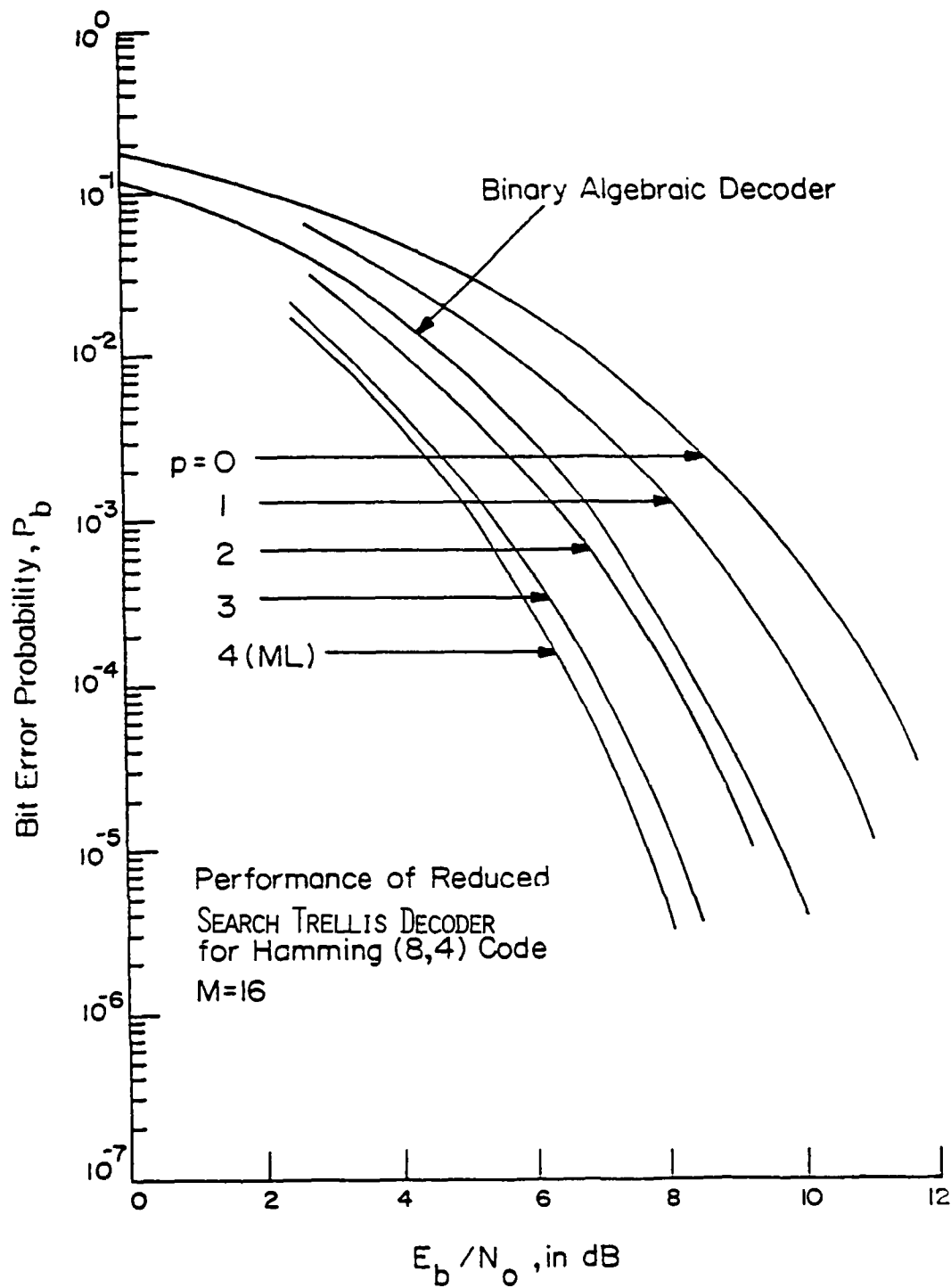
Figure 5

Performance of Reduced-Search Trellis Decoder for Hamming $(8,4)$ Code
with $M=2^4$ and Various p.
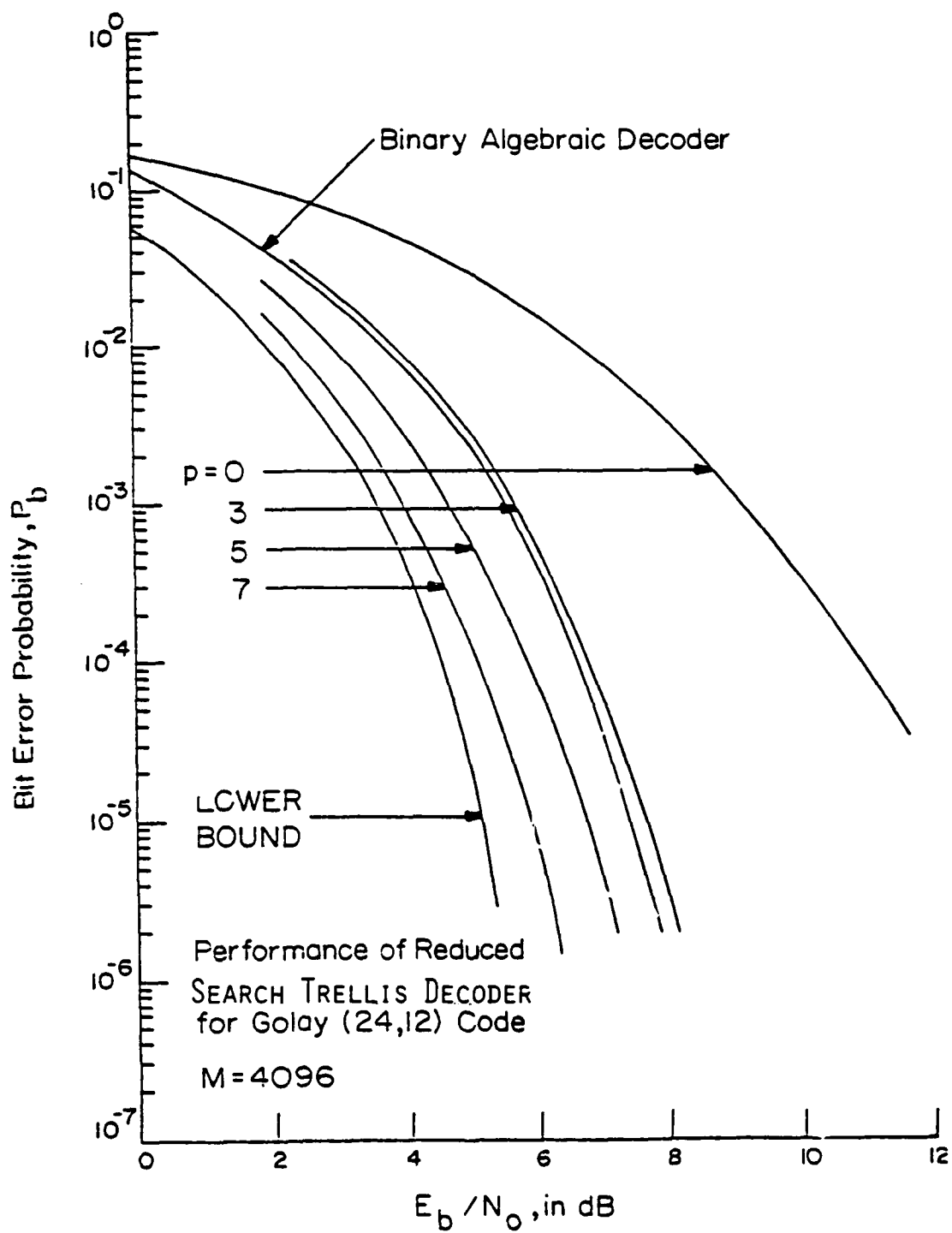
Figure 6

Performance of Reduced-Search Trellis Decoder for Golay (24,12) Code
with $M=2^{12}$ and Various p.
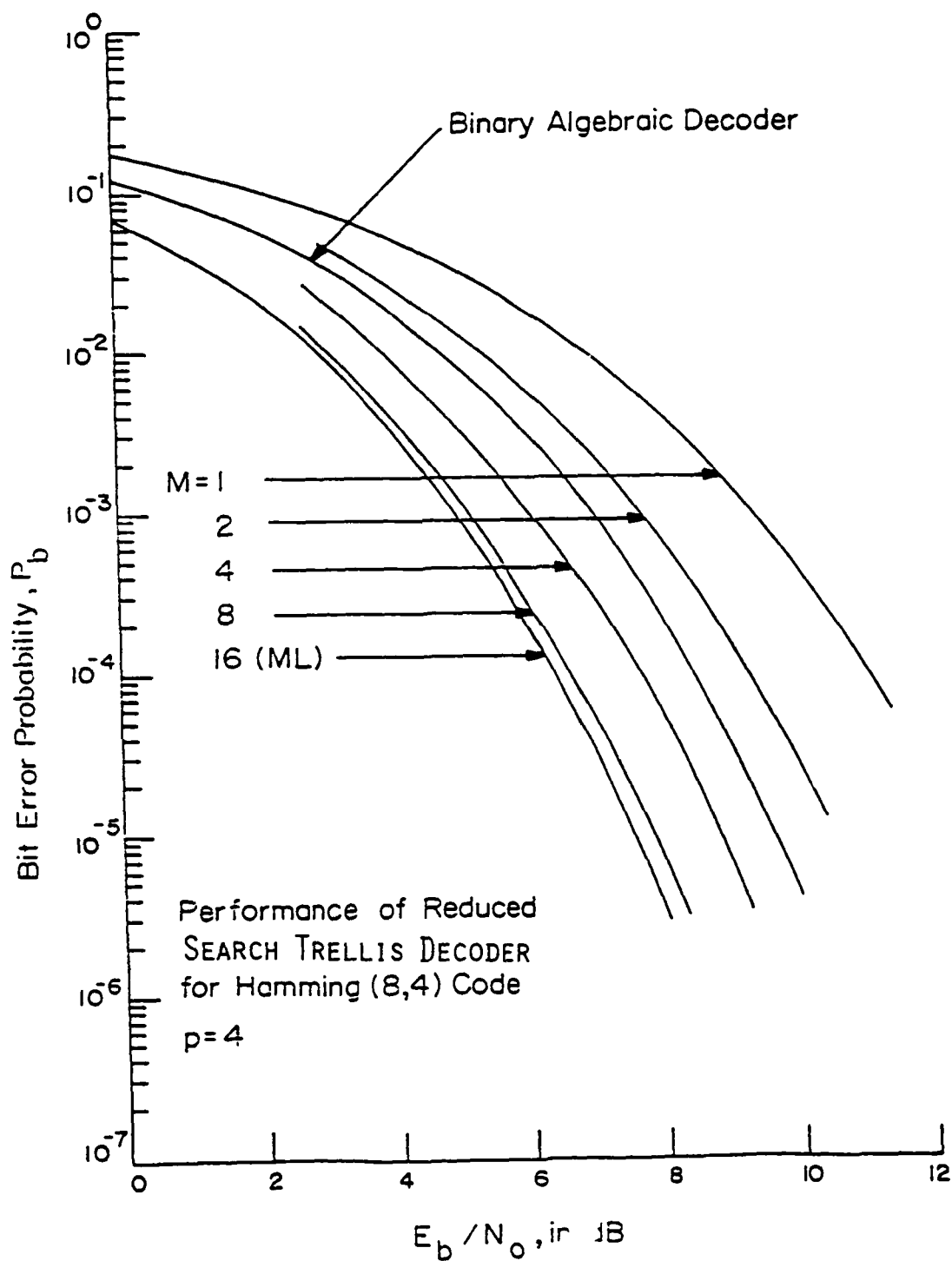
Figure 7

Performance of Reduced-Search Trellis Decoder for Hamming (8,4) Code
with p=4 and Various M.
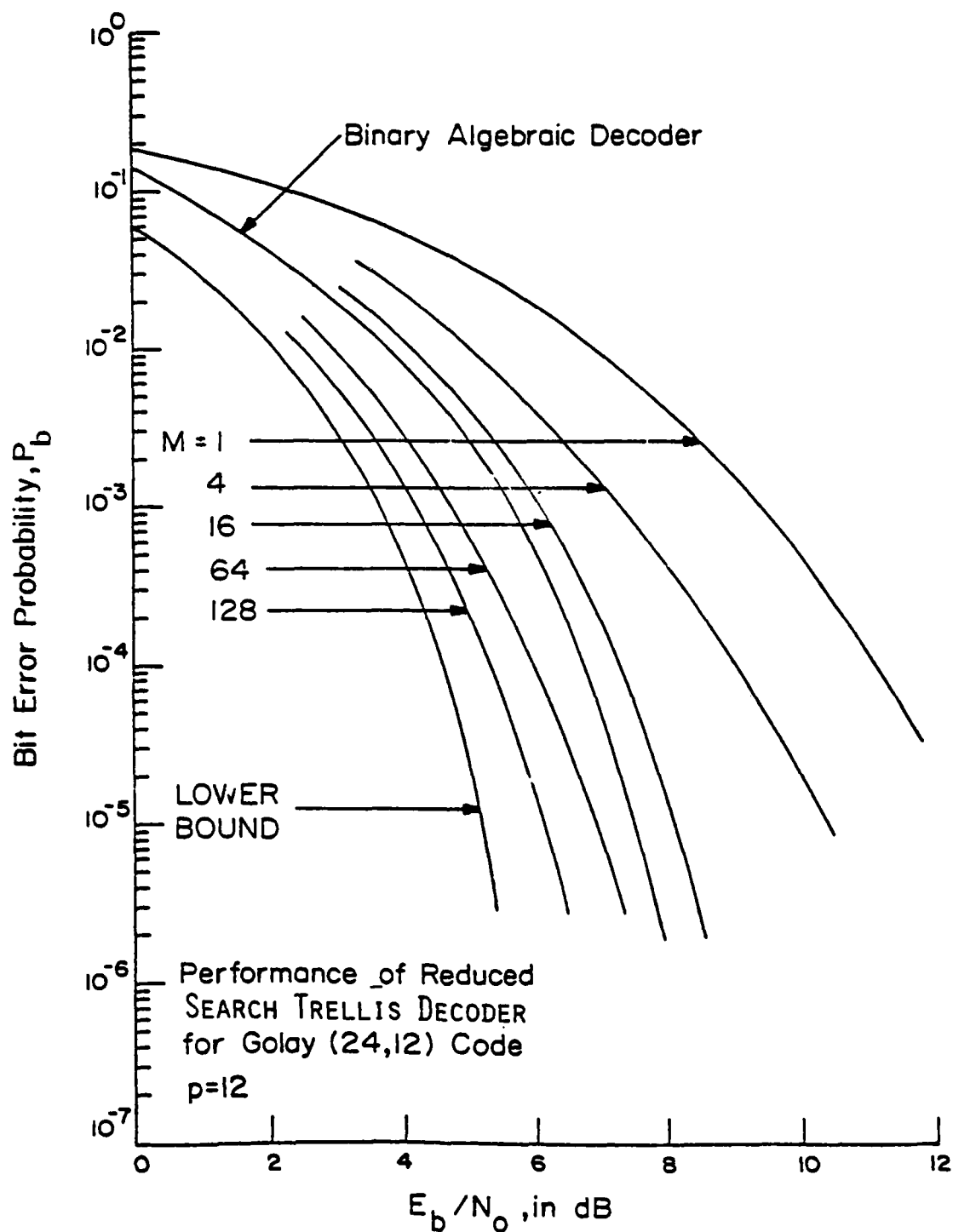
Figure 8

Performance of Reduced-Search Trellis Decoder for Golay
(24,12) Code with p=12 and Various M.
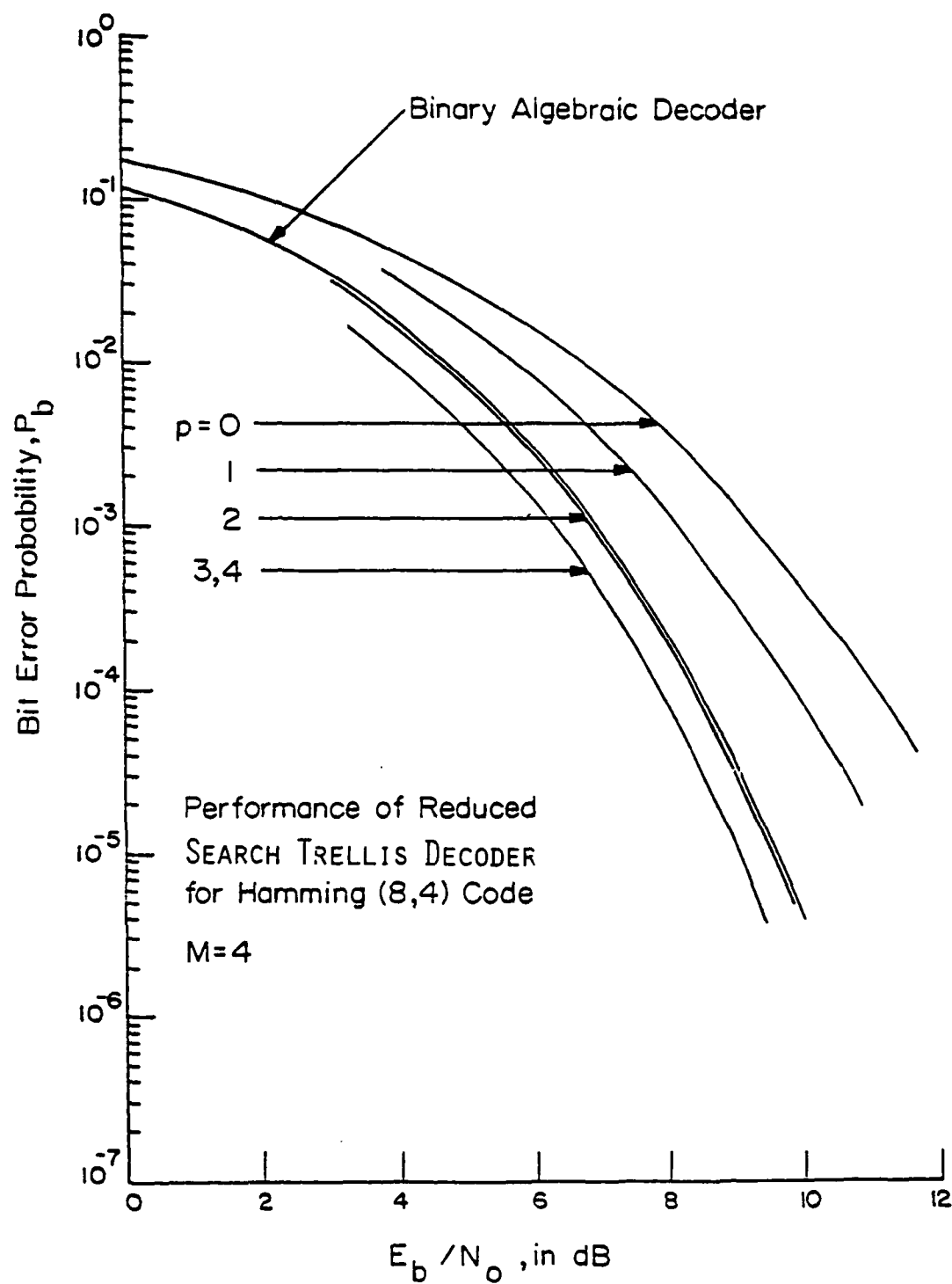
Figure 9

Performance of Reduced-Search Trellis Decoder for
Hamming (8,4) Code with M=4 and Various p.
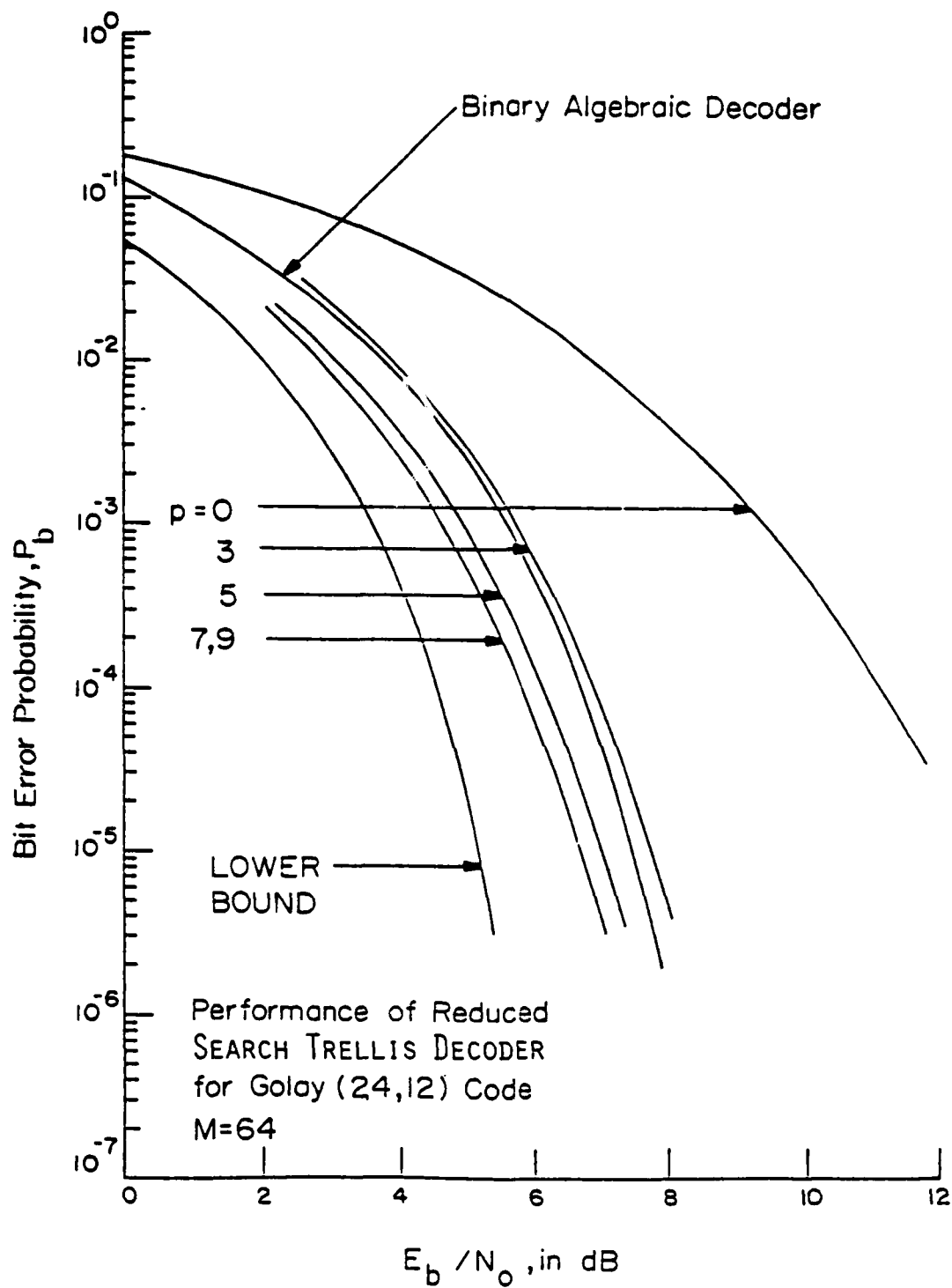
Figure 10

Performance of Reduced-Search Trellis Decoder for
Golay (24,12) Code with M=64 and Various p.

2-26

PART III

NEW SHORT CONSTRAINT LENGTH CONVOLUTIONAL CODE

CONSTRUCTIONS FOR SELECTED RATIONAL RATES

I. Introduction:

The use of Viterbi decoding and sequential decoding techniques to achieve reliable communications has increased significantly over the past decade. As a result there has been a commensurate increase in the need for good convolutional code constructions. In the past, much effort has been expended in finding optimal, i.e., good in some carefully defined sense, low rate R=1/n convolutional codes. In general, convolutional codes used in conjunction with Viterbi decoding should possess a maximum free distance property, while for codes used with sequential decoding the column distance profile property is important (cf. [1]). Some of the early optimal binary convolutional codes of practical interest in connection with Viterbi decoding were reported by Odenwalder [2], and Larsen [3]. These were short constraint length convolutional codes with maximal free distance for rates R=1/2, 1/3 and 1/4. Later, binary convolutional codes at these same rates were reported by Johannesson [1], [4] possessing an optimum column distance profile. In each of these cases the code constructions were determined by computer search methods due to the lack of any analytical procedures for obtaining optimal rate R=1/n convolutional codes. In particular, the codes reported by Larsen [3] were found by a judicious choice of the code generating polynomials followed by computer verification of their free distance.

In many applications, bandwidth restrictions are quite severe thereby dictating higher rate R=b/n channel codes if effective error-control protection is to be provided. Unfortunately, very little progress has been made in finding good convolutional codes for arbitrary rational rates greater than 1/2. Early work in developing the algebraic structure of high rate convolutional codes aas initiated by Forney [5], [6]. Specifically, Forney developed a linear correspondence between the states of a rate R=b/n convolutional

encoder with code generator matrix $\underline{\underline{G}}$ and the states of a corresponding syndrome former $\underline{\underline{H}}^{\dagger}$. Here $\underline{\underline{H}}^{\dagger}$ denotes the transpose of the generator matrix corresponding to an encoder of the code dual to the code generated by $\underline{\underline{G}}$. However, Forney's results have stimulated only a very limited number of rational rate code construction investigations. Generally, these investigations have centered on code rates of the form R=(n-1)/n. Paaske [7] has provided tabulations of short constraint length binary convolutional codes with maximal free distance only for rates 2/3 and 3/4. Furthermore, Paaske's results were obtained by computer search procedures due to the unavailability of strictly analytic methods. Results of a computer search for systematic convolutional codes with rates R=(n-1)/n for n=3,4,...,8 have been given by Hagenauer [8]. These codes, which are used in conjunction with sequential decoding, are good in the sense that they maximize a column distance function. Another class of high rate R=(n-1)/n convolutional codes have been reported by Wu [9]. These codes are convolutional self-orthogonal codes (CSOC's) which are known to be threshold decodable. Wu has provided extensive tabulations of CSOC's for n=3,4,...,14.

A class of punctured convolutional codes of rate R=(n-1)/n have been investigated by Cain, et al. [10] using computer searches. This class of codes is of interest since the implementation of Viterbi decoders for high rate convolutional codes is greatly simplified if the code structure is that of a punctured low rate code. As an example, suppose a rate R=1/2 code is used with every fourth encoder output bit deleted. This code will produce three channel bits for every two information bits, i.e., it will be a R=2/3 code. Hence, the R=2/3 code was constructed by periodically deleting bits from a R=1/2 code, or by puncturing the code. The advantage is that, after

appropriate modification of the received bit stream, the Viterbi decoder can be implemented as a R=1/2 decoder requiring only binary comparisions at each decoder state. One disadvantage is that by puncturing a R=1/2 code its free distance is reduced. We expect this to be the case, however, since high rate convolutional codes generally have smaller free distance profiles than low rate R=1/n codes. The free distance d_f of a rate R=(n-1)/n convolutional code obtained by puncturing a code of rate R=1/n is almost always equal to the bound for standard convolutional codes. However, in some cases d_f for a punctured code is less than d_f for a standard code at the same rate and constraint length.

Recently, a new class of time-invariant binary convolutional codes have been defined. Lauer [11] describes the construction of some optimal partial-unit-memory (PUM) codes. Here the encoders, at rational rates R=b/n, do not require full storage of the previous subblock of b information bits. The codes are optimal in the sense of having maximum free distance for a given rate and constraint length. Unfortunately, code constructions for rational rates are only provided for two R=2/3 codes.

The purpose of this paper is to present good rational rate convolutional code constructions for rates R=(n-k)/n, k=1,2,...,n-1 with n=2,3,...,8 and constraint lengths K=3,4,...,8. A tabulation of codes at these rates will significantly extend the existing results of rates 2/3 and 3/4 for standard convolutional codes [7]. The rational rate codes tabulated herein are short constraint length, nonsystematic, binary convolutional codes with maximum free distance for use with Viterbi decoding.

II. Preliminaries:

Figure 1 illustrates a typical nonsystematic binary convolutional encoder. Here a convolutional code with constraint length K and rate R-b/n is represented as a shift register of length K coupled with n multi-input modulo-2 adders. A group of b information bits are shifted into the shift register and the outputs of the n adders are sampled and transmitted sequentially. The code itself is determined by the connections between the shift register stages and the modulo-2 adders. All codes in the sequel will be specified by n connection vectors, one for each adder, and denoted $\underline{g}_1, \underline{g}_2, \ldots, \underline{g}_n$. The j'th component of $\underline{g}_i$ is a 1 if stage j of the shift register is connected to the i'th adder, otherwise the j'th component is zero. The code connection vectors are usually given in octal notation and are right-justified.

The criterion of goodness employed here is that of maximizing the free distance of the code at a specified rate and constraint length. Hence, it is desirable to make use of an upper bound on the free distance, or unrestricted minimum distance, of a confolutional code. For rate R=1/n codes an upper bound has been given by Heller [12]. This bound has been obtained by utilizing the fact that a terminated binary convolutional codes with L information bits is a group code. For arbitrarily large L the bound is defined accoridng to

$$d_f \leq \min_{1 \leq \ell} \left\lfloor \frac{2^{\ell-1}}{2^{\ell}-1} (K+\ell-1)n \right\rfloor \overset{\Delta}{=} d_H \ , \tag{1}$$

where $\lfloor x \rfloor$ deontes the largest integer less than or equal of x, and K is the code constraint length. Odenwalder [2] has shown that if d_H is odd, then the bound of (1) can sometimes be improved. In particular, it has been shown that if (1) is optimized with $\ell=h$ and the inequality given by

$$d_H \leq \frac{2^{h-1}}{2^h-1} \{n(h+K-1)-1+2^{1-h}\} \qquad (2)$$

is not satisfied, then d_H may be decreased by one. That is,

$$d_f \leq d_H - 1 \quad . \qquad (3)$$

The improved upper bound has been found to be very tight at small constraint lengths.

A modified version of the Heller bound (1) is used to upper bound the free distance of a rational rate $R=b/n$ convolutional code. In terms of the code parameters b, n and K the bound is given by

$$d_f \leq \min_{I \leq i} \left\lfloor \frac{2^{i-1}}{2^i-1}(K+i-b)\frac{n}{b} \right\rfloor \stackrel{\Delta}{=} d_M \qquad (4)$$

where, $\lfloor x \rfloor$ again denotes the largest integer less than or equal to x and

$$I= \begin{cases} 1 & \text{if } K<2b-1 \\ b & \text{if } K \geq 2b-1 \; . \end{cases} \qquad (5)$$

The two conditions on I described in (5) have been found to be necessary because when the shift register length K is not large enough to retain a group of b information bits for more than one shift cycle the distance properties of the code are significantly reduced. If d_M is odd, the bound in (4) can sometimes be improved in a fashion similar to that described earlier. If (4) is optimized with i=h and the inequality now given by

$$d_M \leq \frac{2^{h-1}}{2^h-1} \{\frac{n}{b}(h+K-b)-1+2^{1-h}\} \qquad (6)$$

is not satisfied, then d_M may be decreased by one. That is, for rate $R=b/n$ binary convolutional codes

$$d_f \leq d_M - 1 \quad . \tag{7}$$

The bounds described above will be used exclusively in the search for good codes.

III. Code Search Procedure:

The procedure used to find new rate R-b/n codes is an extension of the search technique outlined by Odenwalder [2] for rate R=1/n codes. This procedure is best described in terms of a state diagram and code trellis approach (cf. [13] for details). The convolutional encoder of Fig. 1 can be considered a finite-state machine with 2^{K-b} states. Hence, a rational rate Viterbit decoder will have 2^{K-b} states. Furthermore, b information bits give rise to 2^b-1 possible non-zero input patterns which may be input to the shift register. In what follows we will assume that the all-zero information sequence is encoded and transmitted across a perfect channel with a rational rate Viterbi decoder being used to decode the received data. The search strategy will be to find the minimum weight (Hamming distance) of any path through the code trellis which diverges from the all-zero path at some point and remerges at any later time. Such paths are called adversaries, wherein the minimum weight of these adversaries is simply the minimum free distance d_v of the code.

In the case of rate R=1/n codes, the search process was started by restricting the first decoded bit to be a one. Then at any time $i \geq K$ the Viterbi decoder will retain 2^{K-1} paths. Each path will be the minimum weight path which diverges from the all-zero state at some point and terminates in a particular state at time i. For large enough i the minimum free distance of the code is equal to the weight of the path which terminates at the all-zero state. Additional information such as 1.) the number of such minimum weight

paths (adversaries) which terminate in each state at each level in the trellis, and 2.) the number of bit errors that these paths represent is also collected.

For a rational rate R=b/n code the above search strategy is employed, however, the search for the minimum free distance must be done for each of the 2^b-1 possible non-zero input information bit patterns. Hence, a total of 2^b-1 minimum free distance paths through the trellis must be found. A sequence of free distances $\{d_{f|1}, d_{f|2}, \ldots, d_{f|2^b-1}\}$, one for each non-zero input pattern, is found for a rate R=b/n code. By definition the free distance d_f of the code is taken to be the minimum over all possible input patterns, i.e.,

$$d_f = \min \{d_{f|1}, d_{f|2}, \ldots, d_{f|2^b-1}\} \quad . \tag{8}$$

It is particularly illuminating at this point to consider a state diagram interpretation. For example, Fig. 2 illustrates the state diagram for a R=2/3, K=4 convolutional code with a specified set of connection vectors. There are four decoder states and three possible non-zero input bit patterns. Starting from the 00 state, the first input bit pattern 01 leaves the 00 state. There are two minimum weight paths at distance 5 with a total of three bit errors. However, for input pattern 11 there is one path at a minimum weight of 3. Hence, by (8) the free distance of the code in Fig. 2 is $d_f=3$.

A modified rational rate Viterbi decoding algorithm constructed by Wismer [14] was used to discover good rational rate convolutional codes. A limited computer search of rational rate codes was performed to obtain good code constructions, i.e., code connection vectors (CCV's), for specified rates R and constraint lengths K. The search procedure is outlined as follows:

Step 1.) Choose rate R=b/n and constraint length K. Obtain a bound on the free distance d_f of the code from (4) and the sequel.

Step 2.) Set the CCV's $\{\underline{g}_1, \underline{g}_2, \ldots, \underline{g}_n\}$ to some initial values.

Step 3.) Apply the algorithm and obtain the sequence of free distances $\{d_{f|1}, d_{f|2}, \ldots, d_{f|2^b-1}\}$, the number of adversary paths and the corresponding number of bit errors in the paths.

Step 4.) Iterate on the CCV's collecting all codes which meed the bound for d_f.

Step 5.) Eliminate all catastrophic codes from the set of candidate codes. Here a code is catastrophic (cf. [15]) if, in terms of its state diagram, there is a closed-loop zero-weight path from some non-zero state back to itself.

Step 6.) Choose the set of codes (CCV's) with the highest average value $\bar{d}_f$ amojng all 2^b-1 input patterns; here we define

$$\bar{d}_f = \frac{1}{2^b-1} \sum_{i=1}^{2^b-1} d_{f|i} \quad .$$ (9)

Step 7.) If the code set of Step 6 contains more than one code, only those codes with the smallest number of bit errors among their adversaries at the minimum distance plus one were retained. If more than one code still remained, the adversaries at the minimum distance plus two were retained, etc.

The codes determined in this fashion are the best code for that rate and constraint length in that the free distance has been maximized and the number of bit errors in the adversaries have been minimized. Results of computer searches for codes at rates R=(n-k)/n, k=1,2,...,n-1 with n=2,3,...,8 and

for constraint lengths K=3,4,...,8 are tabulated in Tables 1-18.

Results for low rate codes R=1/5,1/6,1/7 and 1/8 indicate that these codes have good error-correcting capability due to their very large free distances (cf. [16]). These explicit low rate code tabulations are useful in that they do not appear in the literature. Results for higher rate codes indicate that the free distance is markedly inferior to the lower rate codes[+]. Increasing the constraint length K beyond 8 will improve the distance profile of these codes, however, the complexity of the search procedure increases exponentially with K. It is noted that several rate 2/3 and 3/4 codes have been found which have a higher $\bar{d}_f$ than those codes reported by Paaske [7].

IV. Performance Evaluation:

Bit error probability performance bounds for rational rate convolutional codes can be obtained using a union bounding technique (cf. [13] for details). The bound for rate R=1/n codes on memoryless channels can be expressed in terms of the code generating function T(D,N) as

$$P_b' \leq K_0 \left. \frac{dT(D,N)}{dN} \right|_{N=1,D=D_0} , \tag{10}$$

where the constants K_0 and D_0 depend upon the particular code employed, the modulation strategy in use and the channel parameters. Evaluation of the derivative of the code generating function is given by the power series expansion

$$\left. \frac{dT(N,D)}{dN} \right|_{N=1} = \sum_{k=d_f}^{\infty} d_k D^k , \tag{11}$$

where c_k represents the total number of bit errors in all the adversaries

---

[+] Recall that for rate R=b/n codes d_f is defined according to (8) which is a rather pessimistic indication of the code error correcting capability. For many input patterns $d_{f|i}$ can be much larger than d_f.

which differ in exactly k symbol positions from the correct path. For a rate $R=b/n$ code, one branch corresponds to b information bits and the bit error probability is then

$$P_b = \frac{1}{b} \sum_{m=1}^{M} P'_{b|m} P_m \quad , \qquad (12)$$

where $P'_{b|m}$ is the conditional probability of a branch error given input pattern m, P_m is the corresponding a priori probability, and $M=2^b-1$ corresponding to the number of non-zero input patterns. Each of these patterns give rise to a minimum distance $d_{f|m}$ and a set of coefficients $c_{\ell|m}$ so that, corresponding to (10) and (11), we have the bound

$$P'_{b|m} \leq K_0 \sum_{\ell=d_{f|m}}^{\infty} c_{\ell|m} D_0^{\ell} \quad . \qquad (13)$$

It follows that the bit error probability can be bounded according to

$$P_b \leq \frac{1}{b} K_0 \sum_{m=1}^{M} \left\{ \sum_{\ell=d_{f|m}}^{\infty} c_{\ell|m} D_0^{\ell} \right\} P_m \quad , \qquad (14)$$

where it is usually assumed that $P_m=1/(2^b-1)$, i.e., that input patterns to the encoder are equally likely. For the particular case of BPSK modulation on the AWGN channel the constants are given as

$$K_0 \triangleq Q\left(\sqrt{\frac{2d_f R E_b}{N_0}} \right) \exp\left\{ \frac{d_f R E_b}{N_0} \right\} \quad , \qquad (15a)$$

and

$$D_0 \triangleq \exp\left\{ -\frac{R E_b}{N_0} \right\} \quad , \qquad (15b)$$

where E_b/N_0 is the energy per information bit normalized to the single-sided noise spectral density N_0 watts/Hz.

Code performance evaluations are provided in Table 19 for selected rational-rate convolutional codes at various channel signal-to-noise ratios (SNR) of practical interest. Table 19 provides both the computed bound (14) on bit error probability P_b, and that obtained by simulation using a rational rate Viterbi decoding algorithm together with BPSK modulation on the AWGN channel. The matched filter outputs were uniformly quantized to 3 bit accuracy. Results indicate performance within 0.2-0.5dB of the bounds which, of course, assume infinitely fine quantization. This is entirely consistent with simulation results described in [16].

V. Summary and Conclusions:

Tabulations of selected rational rate convolutional code constructions have been provided. These binary short constraint length codes were obtained by a limited computer search using a modified rational rate Viterbi decoding algorithm. The codes are best in the sense that, for a given rate and constraint length, the reported code possesses the maximum free distance profile and the minimum number of adversaries in the weight spectrum. An explicit expression has been provided for computing bounds on the bit error probability directly from the weight spectrum of a specific code and the channel parameters. We have shown through simulation that this bound is quite useful in describing code performance.

The codes reported herein have immediate application in the study of combined source-channel coding in the context of image transmission [17], [18]. In addition, these codes are expected to have a number of applications in coding for burst or impulsive noise channels [19].

References

1. R. Johannesson, "Robustly Optimal Rate One-Half Binary Convolutional Codes", IEEE Trans. Commun. Tech., vol. IT-21, pp. 464-468, July 1975.

2. J. P. Odenwalder, "Optimal Decoding of Convolutional Codes", Ph.D. dissertation, Dept. Syst. Sci., Sch. Eng. Appl. Sci., Univ. California, LA, 1970.

3. K. J. Larsen, "Short Convolutional Codes with Maximal Free Distance for Rates 1/2, 1/3, and 1/4", IEEE Trans. Inform. Theory, vol. IT-19, pp. 371-372, May 1973.

4. R. Johannesson, "Some Rate 1/3 and 1/4 Binary Convolutional Codes with an Optimum Distance Profile", IEEE Trans. Inform. Theory, vol. IT-23, pp. 281-283, March 1977.

5. G. D. Forney, Jr., "Convolutional Codes I: Algebraic Structure", IEEE Trans. Inform. Theory, vol. IT-16, pp. 720-738, Nov. 1970.

6. G. D. Forney, Jr., "Structural Analysis of Convolutional Codes via Dual Codes", IEEE Trans. Inform. Theory, vol. IT-19, pp. 512-518, July 1973.

7. E. Paaske, "Short Binary Convolutional Codes with Maximal Free Distance for Rates 2/3 and 3/4", IEEE Trans. Inform. Theory, vol. IT-20, pp. 683-689, Sept. 1974.

8. J. Hagenauer, "High Rate Convolutional Codes with Good Distance Profiles", IEEE Trans. Inform. Theory, vol. IT-23, pp. 615-618, Sept. 1977.

9. W.W. Wu, "New Convolutional Codes-Part I", IEEE Trans. Commun., vol. COM-23, pp. 942-955, Sept. 1975.

10. J. B. Cain, G. C. Clark, Jr. and J. M. Geist, "Punctured Convolutional Codes of Rate (n-1)/n and Simplified Maximum Likelihood Decoding", IEEE Trans. Inform. Theory, vol. IT-25, pp. 97-100, Jan. 1979.

11. G. S. Lauer, "Some Optimal Partial-Unit-Memory Codes", IEEE Trans. Inform. Theory, vol. IT-25, pp. 240-243, March 1979.

12. J. A. Heller, "Short Constraint Length Convolutional Codes", Jet Propul. Lab., Calif. Inst. Tech., Pasadena, CA. Space Programs Summary 37-54, vol. 3, pp. 171-174, Dec. 1968.

13. A. J. Viterbi, "Convolutional Codes and Their Performance in Communication Systems", IEEE Trans. Commun. Tech., vol. COM-19, pp. 751-772, Oct. 1971.

14. L. D. Wismer, "Rational Rate Viterbi Encoding/Decoding System", M.S.Thesis, ECSE Dept., Rensselaer Polytechnic Institute, Troy, NY, in preparation.

15. J. L. Massey and M. K. Sain, "Inverse of Linear Sequential Circuits", IEEE Trans. Computers, vol. C-17, pp. 330-337, 1968.

16. J. A. Heller and I.M. Jacobs, "Viterbi Decoding for Satellite and Space Communication", IEEE Trans. Commun. Tech., Vol. COM-19, pp-835-848, Oct. 1971.

17. J. W. Modestino and D. G. Daut, "Combined Source-Channel Coding of Images", IEEE Trans. Commun., Vol. COM-27, pp. 1644-1659, Nov. 1979.

18. J. W. Modestino, D. G. Daut and A. L. Vickers, "Combined Source-Channel Coding of Images Using the Block Cosine Transform", Proc. of Nat'l. Telecommunications Conference, Houston, Texas, Dec. 1980.

19. P. D. Shaft, "Lot-Rate Convolutional Code Applications in Spread-Spectrum Communications", IEEE Trans. Commun., Vol. COM-25, pp. 815-821, Aug. 1977.

b information bits

K-STAGE SHIFT REGISTER

n modulo-2 adders

Channel Symbol Sequence
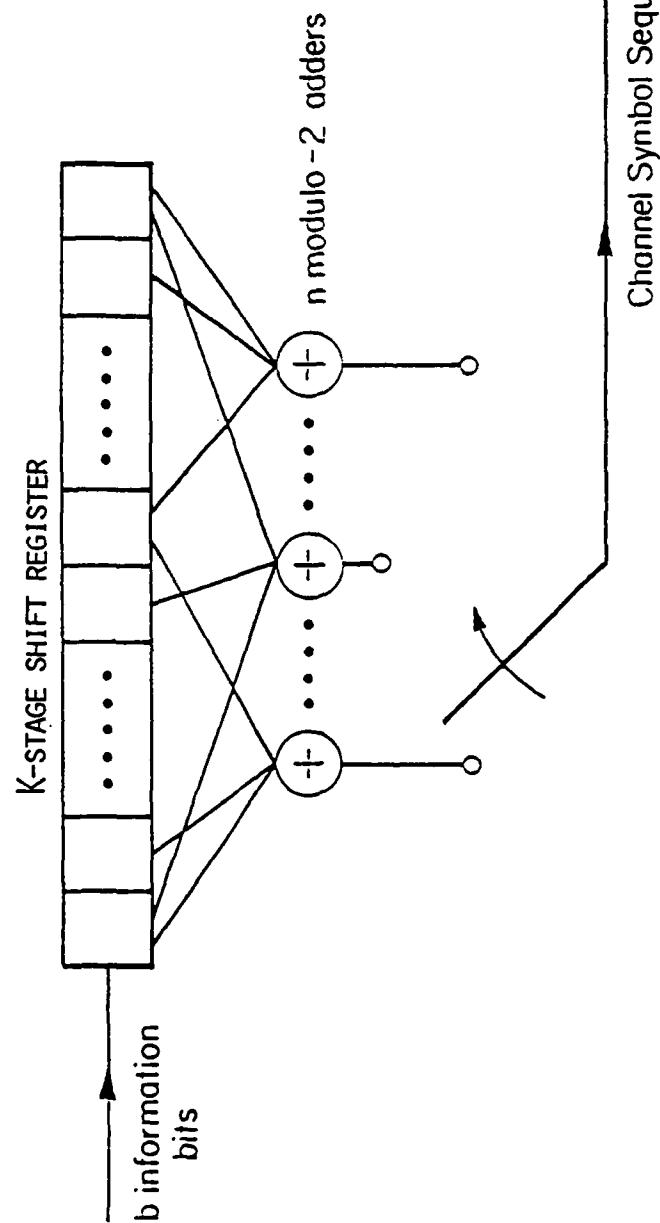
Figure 1

Rate R=b/n Binary Convolutional Encoder

3-15

CCV's (binary): $\begin{Bmatrix} 1111 \\ 0110 \\ 1101 \end{Bmatrix}$

XX – Input bit pattern
(XXX) – Encoder output pattern
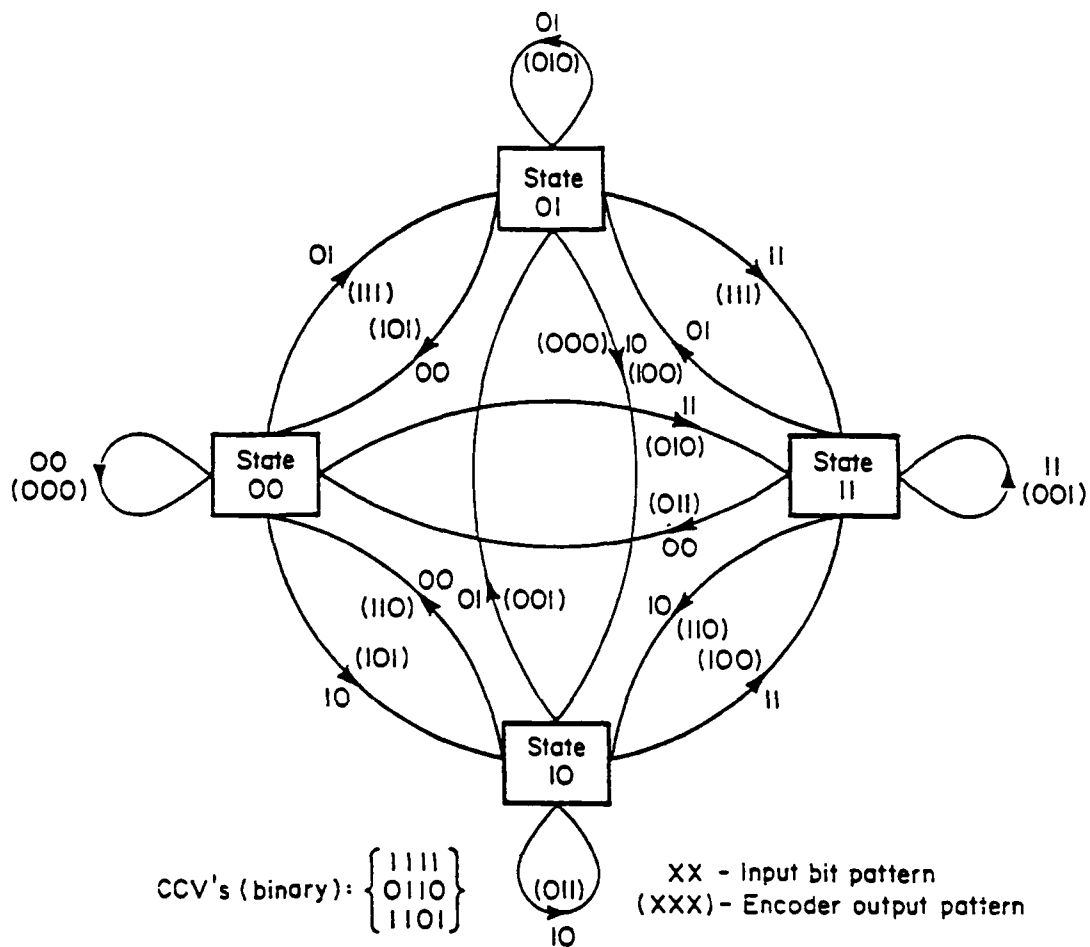
Input Pattern	Minimum Distance	Number of Paths	Number of Bit Errors
01	5	2	3
10	4	1	1
11	3	1	2

Figure 2

State Diagram for R=2/3, K=4 Convolutional Code

Constraint Length, K	Code (Octal)			Free Distance	
				achieved	bound
3	3	6	2	2	2
4	17	06	15	3	4
5	33	15	22	4	4
6	27	75	72	5	6
7[†]	177	055	112	6	6
8[†]	236	155	337	7	7

† Codes found by Paaske [7].

Table 1

Best Rate 2/3 Convolutional Codes

Constraint Length, K	Code (Octal)				Free Distance	
					achieved	bound
4	13	15	02	14	2	2
5	36	14	32	07	3	3
6	13	25	61	47	4	4
7	127	045	106	172	4	4
8	045	124	216	357	5	6

Table 2

Best Rate 3/4 Convolutional Codes

| Constraint | Code (Octal) | | | | | Free Distance | |
Length, K						achieved	bound
3	7	7	7	5	5	13	13
4	17	17	13	15	15	16	16
5	37	27	33	25	35	20	20
6	75	71	73	65	57	22	22
7	175	131	135	135	147	25	25
8	257	233	323	271	357	28	28

Table 3

Best Rate 1/5 Convolutional Codes

| Constraint | Code (Octal) | | | | | Free Distance | |
Length, K						achieved	bound
3	3	3	6	6	2	4	4
4	17	07	11	12	04	6	6
5	12	12	31	27	37	8	8
6	27	71	52	65	57	10	10
7	071	166	112	055	177	11	11
8	247	366	171	266	373	12	12

Table 4

Best Rate 2/5 Convolutional Codes

Constraint Length, Z	Code (Octal)					Free Distance	
						achieved	bound
4	17	03	06	12	04	3	3
5	37	15	26	13	34	4	4
6	35	23	75	61	47	5	5
7	034	127	045	106	172	6	6
8	334	044	124	216	357	7	7

Table 5

Best Rate 3/5 Convolutional Codes

Constraint Length, K	Code (Octal)					Free Distance	
						achieved	bound
5	13	04	11	26	36	2	2
6	67	15	26	52	57	2	3
7^{+}	013	023	056	132	174	3	4
8^{+}	237	274	156	255	337	3	4

$^{+}$All $d_f = 4$ codes found were catastrophic.

Table 6

Best Rate 4/5 Convolutional Codes

Constraint Length, K	Code (Octal)			Free Distance	
				achieved	bound
3	7	7	7	16	16
	7	5	5		
4	17	17	13	20	20
	13	15	15		
5	37	35	27	24	24
	33	25	35		
6	73	75	55	27	27
	65	47	57		
7	173	151	135	30	30
	135	163	137		
8	253	375	331	34	34
	235	313	357		

Table 7

Best Rate 1/6 Convolutional Codes

Constraint Length, K	Code (Octal)			Free Distance	
				achieved	bound
6	55	05	11	2	2
	20	02	76		
7	025	071	123	2	3
	046	111	175		
8	342	362	065	3	4
	116	213	377		

Table 8

Best Rate 5/6 Convolutional Codes

Constraint Length, K	Code (Octal)				Free Distance	
					achieved	bound
3	7	7	7	7	18	18
	5	5	5			
4	17	17	13	13	23	23
	13	15	15			
5	35	27	25	27	28	28
	33	35	37			
6	53	75	65	75	32	32
	47	67	57			
7	165	145	173	135	36	36
	135	147	137			
8	275	253	375	331	40	40
	235	313	357			

Table 9

Best Rate 1/7 Convolutional Codes

Constraint Length, K	Code (Octal)				Free Distance	
					achieved	bound
3	7	3	5	6	6	6
	6	2	2			
4	05	06	12	15	9	9
	15	13	17			
5	11	36	32	12	11	11
	23	35	37			
6	33	55	72	47	14	14
	25	53	75			
7	073	132	071	166	16	16
	112	055	177			
8	312	125	247	366	18	18
	171	266	373			

Table 10
Best Rate 2/7 Convolutional Codes

Constraint Length, K	Code (Octal)				Free Distance	
					achieved	bound
4	17 14	13 04	16 10	02	4	4
5	06 26	24 34	15 37	13	6	6
6	45 57	21 43	36 71	62	8	8
7	166 122	055 061	034 057	165	8	8
8	245 124	216 216	334 357	045	10	10

Table 11

Best Rate 3/7 Convolutional Codes

Constraint Length, K	Code (Octal)				Free Distance	
					achieved	bound
5	13 25	07 35	31 37	23	4	4
6	11 26	14 52	15 57	67	4	4
7	115 056	010 132	013 174	023	6	6
8	130 156	067 255	237 337	274	6	7

Table 12

Best Rate 4/7 Convolutional Codes

Constraint Length, K	Code (Octal)				Free Distance	
					achieved	bound
6	36	20	05	55	2	2
	02	11	76			
7	025	111	172	147	3	3
	156	122	177			
8	026	034	270	065	4	4
	116	213	377			

Table 13

Best Rate 5/7 Convolutional Codes

Constraint Length, K	Code (Octal)				Free Distance	
					achieved	bound
7	003	005	010	021	2	2
	041	101	176			
8	207	111	123	252	2	3
	345	261	336			

Table 14

Best Rate 6/7 Convolutional Codes

Constraint Length, K	Code (Octal)				Free Distance achieved	bound
3	7	7	5	5	21	21
	5	7	7	7		
4	17	17	13	13	26	26
	13	15	15	17		
5	37	33	25	25	32	32
	35	33	27	37		
6	57	73	51	65	36	36
	75	47	67	57		
7	153	111	165	173	40	40
	135	135	147	137		
8	275	275	253	371	45	45
	331	235	323	357		

Table 15

Best Rate 1/8 Convolutional Codes

Constraint Length, K	Code (Octal)				Free Distance achieved	bound
4	15	12	04	14	5	5
	02	16	13	17		
5	05	06	24	15	7	7
	13	26	34	37		
6	15	42	23	61	8	8
	51	36	75	47		
7	132	166	055	034	10	10
	165	122	061	057		
8[†]	274	045	124	216		
	357	245	216	334	11	12

[†]Partial Search

Table 16

Best Rate 3/8 Convolutional Codes

| Constraint | Code (Octal) | | | | Free Distance | |
Length, K					achieved	bound
6	53 05	60 11	02 76	55 36	3	3
7	076 056	025 172	122 147	111 177	4	4
8	320 116	026 270	213 065	034 377	5	5

Table 17

Best Rate 5/8 Convolutional Codes

| Constraint | Code (Octal) | | | | Free Distance | |
Length, K					achieved	bound
8	003 041	004 100	011 201	020 377	2	2

Table 18

Best Rate 7/8 Convolutional Codes

R=2/3, K=4 Code	E_b/N_0		
	3dB	4dB	5dB
Computed Bound[†], P_b	7.39×10^{-3}	1.14×10^{-3}	1.54×10^{-4}
Simulation Result, P_b	1.03×10^{-2}	2.59×10^{-3}	5.46×10^{-4}

R=3/4, K=6 Code	E_b/N_0		
	3dB	4dB	5dB
Computed Bound[†], P_b	3.53×10^{-3}	2.35×10^{-4}	1.15×10^{-5}
Simulation Result, P_b	1.80×10^{-2}	2.91×10^{-3}	1.72×10^{-4}

R=1/5, K=4 Code	E_b/N_0		
	3dB	4dB	5dB
Computed Bound[†], P_b	1.50×10^{-3}	2.00×10^{-4}	1.80×10^{-5}
Simulation Result, P_b	2.11×10^{-3}	4.08×10^{-4}	2.53×10^{-5}

† Computed Bound Evaluated from Eqn. (14), with $P_m = 1/(2^b - 1)$

Table 19

Performance Evaluation for Selected Rational Rate
Convolutional Codes; Viterbi Decoding on an AWGN
Channel Employing a BPSK Modulation Strategy.

PART IV

MODELING AND ANALYSIS OF SELECTED RECEIVER PERFORMANCE

IN IMPULSIVE NOISE CHANNELS

I. Introduction:

A considerable body of knowledge exists concerning the performance of digital communication systems operating on the additive white Gaussian noise (AWGN) channel (cf. [1]-[4] for comprehensive treatment). The major impetus for this concentration on the AWGN channel has been the justification of the Gaussian model on physical grounds for a large number of important applications; the deep space channel most notably. No doubt, the comprehensive coverage in this case has been made possible by the analytical tractability of the AWGN model. In an increasing number of important applications, however, the Gaussian model provides an entirely inappropriate description of the prevailing noise environment. A number of such applications include: communication systems operating in the ELF/VLF frequency range; data transmission on the switched telephone network; wideband FM systems operating close to or below threshold; VHF/UHF communication systems operating in the vicinity of large metropolitan areas; HF and Troposcatter long-distance communication systems; and military communication systems subject to wideband jamming.

While the noise producing mechanism is decidedly different in each of the above examples, in each case the noise environment can be described as a linear combination of a Gaussian and an impulsive noise process. This is a fairly interesting class of random processes and, as indicated above, rather rich in practical applications. Furthermore, there is ample justification for this model on both physical and mathematical grounds. Finally, with some assumptions on the statistics of the impulse process, this class of random processes possesses a certain degree of analytical tractability.

This paper then is concerned with the modeling and analysis of the error probability performance of selected modulation strategies operating in narrowband impulsive noise. A generalized impulsive noise model is described which consists of a linear combination of a narrowband shot noise process and AWGN. The low-density shot noise is generated by exciting a fixed linear dynamical system by a stationary point process (s.p.p.) described in terms of its interarrival distribution. We consider the particular case of Gamma distributed interarrival times. Some of the low-order statistical properties of this model are described in conveniently parameterized form which allows calibration to a wide variety of applications, such as described above.

The receiver structures considered consist of a conventional data demodulator, implemented as a linear matched filter, preceded by nonlinear front-end processing. Performance results are described for several modulation strategies including binary coherent phase-shift keying (BPSK), differentially coherent phase-shift keying (DPSK), quadrature phase-shift keying (QPSK), binary noncoherent frequency-shift keying (BFSK), and coherent minimum shift keying (MSK). These results are carefully parameterized by the channel and receiver characteristics. Analytical results are provided where possible, otherwise we have made extensive use of computer simulation results obtained on the R.P.I. Interactive Communications Simulator (ICS) as described in [5]. This is an extensive hardware/software system allowing realistic and flexible simulation of a wide variety of point-to-point digital communication links.

This paper is organized as follows: We describe the channel signal and noise model in Section II, followed by a treatment of selected low-order statistical properties of the noise model in Section III. This latter

4-3

information is useful in calibrating the assumed noise model against real-world impulsive noise situations. We do not attempt such a calibration here but rather provide a careful parameterization of the problem which hopefully can be applied to a wide variety of impulsive noise environments. A comprehensive treatment of the performance of linear matched filter reception in impulsive noise is provided in Section IV. These results illustrate both quantitatively and qualitatively the severe degradation in performance due to small amounts of impulsive noise. In Section V we demonstrate the effectiveness of selected nonlinear receivers in this environment. The receiver structures here consist of linear front-end processing together with selected zero-memory nonlinear (ZMNL) devices motivated by optimum weak signal results. A summary and conclusions can be found in Section VI.

II. Channel Signal and Noise Model:

In what follows we make extensive use of complex narrowband representations of all signal and noise processes. Specifically, the received signal is given by

$$r(t) = \sqrt{2} \, \text{Re}\{\tilde{r}(t)e^{j2\pi f_c t}\} \, , \qquad (1)$$

where f_c is an <u>assumed known</u> carrier frequency in Hz, and $\tilde{r}(t)=r_c(t)-jr_s(t)$ is the complex envelope expressed in terms of lowpass waveforms $r_c(t)$ and $r_s(t)$ representing the inphase and quadrature (I/Q) components, respectively. The complex envelope $\tilde{r}(t)$ is furthermore assumed of the form

$$\tilde{r}(t) = \tilde{s}(t) + \tilde{n}(t) \, , \qquad (2)$$

where $\tilde{s}(t)$ is the complex envelope of the received signal component and $\tilde{n}(t)$ is a complex noise process representing the non-Gaussian impulsive noise environment. We consider each of these components separately.

4-4

A. *Channel Signal Model*: We assume the signal energy is given by[†]

$$E_s = \int_0^{T_s} |\bar{s}(t)|^2 dt \quad , \tag{3}$$

where T_s is the channel symbol (baud) interval. Furthermore, we restrict attention to digital signaling formats such that $\bar{s}(t)$ has the representation

$$\bar{s}(t) = \sqrt{\frac{E_s}{T_s}} \sum_i [C_{1,i} u_c(t-2^k i T_s - \tau) + j C_{2,i} u_s(t-2^k i T_s - \tau)] e^{j\theta} \quad . \tag{4}$$

Here, depending upon the modulation strategy employed, $u_c(t)$ and $u_s(t)$ are appropriately defined baseband waveforms modulating the I/Q rails. Similarly, the quantities $C_{1,i}$, $C_{2,i}$ depend upon the binary[††] data sequence $\{x_i\}$ to be transmitted in a manner specific to the modulation strategy in use. The quantity k in (4) assumes the values 0 or 1, with the choice k=1 generally corresponding to the case of staggered overlapping baseband waveforms as in MSK. Finally, the quantities τ and θ in (4) are, in general, random timing epoch and phase offset, respectively. In what follows we neglect the effects of symbol synchronization and phase tracking errors, although it is expected that in practice these effects will have a profound influence on overall system performance.

Some specific examples of digital modulation formats which can be expressed in the form (4) are provided below. A summary of such representations is given in Table 1.

Coherent BFSK: Here the complex signal envelope is of the form

$$\bar{s}(t) = \sqrt{\frac{E_s}{T_s}} \sum_i x_i u_0(t-iT_s-\tau) e^{j\theta} \quad , \tag{5}$$

---

† We specifically restrict attention to equal energy signaling alphabets.
†† In what follows we assume $x_i = \pm 1$.

where the binary data sequence $\{x_i\}$ assumes values ± 1, and $u_0(t)$ is the unit pulse waveform

$$u_0(t) = \begin{cases} 1 & ; \quad -T_s/2 \le t \le T_s/2 \\ 0 & ; \quad \text{elsewhere,} \end{cases} \qquad (6)$$

Thus, $\tilde{s}(t)$ in this case is of the form (4) with $C_{1,i}=x_i, C_{2,i}=0, k=0$, and $u_c(t)=u_0(t)$ while $u_s(t)=0$.

Noncoherent BFSK: In this case, again assuming $x_i=\pm 1$, the complex signal envelope is given by

$$\tilde{s}(t) = \sqrt{\frac{E_s}{T_s}} \sum_i [u_c(t-iT_s-\tau)+jx_i u_s(t-iT_s-\tau)]e^{j\theta_i} , \qquad (7)$$

where[+] $\{\theta_i\}$ is an independent and identically distributed (i.i.d.) sequence uniformly distributed over $[-\pi,\pi]$. The baseband modulating waveforms are now given by

$$u_c(t) = \cos(\Delta\omega t/2)u_0(t), \qquad (8a)$$

and

$$u_s(t)=\sin(\Delta\omega t/2)u_0(t) , \qquad (8b)$$

with $u_0(t)$ described by (6). Here, $\Delta\omega$ is the tone spacing in radians/second, and is a multiple of $2\pi/T_s$ to insure orthogonality. The instantaneous radian frequency is then $2\pi f_c \pm \Delta\omega/2$ during successive baud intervals. Again, $\tilde{s}(t)$ is of the form (4) with $C_{1,i}=e^{j\theta_i}$, $C_{2,i}=x_i e^{j\theta_i}$, $k=0$, and $u_c(t)$, $u_s(t)$ defined by (8).

Coherent QPSK: The complex envelope of the transmitted signal is now of the form

$$\tilde{s}(t) = \sqrt{\frac{2E_b}{T_s}} \sum_i [x_{2i}u_c(t-iT_s-\tau)+jx_{2i+1}u_s(t-iT_s-\tau)]e^{j\theta} , \qquad (9)$$

[+] Without the sequence $\{\theta_i\}$, as described here, the phase could be estimated on the basis of past transmissions thereby violating the assumption of non-coherent reception.

where in this case

$$u_c(t) = u_s(t) = (1/\sqrt{2})u_0(t) \quad . \tag{10}$$

Note the factor $2E_b$, where E_b is the energy per bit, since now two symbols are transmitted for each channel use. The QPSK signal can be considered the sum of two independent BPSK signals in quadrature. Clearly, $\tilde{s}(t)$ is of the form (4) with $E_s = 2E_b$, $C_{1,i} = x_{2i}$, $C_{2,i} = x_{2i+1}$, $k=0$, and $u_c(t)$, $u_s(t)$ given by (10).

Coherent MSK: The complex envelope of the MSK signal can be represented in the form

$$\tilde{s}(t) = \sqrt{\frac{E_s}{T_s}} \sum_i [x_{2i} u_c(t-2iT_s-\tau) + jx_{2i+1} u_s(t-2iT_s-\tau)]e^{j\theta}, \tag{11}$$

where now

$$u_c(t) = \cos(\pi t/2T_s)u_0'(t) \quad , \tag{12a}$$

and

$$u_s(t) = \sin(\pi t/2T_s)u_0'(t-T_s) \quad , \tag{12b}$$

with $u_0'(t) = u_0(t/2)$, i.e.,

$$u_0'(t) = \begin{cases} 1 & ; \quad -T_s \le t \le T_s \\ 0 & ; \quad \text{elsewhere} \quad . \end{cases} \tag{13}$$

Representation in the form (4) is rather obvious where we note that now $k=1$ is required.

B. _Channel Noise Model_: The complex envelope $\tilde{n}(t)$ of the additive noise is assumed modeled as a linear combination of a generalized shot noise process, typically low density [+], and WGN. In particular,

$$\tilde{n}(t) = \tilde{y}(t) + \tilde{w}(t) \quad , \tag{14}$$

where $\tilde{w}(t) = w_c(t) - jw_s(t)$ is a zero-mean complex WGN process with I/Q components, $w_c(t)$ and $w_s(t)$, respectively, mutually independent lowpass WGN processes each

---

[+] By low-density we mean that the interarrival times of the impulses are relatively long compared to typical impulse durations.

possessing double-sided noise spectral density $N_0/2$ watts/Hz. The shot noise component $\tilde{y}(t)$ accounts for the relatively infrequent high-level and time-resolved impulse noise hits due to atmospheric discharge phenomenon, or various contributions due to man-made noise or pulse jamming. The Gaussian noise component $w(t)$, on the other hand, is due to a combination of front-end noise and the larger number of low-level and overlapping impulse hits. The latter contribution is expected to exhibit Gaussian behavior from central limit theorem considerations.

The shot noise component can be modeled as the output of a linear time-invariant filter excited by a complex amplitude modulated impulse train or point process at its input. The filter generating the complex shot noise process $\tilde{y}(t)$ is assumed to possess impulse response $\bar{h}(t)$, or equivalently system transfer function $\bar{H}(s)$. A block diagram of the channel noise model is illustrated in Fig. 1. The impulse response $\bar{h}(t)$ will in general be complex possessing an *inphase component* $h_c(t)$ *and a quadrature component* $h_s(t)$. The complex input $\tilde{u}(t)$ to the linear filter generating the shot noise component is assumed of the form

$$\tilde{u}(t) = \sum_{i=1}^{N(t)} \tilde{u}_i \delta(t-t_i) \quad . \tag{15}$$

Here $\{\tilde{u}_i\}$ is an appropriately defined complex i.i.d. weighting sequence and $\{N(t), t \geq 0\}$ is a point process, in particular a counting process [6]-[8], whose event times are described by the sequence $\{t_i\}$. We will be particularly interested in stationary renewal counting processes possessing Gamma distributed interarrival times with probability density function (p.d.f.)

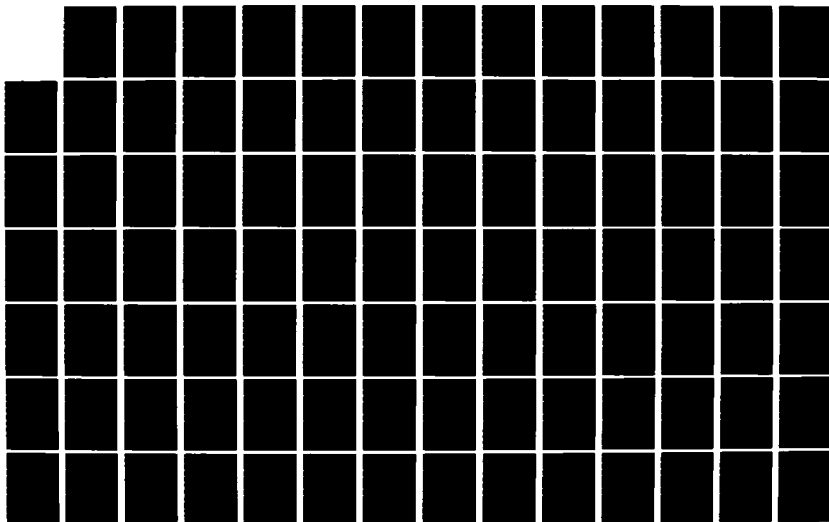$$f(x) = \frac{x^{\nu-1}}{\Gamma(\nu)\beta^\nu} \exp\{-x/\beta\} \quad ; \quad x \geq 0 \quad , \tag{16}$$

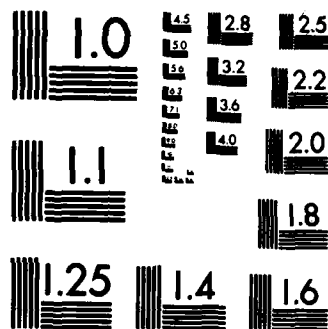MICROCOPY RESOLUTION TEST CHART
NATIONAL BUREAU OF STANDARDS-1963-A

where $\nu \geq 1$, and the parameter β is defined according to $\beta = 1/\nu\lambda$ with $\lambda \geq 0$ fixed. The quantity λ represents the average number of events per unit time. This quantity will generally be specified in units normalized to the baud duration T_s seconds. Specification of the two parameters ν and λT_s, then, completely defines the point process $\{N(t), t \geq 0\}$.

For example, if $\nu = 1$ then

$$f(x) = \lambda e^{-\lambda x} \quad ; \quad x \geq 0 \quad . \tag{17}$$

This is the exponential distribution. In this case, $\{N(t), t \geq 0\}$ is Poisson with λ the average number of hits per unit time. Another special case is obtained by letting $\nu \to \infty$ while holding λ fixed. The result is

$$f(x) = \delta(x - 1/\lambda) \quad . \tag{18}$$

In this case, the impulses are periodic with rate λ per unit time. By introducing the class of driving point processes described here, we have a conveniently parameterized impulsive noise model which includes these two extremes as special cases. The class of point processes $\{N(t), t \geq 0\}$, and hence $\tilde{u}(t)$, is easily generated on a digital machine.

In what follows we will assume that the complex impulse amplitudes are of the form $\tilde{u}_i = R_i e^{-j\theta_i}$ with $\{R_i\}$ an i.i.d. sequence possessing common p.d.f. $f_r(\cdot)$, while $\{\theta_i\}$ is likewise an i.i.d. sequence uniformly distributed over $[-\pi, \pi]$. Although many choices for $f_r(\cdot)$ are possible, we will restrict attention to two which are specifically motivated by related ELF/VLF noise modeling work [9]-[12]. The first choice is the power-Rayleigh or Wiebull distribution with

$$f_r(R) = \frac{\alpha}{R_0^\alpha} R^{\alpha-1} \exp\{-(R/R_0)^\alpha\} \quad ; \quad R \geq 0, \tag{19}$$

where the characteristic exponent α lies in the range $0 < \alpha \leq 2$ and R_0 is a scale parameter given by

$$R_0 = \left[\frac{E\{R^2\}}{\Gamma(1+2/\alpha)}\right]^{\frac{1}{2}} \tag{20}$$

Another useful choice is the lognormal distribution with

$$f_r(R) = \frac{1}{\sqrt{2\pi}\sigma R}\,\exp\left\{-\frac{(\ln R - \mu)^2}{2\sigma^2}\right\} \quad ; \quad R \geq 0 \quad . \tag{21}$$

Here μ and σ^2 are the mean and variance, respectively, of a Gaussian variate g for which $R = e^g$. In this case, for fixed value of μ, it is convenient to describe the scale parameter in terms of the quantity

$$V_d = 10 \log_{10}\frac{E\{R^2\}}{E^2\{R\}} \simeq 4.343\sigma^2 \quad . \tag{22}$$

These two distributions are sufficiently general to exhibit the broad-tailed distributions typical of many observed impulsive noise situations.

Under the preceding assumptions, it follows that the I/Q components of the shot noise process can be generated as illustrated in Fig. 2 according to

$$y_c(t) = \sum_{i=1}^{N(t)} R_i[h_c(t-t_i)\cos\theta_i - h_s(t-t_i)\sin\theta_i], \tag{23a}$$

and

$$y_s(t) = \sum_{i=1}^{N(t)} R_i[h_s(t-t_i)\cos\theta_i + h_c(t-t_i)\sin\theta_i] \quad . \tag{23b}$$

Here $h_c(t)$ and $h_s(t)$ are, as described previously, the I/Q components of the complex impulse response function $\tilde{h}(t)$. We will assume that $h_c(t)$ and $h_s(t)$ are both equal to the same impulse response function $h_0(t)$. Several choices for $h_0(t)$ are possible. For example, the simplest choice is the pulse waveform of duration T_c seconds as illustrated in Fig. 3. The corresponding impulse response is

$$h_0(t) = u_{-1}(t) - u_{-1}(t-T_c) \quad , \tag{24}$$

where $u_{-1}(t)$ is the unit step function

$$u_{-1}(t) = \begin{cases} 1 & ; \quad t \geq 0 \\ 0 & ; \quad t < 0 \end{cases} \qquad (25)$$

Generally it will be the case that $\lambda T_c \ll 1$ so that the resulting shot noise process is truly low-density. Other choices of characteristic pulse shape $h_0(t)$ are provided in Table 2 together with some other pertinent parameters to be described in what follows.

Finally, the last component of the impulsive noise model to be specified is the quantity

$$\gamma^2 = \frac{E\{|\tilde{y}(t)|^2\}}{N_0} \, , \qquad (26)$$

which represents the ratio of the mean-square value of the shot noise component to the double-sided noise spectral density of the AWGN component. The units of γ^2 are in Hz, or equivalently $\sec^{-1}$. In what follows we will be more interested in the dimensionless quantity $\gamma^2 T_s$, representing the power in the shot noise normalized to that of AWGN component when measured in a double-sided noise-bandwidth equal to the baud rate $f_s = 1/T_s$.

For a fixed choice of model parameters the scale parameters associated with the amplitude p.d.f. $f_r(\cdot)$ can be adjusted to achieve a specified value of $\gamma^2 T_s$. In particular, it is easily shown, following the approach in [13]-[15], that the stationary input point process $\tilde{u}(t)$ described by (15) and the sequel possesses power spectral density $S_{\tilde{u}\tilde{u}}(\omega) = \lambda E\{R^2\}$ independent of the value of ν. It follows that the power spectral density of the low-density shot noise process is given by

$$S_{\tilde{y}\tilde{y}}(\omega) = 2\lambda |H_0(j\omega)|^2 E\{R^2\} \, , \qquad (27)$$

from which we obtain

$$E\{|\tilde{y}(t)|^2\} = 4\lambda B |H_0(0)|^2 E\{R^2\} \quad . \qquad (28)$$

4-11

Here,

$$B \triangleq \frac{\frac{1}{2\pi} \int_{-\infty}^{\infty} |H_0(j\omega)|^2 d\omega}{2|H_0(0)|^2}, \tag{29}$$

is the equivalent single-sided rectangular bandwidth in Hz and is provided in Table 2 for each of the characteristic pulse shapes considered. Also provided in Table 2 is the mean-square value $E\{|\tilde{y}(t)|^2\}$ of the shot-noise component where all parameters are conveniently expressed in dimensionless form allowing explicit evaluation of $E\{R^2\}$, and hence the scale parameter associated with $f_r(\cdot)$, for a fixed value of $\gamma^2 T_s$.

III. Statistical Characterization of Noise Model:

In this section we describe some of the low-order statistics which provide a partial, although useful, characterization of the impulsive noise model described in the preceding section. Since most of the literature on noise measurements, particularly on the measurement of atmospheric noise, have dealt almost exclusively with the envelope process $A(t)=|\tilde{n}(t)|$, we concentrate on envelope statistics. While many choices are possible we consider two envelope statistics: the amplitude probability distribution (APD), and the average level crossing rate (ALCR). These two statistics are not only illustrative of impulsive noise effects, but data are generally available for gross calibration purposes. We consider each of these statistics separately.

A. _Amplitude Probability Distribution (APD)_: If[†] $f_a(\cdot)$ represents the first-order p.d.f. of the envelope process $A(t)$, then the APD is merely the probability

$$Q_a(x) = \int_x^{\infty} f_a(\xi)d\xi , \tag{30}$$

---

† We will assume steady-state conditions and suppress any explicit functional dependence upon time in describing first-order distributions.

of exceeding the fixed level x. In evaluating APD's, as well as ALCR's, it is convenient to normalize the fixed level x to the rms value of the envelope. Because of the presence of the AWGN component, however, this rms value is unbounded. Thus, it is necessary in evaluating APD's and ALCR's to assume that the noise process $\tilde{n}(t)$ is observed through a fictitious measurement filter of finite single-sided equivalent rectangular bandwidth B' Hz.

The question of choosing an appropriate bandwidth for evaluating APD's poses some difficulties. In particular, if the measurement bandwidth B' is not appreciably larger than that of the shot noise component then the actual shape of the APD curve can be expected to depend upon B'. If, on the other hand, B' is much larger than the bandwidth of the shot noise component then the shot noise is unaffected by the presence of this fictitious measurement filter. In this case, changing B' merely allows more or less AWGN thereby scaling the APD curves up or down without affecting the shape. Similar comments apply in the case of ALCR's. We assume then that B'>>B, with B the equivalent rectangular bandwidth of the shot noise component given by (29). The total mean-square value of the "filtered" impulsive noise $\tilde{n}'(t)$ is then given by

$$\sigma_{\tilde{n}'}^2 = \sigma_{\tilde{y}}^2 + \sigma_{\tilde{w}'}^2 \quad , \tag{31}$$

where $\sigma_{\tilde{y}}^2 = E\{|\tilde{y}(t)|^2\}$ is unaffected by the action of the filter and $\sigma_{\tilde{w}'}^2 \stackrel{\Delta}{=} 2N_0 B'$. We now proceed to an evaluation of the APD for this "filtered" impulsive noise process.

From (30), the difficulty in evaluating the APD is directly related to the ability of determining the p.d.f. $f_a(\cdot)$. While the exact evaluation of $f_a(\cdot)$ is extremely difficult in general, evaluation of the characteristic

function (ch.f.) is relatively straightforward in some special cases. This allows evaluation of $f_a(\cdot)$, and hence $Q_a(\cdot)$, by numerical techniques.

The joint ch.f. of the I/Q components[+] $n_c'(t)$ and $n_s'(t)$, respectively, is given by

$$\psi_{n_c', n_s'}(v_1, v_2) = E\{\exp[j(v_1 n_c'(t) + v_2 n_s'(t))]\}$$

$$= \psi_{y_c, y_s}(v_1, v_2) \psi_{w_1', w_2'}(v_1, v_2) \quad , \tag{32}$$

where we have made use of the independence of the shot noise and WGN components. Clearly,

$$\psi_{w_1', w_2'}(v_1, v_2) = \exp\{-\frac{N_0 B'}{2}[v_1^2 + v_2^2]\}$$

$$= \exp\{-\sigma_w^2 \beta^2 / 2\} \quad , \tag{33}$$

where for convenience we have defined $\sigma_w^2 \overset{\Delta}{=} N_0 B'$ and $\beta \overset{\Delta}{=} \sqrt{v_1^2 + v_2^2}$. The quantity $\sigma_w^2 = \sigma_{w'}^2/2$ represents the common variance of the I/Q components of the filtered background Gaussian component $\tilde{w}'(t)$. Similarly, the joint ch.f.

$$\psi_{y_c, y_s}(v_1, v_2) = E\{\exp[j(v_1 y_c(t) + v_2 y_s(t))]\} \quad , \tag{34}$$

of the shot noise component can be shown to depend upon v_1, v_2 only through β. It follows that the joint ch.f. $\psi_{n_c', n_s'}(v_1, v_2)$ then depends only upon β. In this case the envelope p.d.f. is given by

$$f_a(A) = \int_0^\infty A\beta J_0(\beta A)\psi_{n_c', n_s'}(\beta)d\beta$$

$$= \int_0^\infty A\beta J_0(\beta A)\psi_{y_c, y_s}(\beta)e^{-\sigma_w^2 \beta^2/2}d\beta \quad , \tag{35}$$

[+] We will distinguish the output components of the fictitious measurement filter with a prime.

where $J_\nu(\cdot)$ is the ordinary Bessel function of the first kind of order ν, and we have made use of (32) and (33) in obtaining this last expression. Finally, it is easily established that the APD given by (30) can be evaluated according to

$$Q_a(x) = 1-x \int_0^\infty J_1(\beta x)\, \psi_{y_c,y_s}(\beta)e^{-\sigma_w^2\beta^2/2}d\beta \quad , \tag{36}$$

which is readily evaluated by quadrature given explicit expression for $\psi_{y_c,y_s}(\beta)$.

The major difficulty in evaluating either $f_a(\cdot)$ or $Q_a(\cdot)$ through (35) and (36), respectively, is the general inability of obtaining concise expressions for the joint ch.f. $\psi_{y_c,y_s}(\beta)$ of the shot noise component. An exception is the case where $\{N(t),\ t\geq 0\}$ is Poisson, i.e., $\nu=1$. In this case it is shown in Appendix A that

$$\psi_{y_c,y_s}(\beta) = \exp\left\{\lambda \int_0^\infty [E_r\{J_0(\sqrt{2}\beta Rh_0(\tau))\} -1]d\tau\right\} . \tag{37}$$

Here, the expectation appearing in the integral is with respect to the random amplitude R of the input pulse process, i.e.,

$$E_r\{J_0(\sqrt{2}\,\beta Rh_0(\tau))\} = \int_0^\infty J_0(\sqrt{2}\beta Rh_0(\tau))f_r(R)dR \quad , \tag{38}$$

where $f_r(\cdot)$ is given by either (19) or (21). Again this quantity can be evaluated in closed form only in special cases. One useful case is when $f_r(\cdot)$ is power-Rayleigh with characteristic exponent $\alpha=1.0$, in which case it is easily shown by straightforward integration that

$$E_r\{J_0(\sqrt{2}\,\beta Rh_0(\tau))\} = [1 + 2R_0^2\beta^2h_0^2(\tau)]^{-\frac{1}{2}} \quad . \tag{39}$$

Substitution into (37) for $h_0(t)=e^{-at}u_{-1}(t)$ yields

$$\psi_{y_c, y_s}(\beta) = \left[\frac{1+\sqrt{1+(a/\lambda)\sigma_{\tilde{y}}^2\beta^2}}{2}\right]^{-\lambda/a} . \tag{40}$$

Here, $\sigma_{\tilde{y}}^2 = E\{|\tilde{y}(t)|^2\}$ is the variance of the shot component and we have made use of (20) together with Table 2 to evaluate the scale parameter R_0 associated with the power-Rayleigh distribution. It is interesting to note that in the high-density case, corresponding to large (λ/a), we have

$$\psi_{y_c, y_s}(\beta) \simeq \exp\{-\frac{1}{2}\sigma_y^2\beta^2\} , \tag{41}$$

where $\sigma_y^2 \stackrel{\Delta}{=} \sigma_{\tilde{y}}^2/2$ is the common variance of the I/Q components of the shot noise process. As expected, the shot noise is Gaussian in this limiting case.

Substitution of (40) into (36) allows evaluation of the APD by quadrature in this special but useful case. The results are illustrated in Fig. 4 using a 64-point quadrature formula. Here we plot the envelope normalized to its rms value versus the percent of time that the ordinate is exceeded. The curves are specifically designed so that a Gaussian distribution (Rayleigh envelope) plots as a straight line of slope -1/2. Observe that the APD's do appear Gaussian at low levels and depart considerably from Gaussian behavior at high levels. Also note that at low levels the curves, although parallel to, are depressed below the Gaussian curve ($\gamma^2 T_s = 0$). The reason for this is that we have chosen to normalize the envelope to the total rms level. From (31) we observe that

$$E\{A^2(t)\} = E\{|\tilde{n}(t)|^2\}$$
$$= \sigma_{\tilde{w}'}^2 \left[1 + \frac{\gamma^2 T_s}{2B'T_s}\right] , \tag{42}$$

so that in the low-level Gaussian region the curves can be expected to be depressed below the straight-line Gaussian characteristic by approximately

$$\Delta_1 = 10 \log_{10}\left[1 + \frac{\gamma^2 T_s}{2B'T_s}\right] , \text{dB} \qquad (43)$$

which is consistent with Fig. 4.

Also included in Fig. 4 are simulation results obtained on the previous-ly described ICS [5]. These results have been obtained using a minimum of 10^7 samples in each case. As can be seen the agreement with the computed results are excellent. In more general cases, the numerical evaluation of APD's according to (36) has proven extremely difficult. The major difficulty is in obtaining closed form expressions for the joint ch.f. $\psi_{y_c,y_s}(\beta)$. In-deed, even in the Poisson case evaluation of $\psi_{y_c,y_s}(\beta)$ according to (37) is difficult and is quite hopeless for non-Poisson input processes, i.e., $\nu>1$. Because of this general intractability of analytical evaluation of APD's, and the relative ease with which accurate simulation results can be obtain-ed we will rely exclusively upon the latter in what follows.

In Fig. 5 we illustrate simulation results for the same situation as in Fig. 4, except now $\alpha=0.5$. Note the much higher probability of exceeding large levels indicating much broader tails to the envelope p.d.f. Also note that even small values of $\gamma^2 T_s$ (3dB say) can have a pronounced effect on the high-amplitude region of the APD. In Fig. 6 we illustrate the effect of varying $B'T_s$ with $\gamma^2 T_s=20$dB and conditions otherwise the same as in Fig. 5. The APD's approach the Gaussian curve in the low-amplitude region with in-creasing $B'T_s$ as predicted by (43). Clearly, increasing $B'T_s$ results in more of the AWGN component being passed by the fictitious measurement filter thereby contributing more heavily to the total mean-square noise. Observe that provided $B'>B$, as is indeed the case in Fig. 6, the APD is affected very little in the high-amplitude region as $B'T_s$ is increased.

The effect of varying the parameter aT_s is illustrated in Fig. 7, again for power-Rayleigh pulse amplitudes with $\alpha=0.5$, $\lambda T_s=0.1$ and $\gamma^2 T_s = 20dB$. For small aT_s there is considerable pulse overlap since then $\lambda/a>1$ and the APD resembles that of Gaussian noise as might be expected from central limit theorem considerations. For larger aT_s values the individual pulses are resolved and the APD departs drastically from Gaussian behavior in the large-amplitude region. Similar comments apply to Fig. 8, where now aT_s is fixed and the normalized pulse arrival rate λT_s is varied. Again, for large λT_s, or equivalently $\lambda/a>>1$, the APD resembles that of Gaussian noise due to the relatively large number of pulse overlaps.

In Fig.'s 9 and 10 we illustrate the effect of varying α and V_d for power-Rayleigh and lognormal pulse amplitudes, respectively. It is clear how by choice of either α or V_d the behavior in the large-amplitude region can be controlled with little effect on the small-amplitude region. Indeed, by appropriate choice of parameter values the corresponding APD's for both power-Rayleigh and lognormal distributed pulse amplitudes can be made to agree quite well, at least for a range of parameter values. This is illustrated in Fig. 11 where the values of α and V_d have been chosen to provide the best correspondence for other parameters held fixed.

Finally, in Fig.'s 12 and 13 we illustrate the effect of changing the characteristic pulse shape and pulse interarrival statistics, respectively. In Fig. 12 we illustrate that the pulse shape has little effect on APD's since there is no noticeable difference for a variety of characteristic pulse waveforms selected from Table 2. Similarly, from Fig. 13 we see that varying the pulse interarrival statistics, while maintaining λT_s constant, has little effect on the APD.

4-18

6. _Average Level Crossing Rate (ALCR)_: Consider the average number $N^+(u)$ of upcrossings per second of a fixed level u by the envelope process $A(t) = |\tilde{n}'(t)|$ appearing at the output of the fictitious measurement filter. The ALCR is then the quantity $N^+(u)T_s$, representing the average number of upcrossings of the level u in a baud or symbol period of duration T_s sec.

In general, explicit evaluation of the ALCR for the impulsive noise model described in the preceeding section is extremely difficult, if at all possible. However, in the particular case where $\tilde{n}'(t)$ is a complex zero-mean Gaussian process (i.e., $\gamma^2 T_s = 0$) with rms bandwidth B_0 Hz, and variance $E\{|\tilde{n}'(t)|^2\} = E\{A^2(t)\} \triangleq A_0$, we have [16], [17],

$$N^+(u)T_s = \sqrt{2\pi}\, B_0 T_s (u/A_0) \exp\{-\tfrac{1}{2}(u/A_0)^2\} \; , \tag{44}$$

where

$$2\pi B_0 \triangleq \sqrt{\frac{\dfrac{1}{2\pi}\displaystyle\int_{-\infty}^{\infty}\omega^2 S_{nn}(\omega)\,d\omega}{\dfrac{1}{2\pi}\displaystyle\int_{-\infty}^{\infty} S_{nn}(\omega)\,d\omega}} \quad , \tag{45}$$

and $S_{nn}(\cdot)$ is the common power spectral density of the assumed independent I/Q components. The ALCR is then readily evaluated as a function of the normalized level u/A_0 for selected choices of $B_0 T_s$. For example, if the measurement filter is flat over the interval[+] $[-B', B']$ we have $B_0 = B'/\sqrt{3}$ allowing explicit evaluation of the ALCR according to (44) as a function of $B'T_s$ where now $A_0 = \sqrt{2N_0 B'}$. In Fig. 14 we illustrate computed results for selected values of $B'T_s$ together with simulation results collected on the ICS. In all cases the simulation results are obtained on the basis of at least 10^7 samples. As can be seen the agreement between computed and simulated results is excellent. Because of this close correspondence, and

[+] Here B' is the equivalent single-sided rectangular bandwidth.

the general intractability of the ALCR in non-Gaussian situations, we will make exclusive use of simulation results in what follows. Finally, before leaving this special case, we should note that even if $\tilde{y}(t)$ were Gaussian the ALCR would depend not only upon $\gamma^2 T_s$ but in a very complicated way upon $B'T_s$ and $B'_0 T_s$, where B'_0 is now the rms bandwidth of the shot noise component. In particular, it is easily seen that the ALCR is still given by (44) where now

$$
B_0 = \frac{B'}{\sqrt{3}} \left[\frac{1+(B'_0/B')^2 \dfrac{3\gamma^2 T_s}{2B'T_s}}{1+\dfrac{\gamma^2 T_s}{2B'T_s}} \right]^{\frac{1}{2}}
$$

In Fig. 15 we illustrate the ALCR for impulsive noise under selected parameter choice for various values of $\gamma^2 T_s$. The parameters correspond to the APD's illustrated in Fig. 5. As can be observed the presence of the shot noise component results in considerably increased crossing rates relative to the case of Gaussian noise alone ($\gamma^2 T_s = 0$) in the large-amplitude region. In the low-amplitude region the curves are parallel to the Gaussian characteristic as to be expected, except they are displaced to the left. Again, this is due to the fact that we have chosen to normalize the abscissa to the total rms value in which case the curves can be expected to be displaced by an amount Δ_1 given by (43). This is illustrated also in Fig. 16 where we vary $B'T_s$ with $\gamma^2 T_s = 20\mathrm{dB}$ and conditions otherwise the same as in Fig. 15.

The effect of varying the parameter aT_s is illustrated in Fig. 17, corresponding to the APD plots in Fig. 7. Again, for small aT_s there is considerable pulse overlap and $n'(t)$ is approximately Gaussian. The ALCR then converges to the dotted curve which is computed according to (44) where B_0 is now evaluated from (46). Similar comments apply to Fig.18 where $aT_s = 2.0$ is fixed

and the normalized pulse arrival rate λT_s is varied. Again, as for the APD's in Fig. 8, for large λT_s, or equivalently $\lambda/a \gg 1$, the ALCR resembles that for Gaussian noise due to the relatively large number of pulse overlaps.

In Fig.'s 19 and 20 we illustrate the effect of varying α and V_d corresponding to Fig.'s 9 and 10, respectively. Again, it is clear how the choice of either α or V_d effects the behavior in the large-amplitude region with little noticeable effect on the small-amplitude nearly-Gaussian region. In Fig. 21 we illustrate how the values of α and V_d can be chosen to provide a close match in ALCR corresponding to the APD results illustrated in Fig. 11.

Finally, in Fig.'s 22 and 23 we illustrate the effect of changing the characteristic pulse shape and interarrival statistics, respectively. These results correspond to APD's illustrated in Fig.'s 12 and 13, respectively. As in the case of APD's, we observe that neither the pulse shape or the interarrival statistics has much effect on the ALCR, provided, of course, λT_s is maintained constant.

IV. Performance of Linear Matched Filter Receivers:

In this section we consider the performance of linear matched filter receivers in noise environments characterized by the previously developed impulsive noise model. Specifically, we evaluate the symbol error probability for each of the modulation strategies described in Section II and summarized in Table 2. It proves convenient to consider separately the cases of coherent (i.e., BPSK, QPSK and MSK) and noncoherent (i.e., DPSK, BPSK) modulation strategies. Indeed, the decision variable is of identical form for each of these two distinct cases. In general, the decision variable can be written as a sum of three separate terms associated with the signal, shot noise, and AWGN components, respectively. The error probability

conditioned upon the shot noise is easily determined as this is merely the corresponding error probability for the AWGN channel. It follows that the overall error probability can then be determined by averaging with respect to the shot noise component. This is the approach to be followed in subsequent developments where we neglect the effects of symbol synchronization and phase tracking errors.

A. _Coherent Modulation_: In this case it is easily seen that individual bit decisions are based upon threshold tests of the sufficient statistics

$$r_{ci} = \text{Re} \left\{ \int_{2^k(i-\frac{1}{2})T_s}^{2^k(i+\frac{1}{2})T_s} \tilde{r}(t)u_c(t-2^k iT_s)dt \right\} \quad ; \; i=0,1,2,\ldots, \quad (47a)$$

and

$$r_{si} = \text{Re} \left\{ \int_{2^k(i-\frac{1}{2})T_s}^{2^k(i+\frac{1}{2})T_s} \tilde{r}(t)u_s(t-2^k iT_s)dt \right\} \quad ; \; i=0,1,2,\ldots, \quad (47b)$$

where $u_c(t)$ and $u_s(t)$ are appropriate baseband waveforms modulating the I/Q rails as described previously in Section II where we recall k=1 for MSK, and k=0 otherwise. For example, in BPSK only the sequence $\{r_{ci}\}$ is employed to determine the binary sequence[†] $\{\hat{x}_i\}$ with

$$\hat{x}_i = \text{sgn } r_{ci} \quad , \; i=0,1,\ldots \quad (48)$$

For either QPSK or MSK, the two sequences $\{\hat{x}_{2i}\}$ and $\{\hat{x}_{2i+1}\}$ are obtained by similar operations upon $\{r_{ci}\}$ and $\{r_{si}\}$, respectively. In general, by appropriate normalization, the decision variable during any given signaling interval can be expressed in the form

$$d = x\sqrt{\frac{2E_b}{N_0}} + y + w \quad . \quad (49)$$

[†] Here $\{\hat{x}_i\}$ represents the hard-decisioned output sequence corresponding to the transmitted sequence $\{x_i\}$.

4-22

Here, E_b is the energy per bit, $x=\pm 1$ is a binary variable corresponding to the transmitted bit, w is a zero-mean unit variance Gaussian variate, and finally

$$y \triangleq (2/\epsilon N_0 2^k T_s)^{\frac{1}{2}} \int_0^{2^k T_s} y_c(t) u_c(t-2^{k-1}T_s) dt$$

$$= \sum_{i=1}^{N(2^k T_s)} z_i g(t_i) \quad , \tag{50}$$

where

$$z_i \triangleq 2(2^k T_s/\epsilon N_0)^{\frac{1}{2}} R_i \cos(\theta_i + \pi/4) \quad ; \quad i=1,2,\ldots, \tag{51a}$$

with[+]

$$\epsilon \triangleq \frac{1}{2^k T_s} \int_0^{2^k T_s} u_c^2(t-2^{k-1}T_s) dt \quad , \tag{51b}$$

and finally

$$g(t) \triangleq \frac{1}{2^k T_s} \int_0^{2^k T_s} h_0(\tau-t) u_c(\tau-2^{k-1}T_s) d\tau \quad . \tag{51c}$$

In developing these expressions we have made explicit use of (23) and the sequel. The $\{t_i\}$ in (50) are, of course, the event times of the underlying point process $\{N(t), t \geq 0\}$.

In any case, using (49) the probability of error under equiprobable signaling can be expressed in the form

$$P_e = \int_{-\infty}^{\infty} Q\left(\sqrt{\frac{2E_b}{N_0}} + \xi\right) f_y(\xi) d\xi \quad , \tag{52}$$

where $f_y(\cdot)$ is the p.d.f. of y given by (50) and

$$Q(x) \triangleq \frac{1}{\sqrt{2\pi}} \int_x^{\infty} \exp\{-y^2/2\} \, dy \quad . \tag{53}$$

Unfortunately, explicit evaluation of $f_y(\cdot)$ is extremely difficult so that

[+] It is easily established that $\epsilon=1$ for BPSK while $\epsilon = \frac{1}{2}$ for both QPSK and MSK.

numerical evaluation of P_e though (52) has proven impractical. In some cases, however, the ch.f. $\psi_y(\cdot)$ is more amenable to evaluation. Indeed, an alternative and more useful expression for error probability in this case is shown in Appendix B to be given by

$$P_e = \frac{1}{2} + \frac{1}{\pi} \int_0^\infty \psi_y(v) \frac{\sin\sqrt{2E_b/N_0}\,v}{v} e^{-v^2/2} dv \; , \tag{54}$$

which is readily evaluated by quadrature given an explicit expression for $\psi_y(\cdot)$.

A useful special case for which the evaluation of $\psi_y(\cdot)$ is relatively straightforward is when $\{N(t), t \geq 0\}$ is Poisson. In this case, y in (50) is then a filtered Poisson process with random amplitude sequence $\{Z_i\}$ and characteristic pulse shape $g(t)$. It follows [6], [7] that

$$\psi_y(v) = \exp\{\lambda \int_{-\infty}^{2^k T_s} [\psi_z(vg(\tau)) - 1] d\tau\} \; , \tag{55}$$

where $\psi_z(\cdot)$ is the common ch.f. of the random amplitude sequence $\{Z_i\}$. In particular, following a development similar to that in Appendix A we easily establish that

$$\psi_z(vg(\tau)) = E_r\{J_0(2\sqrt{2^k T_s/\epsilon N_0} \; vRg(\tau))\}, \tag{56}$$

where, as in (38), $E_r\{\cdot\}$ indicates expectation with respect to the random amplitude of the input pulse process generating the shot noise. Again, this quantity, and hence $\psi_y(v)$, can be evaluated only in special cases.

One useful case where $\psi_z(\cdot)$ can be explicitely evaluated is when R is power-Rayleigh with characteristic exponent $\alpha = 1.0$, where from (39) we have

$$\psi_z(vg(\tau)) = [1 + 4(2^k T_s/\epsilon N_0) R_0^2 v^2 g(\tau)]^{-\frac{1}{2}}, \tag{57}$$

with R_0 again the scale parameter associated with the power-Rayleigh distri-

4-24

bution given by (20). In Appendix C it is shown that for the particular case[†]
of coherent BPSK and with characteristic pulse shape $h_0(t) = e^{-at}u_{-1}$ we have

$$\psi_y(v) = \psi_y^-(v)\psi_y^+(v) \quad , \tag{58}$$

with

$$\psi_y^-(v) \triangleq \left[\frac{1+\sqrt{1+\zeta K^2 v^2}}{2} \right]^{-\lambda T_s/aT_s} \quad , \tag{59a}$$

and

$$\psi_y^+(v) \triangleq \left[\frac{1+\sqrt{1+\zeta v^2}}{1+\zeta K v^2+\sqrt{(1+\zeta v^2)(1+\zeta K^2 v^2)}} \right]^{-\lambda T_s/aT_s\sqrt{1+\zeta v^2}} \tag{59b}$$

$$\cdot \exp\left\{ \lambda T_s\left[\frac{1}{\sqrt{1+\zeta v^2}} - 1 \right] \right\} \quad ,$$

where

$$\zeta \triangleq \frac{2\lambda^2 T_s}{(\lambda T_s)(aT_s)} \quad ; \quad K \triangleq (1-e^{-aT_s}) \quad . \tag{59c}$$

The two quantities $\psi_y^-(v)$ and $\psi_y^+(v)$ can be interpreted as the contributions
from impulses occurring prior to the signaling interval and during the sig-
naling interval, respectively. At any rate, substitution of this express-
ion for $\psi_y(v)$ into (54) allows numerical evaluation of the resulting error
probability.

In Fig. 24 we illustrate typical computed results using a 64-point
quadrature formula for various values of λT_s with $aT_s=4.0$ and $\gamma^2 T_s=20$dB.
The P_e curves here and in the sequel have been plotted versus the quantity
E_b/N_0 which is the energy per bit normalized to the spectral density of the
AWGN component. We have also indicated in Fig. 24 the error probability
performance in the absence of impulsive noise as well as the approximate
performance if all the noise were Gaussian and under the assumption[††] $BT_s>1$.

---

† Actually, the indentical result holds for QPSK while the results for MSK
  are considerably more complicated.

†† Here B is the equivalent rectangular bandwidth of the shot noise component.

Specifically, under the latter assumption the total noise environment is
Gaussian with a power spectral density approximately flat over the matched
filter bandwidth ($1/T_s$ Hz) at the value

$$S_{nn}(\omega) = \frac{N_0}{2} + S_{yy}(0)$$
$$= \frac{N_0}{2} \left[1 + \frac{\gamma^2}{2B} \right] \quad , \tag{60}$$

where $S_{yy}(\omega)$ is the common power spectral density of the I/Q components of
the shot noise and we have made use of the fact

$$S_{yy}(0) = \frac{E\{y_c^2(t)\}}{2B} = \frac{\gamma^2}{2B}(N_0/2) \quad . \tag{61}$$

It follows that the error probability in this environment is simply the
corresponding result for the background AWGN alone shifted to the right by

$$\Delta_2 = 10 \log_{10} \left[1 + \frac{\gamma^2 T_s}{2BT_s} \right] dB \quad . \tag{62}$$

According to Table 2, for the case treated here BT_s=1 so the condition BT_s>1
is not quite satisfied. Nevertheless, we see that for large λT_s, or equiv-
alently large λ/a, the error probability does indeed converge to the approx-
imate asymptotic performance.

Finally, observe that simulation results have also been included in
Fig. 24 indicating close correspondence with the computed results. The
simulation results were again obtained on the ICS. Because of this close
correspondence between simulated and computed results and the general
intractability of analytical evaluation in more general cases, we will make
exclusive use of simulation results in what follows.

In Fig. 25 we illustrate the effect of $\gamma^2 T_s$ on error probability per-
formance with BPSK modulation and typical parameter choices corresponding
to the APD results in Fig. 5. Here it is clear that even a small amount of

impulse noise can have a disastrous effect on the error probability perform-
ance. The corresponding effect of the parameter aT_s on P_e with other
parameters held fixed is illustrated in Fig. 26. For small aT_s, or equivalently
large λ/a, the pronounced broad tails are absent and P_e does decrease rapidly
with increasing E_b/N_0 as the total noise environment is then approximately Gauss-
ian. The results here correspond to APD's illustrated previously in Fig. 7.

In Fig.'s 27 and 28, we illustrate the effect on P_e of α and V_d for the
power-Rayleigh and lognormal distributions, respectively. For the parameter
choices considered, $BT_s>1$ while $\lambda/a>1$ so the performance is expected to be given
by our approximate result valid under the assumption the total noise environment
is Gaussian. As can be seen this is true only for relatively large α or small
V_d. In Fig. 29 we illustrate that if α and V_d are chosen, as in Fig. 11 to
provide a close match in APD, then the resulting error probability performance
is likewise quite close. This is further illustrated in Fig. 30 where, for a
unipolar pulse, varying the characteristic pulse shape has little effect on P_e,
as observed previously for APD's in Fig. 12. For a bipolar pulse, on the other
hand, P_e improves with increasing ωT_s since then the matched filter is able to
average the effects of the impulse noise component. Similarly, in Fig. 31 we
demonstrate that varying ν, and hence the pulse interarrival distribution, has
little effect on P_e consistent with APD behavior illustrated in Fig. 13.

Finally, in Fig. 32 we illustrate some typical results employing other
coherent modulation strategies. As expected, the QPSK results are nearly
identical to those for BPSK with only minor differences from the behavior of MSK.

B. *Noncoherent Modulation*: We will be specifically concerned with the error
probability performance of noncoherent BFSK and DPSK. By exploiting well-
known analogies [18] between these two modulation strategies it is possible
to develop a unified approach. Consider first the case of BFSK where

individual bit decisions are generally made on the complex matched filter outputs.

$$\tilde{r}_{i,k} = \int_{(i-\frac{1}{2})T_s}^{(i+\frac{1}{2})T_s} \tilde{r}(t)\tilde{u}_k^*(t-iT_s)dt; \quad \begin{matrix} i=0,1,2,\dots \\ k=0,1, \end{matrix} \quad (63)$$

where $\tilde{u}_k(t)$, $k=0,1$ are appropriately defined complex waveforms associated with each of the binary symbols to be transmitted. Specifically,

$$\tilde{u}_k(t) = u_c(t)+jx_k u_s(t) \quad ; \quad k=0,1 \quad (64)$$

with $x_k=(2k-1)$, $k=0,1$ and $u_c(t)$, $u_s(t)$ the appropriate baseband I/Q waveforms from Table 1.

Final bit decisions for BFSK are then based upon a threshold test on the statistics

$$z_i = |\tilde{r}_{i,1}|^2 - |\tilde{r}_{i,0}|^2 ; \quad i=0,1,\dots, \quad (65)$$

such that the declared binary sequence $\{\hat{x}_i\}$ is

$$\hat{x}_i = \text{sgn } z_i \quad . \quad (66)$$

After appropriate normalization, the statistics given by (63) evaluated during any one signaling interval are of the generic form

$$\tilde{d}_0 = \left(\frac{1-x}{2}\right)\sqrt{\frac{2E_b}{N_0}} e^{j\theta}+\tilde{y}_0+\tilde{w}_0 \quad , \quad (67a)$$

and

$$\tilde{d}_1 = \left(\frac{1+x}{2}\right)\sqrt{\frac{2E_b}{N_0}} e^{j\theta}+\tilde{y}_1+\tilde{w}_1 \quad , \quad (67b)$$

for $k=0,1$, respectively. Here, $x=\pm1$ represents the transmitted bit while θ is an unknown phase offset assumed uniformly distributed over $[-\pi,\pi]$. The quantities $\tilde{w}_k$, $k=0,1$, are mutually independent zero-mean complex Gaussian variates whose real and imaginary components are each of unit variance. Finally, $\tilde{y}_k$, $k=0,1$ represent contributions due to the shot noise component defined according to $\tilde{y}_k=y_{k,c}-jy_{k,s}$ with

$$y_{k,c} = \mathrm{Re}\left\{\sqrt{\frac{2}{N_0 T_s}} \int_0^{T_s} \tilde{y}(t)\tilde{u}_k^*(t-T_s/2)dt\right\}$$

$$= \sum_{i=1}^{N(T_s)} z_i^{(k,c)} g(t_i) \quad ; \quad k=0,1 \quad , \tag{68a}$$

while

$$y_{k,s} = - \mathrm{I_m}\left\{\sqrt{\frac{2}{N_0 T_s}} \int_0^{T_s} \tilde{y}(t)\tilde{u}_k(t-T_s/2)dt\right\} \tag{68b}$$

$$= \sum_{i=1}^{N(T_s)} z_i^{(k,s)} g(t_i) \quad ; \quad k=0,1 \quad .$$

Here, $g(t) \triangleq \sqrt{g_c^2(t)+g_s^2(t)}$ with

$$g_c(t) \triangleq \frac{1}{T_s} \int_0^{T_s} h_0(\tau-t)u_c(\tau-T_s/2)d\tau \quad , \tag{69a}$$

while

$$g_s(t) \triangleq \frac{1}{T_s} \int_0^{T_s} h_0(\tau-t)u_s(\tau-T_s/2)d\tau, \tag{69b}$$

and finally

$$z_i^{(0,c)} = 2(T_s/N_0)^{\frac{1}{2}}R_i\cos(\theta_i+\pi/4-\phi_i) \quad , \tag{70a}$$

$$z_i^{(0,s)} = 2(T_s/N_0)^{\frac{1}{2}}R_i\sin(\theta_i+\pi/4-\phi_i) \quad , \tag{70b}$$

while

$$z_i^{(1,c)} = 2(T_s/N_0)^{\frac{1}{2}}R_i\cos(\theta_i+\pi/4+\phi_i) \quad , \tag{70c}$$

$$z_i^{(1,s)} = 2(T_s/N_0)^{\frac{1}{2}}R_i\sin(\theta_i+\pi/4+\phi_i) \quad , \tag{70d}$$

with $\phi_i \triangleq \tan^{-1}g_s(t_i)/g_c(t_i)$.

We now show the relationship of noncoherent DPSK to BFSK following the development in [18]. Specifically, for DPSK individual bit decisions are made on the basis of the single sequence of complex matched filter outputs

$$r_i = \int_{(i-\frac{1}{2})T_s}^{(i+\frac{1}{2})T_s} \tilde{r}(t) u_c(t-iT_s) dt \quad ; \quad i=0,1,2,\ldots , \tag{71}$$

where $u_c(t)=u_0(t)$ is the corresponding baseband waveform from Table 1. Final decisions are then made on the statistics

$$z_i = \text{Re}\{\tilde{r}_i \tilde{r}_{i-1}^*\} \quad ; \quad i=0,1,2,\ldots \tag{72}$$

with the declared sequence $\{\hat{x}_i\}$ computed according to (66). As shown in [18], this last statistic can be expressed in the form

$$z_i = |\tilde{r}'_{i,1}|^2 - |\tilde{r}'_{i,0}|^2 \quad ; \quad i=0,1,2,\ldots , \tag{73}$$

which is functionally identical to (64) for BFSK where now

$$\tilde{r}'_{i,1} = \frac{\tilde{r}_i + \tilde{r}_{i-1}}{2} \quad ; \quad \tilde{r}'_{i,0} = \frac{\tilde{r}_i - \tilde{r}_{i-1}}{2} \quad . \tag{74}$$

The sequences $\{\tilde{r}'_{i,k}\}$, $k=0,1$ can then be computed according to

$$\tilde{r}'_{i,k} = \int_{(i-3/2)T_s}^{(i+\frac{1}{2})T_s} \tilde{r}(t) u'_k(t-iT_s) dt \quad ; \quad \begin{matrix} i=0,1,2,\ldots \\ k=0,1, \end{matrix} \tag{75}$$

where

$$u'_1(t) \triangleq \frac{u_c(t)+u_c(t+T_s)}{2} \quad , \tag{76a}$$

and

$$u'_0(t) \triangleq \frac{u_c(t)-u_c(t+T_s)}{2} \quad . \tag{76b}$$

Normalized versions of the decision statistics given by (75) computed during any one signaling interval, corresponding to those given by (67) for BFSK, are then[+]

[+] We assume that the preceding baud symbol is known so that the possibility of paired errors is neglected in this formulation.

$$\tilde{d}_0' = \left(\frac{1-x}{2}\right)\sqrt{\frac{4E_b}{N_0}}\ e^{j\theta} + \tilde{y}_0' + \tilde{w}_0 \quad , \tag{77a}$$

and

$$\tilde{d}_1' = \left(\frac{1+x}{2}\right)\sqrt{\frac{4E_b}{N_0}}\ e^{j\theta} + \tilde{y}_1' + \tilde{w}_1 \tag{77b}$$

Here, the quantities $\tilde{w}_k$, $k=0,1$ are Gaussian noise components with identical interpretation as in (67) and the sequel. Likewise, the components $\tilde{y}_k$, $k=0,1$ are due to the shot noise where now $\tilde{y}_k' = y_{k,c} - jy_{k,s}$ with

$$y_{k,c}' = \sum_{i=1}^{N(2T_s)} Z_{i,c}' g_k'(t_i) \quad ; \quad k=0,1 \quad , \tag{78a}$$

and

$$y_{k,s}' = \sum_{i=1}^{N(2T_s)} Z_{i,s}' g_k'(t_i) \quad ; \quad k=0,1 \tag{78b}$$

where now

$$g_1'(t) \triangleq \frac{1}{2T_s} \int_0^{2T_s} h_0(\tau-t)d\tau \quad , \tag{79a}$$

while

$$g_0'(t) = \frac{1}{2T_s}\left\{ \int_0^{T_s} h_0(\tau-t)d\tau - \int_{T_s}^{2T_s} h_0(\tau-t)d\tau \right\} \quad . \tag{79b}$$

The corresponding random amplitudes in this case are

$$Z_{i,c}' = 2(T_s/N_0)^{\frac{1}{2}} R_i \cos(\theta_i + \pi/4) \quad , \tag{80a}$$

and

$$Z_{i,s}' = 2(2T_s/N_0)^{\frac{1}{2}} R_i \sin(\theta_i + \pi/4) \quad . \tag{80b}$$

A few comments are in order concerning the form of the normalized decision statistics in (67) and (77) for noncoherent BFSK and DPSK, respectively. In the absence of the shot noise component, it is clear that DPSK offers a 3dB advantage over BFSK which is a well-known result for the AWGN channel. In the presence of shot noise, however, the performance can be decidely different due to the distinct difference in the corresponding shot

noise contributions $\bar{y}_k$ and $\bar{y}_k'$. Furthermore, although the shot noise components in the two matched filter outputs are uncorrelated in the sense that $E\{\bar{y}_0 y_1^*\} = E\{\bar{y}_0' \bar{y}_1'^*\}= 0$, it can not be inferred that they are therefore statistically independent. This severely complicates the analysis of error probability.

Based upon the preceding, a unified approach to the evaluation of bit error probability can be formulated. Specifically, assume that a "0" has been transmitted $(x=-1)$, then an error is made with BFSK if $d_0 \overset{\Delta}{=} |\tilde{d}_0| < |\tilde{d}_1| \overset{\Delta}{=} d_1$ so that

$$P_e = \Pr\{d_0 < d_1\} \ . \tag{81}$$

Similar expressions hold for DPSK with $d_k' \overset{\Delta}{=} |\tilde{d}_k'|$ $k=0,1$ replacing the corresponding unprimed quantities. In what follows we consider BFSK exclusively and merely state the corresponding results for DPSK.

Clearly, the error probability can be determined as

$$P_e = \int_{-\infty}^{\infty}\int_{-\infty}^{\infty}\int_{-\infty}^{\infty}\int_{-\infty}^{\infty} \Pr\{d_0 < d_1 | y_{0,c}, y_{0,s}, y_{1,c}, y_{1,s}\} f(y_{0,c}, y_{0,s}, y_{1,c}, y_{1,s})$$
$$dy_{0,c} dy_{0,s} dy_{1,c} dy_{1,s} \ , \tag{82}$$

where $\Pr\{d_0 < d_1 | y_{0,c}, y_{0,s}, y_{1,c}, y_{1,s}\}$ is the conditional error probability given $y_{0,c}, y_{0,s}, y_{1,c}, y_{1,s}$, or equivalently $\bar{y}_0$ and $\bar{y}_1$, and $f(y_{0,c}, y_{0,s}, y_{1,c}, y_{1,s})$ is the corresponding joint p.d.f. This expression then provides a parallel to (52) for coherent modulation. Indeed, following the development in [18], the conditional error probability is easily shown to be given by

$$\Pr\{d_0 < d_1 | y_{0,c}, y_{0,s}, y_{1,c}, y_{1,s}\} = Q(\sqrt{a}, \sqrt{b}) - \frac{1}{2} \exp\left\{-\frac{a+b}{2}\right\} I_0(\sqrt{ab}) \ , \tag{83}$$

where

$$Q(a,b) \overset{\Delta}{=} \int_b^{\infty} x \exp\left\{-\frac{a^2+x^2}{2}\right\} I_0(ax) dx \ , \tag{84}$$

4-32

is Marcum's Q-function [19] and $I_0(\cdot)$ is the modified Bessel function of the first kind of order zero. The quantities a and b in (83) are defined according to

$$a = \frac{1}{2}(y_{1,c}^2 + y_{1,s}^2) \quad , \tag{85a}$$

and

$$b = \frac{1}{2}\left\{(y_{0,c} + \sqrt{\frac{2E_b}{N_0}}\cos\theta)^2 + (y_{0,s} + \sqrt{\frac{2E_b}{N_0}}\sin\theta)^2\right\} \tag{85b}$$

for BFSK while

$$a = \frac{1}{2}(y_{1,c}'^2 + y_{1,s}'^2) \quad , \tag{86a}$$

and

$$b = \frac{1}{2}\left\{(y_{0,c}' + \sqrt{\frac{4E_b}{N_0}}\cos\theta)^2 + (y_{0,s}' + \sqrt{\frac{4E_b}{N_0}}\sin\theta)^2\right\} \quad , \tag{86b}$$

for DPSK[†]. As in the evaluation of P_e through (52) for coherent modulation, use of (82) for noncoherent modulation is somewhat impractical due to the general inability of obtaining concise expressions for the joint p.d.f. $f(y_{0,c}, y_{0,s}, y_{1,c}, y_{1,s})$.

In Appendix D we show that the error probability can alternatively be written in terms of ch.f.'s according to

$$P_e = \frac{1}{2} + \frac{1}{2\pi}\int_{-\infty}^{\infty} \frac{\psi_{d_0,d_1}(-v,v|x=-1)}{jv}dv \quad , \tag{87}$$

where $\psi_{d_0,d_1}(v_0,v_1|x=-1)$ is the conditional joint ch.f. of the decision variables d_0 and d_1 given x=-1 was transmitted. This result is then analogous to the development in Appendix C leading to (54) for coherent modulation. Unfortunately, for the situation considered here the evaluation of the joint

---

[†] In this case, of course, the joint p.d.f. in (81) must be replaced by $f(y_{0,c}', y_{0,s}', y_{1,c}', y_{1,s}')$.

ch.f. $\psi_{d_0,d_1}(v_0,v_1)$, although possible in some special cases, becomes un-
wieldy in general[+]. As a result we resort exclusively to simulation results
in what follows.

In Fig. 33 we illustrate the performance of BFSK for the case of Poisson
arrivals and power-Rayleigh distributed pulse amplitudes with $\alpha=1.0$. The
characteristic pulse shape is $h_0(t)=e^{-at}u_{-1}(t)$ with $aT_s=4.0$ and $\gamma^2T_s=20dB$.
Observe the convergence to the equivalent all-Gaussian performance with
increasing λT_s. Similar results are illustrated in Fig. 34 for DPSK. Note the
3dB performance advantage of DPSK vis-à-vis BFSK for large λT_s when the total
noise environment is close to Gaussian. For smaller λT_s, or more impulsive
noise situations, this performance advantage can be considerably reduced.
In Fig.'s 35 and 36 we illustrate the performance of both BFSK and DPSK as
a function of γ^2T_s for selected parameter choices. Finally, in Fig.'s 37
and 38 we illustrate the error probability behavior as a function of aT_s.
As in previous work, little sensitivity was observed for either BFSK or DPSK
to characteristic pulse shape, interarrival statistics, or pulse amplitude
distribution provided the APD's were matched as in Fig. 11.

V. Nonlinear Receiver Performance:

The preceding section has demonstrated the often catastrophic effect of
impulse noise on linear matched filter reception. Clearly, some form of
nonlinear front-end processing of the limiting or saturating variety should
provide some protection against the large pulse amplitudes which, although
occurring relatively infrequently, contain a large portion of the overall
signal energy. This point has been argued previously [20]-[25], although
to date, little progress has been made in developing a general approach.

[+] Note that part of the difficulty is due to the fact that d_0,d_1 are not
necessarily statistically independent.

4-34

The alternative is to propose a class of nonlinear characteristics and explore the resulting performance as a function of various parameter choices defining these nonlinearities. Unfortunately, even here a comprehensive treatment has not yet been provided.

In what follows we assume nonlinear predetection processing preceding a conventional matched filter data demodulator as illustrated in Fig. 39. Specifically, we assume a configuration consisting of a zero-memory nonlinear (ZMNL) characteristic sandwiched between two narrowband filters possessing equivalent rectangular bandwidths B_1' and B_2' respectively. Actually, provided $B_2'T_s \gg 1$ the second filter has little effect on performance followed as it is by the narrowband matched filter. Thus, performance will be determined chiefly by the first filter preceding the ZMNL characteristic. The quantity $B_1'T_s$ then plays the same role as in the fictitious measurement filter used in describing the APD's and ALCR's.

The class of ZMNL characteristics to be considered can be implemented as illustrated in Fig. 40 where $g(\cdot)$ is in general some linear function of the signal envelope $R(t)=|\tilde{r}(t)|$. For example, with $g(R)=1/R$, the result can easily be seen to be a narrowband hard-limiter with zero phase distortion. The chief motivation for restriction to nonlinear processing structures of this form lies in some related work [26] where it is shown that, under the assumption of independent noise samples and weak or threshold signals, the optimum ZMNL characteristic is of the form[+]

$$g_{\ell 0}(R) = - \frac{d \, \ell n \, f(R)}{R \, dR} \, , \qquad (88)$$

where $f(R)=f_a(R)/2\pi R$ with $f_a(\cdot)$ the envelope p.d.f. of the filtered impulse

---

[+] In [26] the characteristic defined by (87) is referred to as "locally optimum", and hence the subscript on $g_{\ell 0}(R)$.

noise process defined by (35) and the sequel. Here the predetection filter rectangular bandwidth B_1' replaces the fictitious measurement filter bandwidth B'. It follows, in particular, that from (35)

$$g_{\ell 0}(R) = \frac{\displaystyle\int_0^\infty \beta^2 J_1(\beta R)\psi_{y_c,y_s}(\beta)e^{-\sigma_w^2\beta^2/2}d\beta}{\displaystyle\int_0^\infty \beta R J_0(\beta R)\psi_{y_c,y_s}(\beta)e^{-\sigma_w^2\beta^2/2}d\beta} \quad , \tag{89}$$

which is again readily evaluated by quadrature provided the joint ch.f. $\psi_{y_c,y_s}(\beta)$ can be determined. As noted previously, this can be accomplished only in special cases.

One useful special case for which this joint ch.f. can be evaluated is when the pulse amplitude distribution is power-Rayleigh distributed with $\alpha = 1.0$ and $h_0(t)=e^{-at}u_{-1}(t)$. The joint ch.f. is then given by (40). In Fig. 41 we illustrate the behavior of [†] $\sigma_n^2{}_,g_{\ell 0}(R)$ versus the envelope normalized to its rms level for selected values of $\gamma^2 T_s$ and with $B_1'T_s=16$. Here the quantity $\sigma_n^2{}_,$ is the common variance of the I/Q components of the filtered noise process $\tilde{n}'(t)$. As can be seen the effect of increasing $\gamma^2 T_s$ is to severely limit and hence de-emphasize the large noise peaks. In Fig. 42 we demonstrate the behavior for various values of $B_1'T_s$ with $\gamma^2 T_s=20$dB. Again for fixed $\gamma^2 T_s$ increasing $B_1'T_s$, assuming $B_1'>B$, allows additional Gaussian noise so that the ZMNL characteristics are merely shifted to the right in accordance with the parameter Δ_1 defined in (43) with $B_1'T_s$ replacing $B'T_s$. Finally, in Fig.'s 43 and 44 we illustrate the effect of aT_s and λT_s, respectively. Note, in particular, that for $\lambda/a \gg 1$ the locally optimum ZMNL

---

† Actually in Fig.'s 41-44 we plot the quantity $\sigma_n^2{}_,g_{\ell 0}(R)$ normalized to its maximum value at R=0, versus $R/\sqrt{A_0}$

approaches the constant value 1.0 which is optimum for Gaussian noise. For more severe noise environments (i.e., smaller α) the optimum ZMNL characteristics exhibit more pronounced limiting behavior and less saturations at large envelope values.

While these results are useful in understanding the behavior of the locally optimum ZMNL characteristic, it remains to approximate this behavior by a practical class of ZMNL characteristics which do not require a priori knowledge of noise statistics since very rarely would they be known in a realistic data communications application. Consequently, we restrict attention to the ZMNL characteristics listed in Table 3 which more or less approximate the behavior of the locally optimum characteristic.

In Fig. 45 we illustrate typical simulated behavior using coherent BPSK modulation and selected characteristics from Table 3. The pulse arrivals are Poisson and $\gamma^2 T_s = 20$dB with $B_1' T_s = 16$. Other pertinent parameters are illustrated in Fig. 45. The predetection filter in all cases possesses a second-order Butterworth characteristic with prescribed equivalent rectangular bandwidth. Also, the appropriate clip levels corresponding to ZMNL characteristics in Table 3 were arbitrarily adjusted to 0dB above the received signal level. While the choice of clip level is obviously an important parameter, we have not attempted to optimize this quantity. The justification for the choice made here is that it clearly eliminates most of the large amplitude peaks while preserving the signal structure. In all subsequent work the clip levels have both held fixed at this value.

As evidenced in Fig. 45, the ZMNL predetection processing can be quite effective in combatting the effects of impulse noise. For example, the algebraic nonlinearity with n=4 provides an improvement over the linear receiver of

4-37

roughly 9dB at $P_e=5\times10^{-3}$. The improvement using the other nonlinear receiver structures is only marginal, although this can be improved considerably in more intensive noise environments and/or through choice of predetection bandwidth. This is illustrated in Fig. 46 where the error probability for a hard-limiting receiver is shown for selected choices of $B_1'T_s$ in a noise environment characterized by $aT_s=20.0$ and $\gamma^2T_s=40$dB representing severe impulse noise. Small values of $B_1'T_s$ not only result in intersymbol interference (ISI) effects which degrades performance, but also disperses or lengthens the characteristic pulse shape making the hard-limiter less effective in suppressing the large noise peaks. For example, even for $B_1'T_s=16$ the impulse response of the filter is approximately 3 times the characteristic pulse shape for $aT_s=20$. The characteristic noise pulse at the output of the filter is then lengthened by roughly a factor of three. The pulse duration is then crudely approximated by an "effective" $a'T_s=20/3\approx7$. In Fig. 47 we illustrate[†] P_e behavior for a hard-limiting receiver as a function of aT_s from which it is clear that performance degrades rapidly for decreasing values of aT_s, and hence less narrowly confined characteristic pulse shape. The conclusion is that the predetection bandwidth, at least[††] for $aT_s\gg1$, should be made as large as possible. For smaller aT_s, the predetection bandwidth requirements are much less severe. This is illustrated to an extent in Fig. 48 where we illustrate results for a hard-limiting receiver both without a filter and with a predetection bandwidth $B_1'T_s=8$. For the smaller aT_s values there is little difference between the two results as was to be expected.

---

† Corresponding results for a linear receiver are illustrated in Fig. 26.

†† And, of course, the simultaneous constraint $\lambda/a\ll1$.

As an illustration of the performance gains to be realized by nonlinear processing and appropriate predetection filtering, the corresponding results in Fig.'s 26 and 47 for $aT_s=20$ indicate a substantial improvement of almost 20dB at $P_e=10^{-3}$. In Fig. 49 we illustrate the P_e behavior of a hard-limiting receiver as a function of $\gamma^2 T_s$ with a fixed, although suboptimum, predetection bandwidth of $B_1' T_s=16$. Wider predetection bandwidths should improve performance in light of previous comments, but this is the widest bandwidth that can be conveniently simulated in the ICS. Nevertheless, the results are useful in demonstrating the dependence upon $\gamma^2 T_s$. Similar results for a receiver employing a 4'th order algebraic nonlinearity are illustrated in Fig.50.

VI. <u>Summary and Conclusions</u>:

We have provided a detailed description of a useful and conveniently parameterized model for impulsive noise. Some of its low-order statistical properties have been investigated both analytically and through simulation Similarly, we have described the error probability performance of a variety of linear and nonlinear receiver structures in noise environments as described by this model. The rationale underlying the use of nonlinear predetect ion processing was described and the performance advantages of such processing illustrated.

While these results should prove useful in the design and development of digital communication systems operating in impulsive noise, much more work remains. Specifically, it is believed that analytical methods although tedious, can be carried much further than described here. This is particularly true for linear receiver performance although somewhat questionable for nonlinear processing structures. At any rate, more comprehensive results, either analytical or through simulation, are required to obtain a complete picture of nonlinear receiver performance in impulse noise as described here.

APPENDIX A

Evaluation of Characteristic Function
of Shot Noise Component for Poisson Arrivals

We are interested in the evaluation of the joint ch.f. of I/Q components of the shot noise component given by

$$\psi_{y_c,y_s}(v_1,v_2) = E\{\exp[j(v_1 y_c(t)+v_2 y_2(t))]\} \tag{A-1}$$

$$= E\{\exp[j\sqrt{2}\sum_{i=1}^{N(t)} R_i h_0(t-t_i)\{v_1\cos(\theta_i+\pi/4)+v_2\sin(\theta_i+\pi/4)\}]\},$$

where we have made use of (23) and the sequel. This last expression can then be written as

$$\psi_{y_c,y_s}(v_1,v_2) = E\{\exp[j\beta\sqrt{2}\sum_{i=1}^{N(t)} z_i h_0(t-t_i)]\} , \tag{A-2}$$

where

$$z_i = R_i\cos(\theta_i+\pi/4-\phi), \quad i=1,2,\ldots, \tag{A-3}$$

with $\phi = \tan^{-1} v_2/v_1$. But the right-hand side of (A-2) is merely the ch.f. of a baseband filtered shot noise component with random amplitude $\sqrt{2}\beta z_i$ and impulse response $h_0(t-t_i)$. While this is difficult to evaluate in general, the result is well known in the case where $\{N(t), t\geq 0\}$ is Poisson. In particular, in this case we have (cf. [6])

$$\psi_{y_c,y_s}(v_1,v_2) = \exp\{\lambda\int_0^\infty [\psi_z(\sqrt{2}\beta h_0(\tau))-1]d\tau\}, \tag{A-4}$$

where $\psi_z(v)=E\{e^{jvz}\}$ is the common ch.f. of the i.i.d. sequence defined according to (A-3). Specifically, we have

$$\psi_z(\sqrt{2}\beta h_0(\tau)) = \int_0^\infty \left[\frac{1}{2\pi}\int_{-\pi}^\pi e^{j\sqrt{2}\beta R h_0(\tau)\cos(\theta+\pi/4-\phi)}d\theta\right]f_r(R)dR \tag{A-5}$$

$$= \int_0^\infty J_0(\sqrt{2}\beta R h_0(\tau))f_r(R)dR ,$$

where we make use of the definition of the Bessel function of the first kind of order zero defined according to

$$J_0(x) = \frac{1}{2\pi} \int_{-\pi}^{\pi} e^{jx\cos(\theta-\zeta)} d\theta \quad . \tag{A-6}$$

It follows then that

$$\psi_{y_c, y_s}(v_1, v_2) = \exp\{\lambda \int_0^{\infty} [E_r\{J_0(\sqrt{2}\beta Rh_0(\tau)\}-1] d\tau\} \quad , \tag{A-7}$$

where $E_r\{\cdot\}$ indicates expectation with respect to the envelope distribution according to the last term on the right-hand side of (A-5).

APPENDIX B

Alternative Error Probability Expression for Coherent Modulation

The error probability for linear matched filter reception employing coherent modulation can be expressed in the form

$$P_e = p_0 \Pr\{d \geq 0 | x = -1\} + p_1 \Pr\{d < 0 | x = 1\} , \qquad (B-1)$$

where d is the decision variable given by (48) and p_0, p_1 are the prior probabilities of x=-1 and x=1, respectively. Under equiprobable signaling we clearly have

$$
\begin{aligned}
P_e &= \Pr\{d \geq 0 | x = -1\} \\
&= 1 - \int_{-\infty}^{0} f_d(\xi | x = -1) d\xi .
\end{aligned}
\qquad (B-2)
$$

In terms of ch.f.'s it is easily shown that

$$
\begin{aligned}
\int_{-\infty}^{0} f_d(\xi | x = -1) d\xi &= \int_{-\infty}^{\infty} u_{-1}(-\xi) f_d(\xi | x = -1) d\xi \\
&= \frac{1}{2} + \frac{1}{2\pi} \int_{-\infty}^{\infty} \frac{\psi_d(v | x = -1)}{jv} dv ,
\end{aligned}
\qquad (B-3)
$$

where $\psi_d(v | x = -1)$ is the conditional ch.f. of d given x=-1. Recall also

$$\psi_d(v | x = -1) = \psi_y(v) \exp\left\{ -j\sqrt{\frac{2E_b}{N_0}}\, v - \frac{1}{2} v^2 \right\} , \qquad (B-4)$$

where $\psi_y(v)$ is the ch.f. of the shot component. Thus,

$$
\begin{aligned}
P_e &= \frac{1}{2} - \frac{1}{2\pi} \int_{-\infty}^{\infty} \frac{\psi_y(v)}{jv} \exp\left\{ -j\sqrt{\frac{2E_b}{N_0}}\, v \right\} e^{-v^2/2}\, dv \\
&= \frac{1}{2} + \frac{1}{\pi} \int_{0}^{\infty} \psi_y(v)\, \frac{\sin\sqrt{2E_b/N_0}\, v}{v} e^{-v^2/2} dv ,
\end{aligned}
\qquad (B-5)
$$

which is readily evaluated by quadrature given the ch.f. $\psi_y(v)$ of the shot noise component.

APPENDIX C

Evaluation of Characteristic Function of Shot Noise
Component at Output of Linear Matched Filter in Special Case

We evaluate the ch.f. $\psi_y(v)$, given by (55), in the special case of coherent BPSK modulation when the input pulse amplitude distribution is power-Rayleigh with characteristic exponent $\alpha=1.0$, and the filter generating the shot noise is described by $h_0(t)=e^{-at}u_{-1}(t)$. In this case we find from (51) that for $t \leq T_s$

$$g(t) = \frac{1}{T_s} \int_{\max(0,t)}^{T_s} e^{-a(\tau-t)} d\tau , \qquad (C-1)$$

or

$$g(t) = \begin{cases} \dfrac{1}{aT_s}[1-e^{-a(T_s-t)}]; & 0 \leq t \leq T_s \\[2mm] \dfrac{e^{at}}{aT_s}[1-e^{-aT_s}] & ; \quad t < 0 , \end{cases} \qquad (C-2)$$

whereupon substitution into (56) yields $\psi_z(\cdot)$. At this point it is convenient to express $\psi_y(v)$ in the form

$$\psi_y(v) = \psi_y^-(v)\psi_y^+(v) \qquad (C-3)$$

where

$$\psi_y^-(v) \triangleq \exp\left\{\lambda \int_{-\infty}^{0} [\psi_z(vg(\tau))-1]d\tau\right\} , \qquad (C-4)$$

has an interpretation as the ch.f. associated with contributions due to past impulses, and

$$\psi_y^+(v) \triangleq \exp\left\{\lambda \int_{0}^{T_s} [\psi_z(vg(\tau))-1]d\tau\right\} , \qquad (C-5)$$

which is the ch.f. associated with impulses occurring during the present signaling interval. We will be particularly interested in evaluation of the integrals appearing in these two expressions.

Consider first the integral appearing in the expression for $\psi_y^-(v)$, i.e.,

$$\int_{-\infty}^{0}[\psi_z(vg(\tau))-1]d\tau = \int_{0}^{\infty}\left\{\frac{1}{\sqrt{1+\zeta'K^2e^{-2at}}}-1\right\}d\tau$$

$$= -\frac{1}{a}\ln\left\{\frac{1+\sqrt{1+\zeta'K^2}}{2}\right\} \quad , \qquad (C-6)$$

where

$$\zeta' \triangleq \frac{4(T_s/N_0)R_0^2v^2}{(aT_s)^2} = \frac{2\gamma^2T_sv^2}{(\lambda T_s)(aT_s)} \quad , \qquad (C-7)$$

and $K \triangleq 1-e^{-aT_s}$. It follows that

$$\psi_y^-(v) = \left[\frac{1+\sqrt{1+\zeta K^2v^2}}{2}\right]^{-\lambda/a} \quad , \qquad (C-8)$$

where we have found it convenient to introduce the parameter

$$\zeta \triangleq \frac{\zeta'}{v^2} = \frac{2\gamma^2T_s}{(\lambda T_s)(aT_s)} \quad . \qquad (C-9)$$

Now consider the integral defining $\psi_y^+(v)$ which is a bit more difficult to evaluate, i.e.,

$$\int_{0}^{T_s}[\psi_z(vg(\tau))-1]d\tau = \int_{0}^{T_s}\left\{\frac{1}{\sqrt{1+\zeta'\left[1-e^{-a(T_s-\tau)}\right]^2}}-1\right\}d\tau \quad , \qquad (C-10)$$

with ζ' as in (C-7). Under the change of variable $x=[1-e^{-a(T_s-\tau)}]$, this last integral expression becomes

$$\int_{0}^{T_s}[\psi_z(vg(\tau))-1]d\tau = \frac{1}{a}\int_{0}^{K}\left\{\frac{1}{\sqrt{1+\zeta'x^2}}-1\right\}\frac{dx}{1-x}$$

$$= I_1 -(1/a)\ln e^{aT_s} \quad , \qquad (C-11)$$

with ζ' and K as above, and

$$I_1 \triangleq \frac{1}{\varepsilon} \int_0^K \left[\frac{1}{\sqrt{1+\zeta'x^2}} \right] \frac{dx}{1-x} \quad . \tag{C-12}$$

Now under the change of variable $y=1/1-x$ we have

$$I_1 = \frac{1}{a} \int_1^{e^{aT}s} \frac{dy}{\sqrt{\zeta'-2\zeta'y+(1+\zeta')y^2}}$$

$$= \frac{1}{a\sqrt{1+\zeta'}} \ln\left\{ \sqrt{\zeta'-2\zeta'y+(1+\zeta')y^2} + y\sqrt{1+\zeta'} - \frac{\zeta'}{\sqrt{1+\zeta'}} \right\}\Bigg|_1^{e^{aT}s} , \tag{C-13}$$

where the last expression is taken from standard integral tables. After some manipulations we have

$$I_1 = \frac{1}{a\sqrt{1+\zeta'}} \ln\left\{ \frac{\sqrt{(1+\zeta')[\zeta'(1-e^{-aT}s)^2+1]} + (1+\zeta')-\zeta'e^{-aT}s}{[1+\sqrt{1+\zeta'}]e^{-\varepsilon T}s} \right\} , \tag{C-14}$$

with the result

$$\int_0^{T_s} [\psi_z(vg(\tau))-1]d\tau = \frac{1}{a\sqrt{1+\zeta'}} \ln\left\{ \frac{1+\zeta'K+\sqrt{(1+\zeta')(1+\zeta'K^2)}}{[1+\sqrt{1+\zeta'}]e^{-aT}s^{[1-\sqrt{1+\zeta'}]}} \right\} \quad . \tag{C-15}$$

Finally, substitution into (C-5) yields

$$\psi_y^+(v) = \left[\frac{1+\sqrt{1+\zeta v^2}}{1+\zeta Kv^2+\sqrt{(1+\zeta v^2)(1+\zeta K^2v^2)}} \right]^{-\lambda/a\sqrt{1+\zeta v^2}} \exp\left\{ \lambda T_s \left[\frac{1}{\sqrt{1+\zeta v^2}} -1 \right] \right\} , \tag{C-16}$$

where again we have made use of the parameter ζ defined according to (C-9).

APPENDIX D

Alternative Error Probability Expression
for Noncoherent Modulation

The error probability for matched filter reception employing noncoherent modulation and equiprobable signaling can be expressed in the generic form

$$P_e = \Pr\{\dot{d}_0 < \dot{d}_1 \mid x=-1\}$$

$$= \int_0^\infty \int_0^{\xi_1} f_{\dot{d}_0,\dot{d}_1}(\xi_0,\xi_1 \mid x=-1)\,d\xi_0\,d\xi_1$$

$$= \int_{-\infty}^\infty \int_{-\infty}^\infty u_{-1}(\xi_1-\xi_0)f_{\dot{d}_0,\dot{d}_1}(\xi_0,\xi_1 \mid x=-1)\,d\xi_0\,d\xi_1 \quad , \qquad (D\text{-}1)$$

where d_0, d_1 are decision variables appropriate for either BFSK or DPSK. Now from Parseval's theorem this last expression leads to

$$P_e = \frac{1}{4\pi^2} \int_{-\infty}^\infty \int_{-\infty}^\infty U(v_0,v_1)\psi_{\dot{d}_0,\dot{d}_1}(v_0,v_1 \mid x=-1)\,dv_0\,dv_1 \quad , \qquad (D\text{-}2)$$

where $\psi_{\dot{d}_0,\dot{d}_1}(v_0,v_1 \mid x=-1)$ is the joint ch.f. of the decision variables d_0,d_1 given that $x=-1$, and

$$U(v_0,v_1) = \int_{-\infty}^\infty \int_{-\infty}^\infty u_{-1}(\xi_1-\xi_0)e^{-j(\xi_0 v_0 + \xi_1 v_1)}\,d\xi_1\,d\xi_0 \quad , \qquad (D\text{-}3)$$

is the Fourier transform of $u_{-1}(\xi_1-\xi_0)$. Clearly, under a change of variable

$$U(v_0,v_1) = \int_{-\infty}^\infty \left\{ \int_{-\infty}^\infty u_{-1}(\tau)e^{-jv_1\tau}\,d\tau \right\} e^{-j(v_0+v_1)\xi_0}\,d\xi_0$$

$$= [\pi\delta(v_1) + \frac{1}{jv_1}][2\pi\delta(v_0+v_1)] \qquad (D\text{-}4)$$

$$= 2\pi^2\delta(v_0)\delta(v_1) + \frac{2\pi\delta(v_0+v_1)}{jv_1} \quad ,$$

where we have made use of obvious transform pairs. Substitution into (D-2) yields

$$P_e = \frac{1}{2} + \frac{1}{2\pi} \int_{-\infty}^\infty \frac{\psi_{\dot{d}_0,\dot{d}_1}(-v,v \mid x=-1)}{jv}\,dv \quad . \qquad (D\text{-}5)$$

References

1. H.L. Van Trees, _Detection, Estimation, and Modulation Theory, Part I:_ Detection, Estimation and Linear Modulation Theory, John Wiley & Sons, Inc., New York, 1968.

2. John M. Wozencraft and I. M. Jacobs, _Principles of Communication Engineering_, John Wiley & Sons, Inc., New York, 1965.

3. E. Arthurs and H. Dym, "On the Optimum Detection of Digital Signals in the Presence of White Gaussian Noise: A Geometric Interpretation and a Study of Three Basic Data Transmission Systems", IRE Trans. on Commun. Systems, Vol. CS-10, pp. 362-372, Dec. 1962.

4. A. J. Viterbi and J. K. Omura, _Principles of Digital Communication and Coding_, McGraw-Hill Book Co., New York, 1979.

5. J. W. Modestino, G. R. Redinbo, K. R. Matis and K. Y. Jung, "Digital Simulation of Communication Systems", Proc. of NTC'79, Washington, D.C., pp. 6.2.1-6.2.7, Nov. 1979.

6. D. L. Snyder, _Random Point Processes_, John Wiley & Sons, Inc., NY, 1975.

7. E. Parzen, _Stochastic Processes_, Holden-Day, Inc., San Francisco, 1962.

8. E. Cinlar, _Introduction to Stochastic Processes_, Prentice-Hall, Inc. Englewood, Cliffs, NJ, 1975.

9. J. W. Modestino, "Modeling of ELF Noise", TR-493, MIT Lincoln Laboratory, Lexington, MA, April 1972.

10. J. Galejs, "Amplitude Distributions of Radio Noise at ELF-VLF", Journal of Geophysical Research, Vol. 71, pp. 201-216, Jan. 1966.

11. W. Q. Cricklow, A.D. Spaulding and C.J. Roubique, _Amplitude Probability Distributions for Atmospheric Radio Noise_, Monograph No. 23, National Bureau of Standards, 1960.

12. B. Sankur, "Modeling of Impulsive Noise and Analysis of Linear and Non-linear Reception in ELF-VLF Noise", Ph.D. thesis, Electrical and Systems Engineering Dept., Rensselaer Polytechnic Institute, Troy, NY, March 1976.

13. F. J. Beutler and O.A.Z. Leneman, "The Theory of Stationary Point Processes", Acta. Math., Vol. 11b, pp. 159-197, 1966.

14. F. J. Beutler and O.A.Z. Leneman, "Random Sampling of Random Processes: Stationary Point Processes", _Information and Control_, Vol. 9, pp.325-346, 1966.

15. F. J. Beutler and O.A.Z. Leneman, "The Spectral Analysis of Impulse Processes", _Information and Control_, Vol. 12, pp. 236-250, 1968.

16. S. O. Rice, "Mathematical Analysis of Random Noise", Bell System Tech. J. Vol. 24, pp. 46-156, 1945.

17. H. Cramer and M. R. Leadbetter, Stationary and Related Stochastic Processes, John Wiley & Sons, Inc., NY, 1967.

18. S. Stein, "Unified Analysis of Certain Coherent and Noncoherent Binary Communications Systems", IEEE Trans. Inform. Theory, Vol. IT-10, pp. 43-51, Jan. 1964.

19. J. I. Marcum, "A Statistical Theory of Target Detection by Pulsed Radar", IRE Trans. on Inform. Theory, Vol. IT-6, pp. 145-168, April 1960.

20. J. W. Modestino, "VLF Noise Modeling and Link Error Performance", TR-1, Systems Engineering Division, Rensselaer Polytechnic Institute, Troy, NY, Feb. 1974.

21. H. C. Hall, Jr., "A New Model for Impulsive Phenomena: Application to Atmospheric Noise Communication Channels", Ph.D. thesis, Electrical Engineering Department, Stanford University, Aug. 1966.

22. A. S. Griffiths, "ELF Noise Processing", TR-490, MIT Lincoln Laboratory, Lexington, MA, Jan. 1972.

23. P. A. Bello and R. Esposito, "Error Probabilities Due to Impulsive Noise in Linear and Hard-Limited DPSK Systems", IEEE Trans. on Commun. Tech., Vol. CT-19, pp. 14-20, Feb. 1979.

24. R. E. Ziemer, "Character Error Probabilities for M-ary Signaling in Impulsive Noise Environments", IEEE Trans. on Commun. Tech., Vol. CT-15, pp. 32-44, Feb. 1967.

25. J. K. Omura and P.D. Shaft, "Modem Performance in VLF Atmospheric Noise", IEEE Trans. on Commun., Tech., Vol. COM-19, pp. 659-668, Oct. 1971.

26. J. W. Modestino and A. Y. Ningo, "Detection of Weak Signals in Narrow-band Non-Gaussian Noise", IEEE Trans. on Inform. Theory, Vol. It-25, pp. 592-600, Sept. 1979.

27. K. Y. Jung, "Digital Communication in the Presence of Impulsive Noise", Ph.D. thesis, Electrical, Computer and Systems Engineering Department, Rensselaer Polytechnic Institute, Troy, NY, in preparation.

Modulation	$c_{1,i}$	$c_{2,i}$	$u_c(t)$	$u_s(t)$	Remarks
BPSK	x_i	0	$u_0(t)$	0	$x_i = \pm 1$
DPSK	$x_i c_{1,i-1}$	0	$u_0(t)$	0	$x_i = \pm 1$ $c_{1,0}$ assumed known
BFSK	$e^{j\theta_i}$	$x_i e^{j\theta_i}$	$\cos(\Delta\omega t/2)u_0(t)$	$\sin(\Delta\omega t/2)u_0(t)$	$x_i = \pm 1$ $\Delta\omega = 2\pi\ell/T$ θ_i - i.i.d. uniform
QPSK	x_{2i}	x_{2i+1}	$(1/\sqrt{2})u_0(t)$	$(1/\sqrt{2})u_0(t)$	$x_i = \pm 1$ $E_s = 2E_b$
MSK	x_{2i}	x_{2i+1}	$\cos(\pi t/2T_s)u_0'(t)$	$\sin(\pi t/2T_s)u_0'(t-T_s)$	$x_i = \pm 1$ I/Q waveforms repeated every $2T_s$ sec.

Note: $u_0(t)$ and $u_0'(t)$ are defined in text.

Table 1

Representations of Some Typical Digital Modulation Formats

Characteristic Pulse Type	Impulse Response $h_0(t)$	System Transfer Function $H_0(s)$	Equivalent Rectangular Bandwidth B, in Hz	Mean-Square Value of Shot-Noise $E[|y(t)|^2]$
Unipolar Pulse	$u_{-1}(t)-u_{-1}(t-T_c)$	$\dfrac{1-e^{-sT_c}}{s}$	$\dfrac{1}{2T_c}$	$2\lambda T_s(T_c/T_s)E(R^2)$
Exponential	$e^{-at}u_{-1}(t)$	$\dfrac{1}{s+a}$	$\dfrac{a}{4}$	$\dfrac{\lambda T_s}{aT_s}E(R^2)$
Decaying Cosine	$e^{-at}\cos\omega_c t\, u_{-1}(t)$	$\dfrac{s+a}{(s+a)^2+\omega_c^2}$	$\dfrac{(a^2+\omega_c^2)(2a^2+\omega_c^2)}{8a^3}$	$\dfrac{\lambda T_s}{aT_s}\left[\dfrac{(aT_s)^2+(\omega_c T_s)^2/2}{(aT_s)^2+(\omega_c T_s)^2}\right]E(R^2)$
Decaying Sine	$e^{-at}\sin\omega_c t\, u_{-1}(t)$	$\dfrac{\omega_c}{(s+a)^2+\omega_c^2}$	$\dfrac{a^2+\omega_c^2}{8a}$	$\dfrac{\lambda T_s}{2aT_s}\left[\dfrac{(\omega_c T_s)^2}{(aT_s)^2+(\omega_c T_s)^2}\right]E(R^2)$

Note: $u_{-1}(t)$ is defined in the text.

Table 2

Characteristic Pulse Waveform and Relevant Parameters

Description	$\sigma_n^2, g(R)$	Comments
Hard-Limiter	$1/R, \ 0<R<\infty$	Ideal Narrowband hard limiter with zero phase distortion
Soft-Limiter	$1 \ ; \ 0<R\leq R_c$ $R_c/R; \ R_c<R<\infty$	Completely defined in terms of clip level R_c
Hole-Puncher	$1 \ ; \ 0<R \leq R_c$ $0 \ ; \ R_c<R<\infty$	Defined in terms of clip level R_c
Algebraic	$\dfrac{1}{1+(R/R_c)^n} \ ; \ 0<R<\infty$	Defined in terms of clip level R_c and parameter n

Table 3

Summary of ZMNL Receiver Characteristics to be Considered.
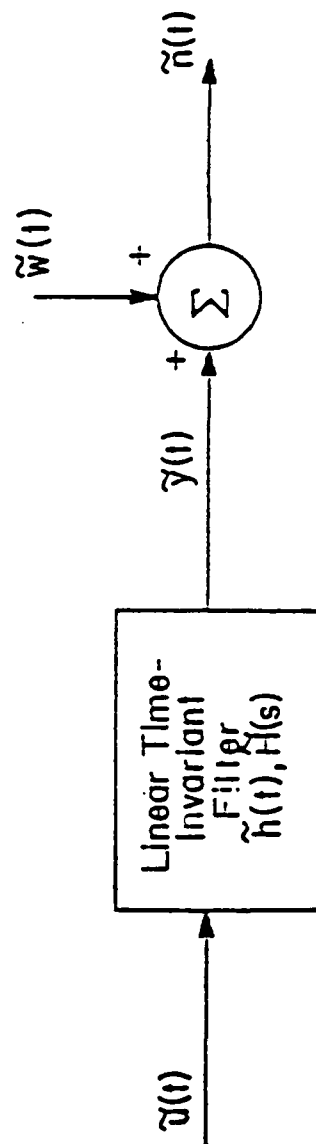
Figure 1

Impulsive Channel Noise Model
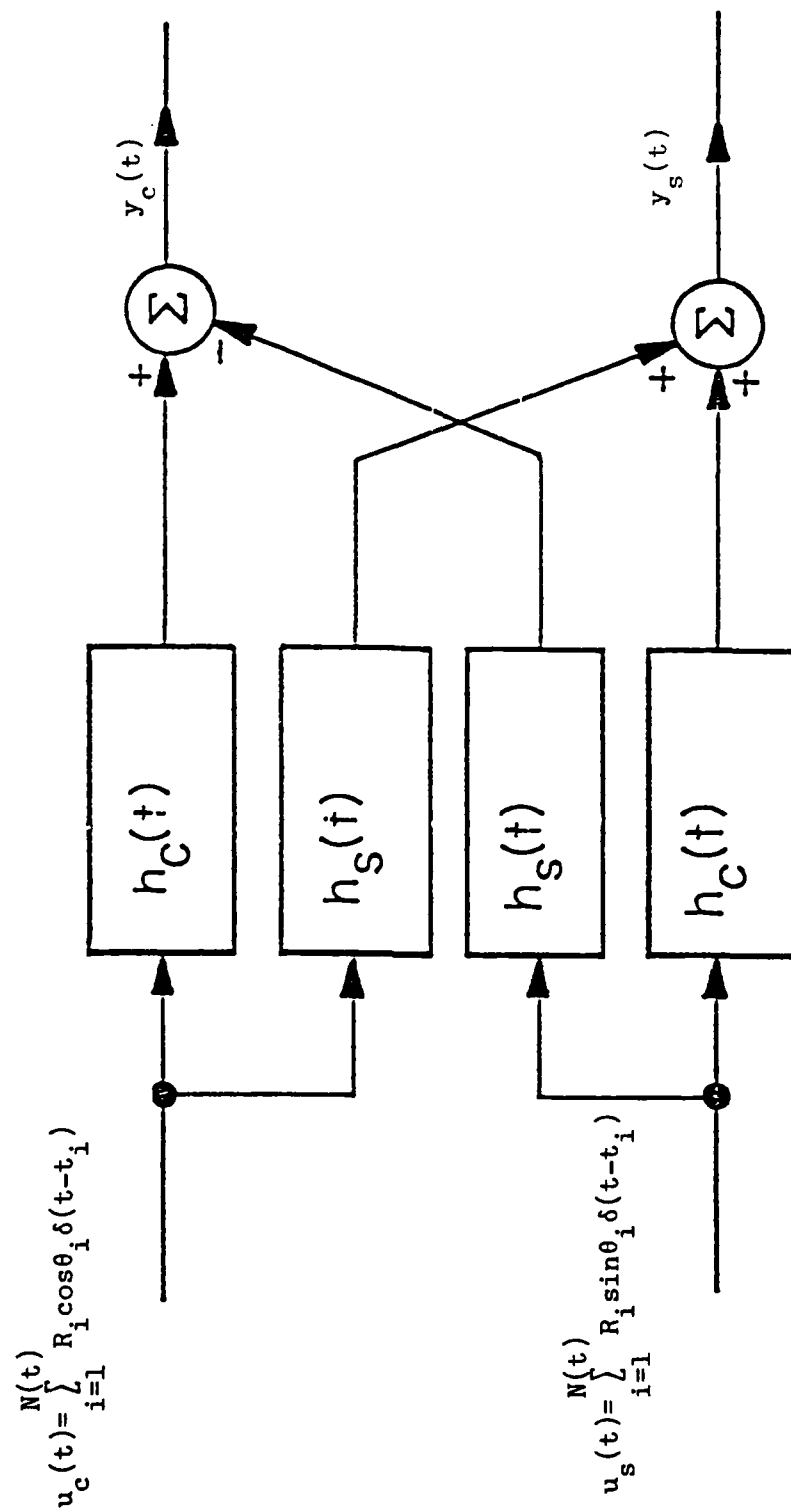
Figure 2

Generation of Inphase and Quadrature
Components of Shot Noise

$$u_c(t) = \sum_{i=1}^{N(t)} R_i \cos\theta_i \delta(t-t_i)$$

$$u_s(t) = \sum_{i=1}^{N(t)} R_i \sin\theta_i \delta(t-t_i)$$

$h_c(t)$

$h_s(t)$

$h_s(t)$

$h_c(t)$

$y_c(t)$

$y_s(t)$
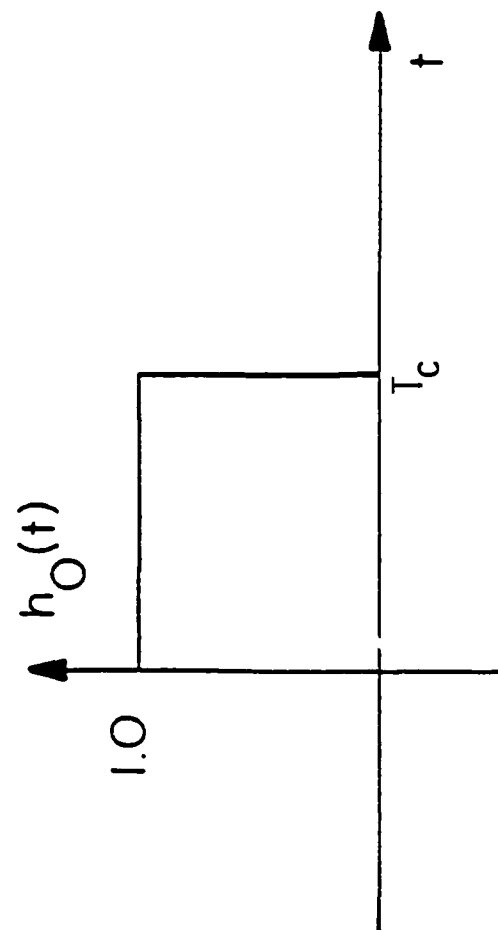
Figure 3

Simple Pulse Waveform Model for
Generating Shot Noise.

4-54

Solid Curve-Computed
Open Circles-Simulated

APD PLOT

AMPLITUDE IN DB ABOVE RMS LEVEL

$\gamma^2 T_s = 3dB$
$=10dB$
$=20dB$
$=30dB$
$=40dB$

Pulse Arrivals:
$\nu=1$ (Poisson)
$\lambda T_s=0.1$

Pulse Shape:
$h_0(t)=e^{-at}u_{-1}(t)$
$aT_s = 2.0$

Pulse Amplitudes:
Power-Rayleigh
$\alpha = 1.0$

Pulse Intensity:
$\gamma^2 T_s$ varying

Measurement Bandwidth:
$B'T_s = 16$

1.0E-07 1.0E-04 1.0E-02 0.10   0.50   0.90 0.95   0.995   0.999   0.9999

EXCEEDANCE PROBABILITY
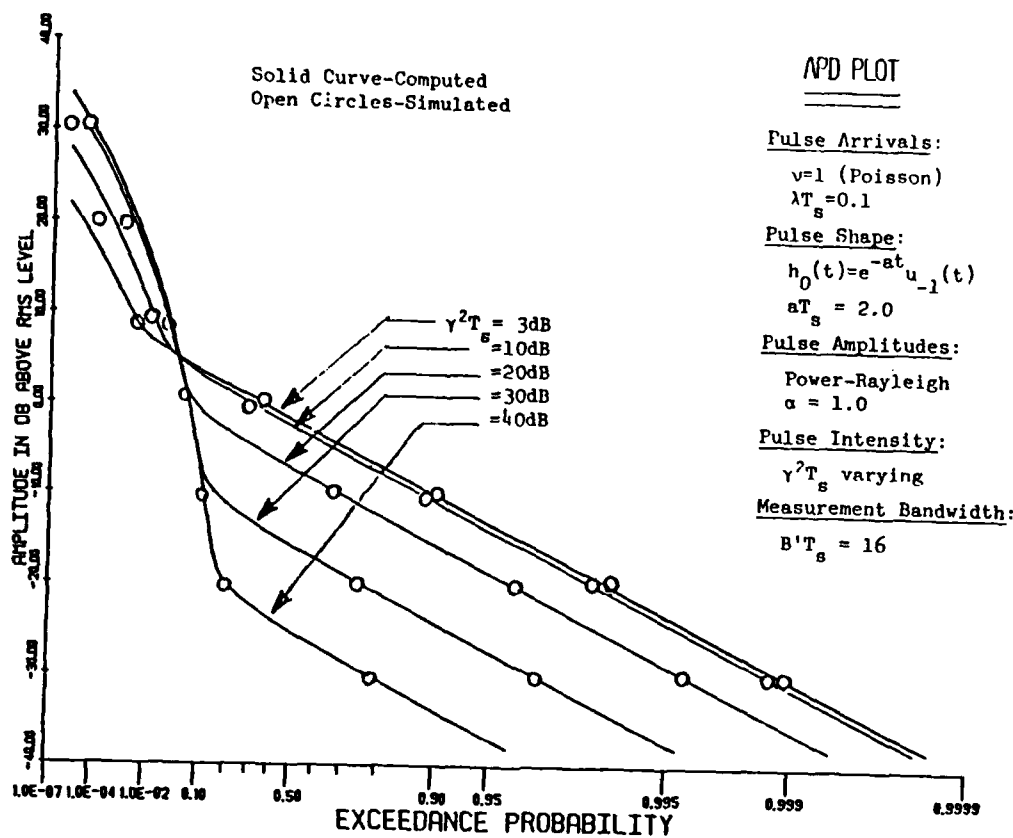
Figure 4

Comparison of Computed and Simulated APD Results for
Special Case of Power-Rayleigh Pulse Amplitude Distri-
bution with Characteristic Exponent $\alpha = 1.0$.
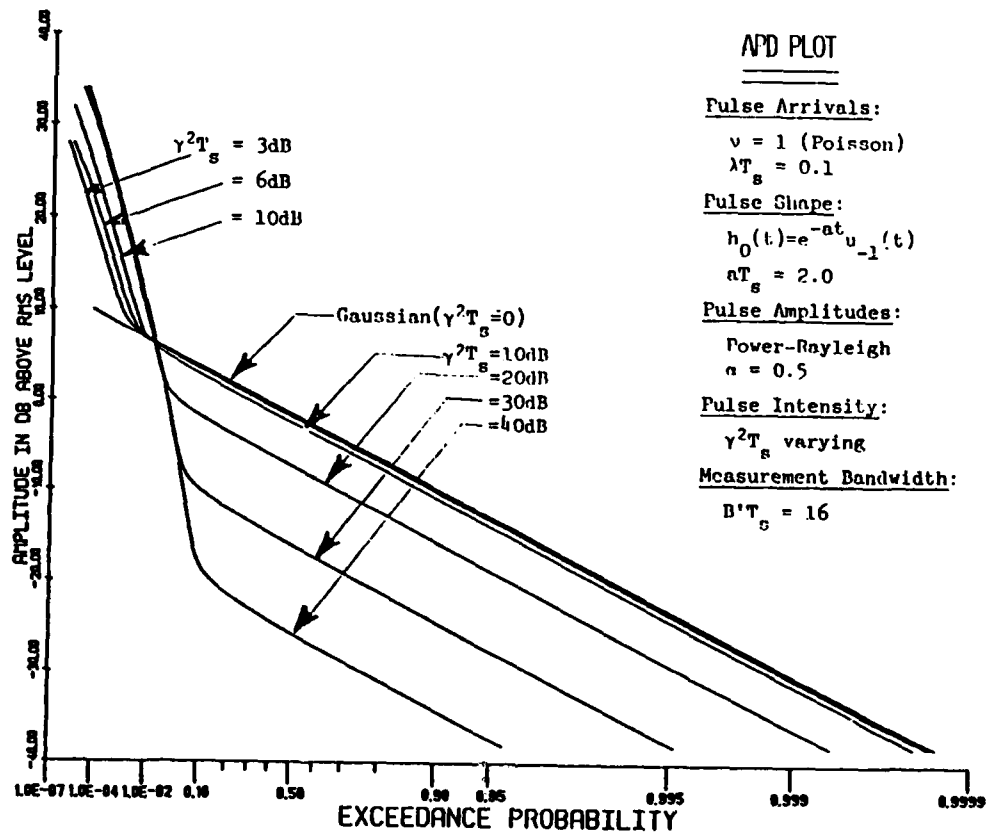
Figure 5

Typical APD Behavior as a Function of $\gamma^2 T_s$ for Selected Parameter Choices.

APD PLOT

Pulse Arrivals:
ν = 1 (Poisson)
$\lambda T_s = 0.1$

Pulse Shape:
$h_0(t) = e^{-at} u_{-1}(t)$
$aT_s = 2.0$

Pulse Amplitudes:
Power-Rayleigh
$a = 0.5$

Pulse Intensity:
$\gamma^2 T_s = 20dB$

Measurement Bandwidth:
$B'T_s$ varying

Gaussian ($\gamma^2 T_s = 0$)
$B'T_s = 1$
= 2
= 4
= 8
=16

AMPLITUDE IN DB ABOVE RMS LEVEL

EXCEEDANCE PROBABILITY
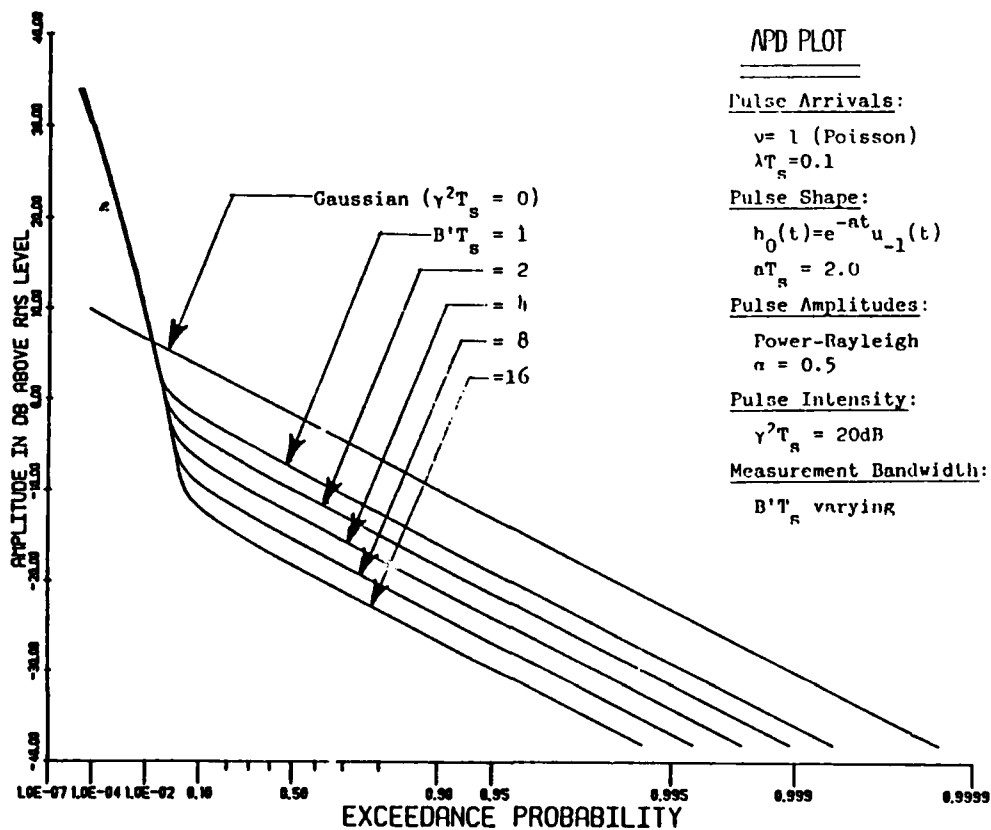
Figure 6

Typical APD Behavior as a Function of $B'T_s$ for Selected Parameter Choices.

APD PLOT

Pulse Arrivals:

$\nu = 1$ (Poisson)

$\lambda T_s = 0.1$

Pulse Shape:

$h_0(t) = e^{-at} u_{-1}(t)$

aT_s varying

Pulse Amplitudes:

Power-Rayleigh

$\alpha = 0.5$

Pulse Intensity:

$\gamma^2 T_n = 20dB$

Measurement Bandwidth:

$B'T_n = 16$

$aT_s = 20.0$

$= 2.0$

$= 1.0$

$= 0.5$

$= 0.1$

Gaussian

AMPLITUDE IN DB ABOVE RMS LEVEL

EXCEEDANCE PROBABILITY
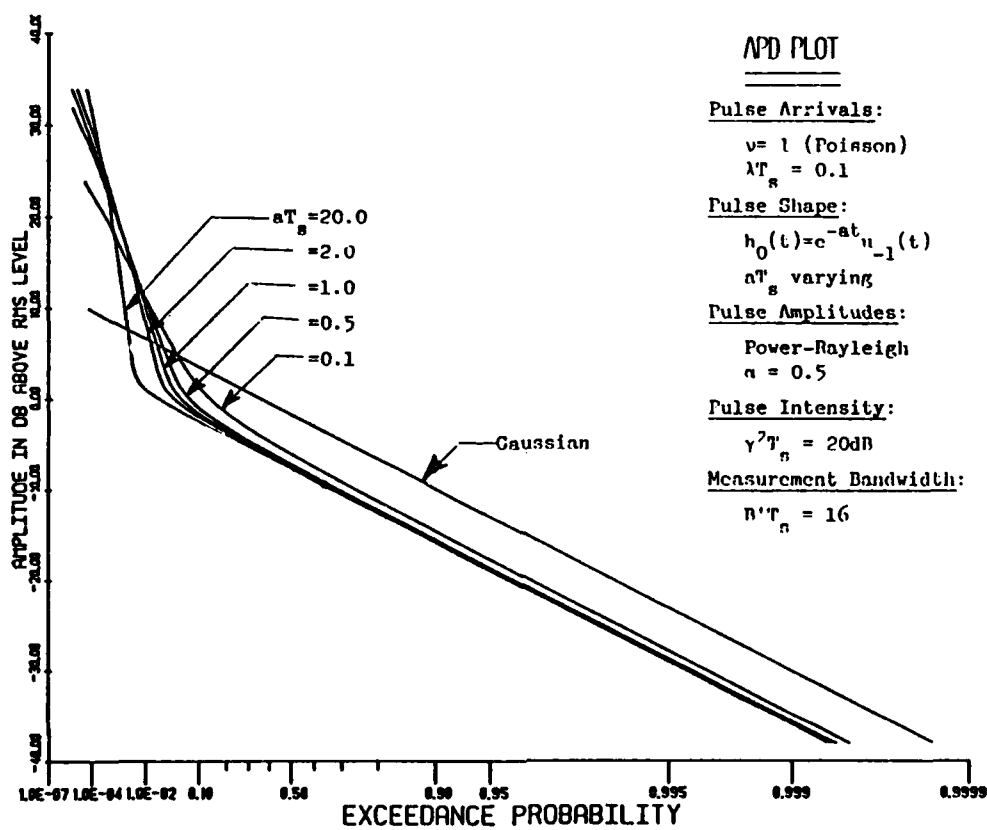
Figure 7

Typical APD Behavior as a Function of aT_s for Selected Parameter Choices.
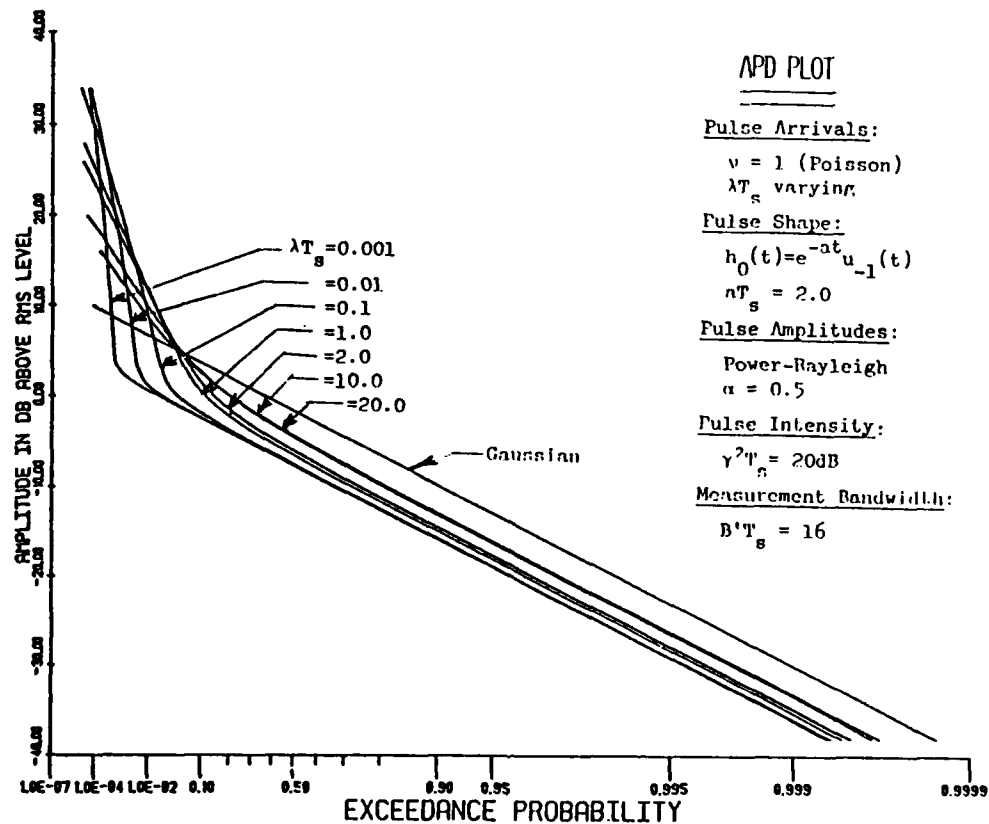
Figure 8

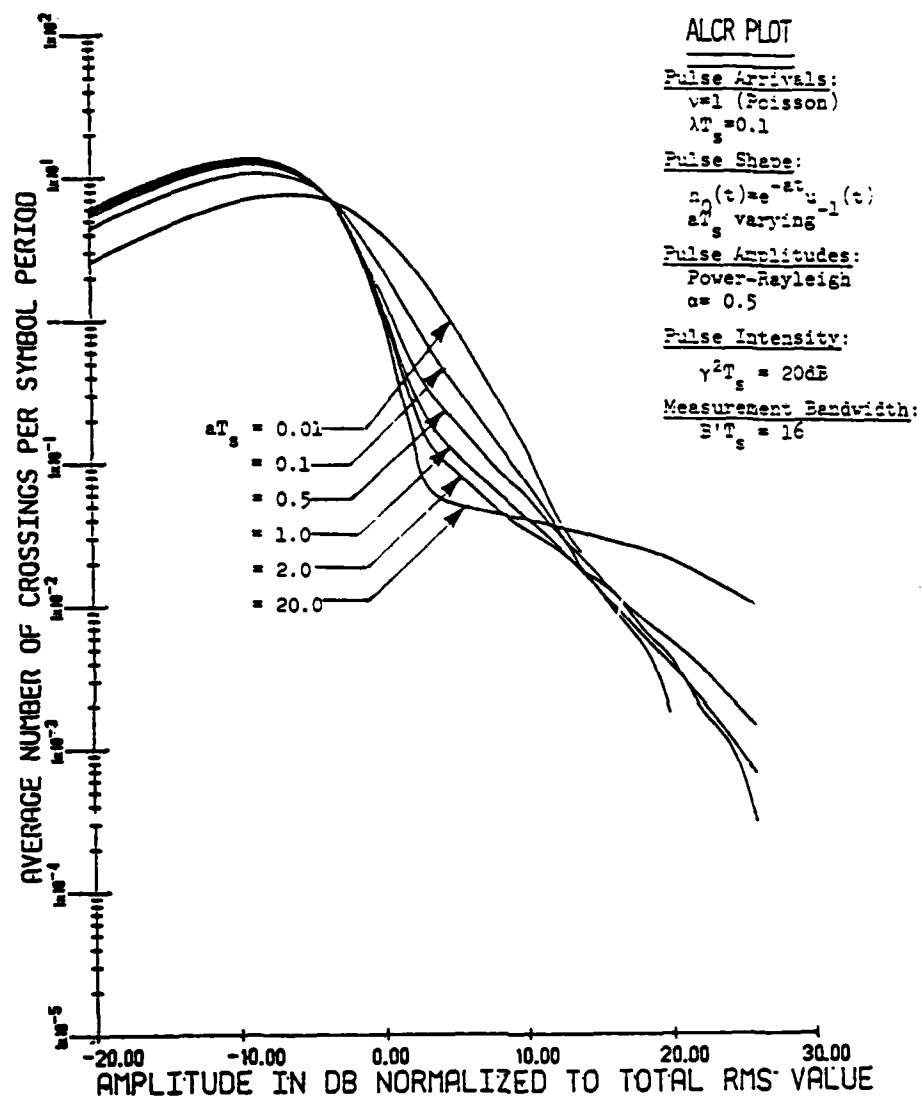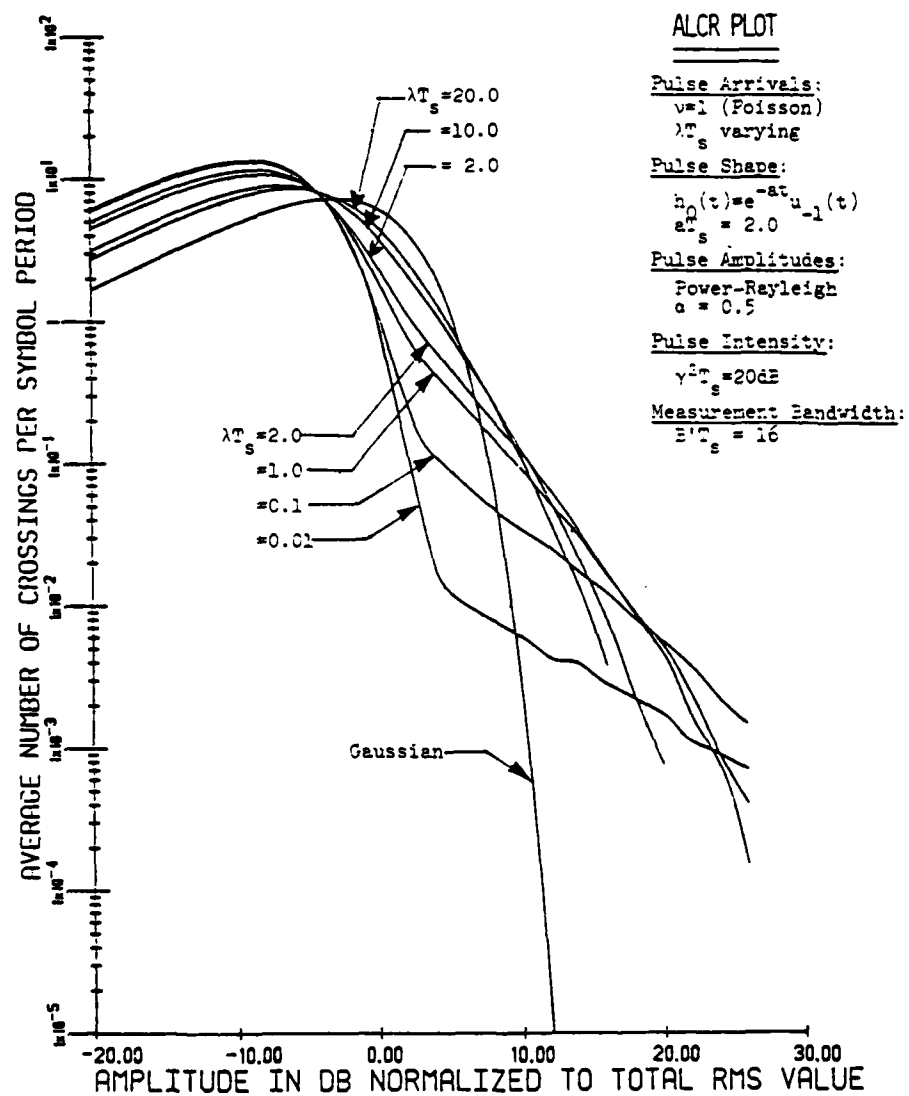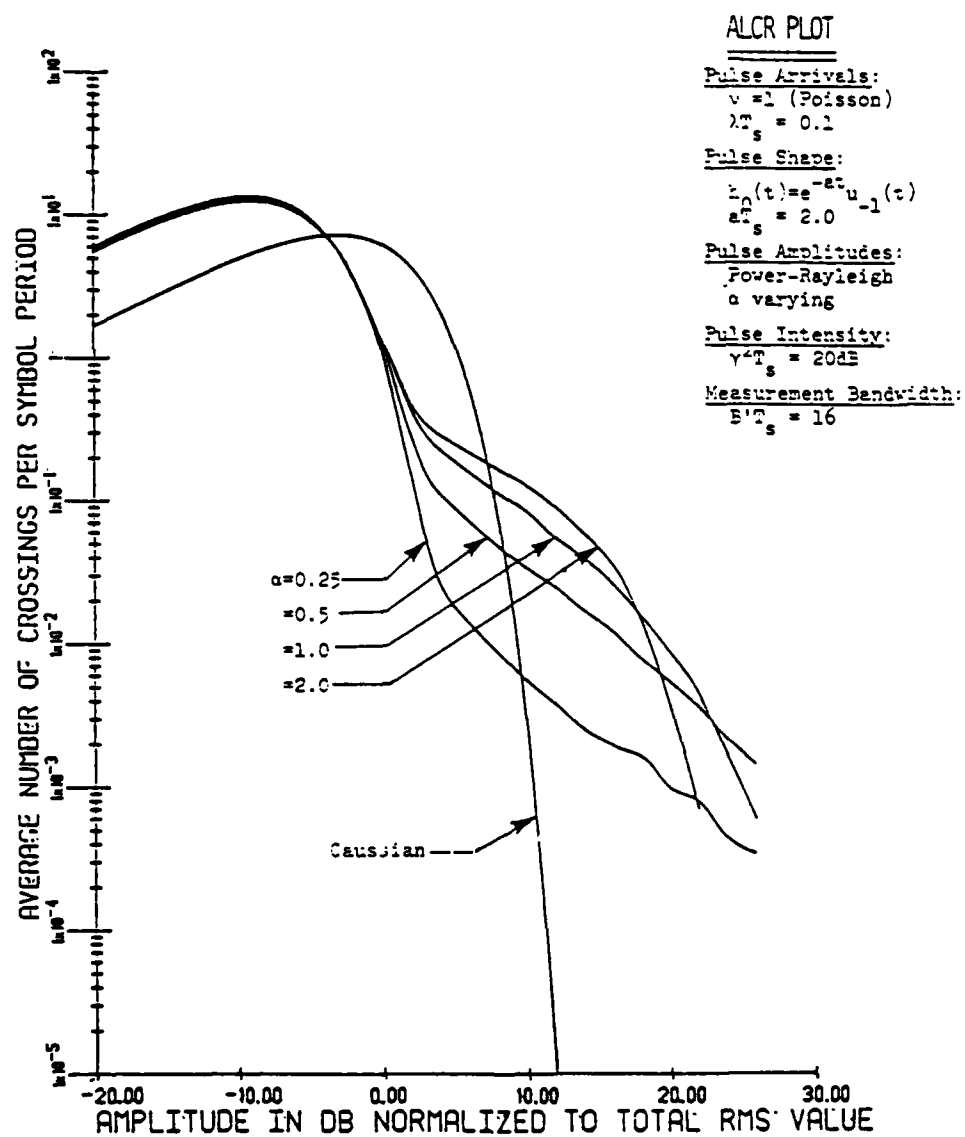Typical APD Behavior as a Function of λT_s for Selected Parameter Choices.
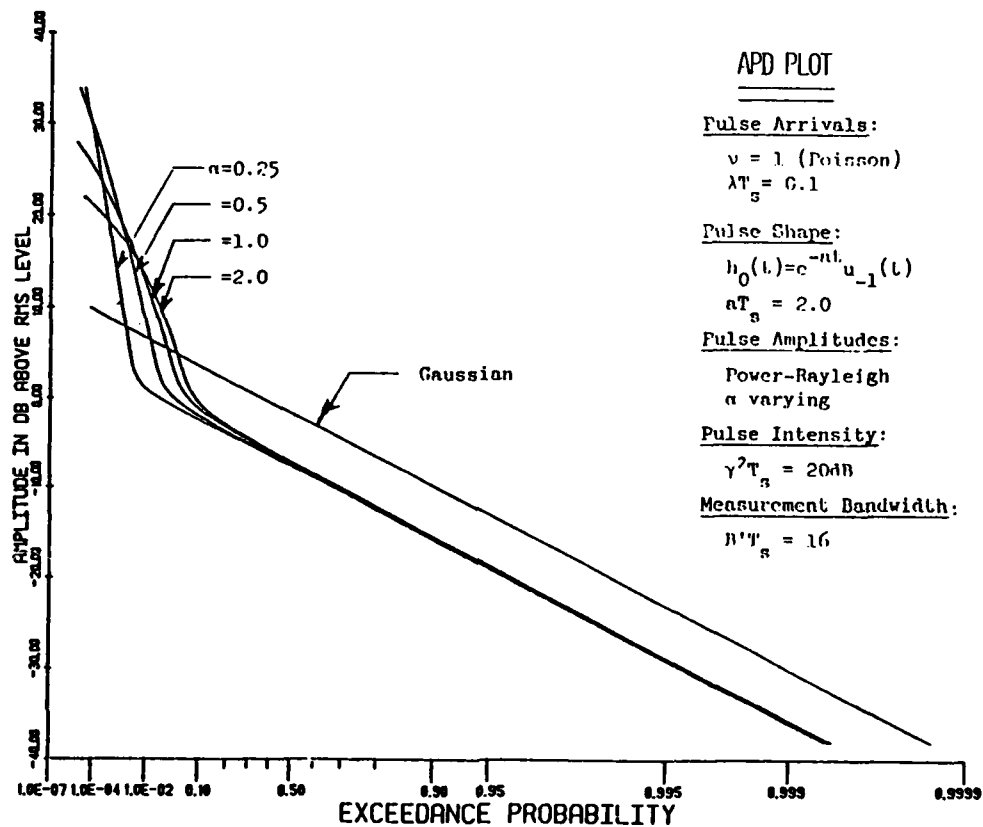
Figure 9

Typical APD Behavior as a Function of Characteristic
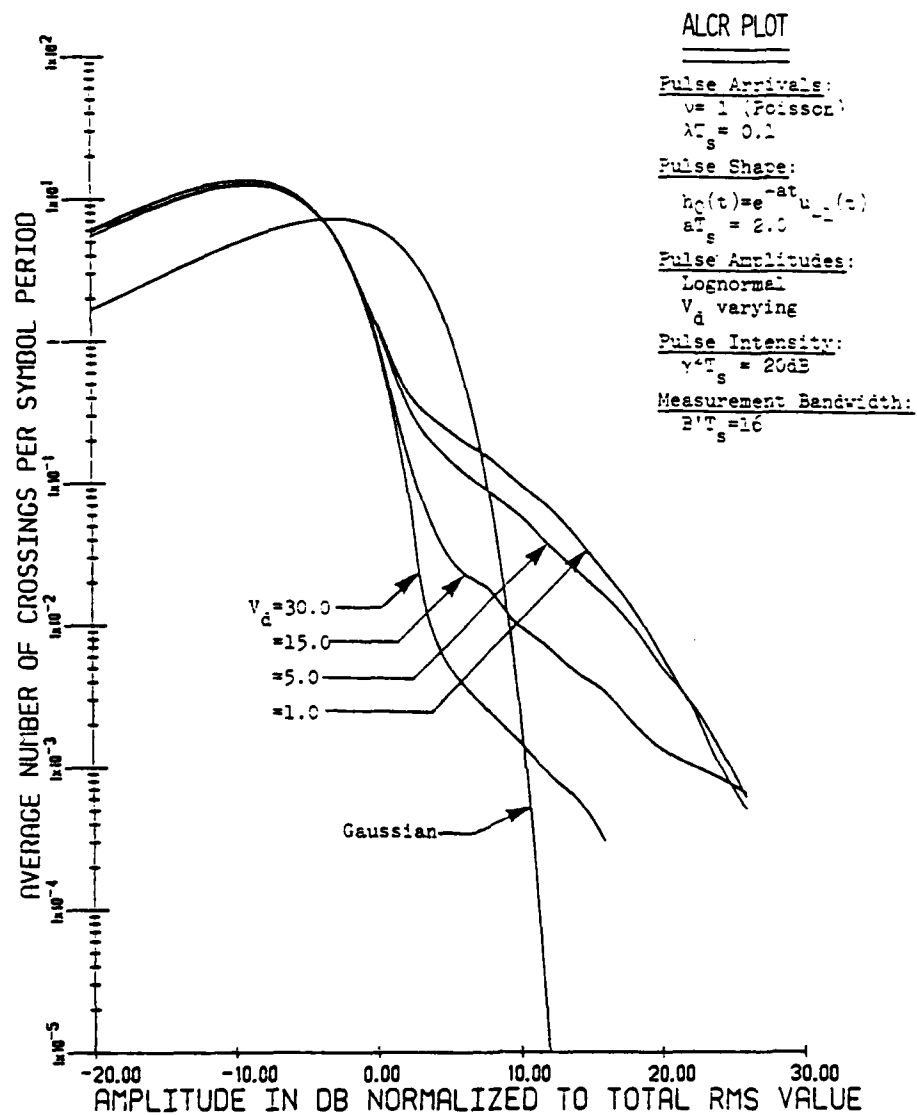Exponent α for Selected Parameter Choices

APD PLOT

Pulse Arrivals:
$\nu = 1$ (Poisson)
$\lambda T_s = 0.1$

Pulse Shape:
$h_0(t) = e^{-at} u_{-1}(t)$
$aT_s = 2.0$

Pulse Amplitudes:
Lognormal
V_d varying

Pulse Intensity:
$\gamma^2 T_s = 20dB$

Measurement Bandwidth:
$B'T_s = 16$

$V_d = 1.0$
$= 5.0$
$= 15.0$
$= 30.0$
Gaussian

AMPLITUDE IN DB ABOVE RMS LEVEL

EXCEEDANCE PROBABILITY
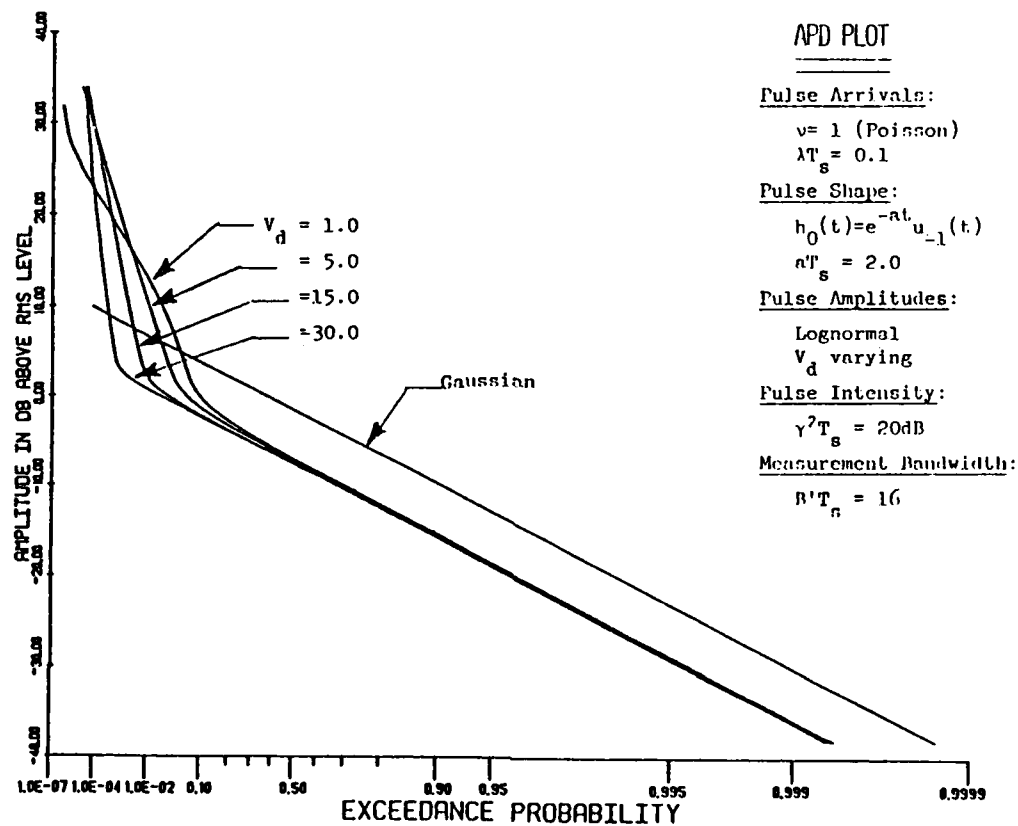
Figure 10

Typical APD Behavior as a Function of V_d
for Selected Parameter Choices.

4-61
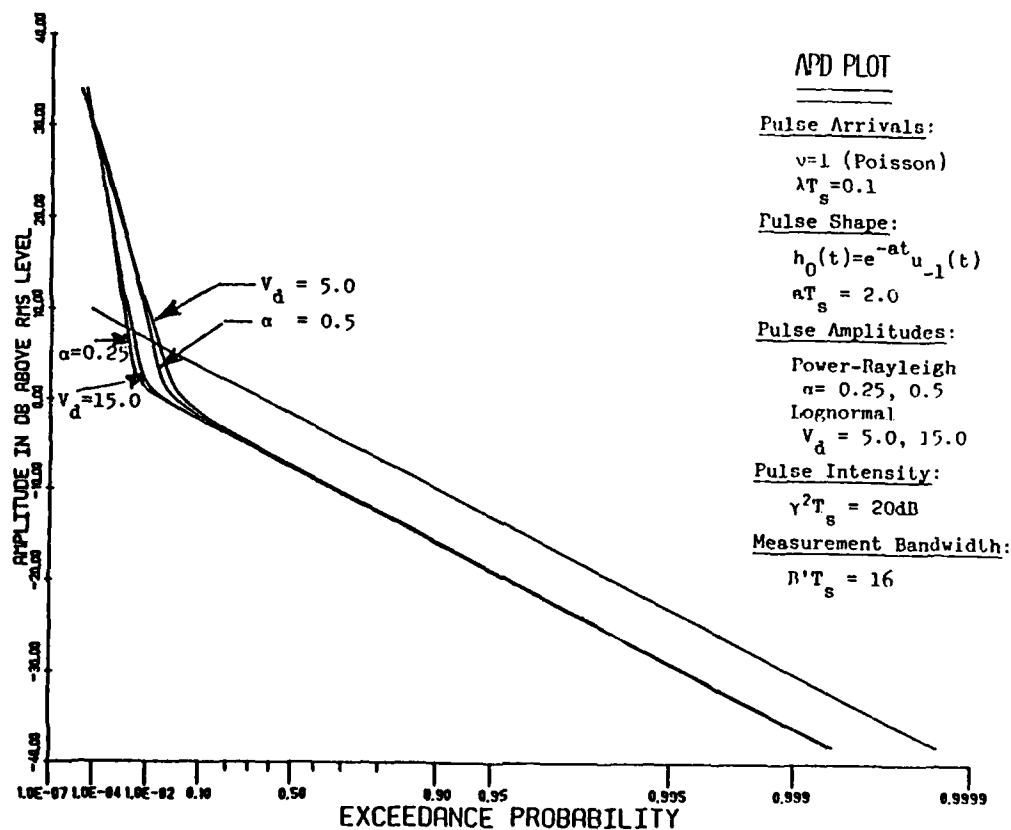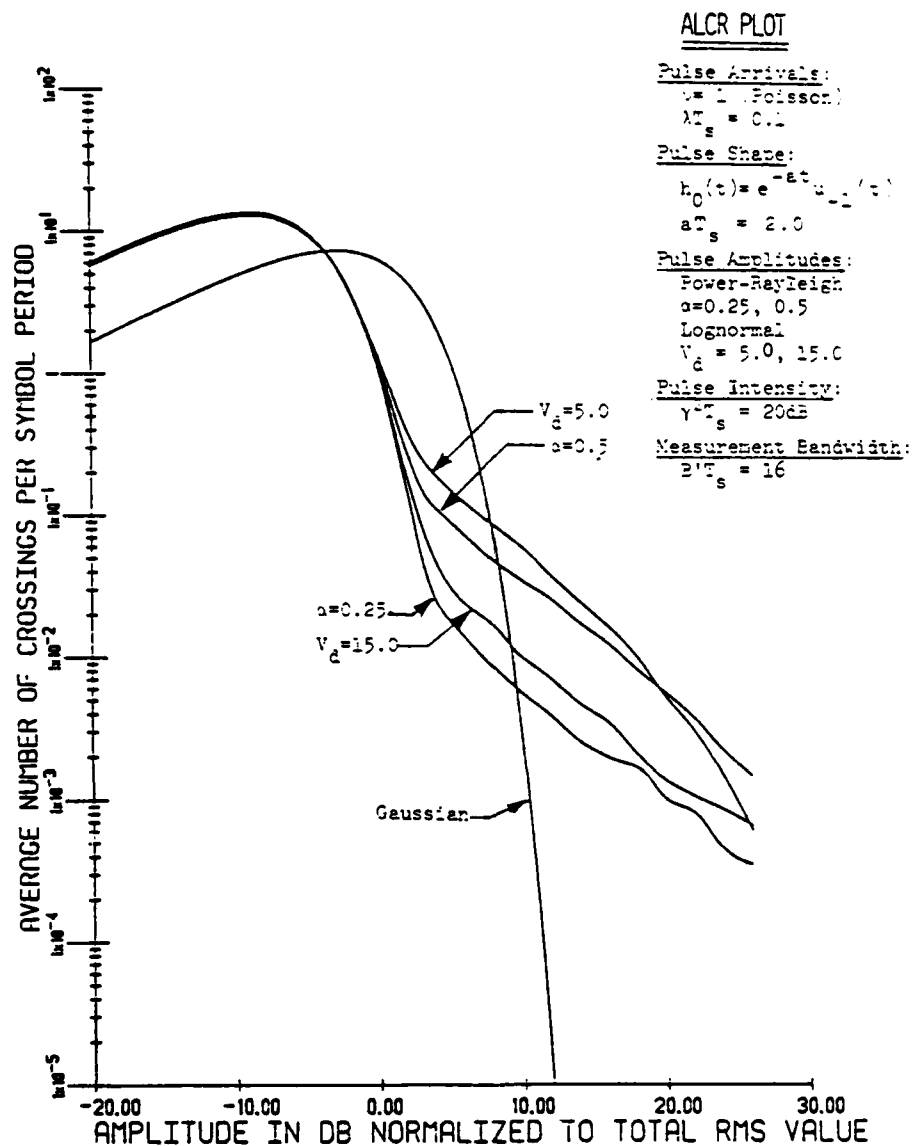
Figure 11

Comparison of APD Behavior for Power-Rayleigh
and Lognormal Distributed Pulse Amplitudes
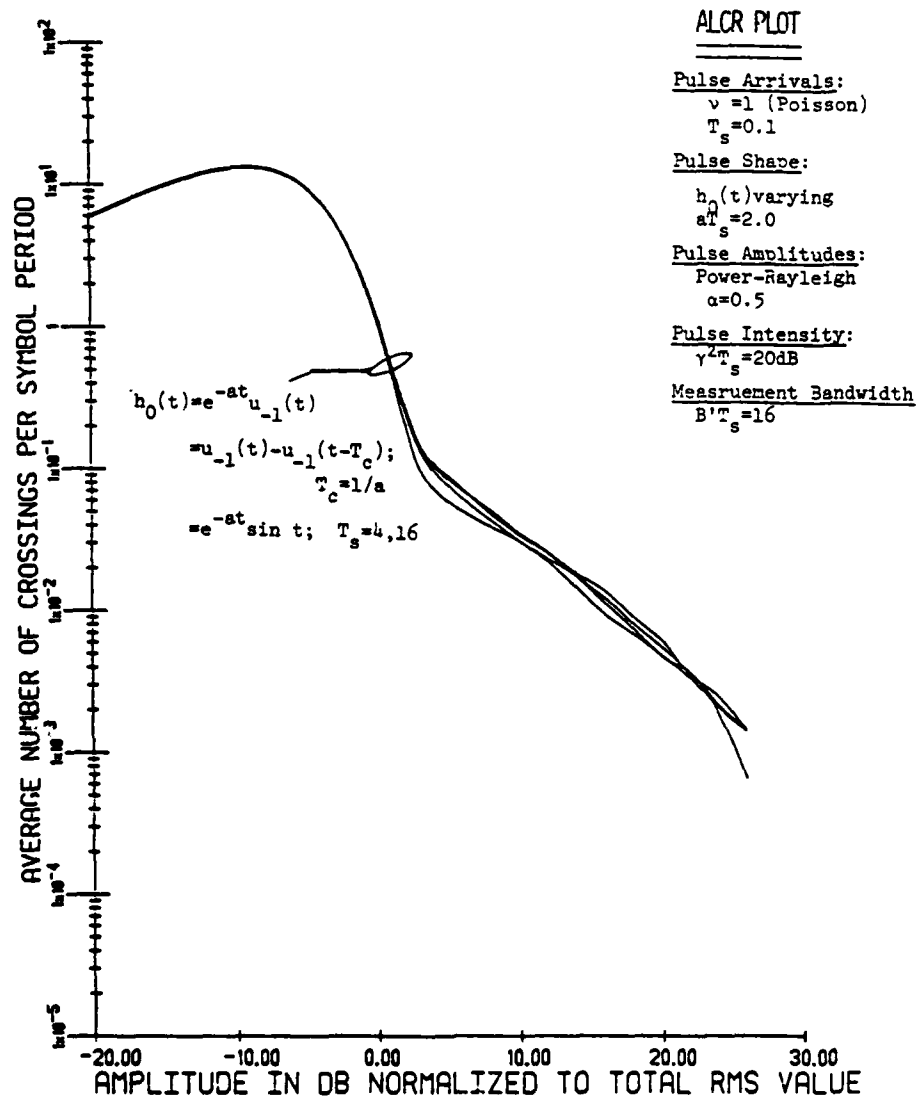under Selected Parameter Choices.

APD PLOT

Pulse Arrivals:

$\nu=1$ (Poisson)
$\lambda T_s = 0.1$

Pulse Shape:

$h_0(t) = e^{-at} u_{-1}(t)$
$aT_s = 2.0$

Pulse Amplitudes:

Power-Rayleigh
$n = 0.25,\ 0.5$
Lognormal
$V_d = 5.0,\ 15.0$

Pulse Intensity:

$\gamma^2 T_s = 20dB$

Measurement Bandwidth:

$B'T_s = 16$

$h_0(t) = e^{-at} u_{-1}(t)$

$= u_{-1}(t) - u_{-1}(t-T_c);\ T_c = 1/a$

$= e^{-at} \sin\omega t\ ;\ \omega T_s = 4,16$

Gaussian

AMPLITUDE IN DB ABOVE RMS LEVEL

EXCEEDANCE PROBABILITY
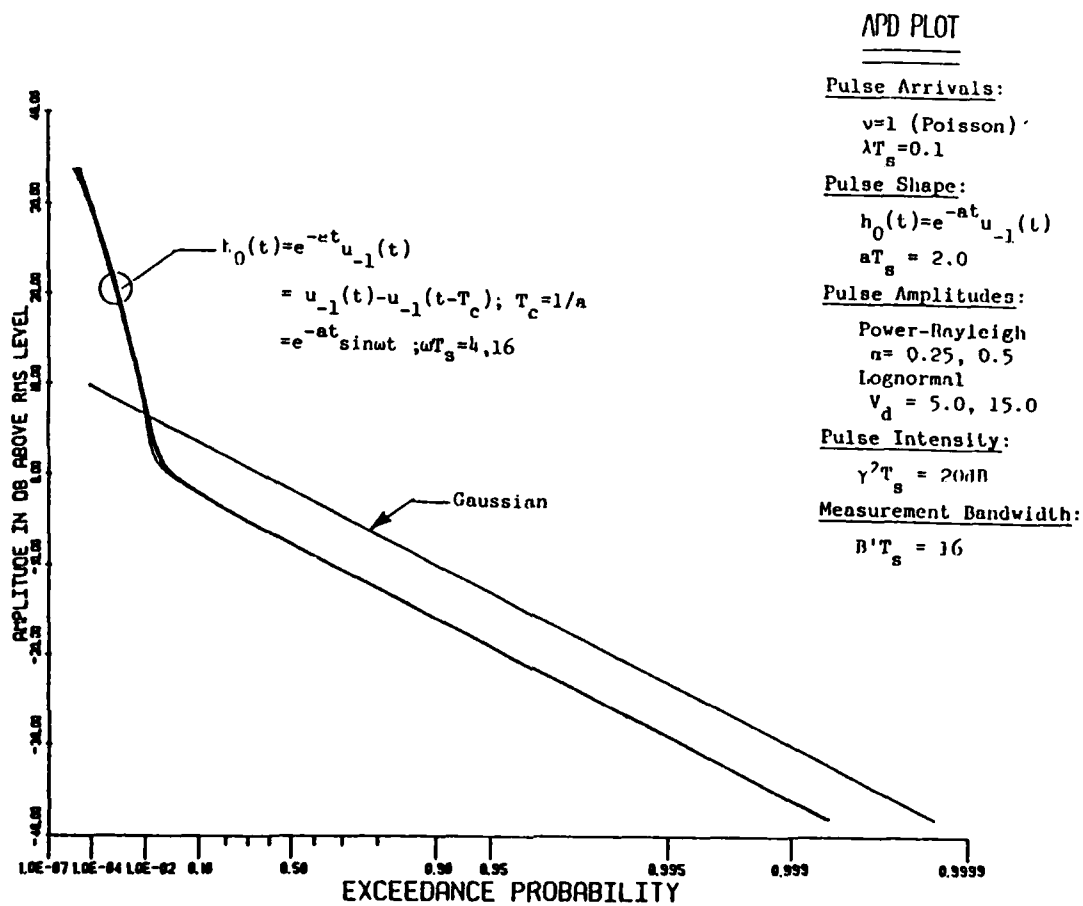
Figure 12

Typical APD Behavior as a Function of Pulse Shape $h_0(t)$
for Selected Parameter Choices.

4-63

APD PLOT

Pulse Arrivals:
ν varying
$\lambda T_s = 0.1$
Pulse Shape:
$h_0(t) = e^{-at} u_{-1}(t)$
$aT_s = 2.0$
Pulse Amplitudes:
Power-Rayleigh
$\alpha = 0.5$
Pulse Intensity:
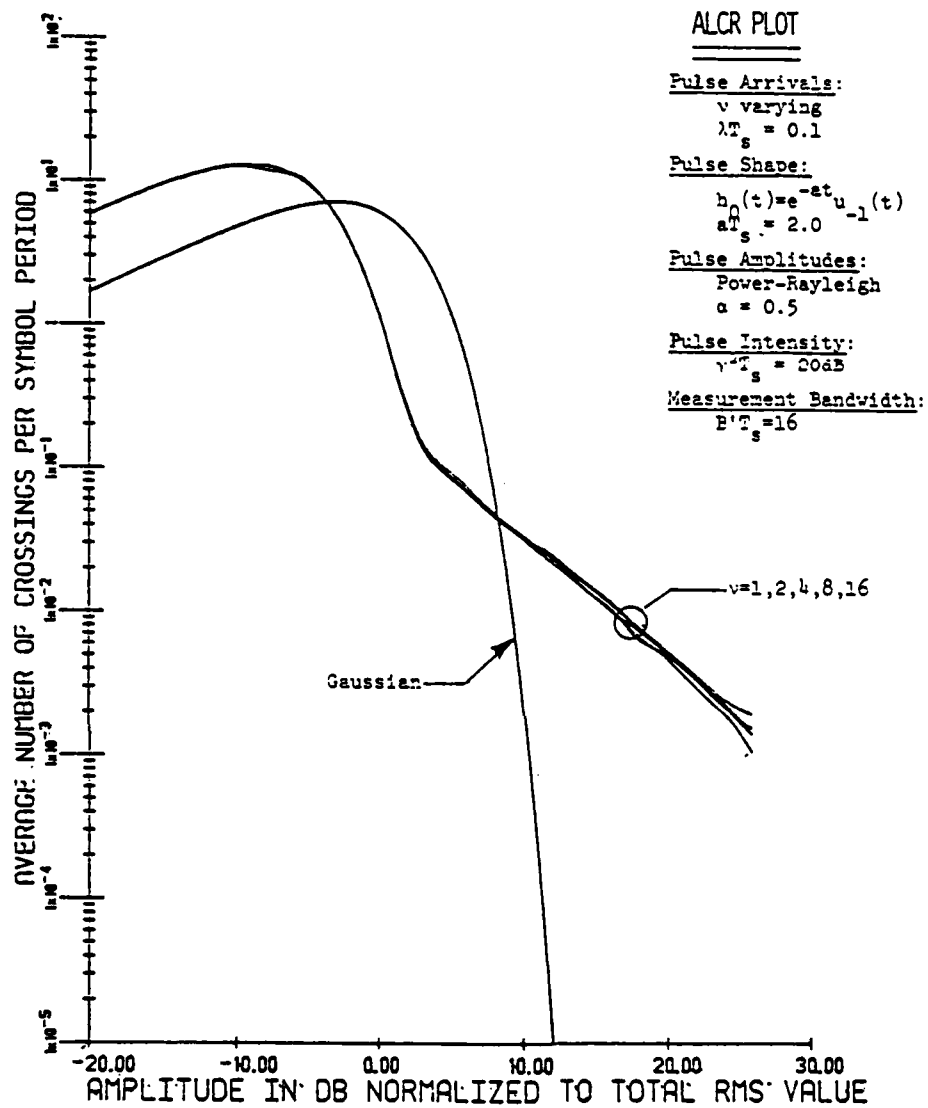$\gamma^2 T_s = 20dB$
Measurement Bandwidth:
$B'T_s = 16$
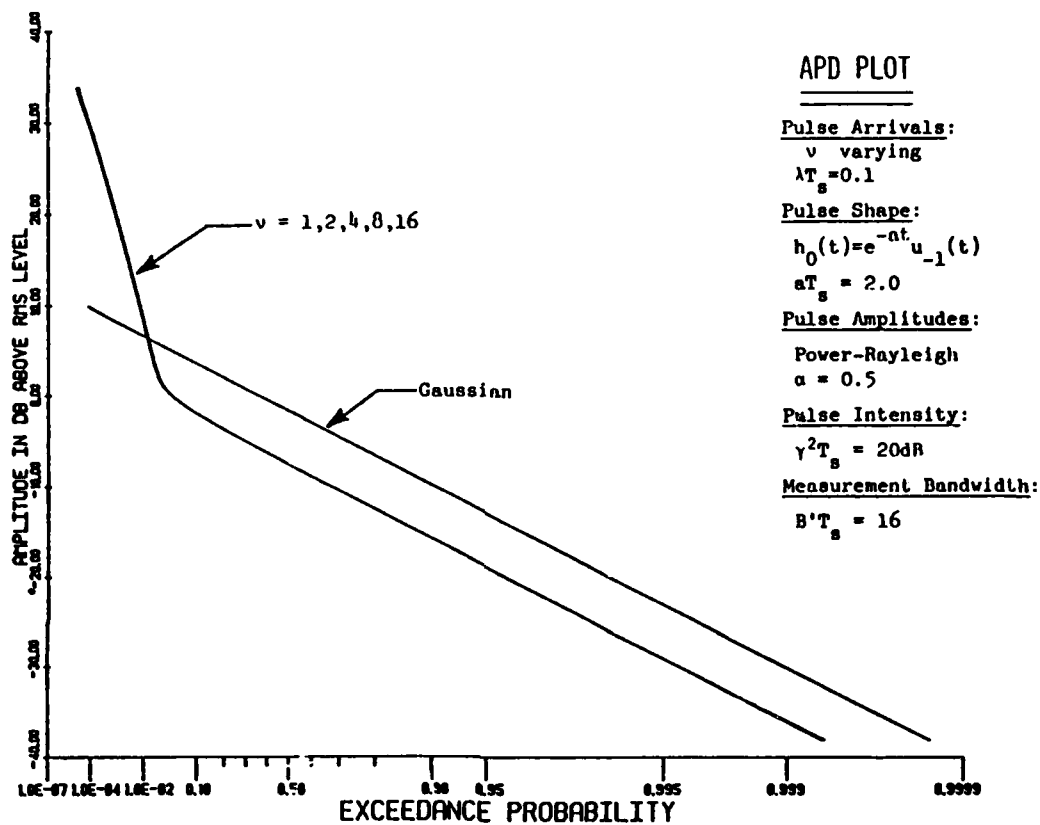
Figure 13

Typical APD Behavior as a Function of ν
for Selected Parameter Choices.
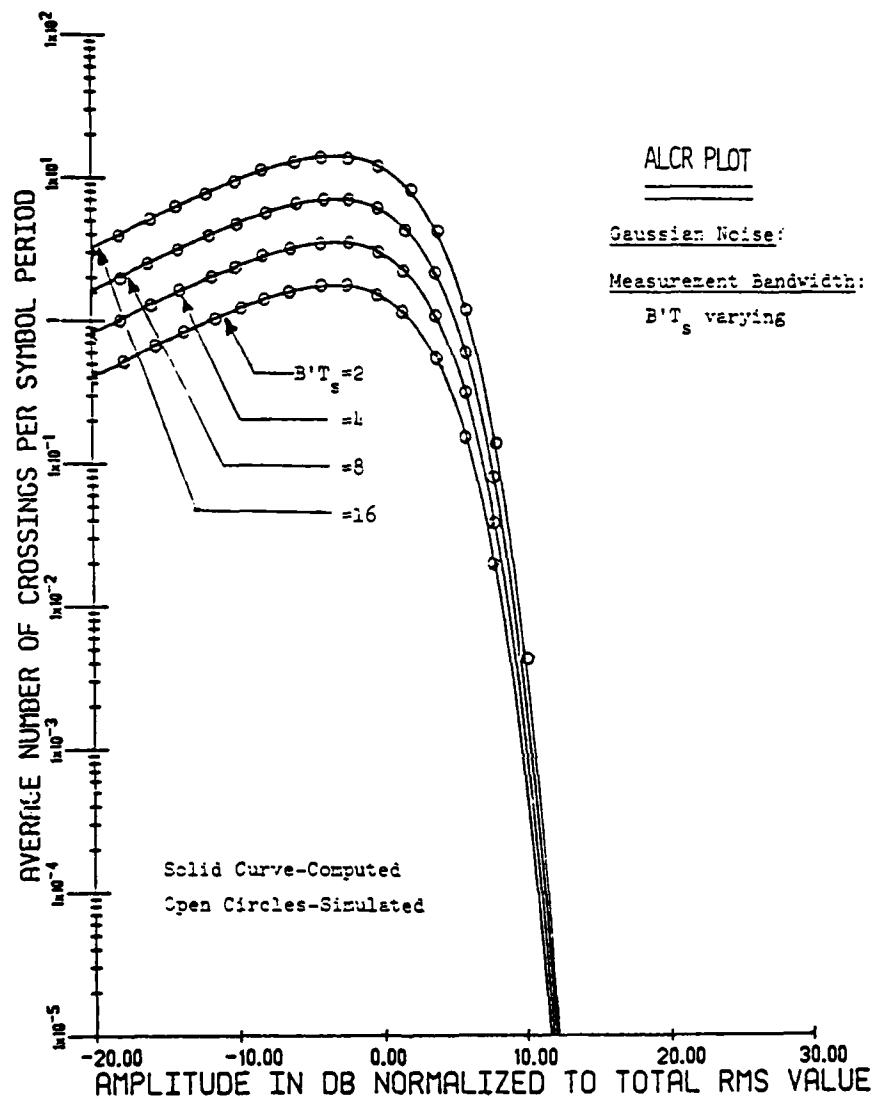
Figure 14

Comparison of Computed and Simulated
ALCR Results for Gaussian Noise.

ALCR PLOT

Pulse Arrivals:
$\nu = 1$ (Poisson)
$\lambda T_s = 0.1$

Pulse Shape:
$h_0(t) = e^{-at} u_{-1}(t)$
$aT_s = 2.0$

Pulse Amplitudes:
Power-Rayleigh
$\alpha = 0.5$

Pulse Intensity:
$\gamma^2 T_s$ varying

Measurement Bandwidth
$F'T_s = 16.0$

AVERAGE NUMBER OF CROSSINGS PER SYMBOL PERIOD

$\gamma^2 T_s = 40db$
$= 30db$
$= 20db$

$\gamma^2 T_s = 20db$
$= 10db$
$= 3db$

Gaussian ($\gamma^2 T_s = 0$)

AMPLITUDE IN DB NORMALIZED TO TOTAL RMS VALUE
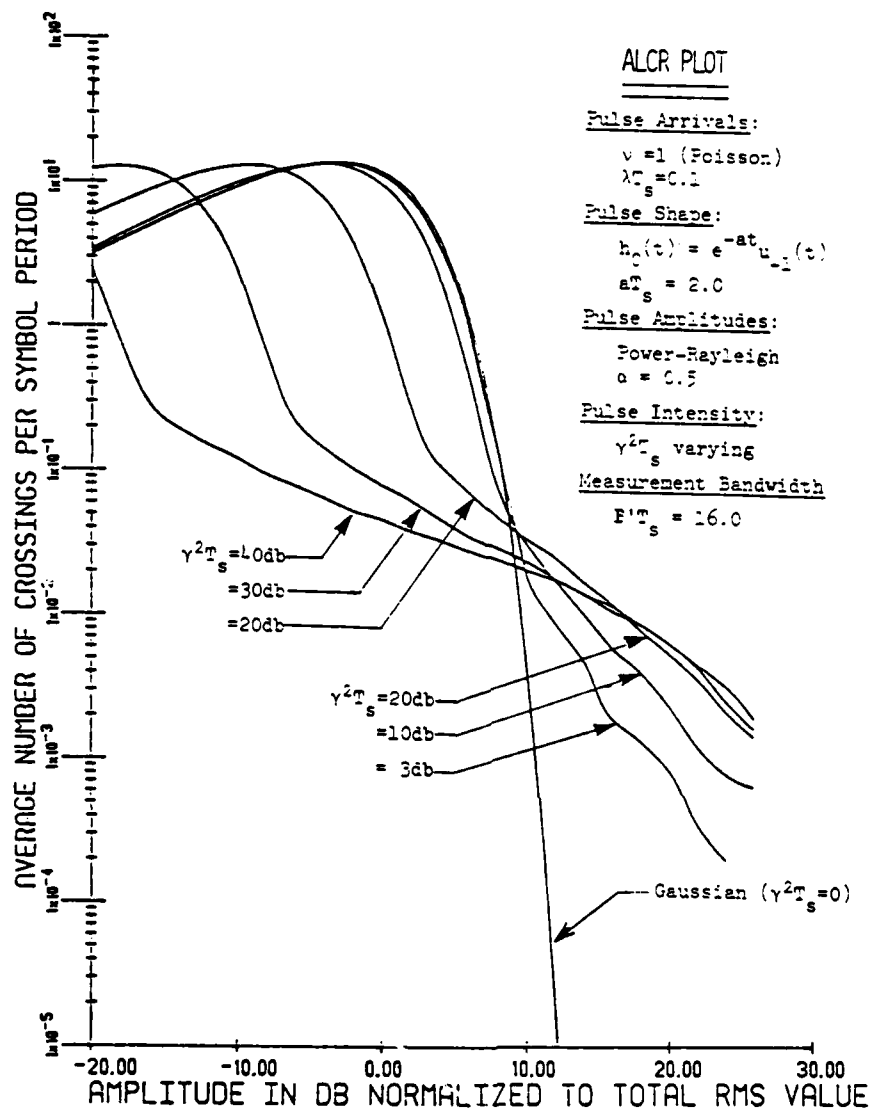
Figure 15

Typical ALCR Behavior as a Function of $\gamma^2 T_s$ for
Selected Parameter Choices.

4-66
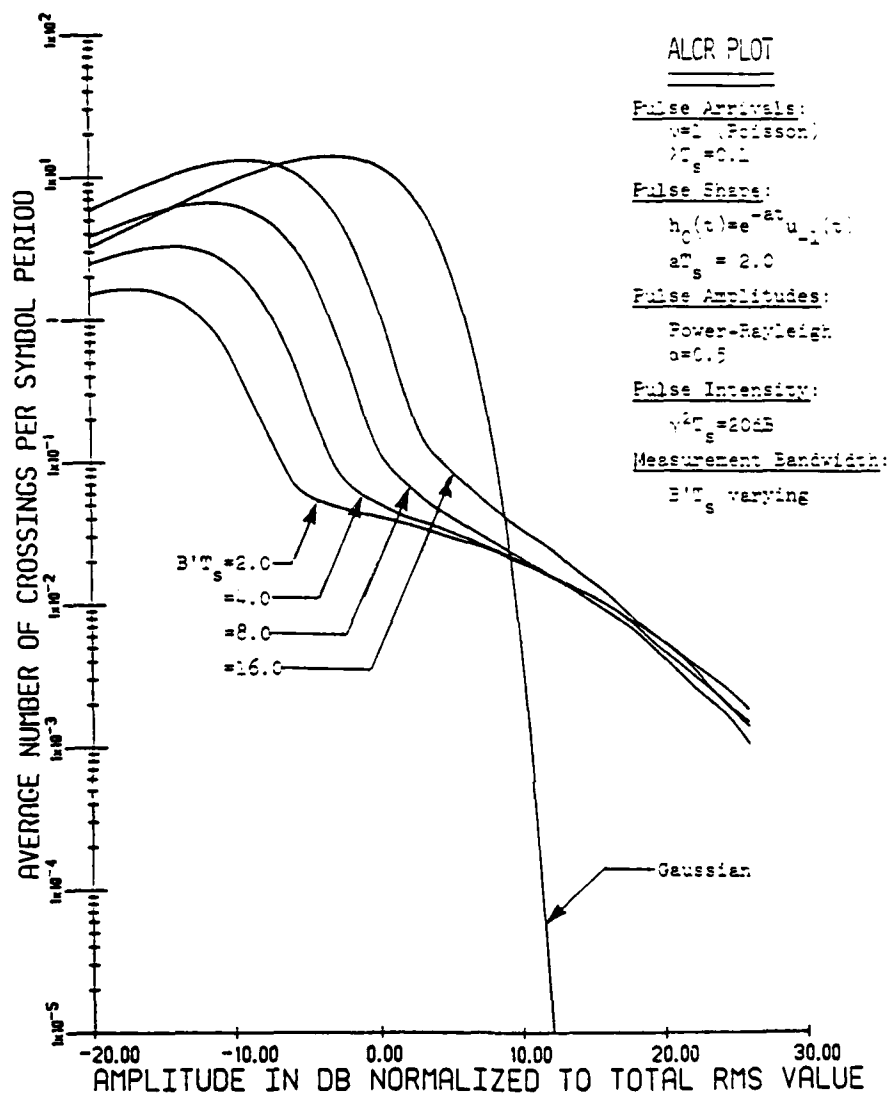
Figure 16

Typical ALCR Behavior as a Function of $B'T_s$
for Selected Parameter Choices.

ALCR PLOT

<u>Pulse Arrivals:</u>
$\nu=1$ (Poisson)
$\lambda T_s = 0.1$

<u>Pulse Shape:</u>
$n_0(t) = e^{-at} u_{-1}(t)$
aT_s varying

<u>Pulse Amplitudes:</u>
Power-Rayleigh
$\alpha = 0.5$

<u>Pulse Intensity:</u>
$\gamma^2 T_s = 20dB$

<u>Measurement Bandwidth:</u>
$B'T_s = 16$

$aT_s = 0.01$
$= 0.1$
$= 0.5$
$= 1.0$
$= 2.0$
$= 20.0$

AVERAGE NUMBER OF CROSSINGS PER SYMBOL PERIOD

AMPLITUDE IN DB NORMALIZED TO TOTAL RMS VALUE

Figure 17

Typical ALCR Behavior as a Function of aT_s
for Selected Parameter Choices.

4-68

Figure 18

Typical ALCR Behavior as a Function of
λT_s for Selected Parameter Choices.

Figure 19

Typical ALCR Behavior as a Function f Characteristic Exponent α for Selected Parameter Choices.

Figure 20

Typical ALCR Behavior as a Function of V_d for
Selected Parameter Choices.

Figure 21

Comparison of ALCR Behavior for Power-
Rayleigh and Lognormal Distributed Pulse
Amplitudes under Selected Parameter Choices.

ALCR PLOT

Pulse Arrivals:
$\nu = 1$ (Poisson)
$T_s = 0.1$

Pulse Shape:
$h_0(t)$ varying
$aT_s = 2.0$

Pulse Amplitudes:
Power-Rayleigh
$\alpha = 0.5$

Pulse Intensity:
$\gamma^2 T_s = 20$dB

Measruement Bandwidth
$B'T_s = 16$

$h_0(t) = e^{-at}u_{-1}(t)$

$= u_{-1}(t) - u_{-1}(t-T_c);$
$T_c = 1/a$

$= e^{-at}\sin t; \quad T_s = 4,16$

Figure 22

Typical ALCR Behavior as a Function of Pulse
Shape $h_0(t)$ for Selected Parameter Choices.

4-73

ALCR PLOT

Pulse Arrivals:
ν varying
$\lambda T_s = 0.1$

Pulse Shape:
$h_0(t) = e^{-at}u_{-1}(t)$
$aT_s = 2.0$

Pulse Amplitudes:
Power-Rayleigh
$\alpha = 0.5$

Pulse Intensity:
$\gamma^2 T_s = 20dB$

Measurement Bandwidth:
$B'T_s = 16$

AVERAGE NUMBER OF CROSSINGS PER SYMBOL PERIOD

$\nu = 1,2,4,8,16$

Gaussian

AMPLITUDE IN DB NORMALIZED TO TOTAL RMS VALUE

Figure 23

Typical ALCR Behavior as a function of
ν for Selected Parameter Choices.

4-74
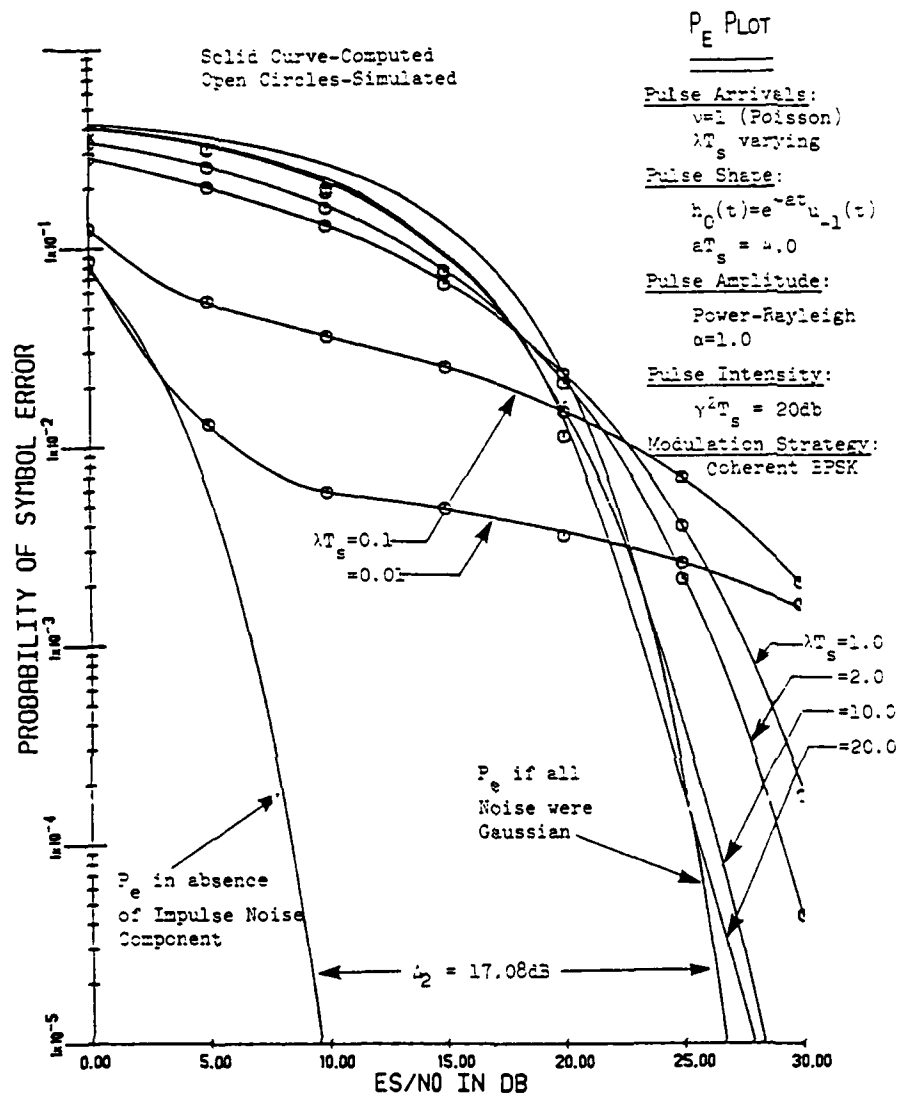
Figure 24

Comparison of Computed and Simulated P_e Results as
a Function of λT_s for Special Case of Power-Rayleigh
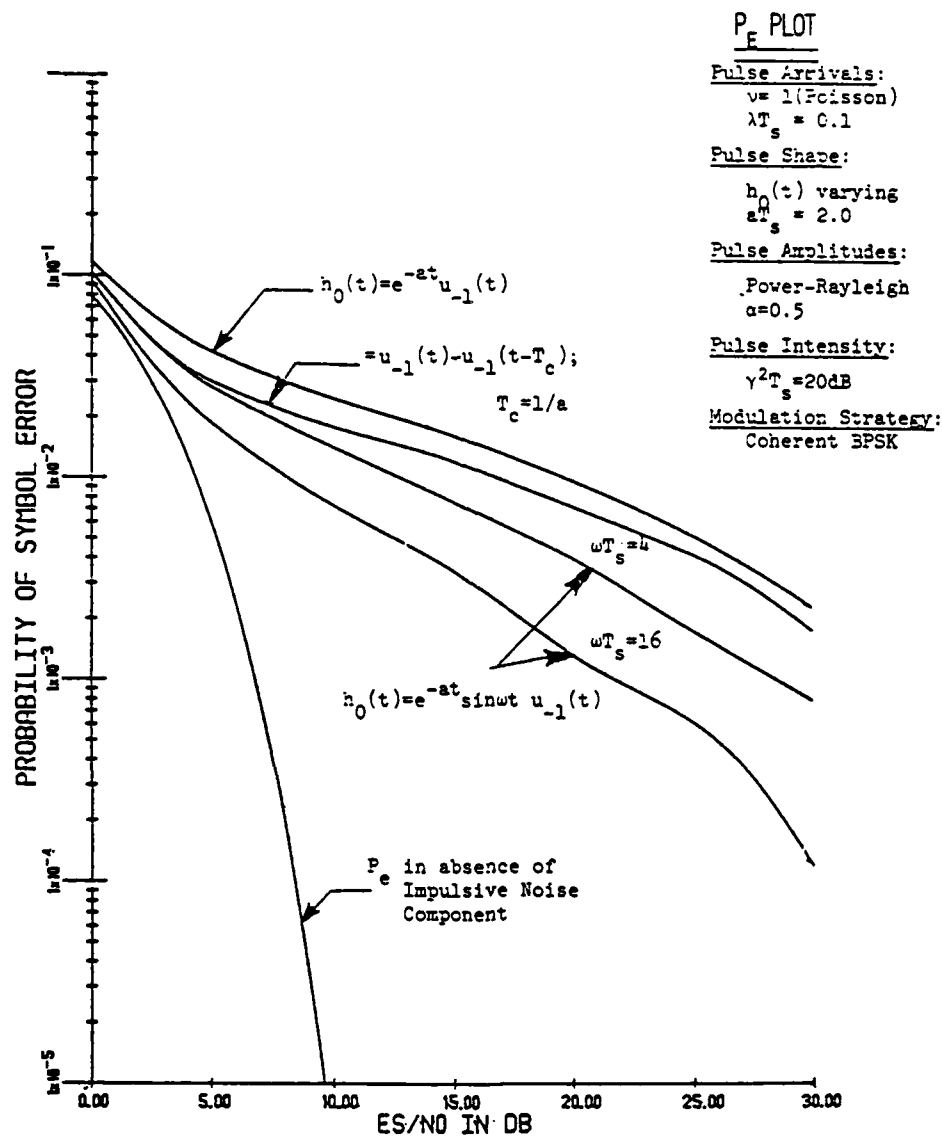Pulse Amplitude Distribution with Characteristic
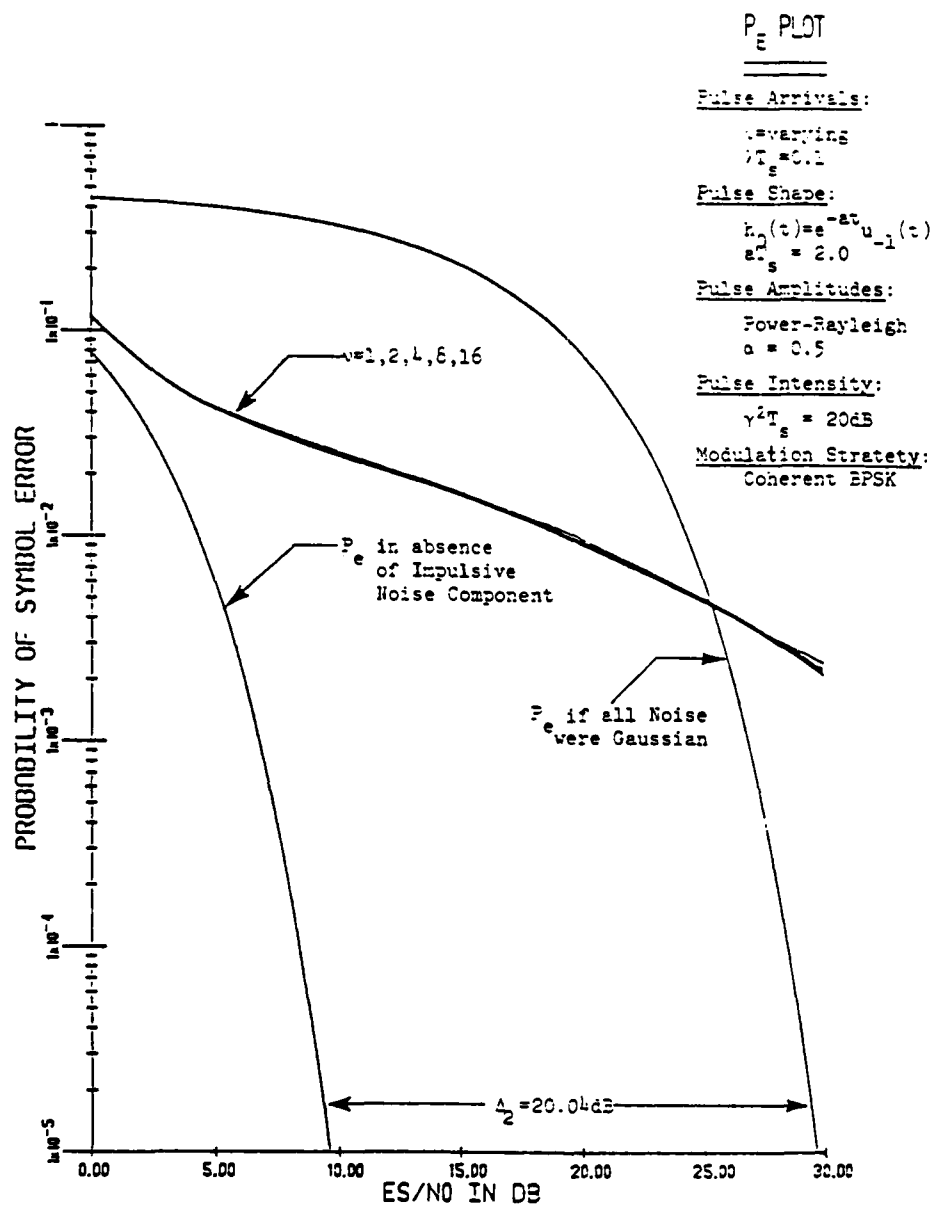Exponent $\alpha=1.0$.

4-75
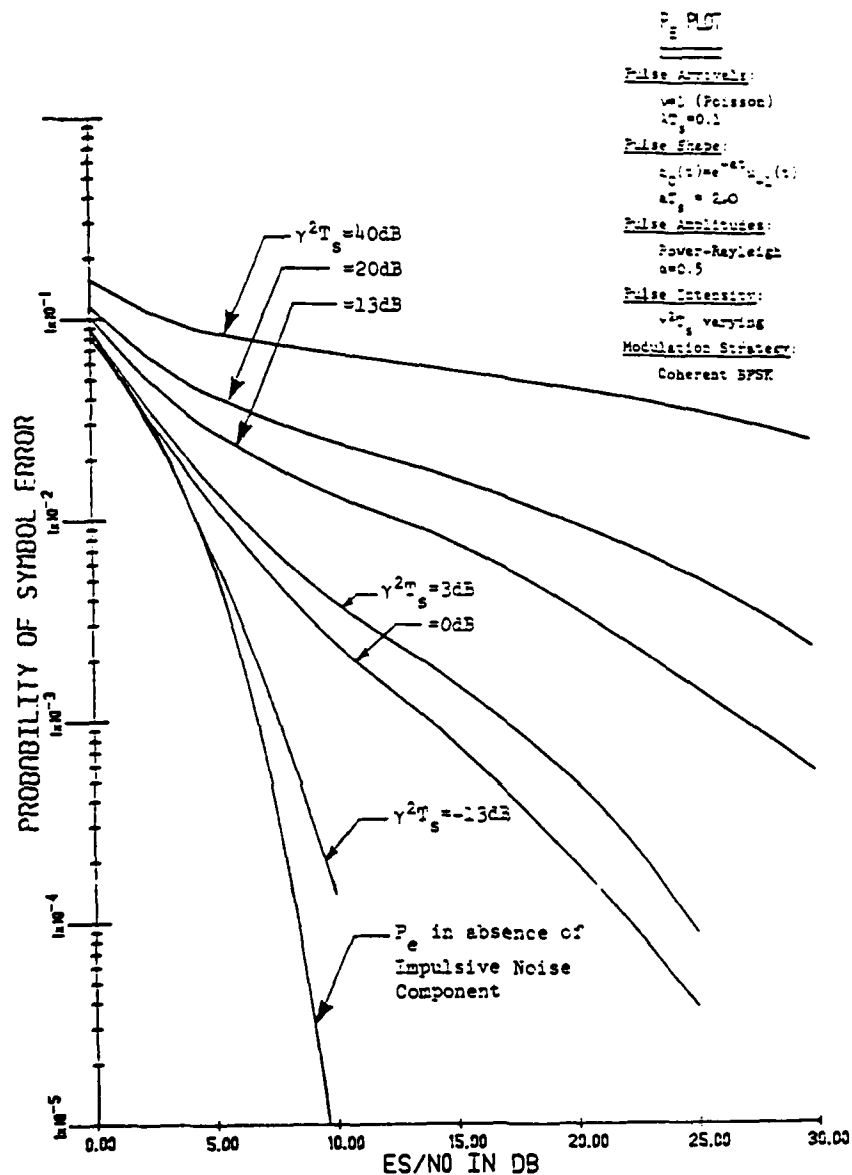
Figure 25

Typical P_e Behavior for Linear Matched Filter Reception as a Function of T_s for Selected Parameter Choices; Coherent BPSK Modulation.

4-76
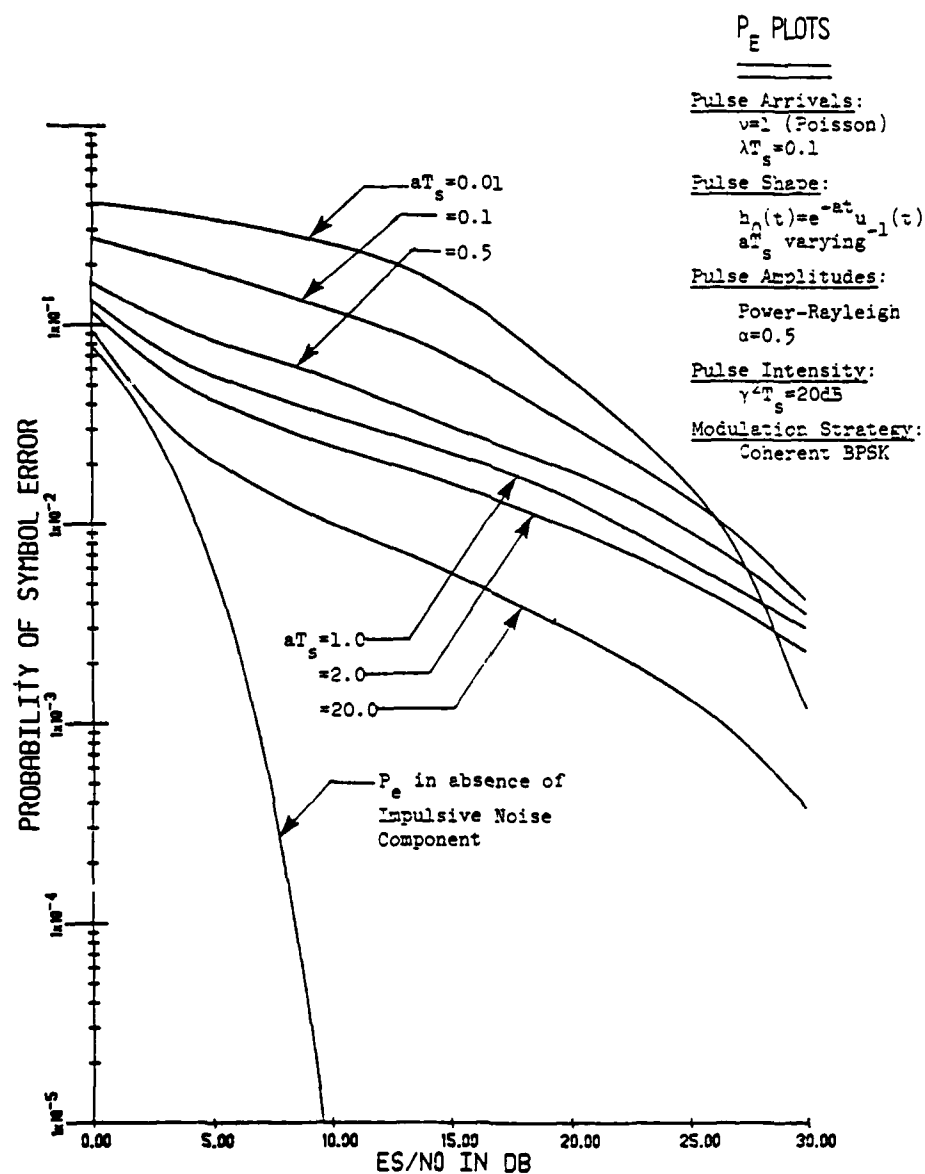
Figure 26

Typical P_e Behavior for Linear Matched Filter Reception as a Function of aT_s for Selected Parameter Choices; Coherent BPSK Modulation.

4-77
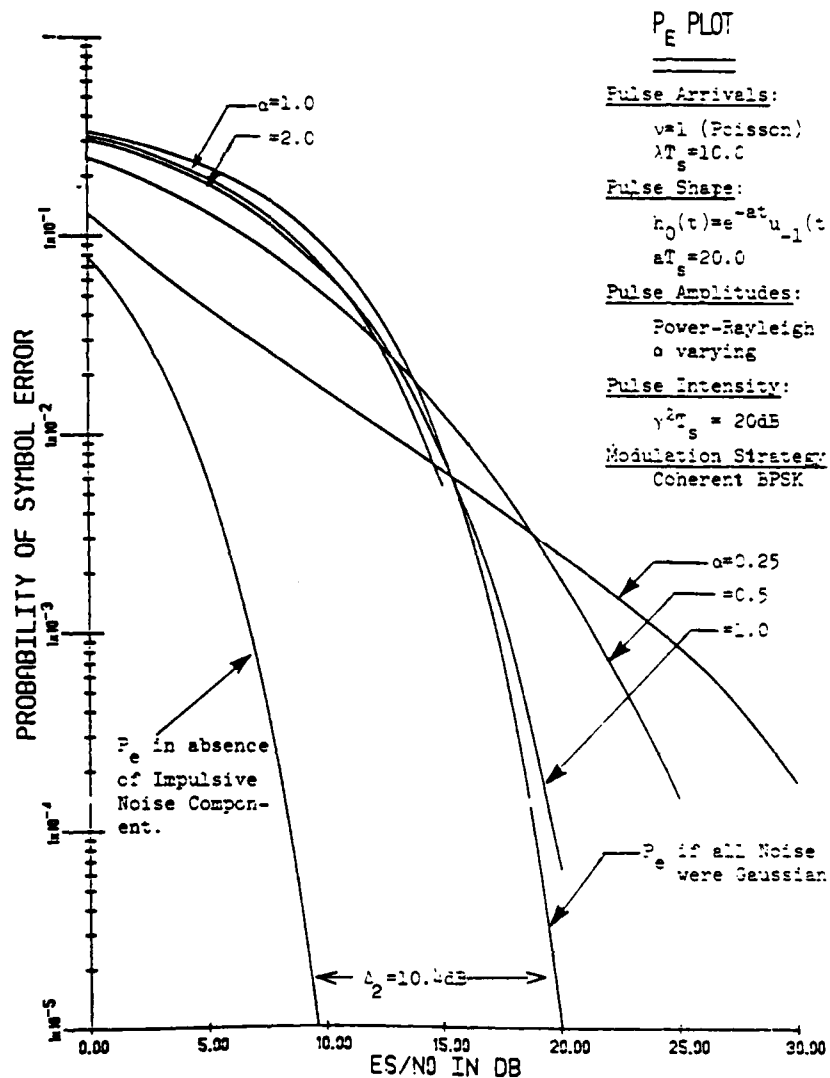
Figure 27

Typical P_e Behavior for Linear Matched Filter Reception as a Function of Characteristic Exponent α for Selected Parameter Choices; Coherent BPSK Modulation.
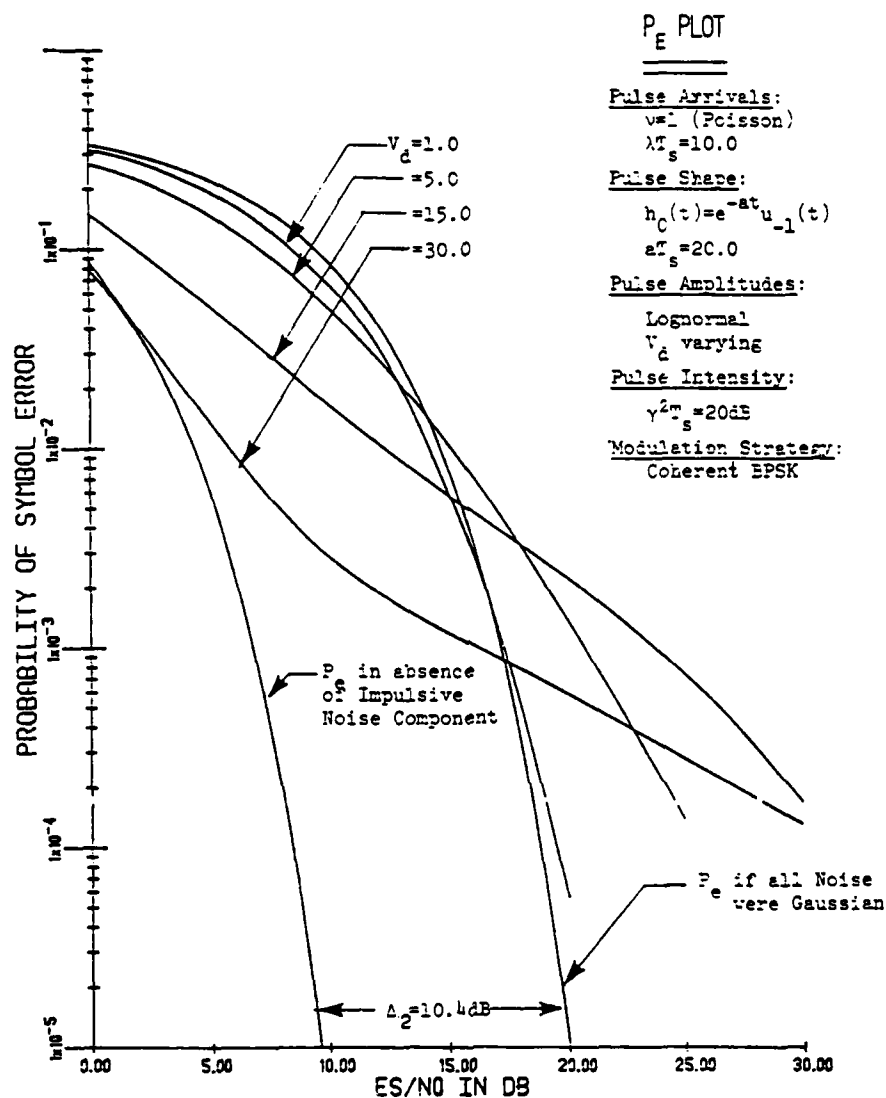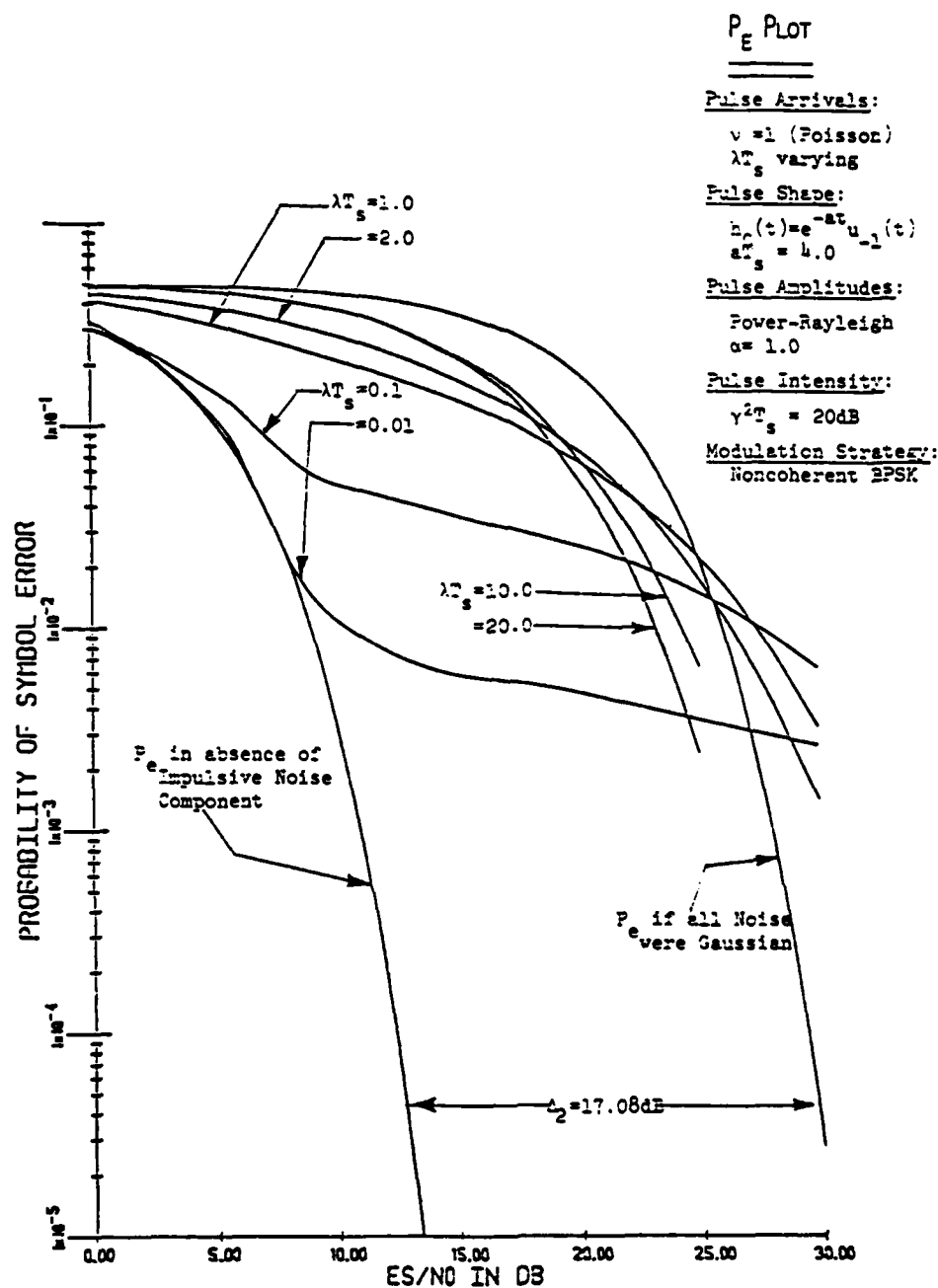
Figure 28

Typical P_e Behavior for Linear Matched Filter Reception as a Function of V_d for Selected Parameter Choices; Coherent BPSK Modulation.
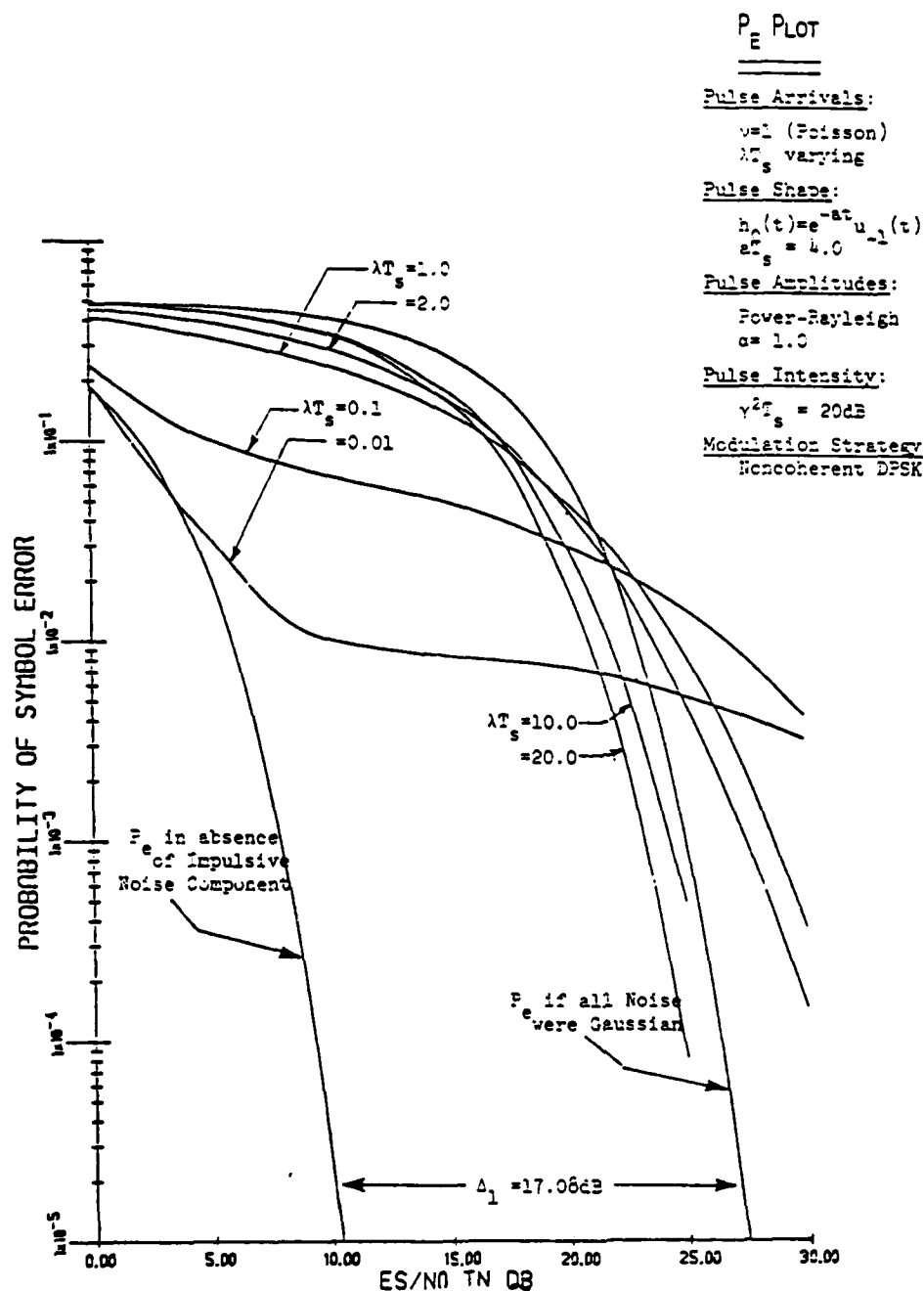
Pulse Arrivals:

$\nu = 1$ (Poisson)

$\lambda T_s = 0.1$

Pulse Shape:

$h_0(t) = e^{-at} u_{-1}(t)$

$aT_s = 2.0$

Pulse Amplitudes:

Power-Rayleigh
Lognormal; α
and V_d varying

Pulse Intensity:

$\gamma^2 T_s = 20$dB

Modulation Strategy:

Coherent BPSK

PROBABILITY OF SYMBOL ERROR

$V_d = 5.0$

$\alpha = 0.5$

$V_d = 15.0$

$\alpha = 0.25$

P$_e$ in absence of
Impulsive Noise
Component

P$_e$ if all Noise
were Gaussian

$A_2 = 20.0$dB

ES/N0 IN DB
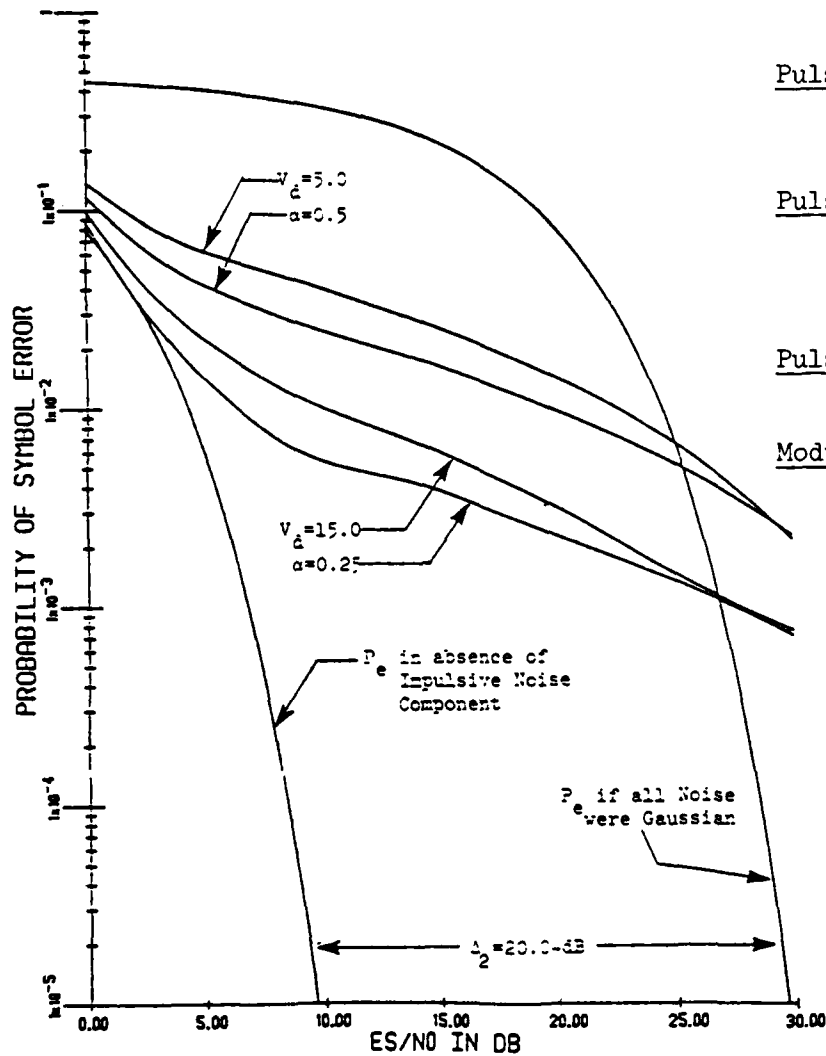
Figure 29

Comparison of P$_e$ Behavior for Linear Matched Filter
Reception with Power-Rayleigh and Lognormal Distri-
buted Pulse Amplitudes under Selected Parameter
Choices; Coherent BPSK Modulation.

4-80

Figure 30

Typical P_e Behavior for Linear Matched Filter Reception as a Function of Pulse Shape $h_0(t)$ for Selected Parameter Choices; Coherent BPSK Modulation.

Figure 31

Typical P_e Behavior for Linear Matched Filter Re-
ception as a Function of ν for Selected Parameter
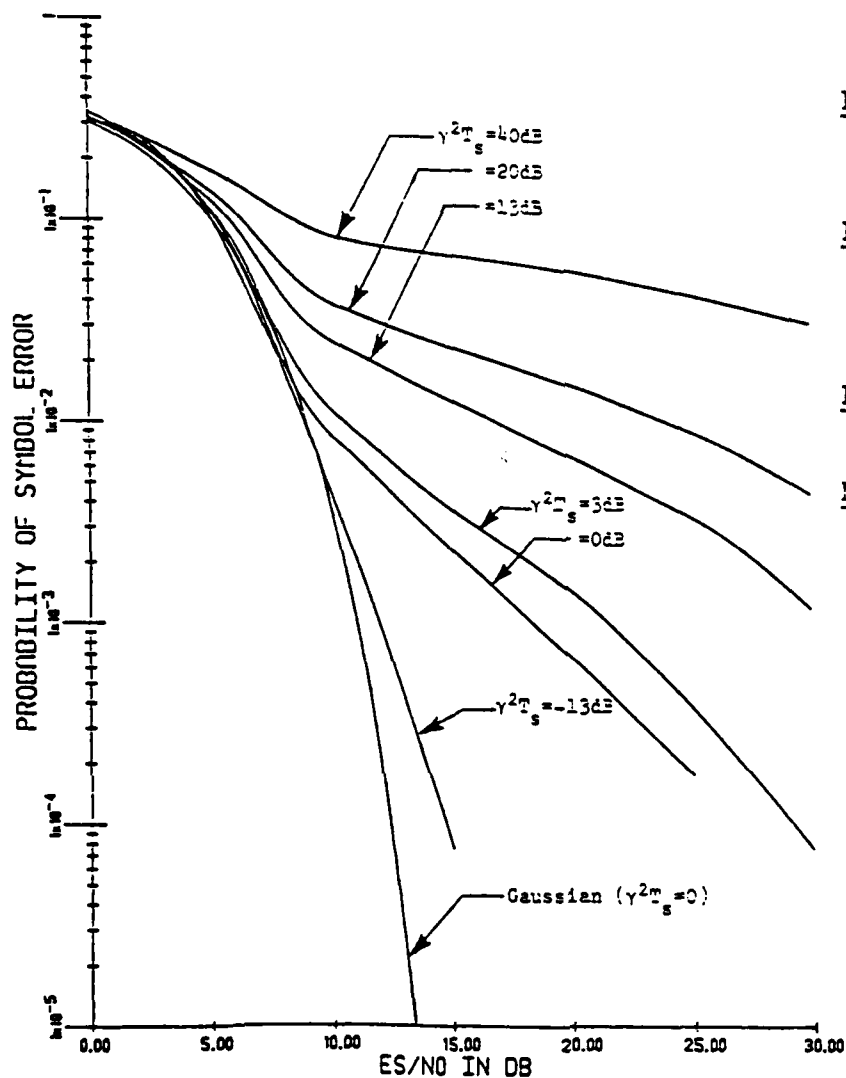Choices; Coherent BPSK Modulation.

4-82

P_E PLOT

Pulse Arrivals:

$\nu = 1$ (Poisson)

$\lambda T_s = 0.1$

Pulse Shape:

$h_0(t) = e^{-at} u_{-1}(t)$

$aT_s = 2.0$

Pulse Amplitudes:

Power-Rayleigh

$\alpha = 0.5$

Pulse Intensity:

$\gamma^2 T_s$ varying

Modulation Strategy:

Various Coherent
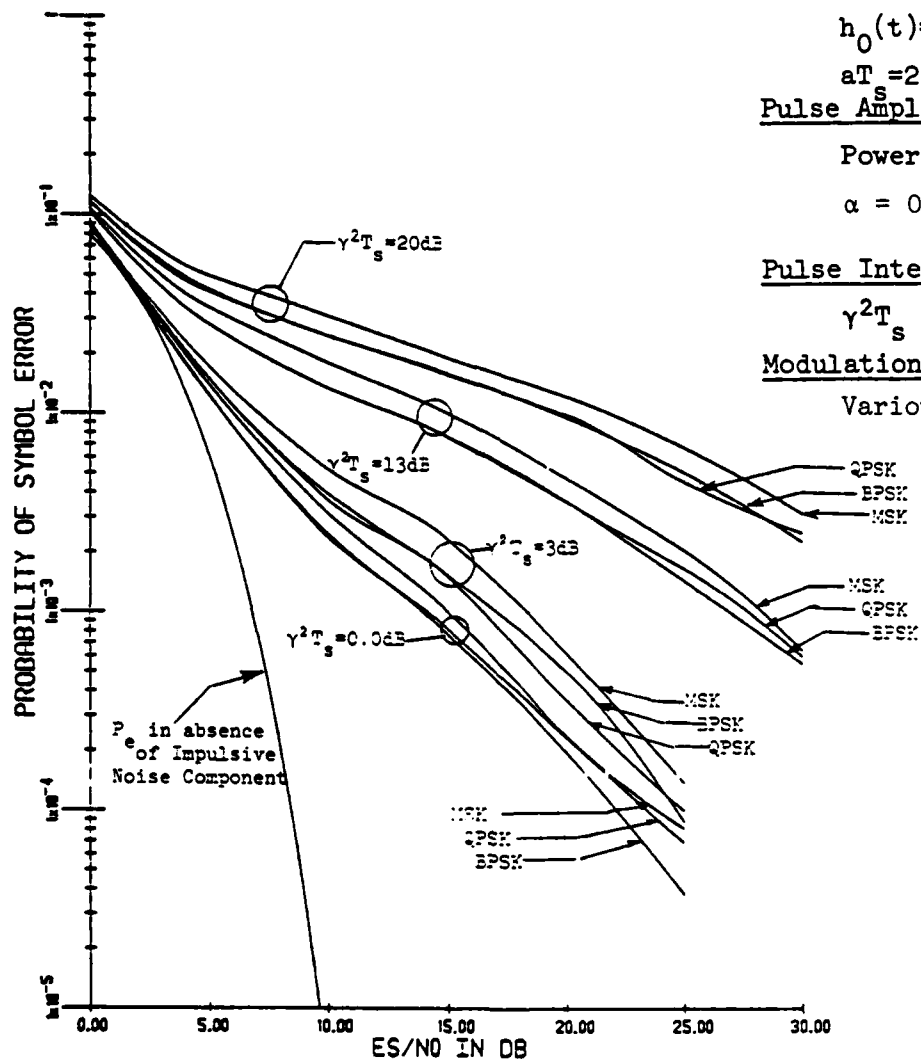
Figure 32

Comparison of P_e Behavior for Various Coherent Modulation Strategies Employing Linear Matched Filter Reception for Selected Parameter Choices.
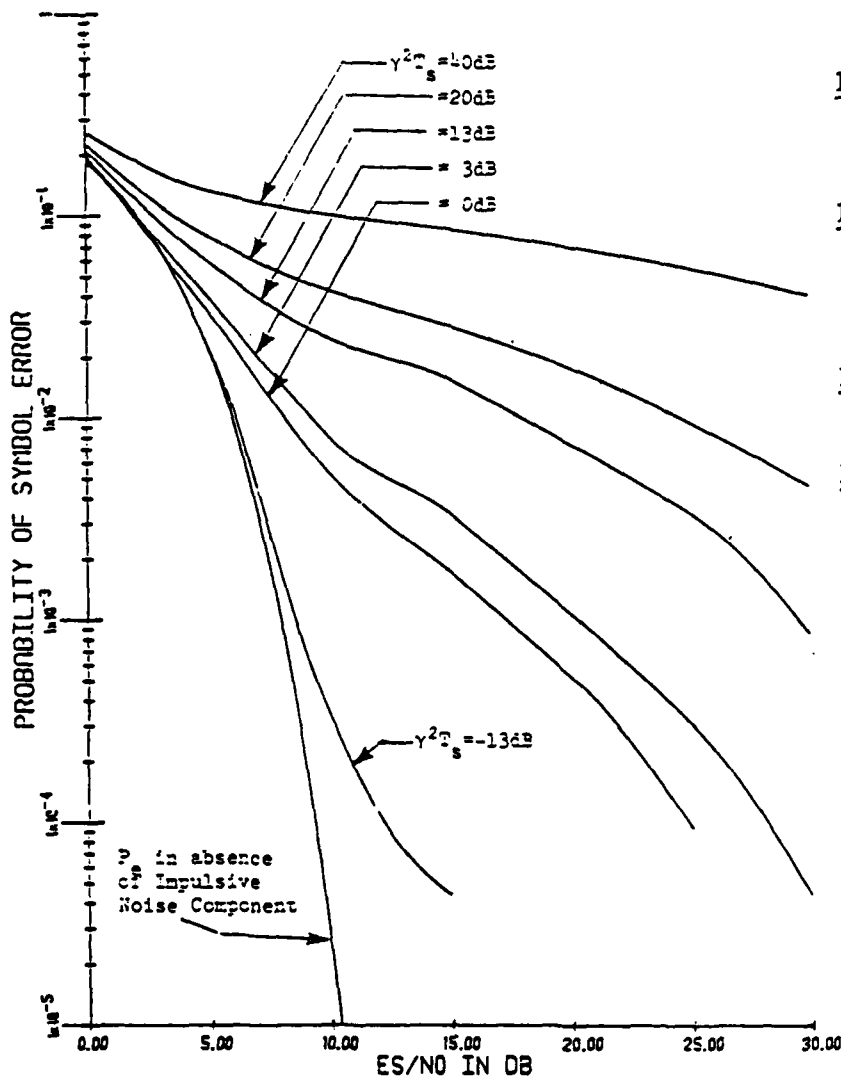
4-83

Figure 33

Typical P_e Behavior for Matched Filter Reception
as a Function of λT_s for Selected Parameter Choices;
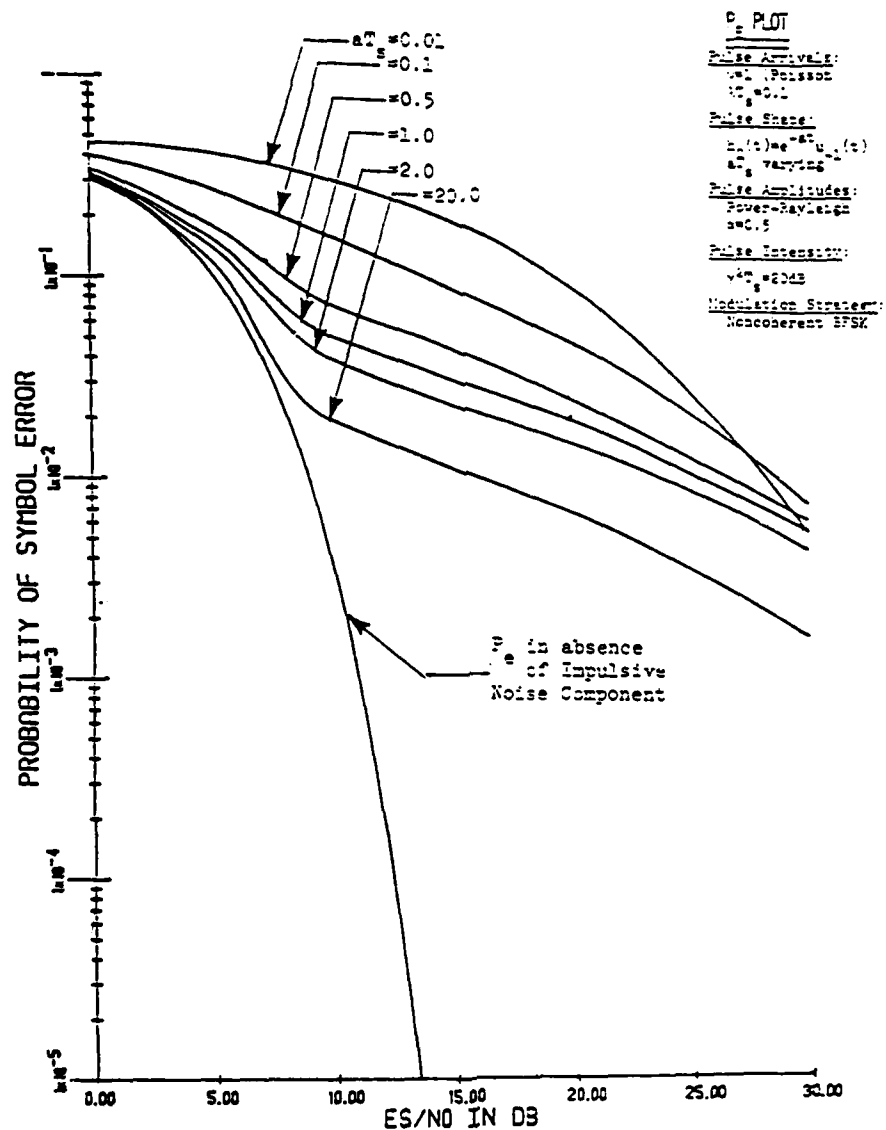Noncoherent BPSK Modulation.

Pulse Arrivals:

ν=1 (Poisson)

λT$_s$ varying

Pulse Shape:

h$_A$(t)=e^{-at}u$_{-1}$(t)

aT$_s$ = 4.0

Pulse Amplitudes:

Power-Rayleigh

α= 1.0

Pulse Intensity:

γ^{2}T$_s$ = 20dB

Modulation Strategy

Noncoherent DPSK

λT$_s$ =1.0

=2.0

λT$_s$ =0.1

=0.01

λT$_s$ =10.0

=20.0

P$_e$ in absence
of Impulsive
Noise Component

P$_e$ if all Noise
were Gaussian

Δ$_1$ =17.08dB

PROBABILITY OF SYMBOL ERROR

1x10^{-1}

1x10^{-2}

1x10^{-3}

1x10^{-4}

1x10^{-5}

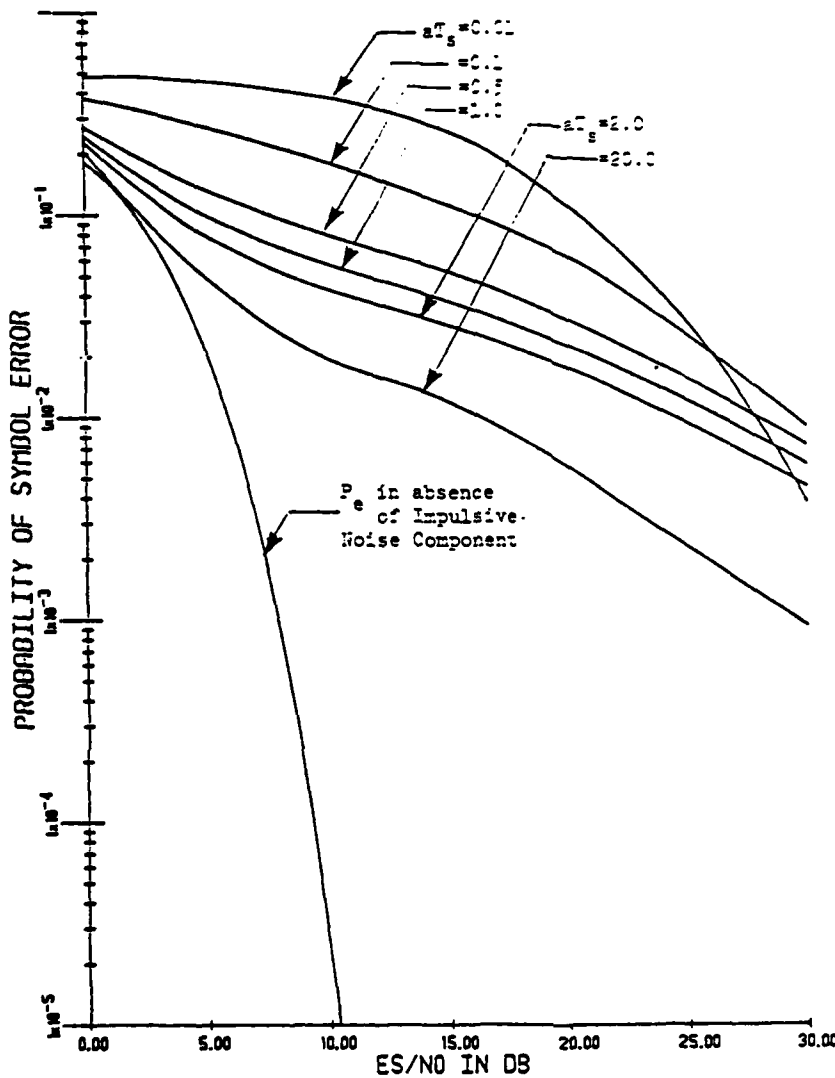0.00   5.00   10.00   15.00   20.00   25.00   30.00

ES/N0 IN DB

Figure 34

Typical P$_e$ Behavior for Matched Filter Reception
as a Function of λT$_s$ for Selected Parameter Choices
Noncoherent DPSK Modulation.

P_E PLOT

Pulse Arrivals:

$\nu = 1$ (Poisson)

$\lambda T_s = 0.1$

Pulse Shape:

$h_0(t) = e^{-at} u_{-1}(t)$

$a T_s = 2.0$

Pulse Amplitudes:

Power-Rayleigh

$\alpha = 0.5$

Pulse Intensity:

$\gamma^2 T_s$ varying

Modulation Strategy:

Noncoherent BFSK

PROBABILITY OF SYMBOL ERROR

$\gamma^2 T_s = 40dB$

$= 20dB$

$= 13dB$

$\gamma^2 T_s = 3dB$

$= 0dB$

$\gamma^2 T_s = -13dB$

Gaussian ($\gamma^2 T_s = 0$)

ES/NO IN DB

Figure 35

Typical P_e Behavior for Matched Filter Reception
as a Function of $\gamma^2 T_s$ for Selected Parameter
Choices; Noncoherent BFSK Modulation.

Figure 36

Typical P_e Behavior for Matched Filter Reception as a Function of $\gamma^2 T_s$ for Selected Parameter Choices; Noncoherent DPSK Modulation.

Figure 37

Typical P_e Behavior for Matched Filter Reception as a Function of aT_s for selected Parameter Choices; Noncoherents BFSK Modulation.
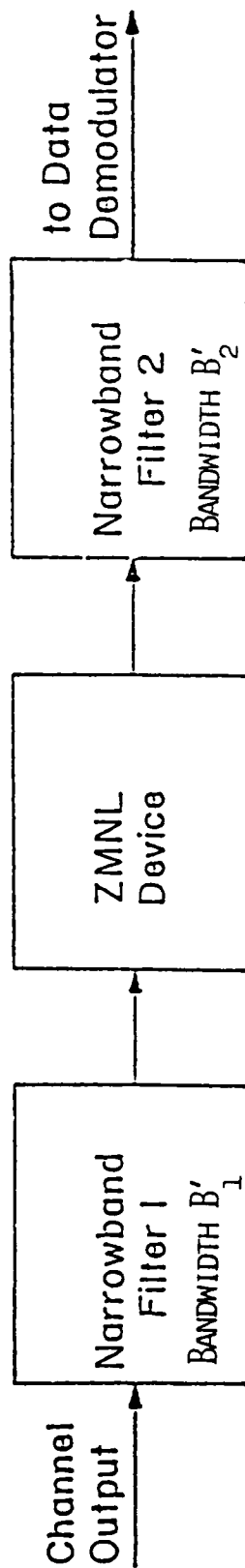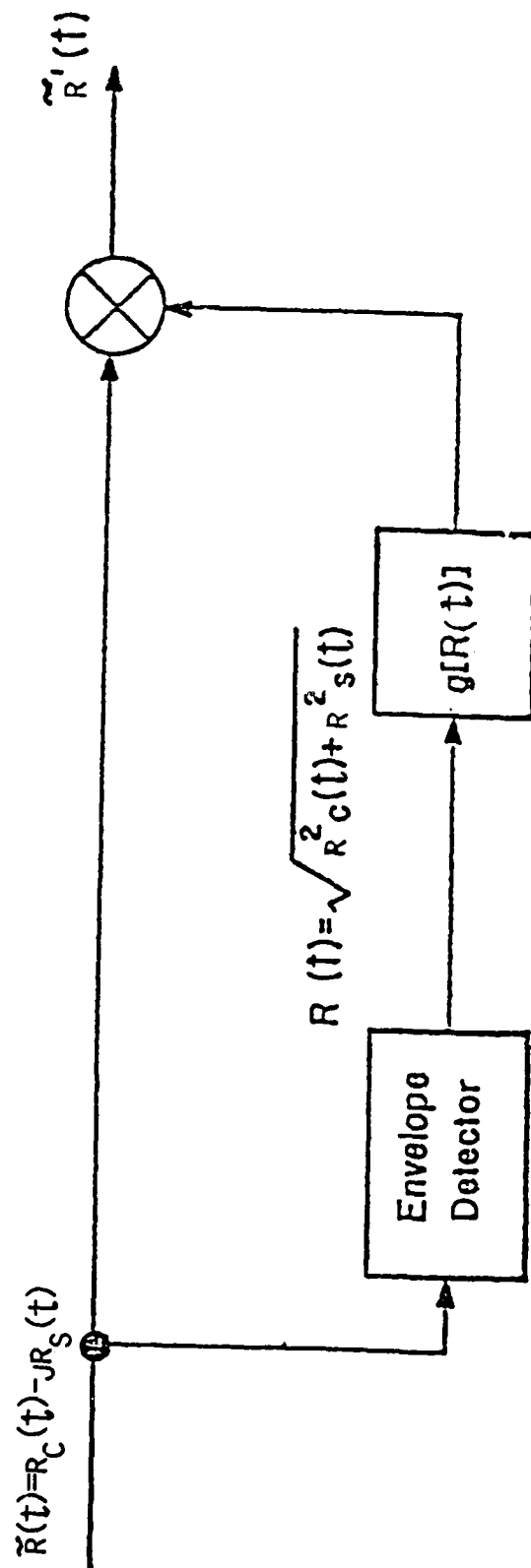
4-83

P_E PLOT

Pulse Arrivals:

$\nu = 1$ (Poisson)

$\lambda T_s = 0.1$

Pulse Shape:

$h_0(t) = e^{-at} u_{-1}(t)$

$aT_s = 2.0$

Pulse Amplitudes:

Power-Rayleigh

$\alpha = 0.5$

Pulse Intensity:

$\gamma^2 T_s = 20dB$

Modulation Strategy:

Noncoherent DPSK

Figure 38

Typical P_e Behavior for Matched Filter Reception as a Function of aT_s for Selected Parameter Choices; Noncoherent DPSK Modulation

Figure 39

Predetection Portion of Receiver

Figure 40

Model for Zero-Memory Nonlinearities of the Limiting Variety.

ZMNL PLOT

Pulse Arrivals:
$\nu = 1$ (Poisson)
$\lambda T_s = 0.1$

Pulse Shape:
$h_0(t) = e^{-at}u_{-1}(t)$
$aT_s = 2.0$

Pulse Amplitudes:
Power-Rayleigh
$\alpha = 1.0$

Pulse Intensity:
$\gamma^2 T_s$ varying

Measurement Bandwidth:
$B'T_s = 16$

$\gamma^2 T_s = 30$

$= 20$

$= 10$

$= 6$

$= 3$

$= 0$

Normalized $\sigma_n^2, \Gamma_{\ell 0}(R)$

Envelope Normalized to RMS Value.
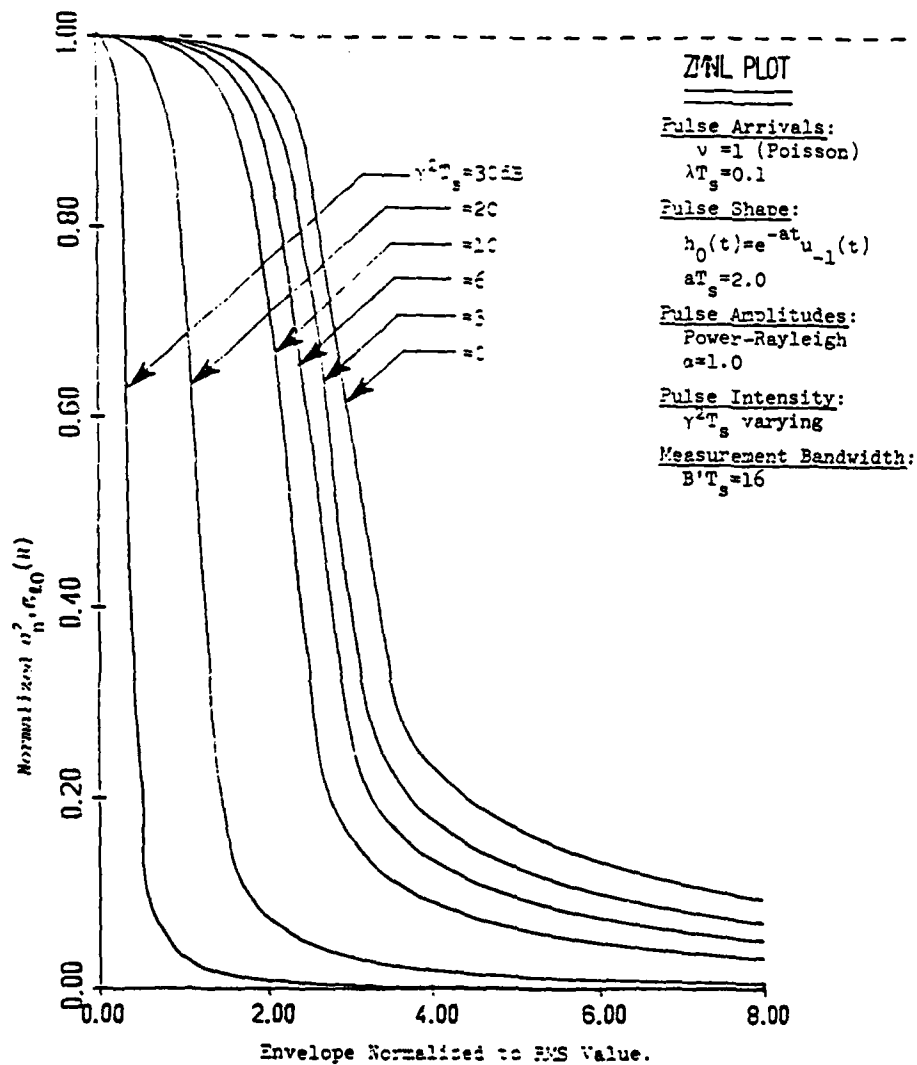
Figure 41

Computed Locally Optimum ZMNL Receiver Characteristic as a Function of $\gamma^2 T_s$ for Selected Parameter Choices.

4-92
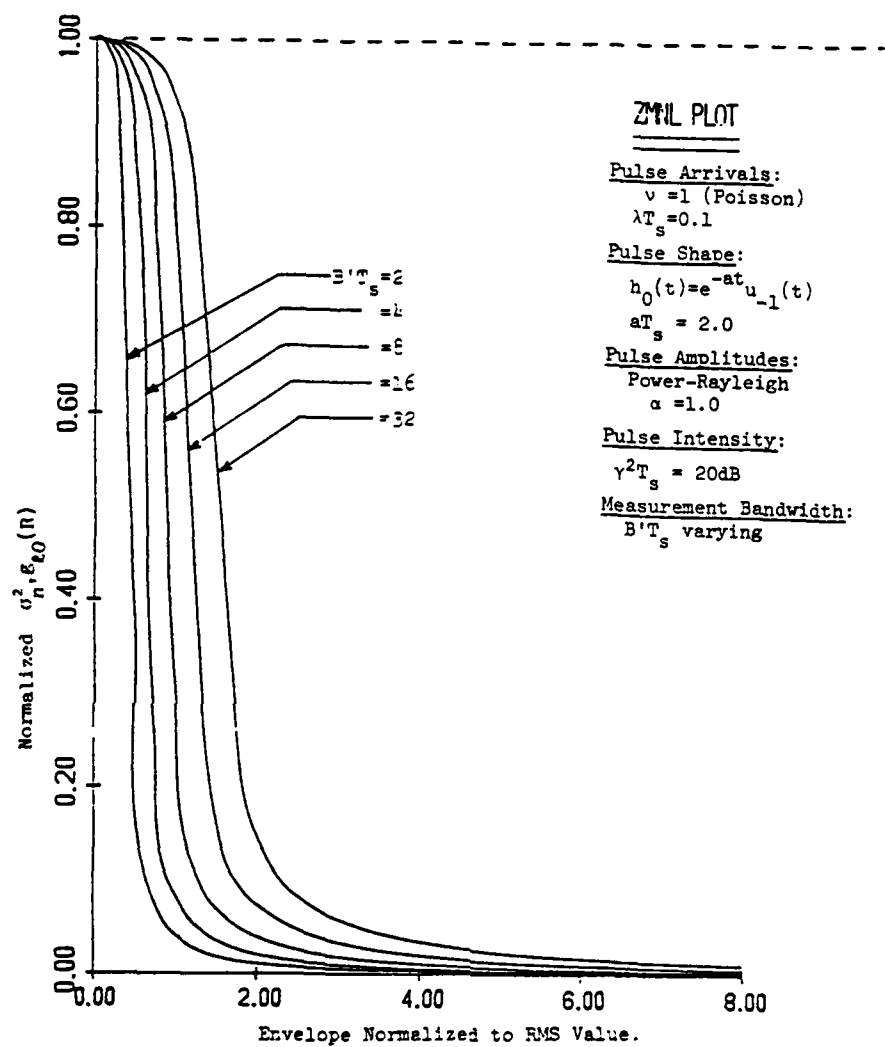
Figure 42

Computed Locally Optimum ZMNL Receiver
Characteristic as a Function of $B'T_s$
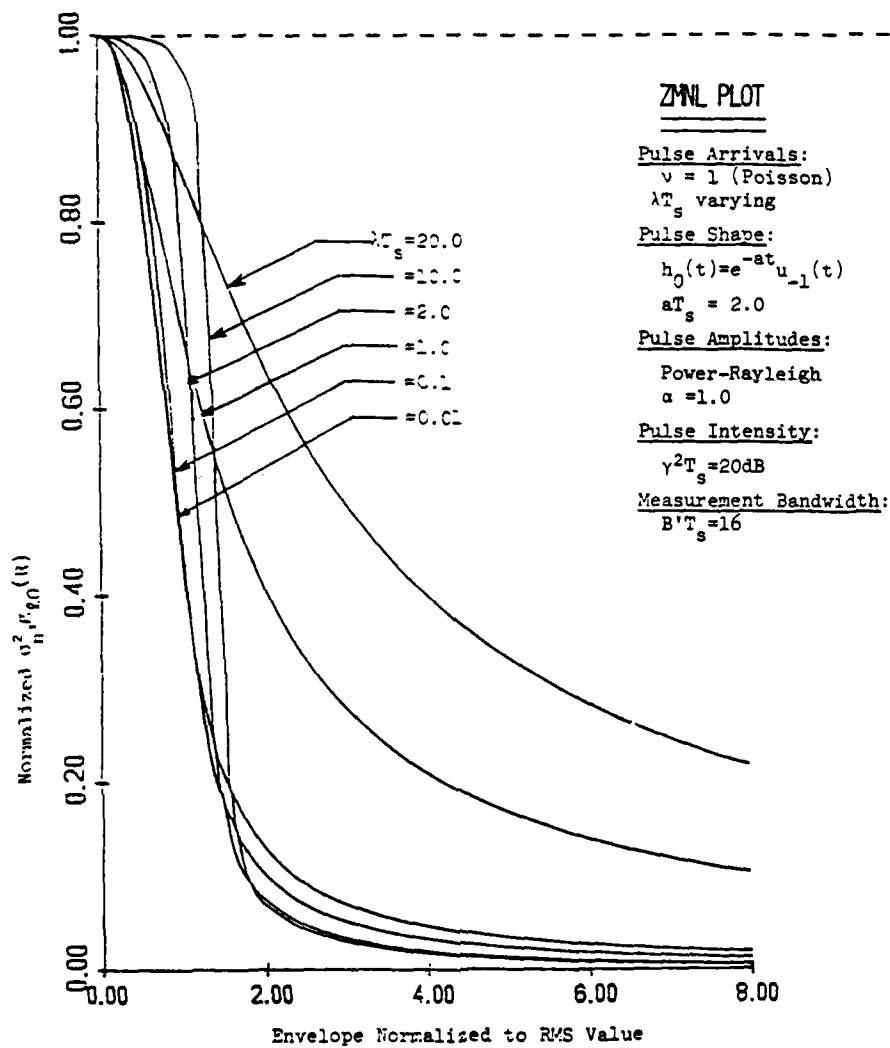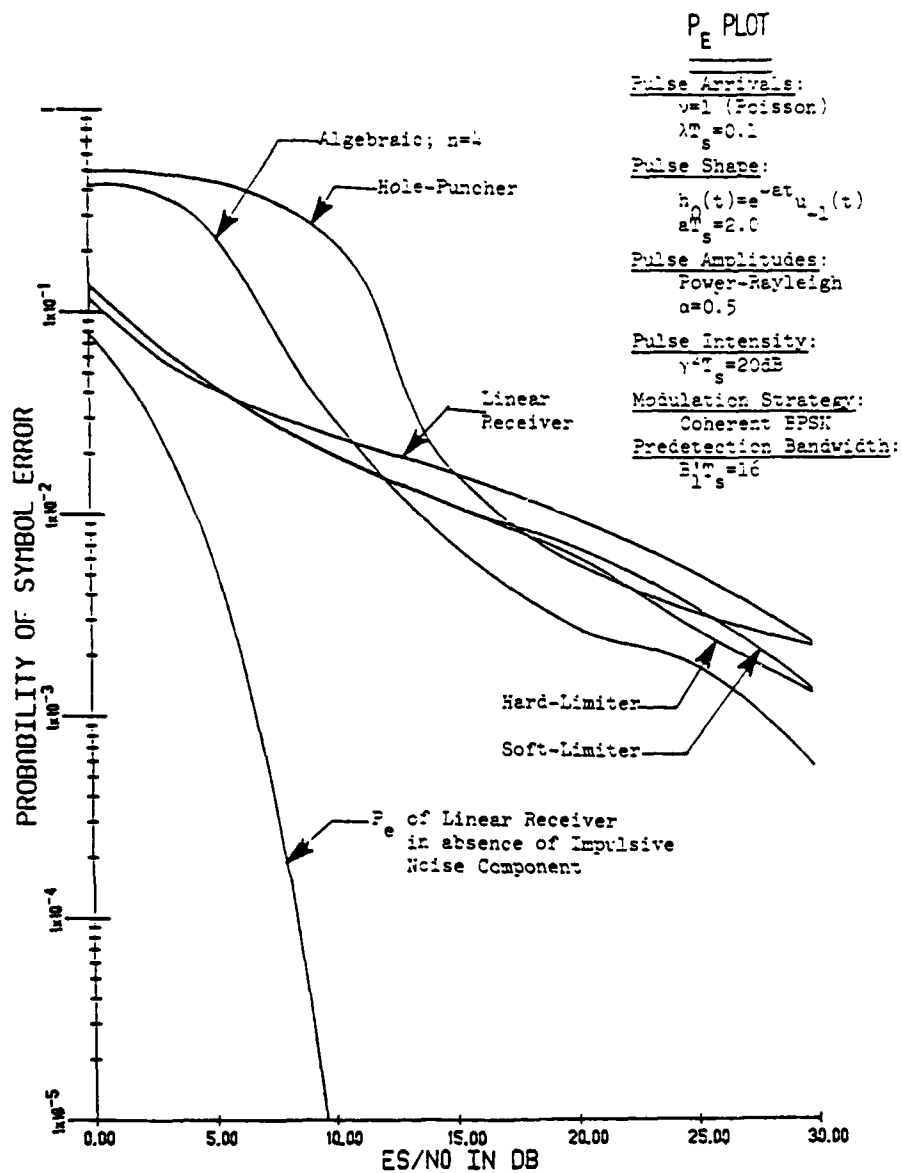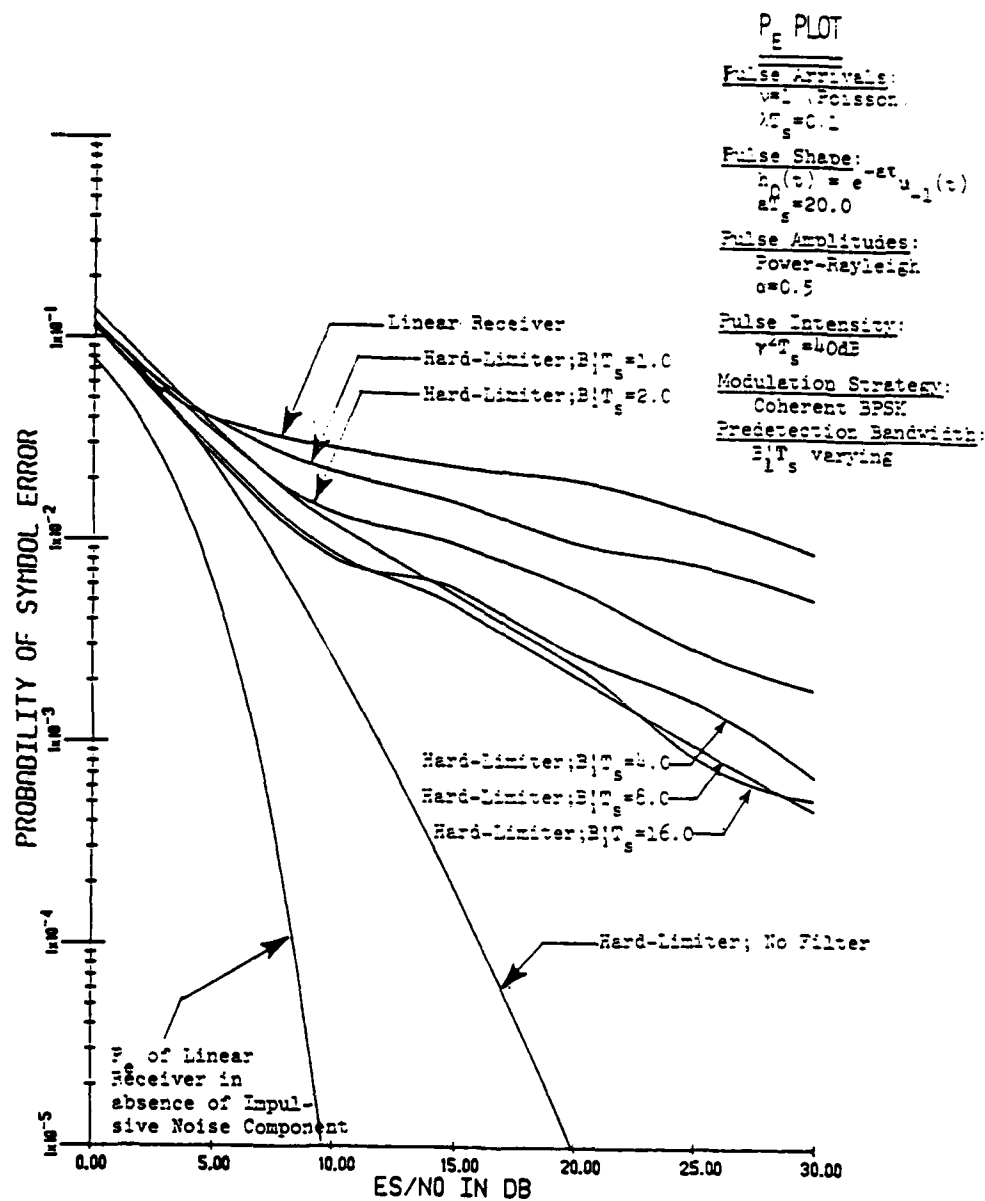for Selected Parameter Choices.

ZMNL PLOT

Pulse Arrivals:
    = 1 (Poisson)
    T_s=0.1

Pulse Shape:
    $h_0(t)=e^{-at}u_{-1}(t)$
    aT_s varying

Pulse Amplitudes:
    Power-Rayleigh
    =1.0

Pulse Intensity:
    T_s=20dB

Measurement Bandwidth:
    $B'T_s$=16

aT_s=0.01
=0.1
=1.0
=2.0
=10.0
=20.0

Normalized $\sigma_n^2 F_{20}(R)$

Envelope Normalized to RMS Value
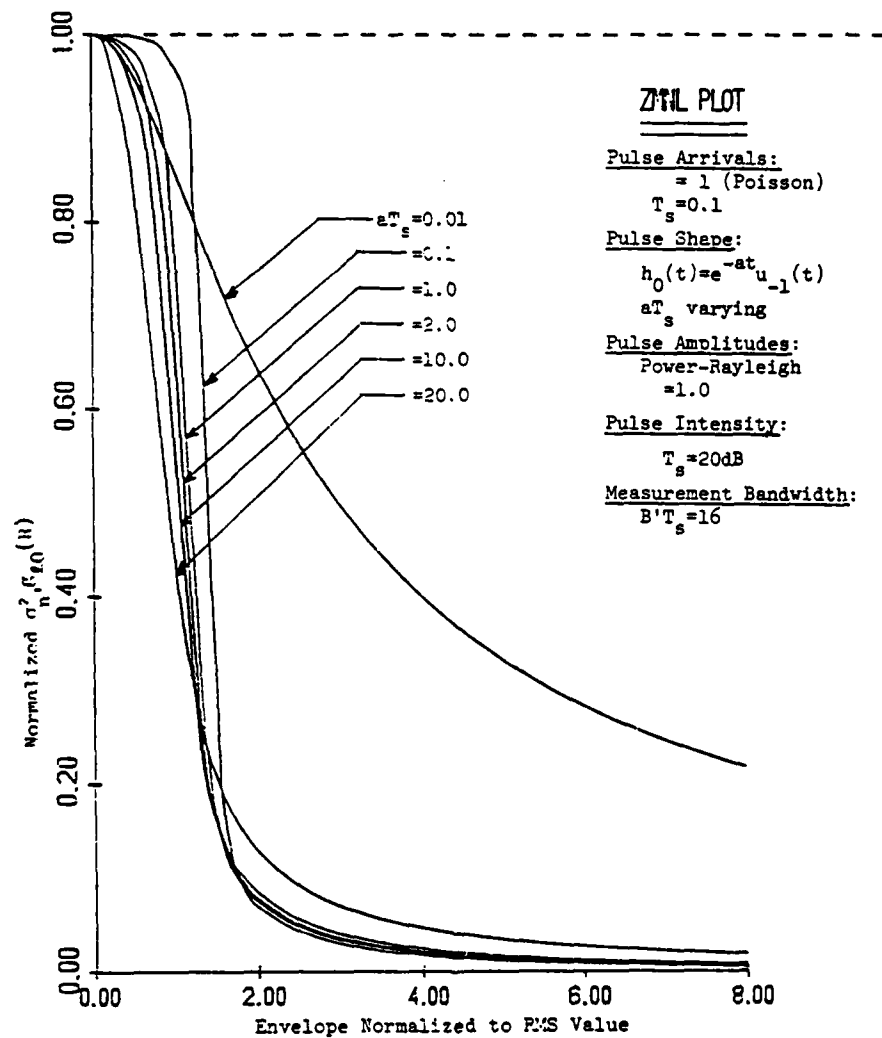
Figure 43

Computed Locally Optimum ZMNL Receiver
Characteristic as a Function of aT_s for
Selected Parameter Choices.

4-94

ZMNL PLOT

Pulse Arrivals:
  $\nu = 1$ (Poisson)
  λT_s varying

Pulse Shape:
  $h_0(t) = e^{-at} u_{-1}(t)$
  $aT_s = 2.0$

Pulse Amplitudes:
  Power-Rayleigh
  $\alpha = 1.0$

Pulse Intensity:
  $\gamma^2 T_s = 20$ dB

Measurement Bandwidth:
  $B'T_s = 16$

Figure 44

Computed Locally Optimum ZMNL Receiver
Characteristic as a Function of λT_s for
Selected Parameter Choices.

Figure 45

Typical P_e Behavior for Selected Linear and
Nonlinear Receiver Structures; Coherent BPSK
Modulation; Clip Levels 0dB Above Signal Level.

4-96

Figure 46

Typical P_e Behavior as a Function of Predetection Bandwidth $B_1^! T_s$ for Selected Parameter Choices; Coherent BPSK Modulation; Hard-Limiter Receiver.
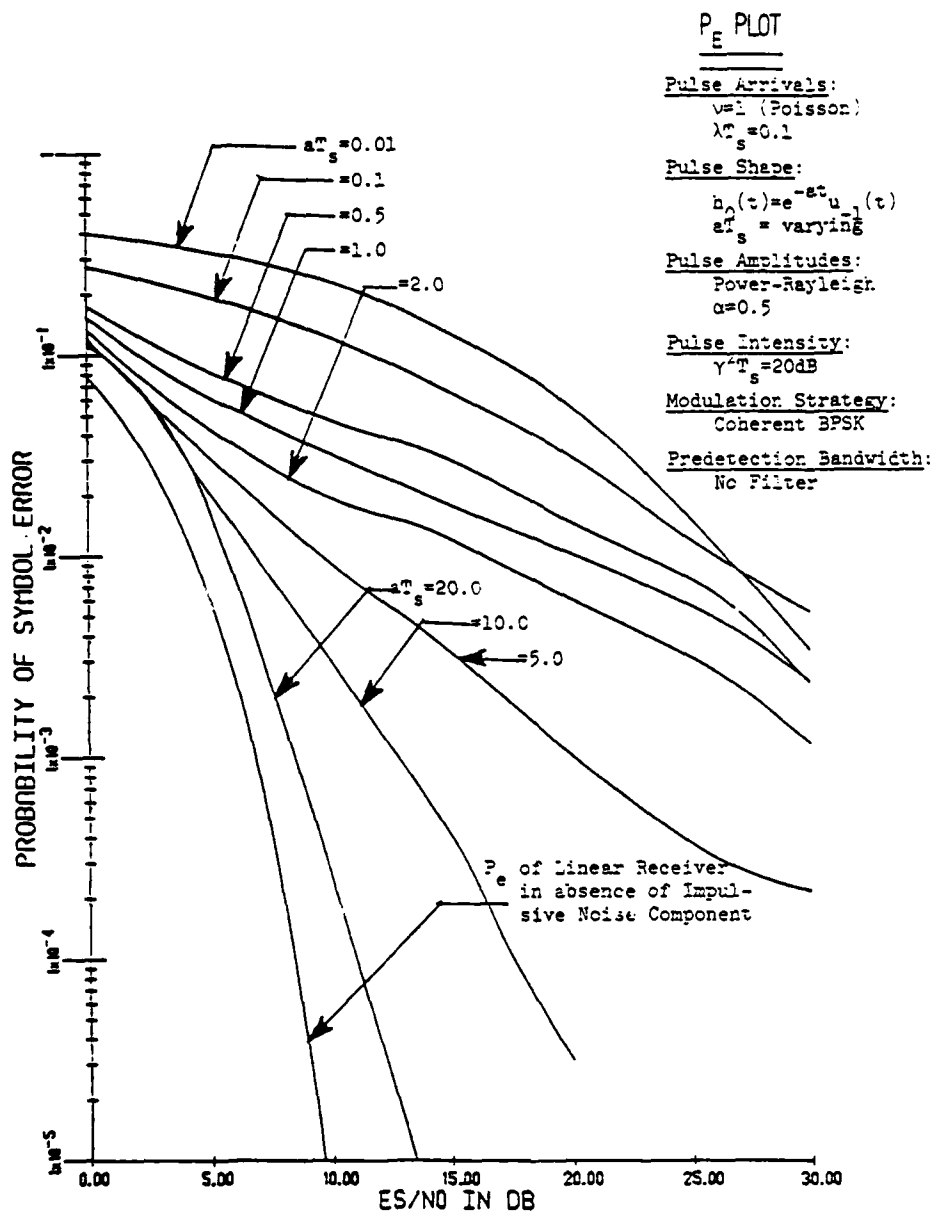
Figure 47

Typical P_e Behavior as a Function of aT_s for
Selected Parameter Choices; Coherent BPSK
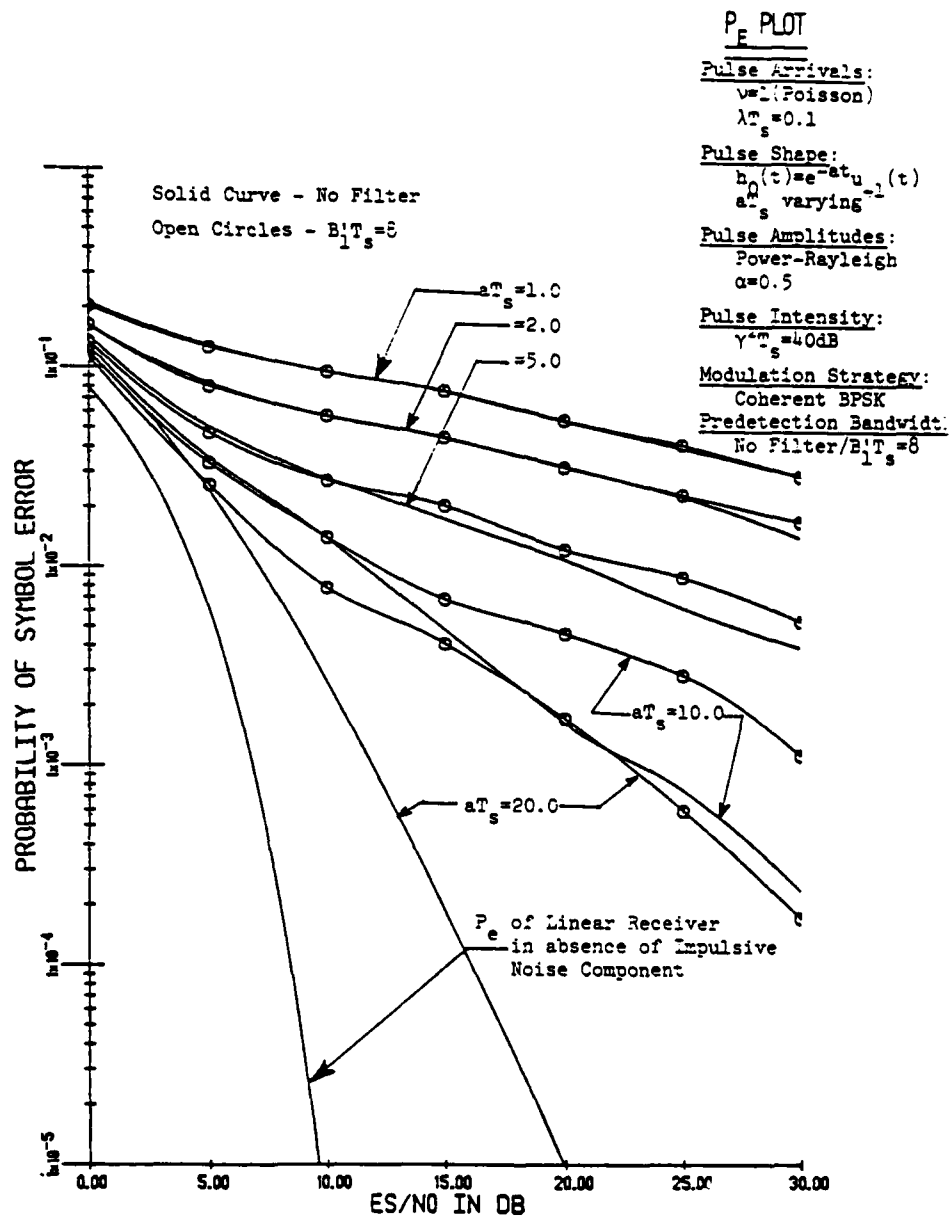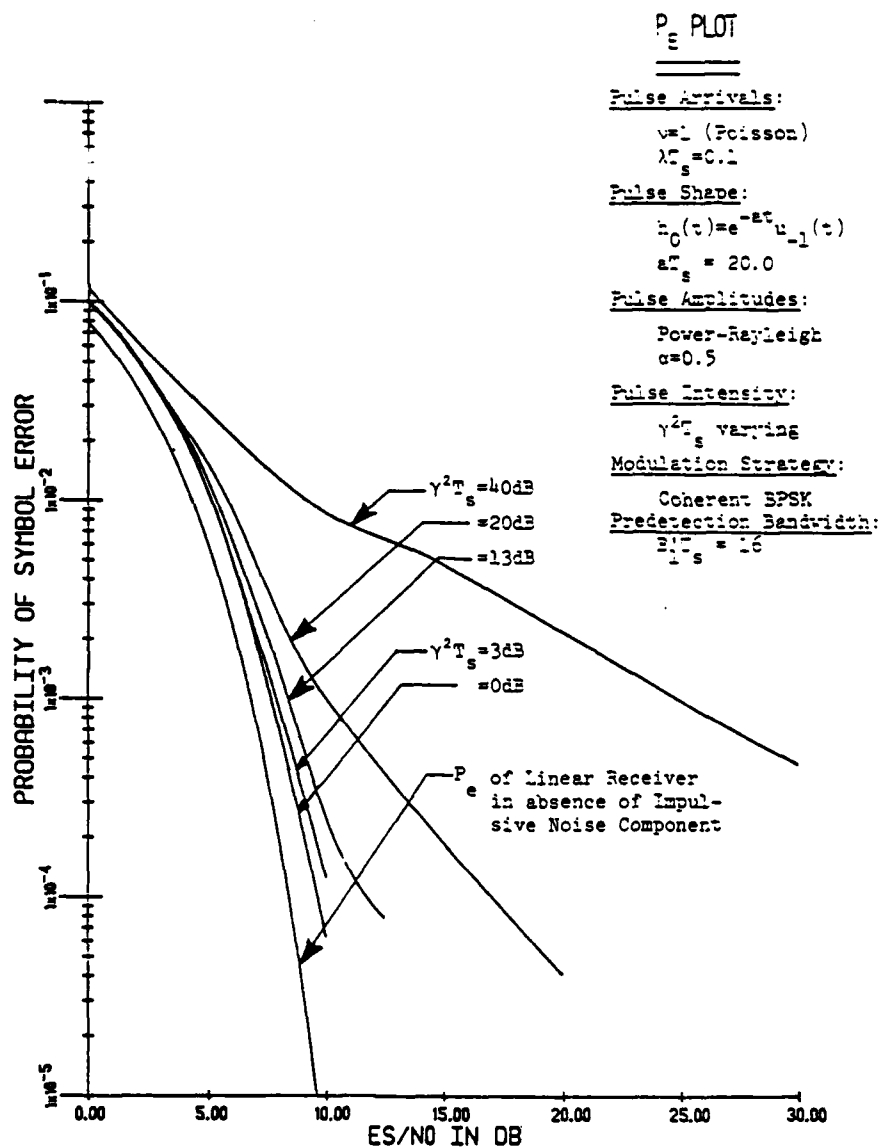Modulation; Hard-Limiter Receiver; No Pre-
Detection Filtering.

Figure 48

Typical P_e Behavior as a Function of aT_s both
with and without Predetection Filter; Coherent
BPSK Modulation; Hard-Limiting Receiver.

Figure 49

Typical P_e Behavior as a Function of $\gamma^2 T_s$ for
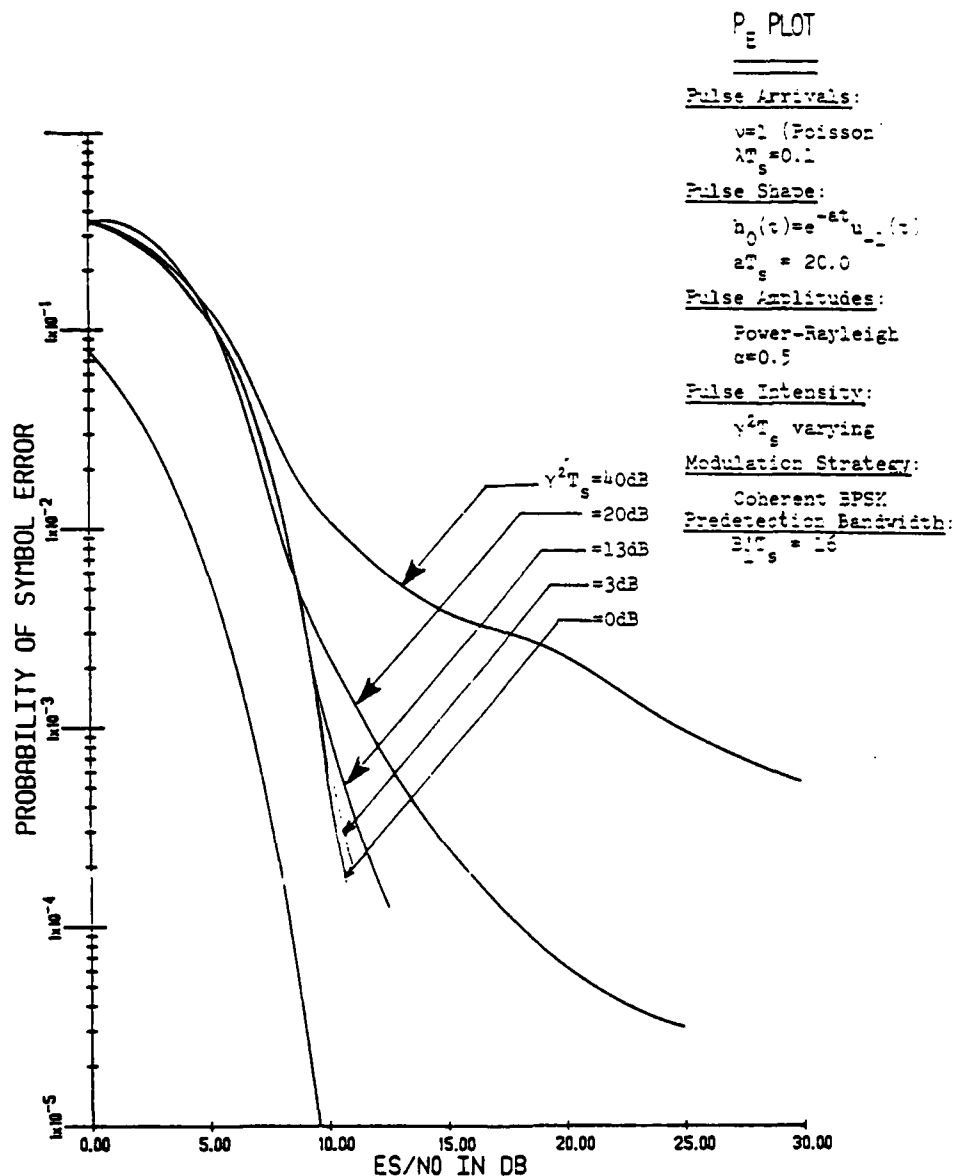Selected Parameter Choices; Coherent BPSK
Modulation; Hard-Limiter Receiver.

Pulse Arrivals:

v=1 (Poisson)
$\lambda T_s = 0.1$

Pulse Shape:

$h_0(t) = e^{-at} u_{-1}(t)$

$a T_s = 20.0$

Pulse Amplitudes:

Power-Rayleigh
$\alpha = 0.5$

Pulse Intensity:

$\gamma^2 T_s$ varying

Modulation Strategy:

Coherent BPSK

Predetection Bandwidth:

$B^T_s = 10$

PROBABILITY OF SYMBOL ERROR

$\gamma^2 T_s = 40dB$

$= 20dB$

$= 13dB$

$= 3dB$

$= 0dB$

ES/NO IN DB

Figure 50

Typical P_e Behavior as a Function of $\gamma^2 T_s$ for
Selected Parameter Choices; Coherent BPSK
Modulation; Algebraic Nonlinear Receiver, n=4,
Clip Level 0dB above Signal Level.

4-101

PART V

INCORPORATION OF ADAPTIVE ARRAY PROCESSING CAPABILITIES

INTO THE INTERACTIVE COMMUNICATION SIMULATOR

I. Introduction:

The analysis and design of digital communication systems has historically focused upon strictly temporal processing. In an increasing number of important applications, however, it is clear that some form of spatial processing is desirable. The spatial processing may be used to steer a beam in the direction of the desired transmitter or to place a null in the direction of an interfering transmitter. Here the interference may be deliberate electronic countermeasures (ECM) or jamming, or unintentional radio-frequency interference (RFI).

A number of systems have been developed or proposed which utilize some form of spatial processing in addition to the conventional temporal processing associated with typical digital communication receivers. However, there has been no systematic and comprehensive study of the subtle interactions between spatial and temporal processing structures in an attempt to identify the tradeoffs and develop an optimum basis for rational design of digital communication systems subject to spatially distributed interference. Part of the difficulty lies in the intractability of a strictly analytical approach. Specifically, although optimum spatial/temporal receiver structures can be determined under precise, and sometimes restrictive, modeling assumptions, the error probability performance of these structures is difficult to analyze. Furthermore, the effects of deviations from modeling assumptions is difficult to establish. Finally, the performance evaluation of suboptimum, and presumably less complex and more robust, processing structures is often hopelessly complicated. As a result, some form of simulation facility is required as an adjunct to ongoing analytical investigations.

In the present report we provide an explicit description of how adaptive array spatial processing structures are to be incorporated into the existing temporal processing capabilities of the RFI Interactive Communications Simulator (ICS). The ICS [1] is an extensive hardware/software system which has been configured to allow realistic simulation of a variety of military, space, and commercial point-to-point communication links with provision for flexible future expansion. The important system design considerations in developing this simulation capability is discussed and the choice of important parameters is described. Also described is the manner in which this capability is to be utilized in ongoing research on digital communications in spatially distributed interference channels. It is expected that this additional spatial processing capability will significantly enhance the usefulness of the ICS as a simulation tool.

In Section II we describe the channel signal and noise modeling assumptions. This is followed by a description of adaptive array processing structures and their incorporation into the ICS in Section III. In Section IV we discuss some future simulation studies to be undertaken. Finally, in Section V we provide a summary and conclusions.

II. Preliminaries:

In what follows we will make extensive use of complex narrowband representations of all signal and noise processes. Specifically, the received signal at the output of the i'th element is given by

$$r_i(t) = \sqrt{2} \, \text{Re}\{\tilde{r}_i(t) e^{j2\pi f_c t}\} \; ; \; i=1,2,\ldots, N \; , \tag{1}$$

where f_c is an <u>assumed known</u> carrier frequency in Hz, and $\tilde{r}_i(t) = r_{ci}(t) - j r_{si}(t)$ is the corresponding complex envelope expressed in terms of lowpass waveforms
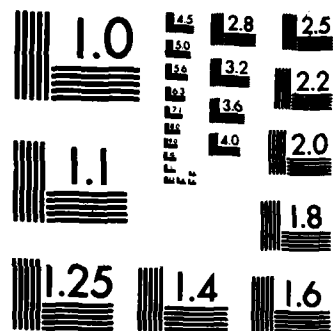
MICROCOPY RESOLUTION TEST CHART
NATIONAL BUREAU OF STANDARDS-1963-A

$r_{ci}(t)$ and $r_{si}(t)$ representing the inphase and quadrature (I/Q) components, respectively. The complex envelope is furthermore assumed of the form

$$\tilde{r}_i(t) = \tilde{s}_{0i}(t) + \tilde{y}_{0i}(t) + \tilde{w}_i(t); \quad i=1,2,\ldots,N, \tag{2}$$

where $\tilde{s}_{0i}(t)$ is the complex envelope of the received signal component at the output of the i'th element, $\tilde{y}_{0i}(t)$ is the complex envelope of the corresponding interference component, and $\tilde{w}_i(t)$ is a complex zero-mean additive white Gaussian noise (AWGN) component. Specifically, $\tilde{w}_i(t) = w_{ci}(t) - jw_{si}(t)$ with $w_{ci}(t)$, $w_{si}(t)$ mutually independent WGN processes each possessing double-sided noise spectral density $N_0/2$ watts/Hz.

The signal component $\tilde{s}_{0i}(t)$ is assumed of the form

$$\tilde{s}_{0i}(t) = \int_{-\infty}^{\infty} \tilde{s}(\tau)\tilde{h}_i(t,\tau)d\tau \; ; \quad i=1,2,\ldots,N, \tag{3}$$

where $\tilde{s}(t)$ is the transmitted signal as it would be received at the output of an ideal isotropic sensor[+] located at the origin of spatial coordinates and excited only by the incident signal field. The quantity $\tilde{h}_i(t,\tau)$ represents the complex spatial/temporal impulse response of the i'th sensor where it is implicitly assumed that the transmitter/sensor geometry is known a priori. Similarly, we assume that

$$\tilde{y}_{0i}(t) = \sum_{j=1}^{J} \int_{-\infty}^{\infty} \tilde{y}_j(t)\tilde{h}_{ij}(t,\tau)d\tau \; ; \quad i=1,2,\ldots,N, \tag{4}$$

where $\tilde{y}_j(t)$ represents the output of an ideal isotropic sensor to the j'th interference source, $j=1,2,\ldots,J$ and $\tilde{h}_{ij}(t,\tau)$ represents the complex impulse response of the i'th sensor to the j'th interference source. Again we assume the quantities $\tilde{h}_{ij}(t,\tau)$, $i=1,2,\ldots,N$; $j=1,2,\ldots,J$ can be described, if only in a statistical sense, given the interferer/sensor geometry.

+ An ideal isotropic sensor is defined as a sensor having unit response to signals incident from all directions and all frequencies.

While the complex spatial/temporal impulse responses $\tilde{h}_{i,j}(t,\tau)$, $i=1,2,$ $\ldots,N,j=0,1,2,\ldots,J$ may be random as well as time varying,[†] we will be specifically interested in the case where these quantities are deterministic time-invariant quantities given the transmitter/interferer/sensor geometry. That is, $\tilde{h}_{ij}(t,\tau)=h_{ij}(t-\tau)$. For example, in the case of a pur time delay of τ_{ij} seconds we have $h_{ij}(t)=\delta(t-\tau_{ij})e^{-j2\pi f_c \tau_{ij}}$. The delta function accounts for the group delay associated with the complex envelope while the complex exponential accounts for the corresponding phase shift of the carrier. It follows from (2) that

$$\tilde{s}_{0i}(t)=\{s_c(t-\tau_{i0})\cos2\pi f_c\tau_{i0}-s_s(t-\tau_{i0})\sin2\pi f_c\tau_{i0}\}$$
$$-j\{s_s(t-\tau_{i0})\cos2\pi f_c\tau_{i0}+s_c(t-\tau_{i0})\sin2\pi f_c\tau_{i0}\} . \qquad (5)$$

If B_0 represents the bandwidth[††] of the signal component $\tilde{s}(t)$ then for the cases of interest in what follows it will always be assumed that $B_0\tau_{i0}\ll1$, $i=1,2,\ldots,$ N. It follows that $\tilde{s}(t-\tau_{i0})\approx\tilde{s}(t)$ so that

$$s_{0i}(t)=\{s_c(t)\cos2\pi f_c\tau_{i0}-s_s(t)\sin2\pi f_c\tau_{i0}\}$$
$$-j\{s_s(t)\cos2\pi f_c\tau_{i0}+s_c(t)\sin2\pi f_c\tau_{i0}\} , \qquad (6)$$

and the terms within braces represent the corresponding I/Q components, respectively. Similarly, the interfering signal component in (4) can be expressed as

$$\tilde{y}_{0i}(t) = \sum_{j=1}^{J} [\{y_{cj}(t)\cos2\pi f_c\tau_{ij}-y_{sj}(t)\sin2\pi f_c\tau_{ij}\}$$
$$-j\{y_{sj}(t)\cos2\pi f_c\tau_{ij}+y_{cj}(t)\sin2\pi f_c\tau_{ij}\}] , \qquad (7)$$

where the terms in braces again represent the corresponding I/Q components. Thus, realization of the signal and noise models merely require specification

---

† For notational convenience we represent $\tilde{h}_i(t,\tau)$ as $\tilde{h}_{i0}(t,\tau)$ allowing concise treatment of all complex impulse response functions.

†† Actually, in what follows we assume that B_0 is the double-sided equivalent rectangular bandwidth in Hz.

of the signal complex envelope $\tilde{s}(t)$, the statistics of the interfering signals $\tilde{y}_j(t)$, $j=1,2,\ldots,J$ and the signal/interferer/sensor geometry as embodied by the delays τ_{ij}, $i=1,2,\ldots,N$, $j=0,1,2,\ldots,J$.

We assume that the signals of interest are described as in [1]. Specifically, we restrict attention to digital signalling formats such that $\tilde{s}(t)$ has the representation

$$\tilde{s}(t) = \sqrt{\frac{E_s}{T_s}} \sum_i [C_{1,i} u_c(t-2^k i T_s - \tau) + j C_{2,i} u_s(t-2^k i T_s - \tau)] e^{j\theta} . \tag{8}$$

Here, depending upon the modulation strategy employed, $u_c(t)$ and $u_s(t)$ are appropriately defined baseband waveforms modulating the I/Q rails. Similarly, the quantities $C_{1,i}, C_{2,i}$ depend upon the binary (i.e.,± 1) data sequence[†] $\{x_i\}$ to be transmitted in a manner specific to the modulation strategy in use. The quantity $\underline{k}$ in (8) assumes the values 0 or 1, with the choice k=1 generally corresponding to the case of staggered overlapping baseband waveforms as in MSK. Finally, the quantities τ and θ in (8) are, in general, random timing epoch and phase offset, respectively. An important part of ongoing research efforts will be the development of appropriate schemes for acquiring and tracking symbol synchronization and carrier phase in the presence of spatially distributed interference. A summary of present modulation capabilities in the ICS and their representation in the form (8) is provided in Table 1.

Finally, the class of interferring signals $\tilde{y}_j(t)$, $i=1,2,\ldots,J$ of interest will typically be burst or impulsive noise processes at specified geometrical locations relative to the origin of spatial coordinates, although we will also consider the case of continuous-wave (CW) interference. In the former case

---

† The sequence $\{x_i\}$ actually represents the output of the channel encoder.

we model $y_j(t)$, $j=1,2,\ldots,J$ as a complex low-density shot noise process as described in detail in Part IV. Specifically, the parameters describing the burst or impulsive noise model are specified for each of the J interferers. An important parameter in each case will be the quantity

$$\gamma_j^2 = \frac{E\{|\tilde{y}_j(t)|^2\}}{N_0} \quad ; \quad j=1,2,\ldots,J \quad , \tag{9}$$

or equivalently $\gamma_j^2 T_s$, which represents the power in the j'th interferer normalized to that of the AWGN component when measured in a double-sided noise bandwidth equal to the baud rate $f_s=1/T_s$. At any rate, the signal power relative to the power from the j'th interferer is then

$$\frac{P_s}{P_j} = \frac{E_s/T_s}{E\{|\tilde{y}_j(t)|^2\}} = \frac{E_s/N_0}{\gamma_j^2 T_s} \quad ; \quad j=1,2,\ldots,J \quad , \tag{10}$$

so that knowing E_s/N_0 and the dimensionaless parameter $\gamma_j^2 T_s$ allows explicit evaluation of the signal-to-interference ratio (SIR). In coded systems it is the quantity E_b/N_0 which serves as the independent variable with $E_s=RE_b$. Here E_b is the energy per information bit and R is the code rate in information bits transmitted per channel use. It follows that the SIR for the j'th interferer is then

$$\frac{P_s}{P_j} = \frac{R(E_b/N_0)}{\gamma_j^2 T_s} \quad ; \quad j=1,2,\ldots,J \quad . \tag{11}$$

A number of pulse shapes are presently available in the ICS for simulating burst or impulsive noise. This will be modified to include Gaussian bursts as well as pulsed CW. It is also intended to provide a continuous Gaussian interference capability as well as CW at a specified off set from the carrier.

In the latter case the interference signal has complex envelope of the form

$$\tilde{y}_j(t) = \sqrt{P_j} \; e^{j2\pi f_j t} \; ; \quad j=1,2,\ldots,J \; , \tag{12}$$

where P_j is the corresponding signal power, and f_j is the frequency offset in Hz. Actually the normalized quantity $f_j T_s$, which is the offset normalized to the baud rate, will be specified. The interference power will now be adjusted for a specified value of $\gamma_j^2 T_s$ where now

$$\gamma_j^2 = \frac{P_j}{N_0} \; ; \quad i=1,2,\ldots,J \; . \tag{13}$$

The SIR is then given by (10) for uncoded systems and by (11) for coded systems.

III. Adaptive Array Simulation:

The signal and interference models have been described in the preceding section. In the present section we describe the adaptive array processing structures to be studied both analytically and through simulation as part of ongoing research efforts. We assume that the appropriate array element outputs are generated as illustrated in Fig. 1. Here the modulation type, E_s/N_0 and transmitter filtering parameters are chosen exactly as in the present ICS. The choice of channel models now includes; AWGN, impulsive, and fading/dispersive channel. To this we will add a fourth option to be called spatially distributed interference channel. As indicated in Fig. 1 the user must then supply the array parameters, the signal location and the interference parameters. We describe each of these quantities separately.

Array Parameters: Here we must specify the number N of elements as well as their location with respect to a phase center or origin of spatial coordinates. We intend to restrict attention to linear arrays consisting of no more than

$N=8$ elements. The location of each element with respect to the origin will be specified in terms of the distance d' in units of the wavelength λ_c at the assumed carrier frequency. The elements will all be assumed omnidirectional

Signal Location: We assume that the signal location is specified as the angle θ_s with respect to broadside as illustrated in Fig. 2. The appropriate element delays τ_{i0} are then easily calculated as

$$\tau_{i0} = \pm \frac{d_i'}{f_c} \sin\theta_s \quad ; \quad i=1,2,\ldots,N , \qquad (14)$$

where the proper algebraic signs must be chosen depending upon which side of the phase center the element lies. The phase factors $\theta_{i0} \overset{\Delta}{=} 2\pi f_c \tau_{i0}$ in (6) can then be computed as $\theta_{i0} = \pm 2\pi d_i' \sin\theta_s, i=1,2,\ldots,N$ in a convenient form independent of the underlying carrier frequency.

Interference Parameters: We intend to limit consideration to no more than $J=4$ interference signals. For each interferer then we must first specify the direction θ_j with respect to broadside as illustrated in Fig. 2. This then allows evaluation of the phase factors $\theta_{ij} \overset{\Delta}{=} 2\pi f_c \tau_{ij}$ in (7) to be computed as $\theta_{ij} = \pm 2\pi d_i' \sin\theta_j, i=1,2,\ldots,N, j=1,2,\ldots,J$. Then the interference type must be chosen. Here the following options will be provided:

1. CW
2. Continuous Gaussian
3. Pulsed CW
4. Gaussian Burst
5. Impulsive Noise

For example, in the case of impulsive noise, as described in Part IV of this report, we must specify the following quantitites:

a. <u>Pulse Arrivals</u>: The parameter ν_j specifying the randomness of pulse arrivals and the quantity $\lambda_j T_s$ specifying pulse arrival rate.

b. <u>Pulse Shape</u>: The quantity $h_{0_j}(t)$ specifying pulse shape as well as the quantity $a_j T_s$ specifying pulse duration.

c. <u>Pulse Amplitudes</u>: Here we must specify the distribution of pulse amplitudes and any scale parameters required.

d. <u>Pulse Intensity</u>: Here we must specify the quantity $\gamma^2 T_s$ representing the interference power to background noise power.

In each of the other choices of interference component similar parameters must be specified as discussed previously in Part IV.

Having discussed how the element outputs are to be generated, we now discuss how these outputs are to be processed in an adaptive fashion. The generic receiver structures to be considered in this study are illustrated in Fig. 3. Here the element outputs $\tilde{r}_i(t)$, $i=1,2,\ldots,N$ are applied as input to a weighting network which adaptively combines these inputs to produce the complex signal $\tilde{r}(t)$. The weighting is performed under control of an appropriately defined adaptive algorithm. We intend to incorporate a variety of adaptive algorithms into the ICS. This will include:

1. The least mean-square (LMS) algorithm

2. The generalized signal-to-noise ratio (GSNR) algorithm.

3. The maximum likelihood (ML) algorithm.

In the case of the LMS algorithm, for example a reference input $d(t)$ is required to develop an error signal $\tilde{e}(t) = \tilde{r}(t) - \tilde{d}(t)$. We propose obtaining this in either of two ways. In the first, called the patched reference mode, we assume a "cheater" line is available from the transmitter so that the reference can be taken as the actual

5-10

transmitted signal, i.e., $\tilde{d}(t)=\tilde{s}(t)$. In the second mode, called the decision-directed mode, the desired signal is obtained through a decision feedback scheme. Here the array output $\tilde{r}(t)$ is processed in a temporal receiver which includes possible predetection processing, matched filtering and possibly error-control decoding. The output decisions, labeled $\hat{a}_i$ in Fig. 3, are accepted as correct and passed through a channel model which is a local replica of the channel encoder and modulator/transmitter cascade including any a priori known signal filtering and/or distortion mechanisms. The output of this model $\hat{\tilde{s}}(t)$ is then an estimate of the actual transmitted signal and in this mode we choose $\tilde{d}(t)=\hat{\tilde{s}}(t)$. This same type of decision-directed processing can be applied to other adaptive algorithms as well and will be thoroughly investigated in the course of ongoing research efforts.

The weighting network in Fig. 3 will be assumed of the form illustrated in Fig. 4. Here the element outputs are first processed in a spatial corr-ection filter which consists of a bank of phase shifters. The phase shift introduced on the i'th branch is the negative of $\theta_{i0}=\pm2\pi d_i'\sin\theta_s$, i=1,2,...,N which was the phase shift experienced by the signal component at angle θ_s as intercepted by the i'th element. The spatial correction filter then merely provides the conjugacy condition to point the array in the direction of the known signal direction. In Fig. 4, the frequency dependent weighting network is represented by a bank of linear filters with system transfer func-tion $H_i(j\omega)$,i=1,2,...,N. Actually, we will assume that these filters are of fixed structure defined in terms of a finite and possibly complex-valued parameter vector $\underline{c}_i$ so that, in particular, $H_i(j\omega)=H(j\omega;\underline{c}_i)$ where the

filtering function $H(j\omega;\tilde{c})$ is known for a fixed value of $\tilde{c}$. It is the parameter vectors $\tilde{c}_i$, i=1,2,...,N which are controlled by the adaptive algorithm. We will be particularly interested in the case where the filters take the form of a tapped delay line or transversal filter as illustrated in Fig. 5. Here the parameters $\tilde{c}_i$, i=1,2,...,N represent the tap weights and as illustrated in Fig. 5 the parameter vector $\tilde{c}^T=(\tilde{c}_1,\tilde{c}_2,...,\tilde{c}_L)$ is of dimension L while L-1 delay elements of T seconds each is required. The resulting transfer function is of the form

$$H(j\omega;\tilde{c}) = \tilde{c}_1+\tilde{c}_2 e^{-j\omega T}+\tilde{c}_3 e^{-j2\omega T}+....\tilde{c}_L e^{-j(L-1)\omega T}$$
$$= \sum_{\ell=1}^{L} \tilde{c}_\ell e^{-j(\ell-1)\omega T} \qquad (15)$$

In our work we will restrict attention to a number of weights no more than L=7. Define the weight vector $\tilde{w}$ then as a concatenation of the $\tilde{c}_i$ vectors such that

$$\tilde{w} = \begin{bmatrix} \tilde{c}_1 \\ \hline \tilde{c}_2 \\ \hline \vdots \\ \vdots \\ \hline \tilde{c}_N \end{bmatrix} \qquad , \qquad (16)$$

which is then of dimension NL. Under the limits imposed previously, this dimension can be no greater than 56, although use of much smaller dimensions will generally be the case. Similarly, if we define the complex L-vectors as $\tilde{x}_i^T(t)=(x_i(t),x_i(t-T),...,x_i(t-(L-1)T))$ and then the NL-vector $\tilde{x}(t)$ as

$$\tilde{x}(t)= \begin{bmatrix} \tilde{x}_1(t) \\ \hline \tilde{x}_2(t) \\ \hline \vdots \\ \vdots \\ \hline \tilde{x}_N(t) \end{bmatrix} \qquad , \qquad (17)$$

the array output $\tilde{r}'(t)$ can then be written as

$$\tilde{r}'(t) = \underline{\tilde{w}}^T \underline{\tilde{x}}(t) \quad . \tag{18}$$

The linear weighting of elements of the vector $\underline{\tilde{x}}(t)$ is then in a form such that standard adaption algorithms can be applied. Finally, we note from Fig. 5 that the actual array output $\tilde{r}(t)$ is a linearly filtered version of $\tilde{r}'(t)$. This post-array filtering could clearly have been incorporated into the pre-detection filtering section of the temporal receiver in Fig. 3. We have chosen to place it here to provide some possible noise filtering before applying this to the adaptive algorithm as indicated in Fig. 3. This filtering can be implemented using existing filtering capabilities of the ICS.

It should be noted at this time that there is no unequivocal guidance in choosing the tap delays in the tapped-delay line filter. Specifically, if B_0 is the double-sided equivalent rectangular bandwidth of the signal $\tilde{s}(t)$ in Hz we would expect that the sampling interval T should satisfy $T \leq 1/2B_0$ and since $B_0 T_s > 1$ this would imply that $T/T_s \leq 1/2$, or a delay no greater than half a baud period. In the existing ICS structure it is convenient to take $T/T_s = 1/2^k$ for some $k \geq 1$ to be specified by the user. This provision will then be provided as a user option otherwise the default condition k=1 will be assumed.

In the preceding we have basically described how the DESIGN Mode of the ICS is to be modified to allow incorporation of an adaptive array processing capability. We now describe how the other operating modes are to be modified. We describe the VALIDATION AND SIMULATION Modes separately.

VALIDATION MODE: At present we have three classes of waveform plotting options; baseband waveforms, channel waveforms, and synchronization waveforms. Within these existing options we will add the option of plotting the prefiltered

array output $\hat{r}'(t)$ as well as the actual array output $\hat{r}(t)$ under the channel waveform category. Actually, the ability to plot $\hat{r}(t)$ is already available and presently labeled "channel output" so this presents no difficulties. Similarly, under the synchronization waveform category it is desirable to add the provision for plotting an estimate of the instantaneous SIR as a function of time and/or snapshots of the instantaneous array spatial pattern. This information would provide some understanding of the "spatial synchronization" properties of the array together with the more conventional time and/or phase synchronization. Since we propose updating the weights no faster than at the baud rate[†] it is not clear that enough data can be collected in the VALIDATION Mode to demonstrate any significant convergence characteristics. This information can best be collected in the much faster SIMULATION Mode and is described in somewhat more detail below. Nevertheless, we will attempt to definitively establish the feasibility of collecting and displaying this information in the VALIDATION Mode since we feel this would be useful for demonstration purposes.

SIMULATION MODE: Here we will be primarily interested in collecting data on symbol error probability P_e and bit error probability P_b in terms of the parameters of the spatially distributed interference channel as well as those of the adaptive array. We will also be interested in more detailed error statistics such as the error-free gap distribution, the Gallager burst statistic, etc. Fortunately this capability already exists in the ICS so this presents no difficulty.

---

† It would appear that to update the weights any faster would produce undesirable signal modulation which would degrade the overall error probability.

It should be noted that the error statistics described in the preceding are obtained by averaging over all modes of the interference and are not exclusively concerned with the transient behavior of the adaptive array as is most work in this area. For impulsive or burst interference character- istics the latter approach simply does not make sense since the adaptive array is generally in a transient state, depending, of course, on the number of interferers and their respective pulse arrival rate. For purely CW or continuous Gaussian interference, on the other hand, the transient behavior of the adaptive array might well be a matter of legitimate concern, although quite pheripheral to the operating error characteristics of the digital communications link. In this case we propose allowing the array to adapt first during an initial acquisition or training period of specified duration during which no error statistics are collected. The weights can then either be frozen at the end of the acquisition period or allowed to continue adapt- ing into the tracking period during which error statistics are collected. An acquisition period will also be provided for impulsive or burst inter- ference although in this case it makes no sense to freeze the weights at the end of this period. The user will be allowed the option of either the patched reference or decision-directed adaptive adjustment mode during either the acquisition or tracking modes. This is entirely consistent with the present structure and operating usage of the ICS and should present little problem in implementation.

Finally, as mentioned previously, we would like to have the ability to plot the instantaneous SIR as a function of time and/or plot snapshots of the instantaneous array pattern. We propose collecting data, to allow

subsequent plotting in the ANALYSIS Mode, of the SIR at multiples of the
array update rate. This can be calculated from knowledge of the instant-
aneous array weight vector and the signal/interference/sensor scenario,
although this is yet to be worked out. Similarly, snapshots of the array
pattern can be calculated from the instantaneous weight vector. These
will likewise be available for display in the ANALYSIS Mode at specified
multiples of the array update weight. A specific scheme for accomplishing
this will be developed and reported upon at some later time.

IV. Research Directions:

The incorporation of an adaptive array processing capability into the
ICS is not to be considered an end in itself but rather to provide a com-
prehensive and flexible simulation tool as an adjunct to parallel analytical
efforts. In this section we describe some initial research directions which
are expected to make extensive use of the ICS in this capacity. These initial
research directions will include the following:

1. Uncoded System Performance: We will be specifically
   interested in the operating error probability per-
   formance of uncoded digital communication systems
   for various signal/interference/sensor scenarios.
   Of particular interest will be impulsive or burst
   interference channels. While the SIR and total SNR
   are easily calculated these quantities do not deter-
   mine error rates in non-Gaussian interference environ-
   ments. Explicit calculation of error rates for special
   cases may be possible but exceedingly tedious and
   simulation results will prove quite useful. We expect
   that nonlinear predetection processing in the temporal

receiver will be required to mitigate the effects of non-Gaussian interference bursts. Experience has indicated that broadband spatial nulls will be required if spatial filtering is to be effective in this environment. We will be particularly interested in uncovering any particular sensitivities of specific modulation strategies to spatially distributed interference.

2. Coded System Performance: We expect that the most efficacious solution to minimizing the effect of spatially distributed interference will consist of a judicious combination of adaptive spatial filtering and either error-control and/or spread-spectrum coding. In impulsive or burst interference channels we expect that the new low-rate convolutional code constructions described in Part III and will prove particularly effective. Similarly, for block codes the reduced complexity soft-decision decoding algorithms in Part II should prove useful. These features, together with a limited spread-spectrum capability, are presently being incorporated into the ICS and some preliminary results for single-element reception are reported in Part I. It is expected that these results will provide useful insight in the adaptive multi-element case. At any rate, some combination of predetection and/or postdetection nonlinear processing is expected to be required in the temporal receiver.

3. Adaptive Algorithms: As noted previously, various adaptive algorithms will be investigated for their suitability in this application. Of particular interest will be the performance in impulsive or burst noise environments. For example, should some

type of performance monitor be provided to sense the presence or absence of interference and allow array adaption only when believed present? How should a performance monitor be implemented? Are specific adaptive algorithms particularly sensitive to spatially distributed interference of the impulsive or burst variety? These and other questions are to be thoroughly explored.

4. Behavior of Ancillary Systems: A number of ancillary systems such as bit synchronizers and phase trackers are required as part of a functioning digital communications receiver. Our interest will be in investigating the behavior of these ancillary systems in the presence of spatially distributed interference and adaptive array processing. Alternative design strategies which provide more robust performance in this environment will be developed and investigated through simulation. The results should prove useful in the development of integrated spatial/temporal processor for digital communications in spatially distributed interference channels.

V. Summary and Conclusions:

We have provided an outline of how an adaptive array processing capability can be incorporated into the existing ICS and have described some initial research directions that will make extensive use of this capability. The structure described here, with appropriate modification as required, will be incorporated into the ICS as part of ongoing efforts. Explicit documentation, as well as simulation results will be reported at frequent intervals.

5-18

References

1. J. W. Modestino, K. R. Matis, K. Y. Jung, and A. L. Vickers, "Design and Implementation of the Interactive Communications Simulator (ICS)", RADC-TR-81-37, April 1981.

Modulation	$C_{1,i}$	$C_{2,i}$	$u_c(t)$	$u_s(t)$	Remarks
BPSK	x_i	0	$u_0(t)$	0	$x_i=\pm 1$
DPSK	$x_i C_{1,i-1}$	0	$u_0(t)$	0	$x_i=\pm 1$, $C_{1,0}$ assumed known
BFSK	$e^{j\theta_i}$	$x_i e^{j\theta_i}$	$\cos(\Delta\omega t/2)u_0(t)$	$\sin(\Delta\omega t/2)u_0(t)$	$x_i=\pm 1$, $\Delta\omega=2\pi\ell/T$, θ_i - i.i.d. uniform
QPSK	x_{2i}	x_{2i+1}	$(1/\sqrt{2})u_0(t)$	$(1/\sqrt{2})u_0(t)$	$x_i=\pm 1$, $E_s=2E_b$
MSK	x_{2i}	x_{2i+1}	$\cos(\pi t/2T_s)u_0'(t)$	$\sin(\pi t/2T_s)u_0'(t-T_s)$	$x_i=\pm 1$, I/Q waveforms repeated every $2T_s$ sec.

Note: $u_0(t)$ and $u_0'(t)$ are defined in text.

Table 1

Representations of Some Typical Digital Modulation Formats

Figure 1

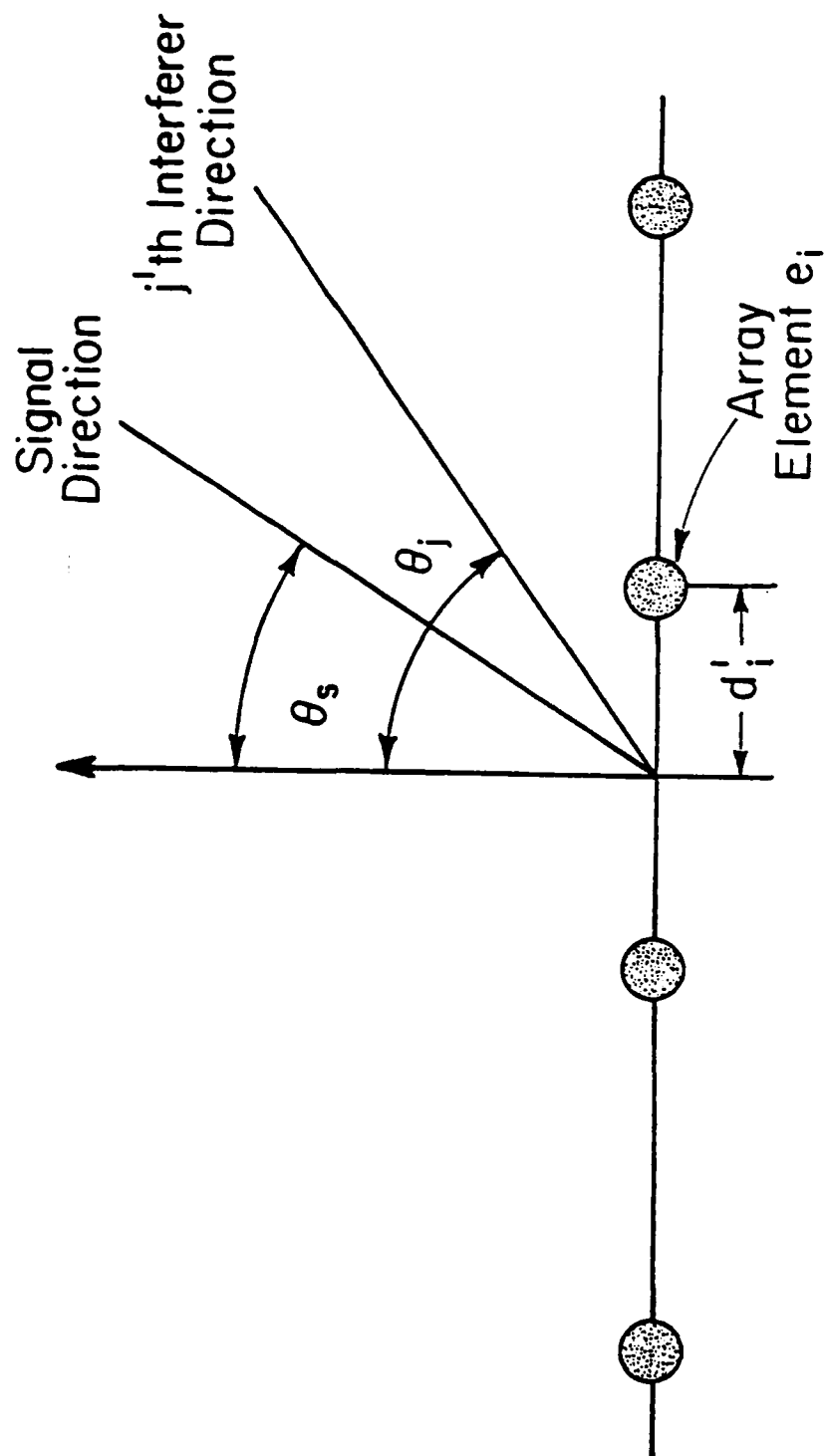Generation of Array Element Output Signals.

Figure 2

Linear Array Geometry Illustrating
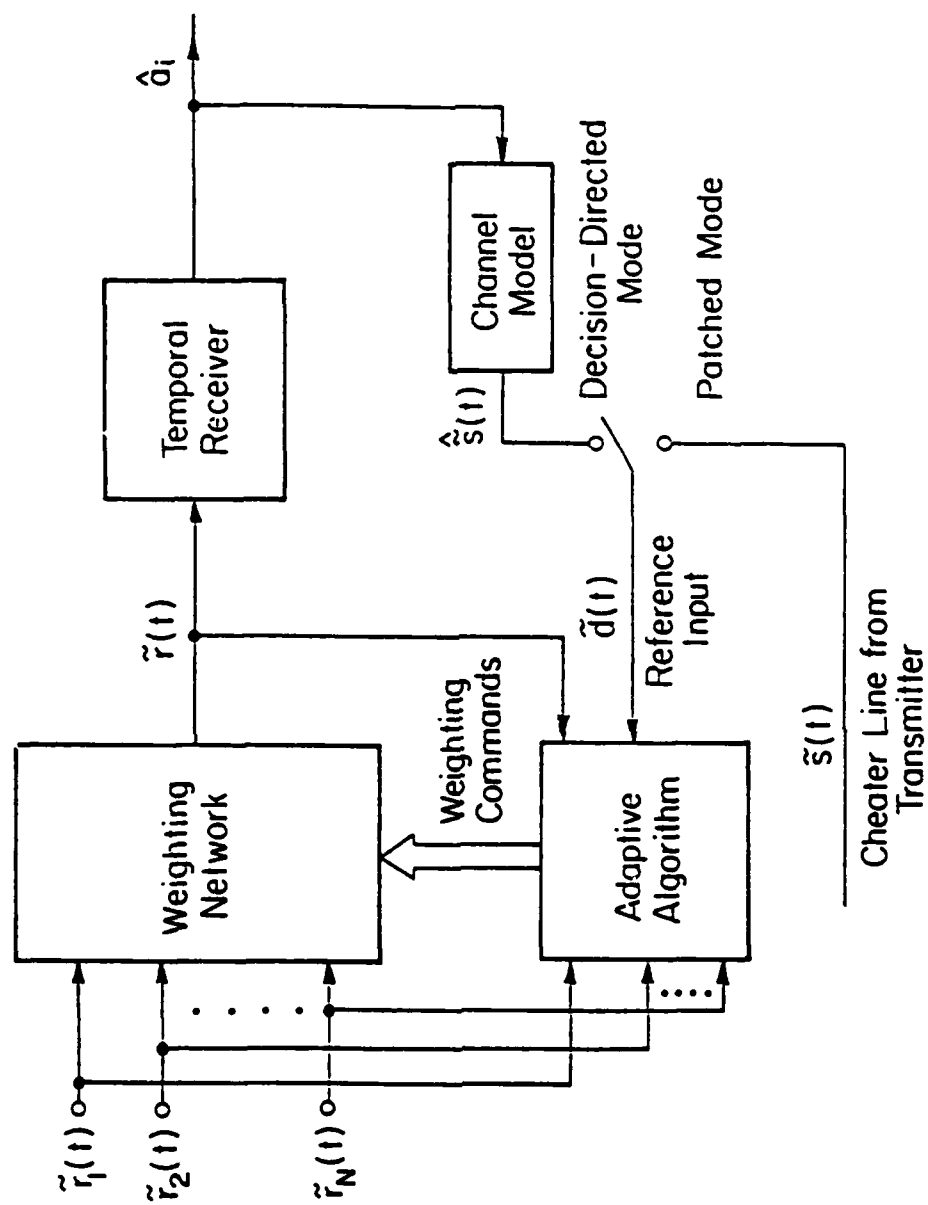Signal and Interference Directions.

Figure 3

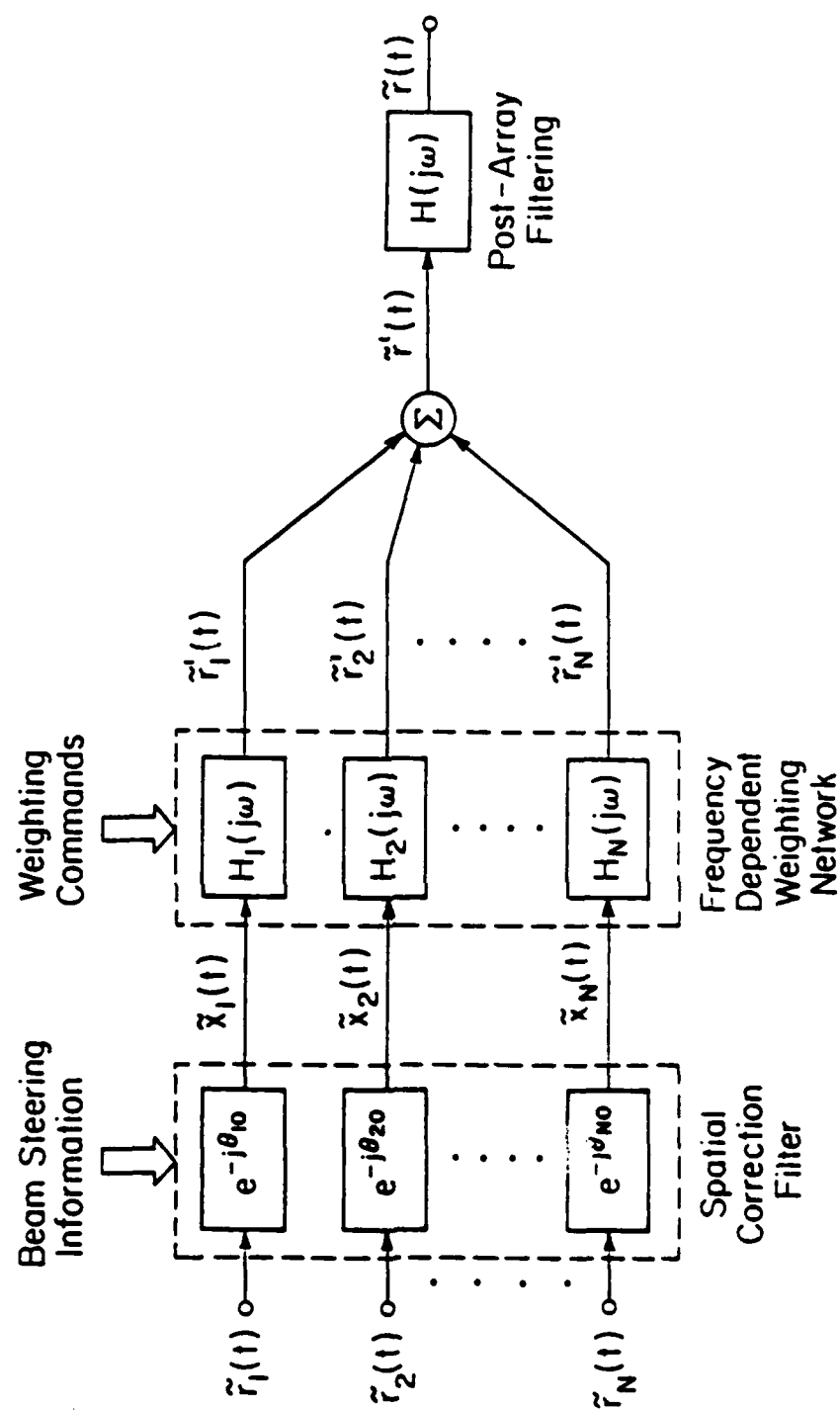Adaptive Array Processing Configuration

Figure 4
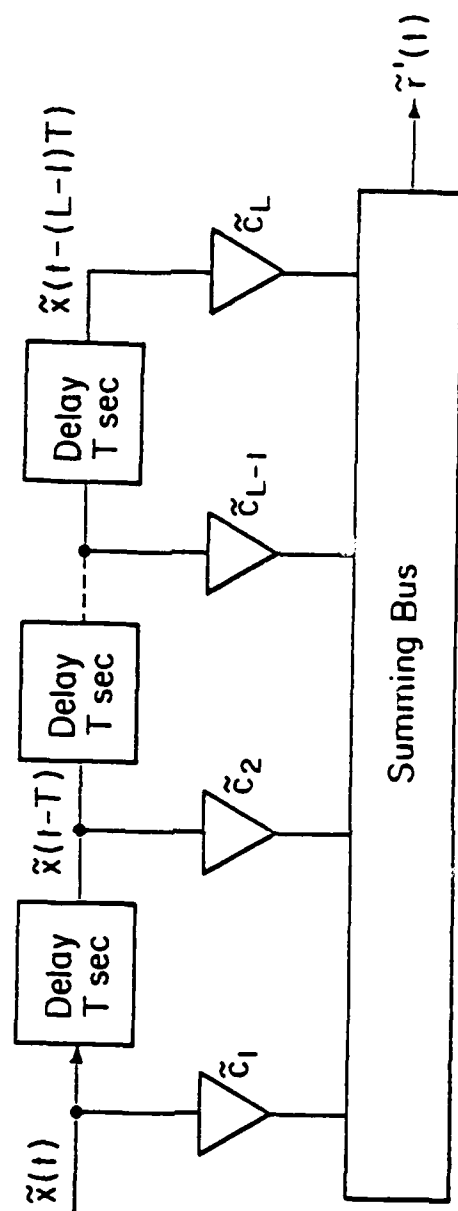
Structure of Element Weighting Network.

Figure 5

Illustration of Complex-Weighted Tapped
Delay Line Filter $H(j\omega; \underline{\tilde{c}})$

END

FILMED

6-83

DTIC